Search for non-resonant Higgs-pair production in the $b\bar{b}b\bar{b}$ final state with the ATLAS detector

ATLAS 実験における非共鳴ヒッグス対生成 $b\bar{b}b\bar{b}$ 終状態事象の探索

Shota HAYASHIDA

High Energy Physics Laboratory
Department of Physics, Nagoya University

February 6, 2023

Abstract

The Standard Model (SM) of particle physics succeeds to describe the origin of particle mass by introducing the electroweak symmetry breaking (EWSB). However, we have not yet experimentally proven the actual structure of the Higgs potential, which is responsible for the EWSB. Several types of the Higgs potential are predicted in new physics scenarios such as electroweak baryogenesis. The Higgs potential can be determined only by measuring the Higgs self-couplings. I thus focus on the trilinear Higgs self-couplings, which is a coupling constant of the interaction of three Higgs bosons.

This thesis presents a search for non-resonant Higgs pair production in the $b\bar{b}b\bar{b}$ final states ($pp \rightarrow HH \rightarrow b\bar{b}b\bar{b}$) using 126 fb^{-1} of proton–proton collisions at a centre-of-mass energy of $\sqrt{s}$ = 13 TeV taken with the ATLAS detector. HH production via the two leading production modes, gluon-gluon fusion (ggF) and vector-boson fusion (VBF), are sensitive to the trilinear Higgs self-coupling (κ_λ) and the two Higgs bosons and two vector bosons ($HHVV$) coupling (κ_{2V}), where κ_λ and κ_{2V} are defined as the coupling ratios with respect to the SM predictions. The $b\bar{b}b\bar{b}$ final state, where both Higgs bosons decay to a pair of $b-$ and $\bar{b}-$quarks, is one of the most sensitive channels thanks to the highest branching ratio. On the other hand, the search in the $b\bar{b}b\bar{b}$ final state is challenging due to a huge amount of QCD multijet background.

I developed a new analysis for the non-resonant $HH \rightarrow b\bar{b}b\bar{b}$. Two orthogonal selections targeting the ggF and VBF production are provided to increase the sensitivity for each production mode. I additionally adopted analysis categorizations in both selections to improve the sensitivity. The crucial key in this analysis is background estimation, because it is hard to model QCD multijet background in simulation. I thus utilized a fully data-driven approach using a novel neural network to properly estimate the background.

No evidence for the HH production is found, and the exclusion limits at 95% confidence level are set on the signal strength, which is defined as the ratio of the observed cross-section to the SM prediction, of the ggF +VBF HH production cross-section, the trilinear Higgs self-coupling and the $HHVV$ coupling. The observed (expected) upper limit on the signal strength is set to 5.4 (8.1). The observed (expected) allowed region on the trilinear Higgs self-coupling is $\kappa_\lambda \in [-3.9, 11.1]$ ($[-4.6, 10.8]$). The observed (expected) allowed region on the $HHVV$ coupling is $\kappa_{2V} \in [-0.03, 2.11]$ ($[-0.05, 2.12]$). These results are consistent with the SM prediction ($\kappa_\lambda = \kappa_{2V} = 1$). They are the first results derived from the analysis targeting non-resonant $HH \rightarrow b\bar{b}b\bar{b}$ and improve these constraints by a factor of 2-4 with respect to the previous analyses. This thesis also presents the interpretation results using Effective Field Theory frameworks.

This thesis additionally presents a statistical combination of three HH analyses in the $b\bar{b}b\bar{b}$, $b\bar{b}\gamma\gamma$ and $b\bar{b}\tau\tau$ final states with up to 139 fb^{-1} of proton–proton collisions at $\sqrt{s}$ = 13 TeV in the ATLAS experiment. The $b\bar{b}b\bar{b}$, $b\bar{b}\gamma\gamma$ and $b\bar{b}\tau\tau$ final states provide the highest sensitivity for the signal strength, the trilinear Higgs self-coupling and the $HHVV$ coupling, and the statistical combination improves the constraints. The observed (expected) upper limit on the signal strength is 2.4 (2.9). The allowed region on the trilinear Higgs self-coupling is $\kappa_\lambda \in [-0.6, 6.6]$ ($[-1.0, 7.1]$) and on the $HHVV$ coupling is $\kappa_{2V} \in [0.07, 2.03]$ ($[0.02, 2.06]$).

Contents

Chapter 1

Introduction

The origin of all *things* in the universe, such as *matter* we are familiar with and fundamental interactions also known as forces, is an ultimate question of human beings. Particle physics has been promoted to answer this question in both theoretical and experimental approaches for over 100 years. There was one crucial problem that can not describe the origin of particle masses until July 2012. With the Higgs boson discovery [1,2] at the ATLAS [3] and CMS [4] experiments at the Large Hadron Collider (LHC) in 2012, the Standard Model (SM) in particle physics has been established. The SM succeeds in explaining the origin of particle masses as well as most of the phenomena in the universe with the quarks and leptons that form *matter*, gauge bosons that transmit forces and the Higgs boson that gives the masses.

The pursuit of particle physics is not over yet after the SM was established. The electroweak symmetry breaking (EWSB) is the key mechanism to describe the origin of particle masses with the Higgs boson in the SM. The Higgs potential is a key factor for the EWSB and is assumed to form a Mexican hat like shape in the SM. However, the actual shape of the Higgs potential has not yet been directly validated by any experiments, and it is the most weakness component in the SM. In addition, there are still some theoretical and cosmological problems in the SM, such as baryon asymmetry of the universe and dark matter. All remaining problems require new physics beyond the Standard Model (BSM). These BSM theories predict several different types of the Higgs potential compared with the SM prediction. Determination of the Higgs potential requires the measurement of the Higgs self-couplings. In particular, the trilinear Higgs self-coupling (λ_{HHH}), which is a coupling constant of the interaction of three Higgs bosons, is considered the only one of the Higgs self-couplings accessible in the current high-energy frontier experiments. Therefore, a measurement of the trilinear Higgs self-coupling is one of the most crucial quests in the particle physics.

To measure the trilinear Higgs self-coupling, I focused on non-resonant Higgs pair (di-Higgs, HH) production in the $b\bar{b}b\bar{b}$ final state ($HH \rightarrow b\bar{b}b\bar{b}$). The two major processes of the HH production are gluon-gluon fusion (ggF) and vector-boson fusion (VBF). These production cross-sections and kinematics directly depend on the trilinear Higgs self-coupling and the two Higgs bosons and two vector bosons ($HHVV$) coupling. By searching for the non-resonant HH production and investigating the kinematic shapes, these couplings can be measured or constrained. The $b\bar{b}b\bar{b}$ final state, where both Higgs bosons decay to a pair of $b-$ and $\bar{b}-$quarks, is one of the most sensitive channels thanks to the highest branching ratio of approximately 34%. However, the $b\bar{b}b\bar{b}$ final state is also a challenging channel due to a huge amount of QCD multijet background.

Two previous searches for the $HH \to b\bar{b}b\bar{b}$ production via ggF process using 36.1 fb^{-1} of proton-proton collisions at a centre-of-mass energy of $\sqrt{s} = 13$ TeV and via VBF process using 126 fb^{-1} of proton-proton collisions were performed in the ATLAS experiment [5–7]. In the previous analyses, no evidence for the $HH \to b\bar{b}b\bar{b}$ production was found. The observed (expected) upper limit on the signal strength, which is defined as the ratio of the observed cross-section to the SM prediction, of the ggF HH cross-section at 95% confidence level was set to 12.9 (20.7), and that of the VBF HH cross-section was 840 (550). The observed (expected) limit interval on κ_λ was in $[-10.9, 20.1]$ ($[-11.6, 18.8]$) and that on κ_{2V} was in $[-0.43, 2.56]$ ($[-0.55, 2.72]$), where κ_λ and κ_{2V} are defined as the ratios to the SM predictions. However, these analyses mainly focused on resonant HH production from a new particle ($X \to HH$), such as a spin-2 Kaluza-Klein graviton predicted in the bulk Randall-Sundrum model [8, 9] and a heavy spin-0 scalar in two-Higgs-double models [10, 11]. This means that they did not aim for measurements of the trilinear Higgs self-coupling and the $HHVV$ coupling and these results are not performed with the maximum sensitivity for these couplings. Since the kinematics of non-resonant and resonant HH production are significantly different, further improvements in the analysis strategy can be expected. Therefore, I decided to develop a new analysis for these coupling measurements, which is the first analysis optimized for the non-resonant $HH \to b\bar{b}b\bar{b}$ production in the ATLAS experiment.

I performed a search for the non-resonant HH production in the $b\bar{b}b\bar{b}$ final state using 126 fb^{-1} of proton-proton collisions at a centre-of-mass energy of $\sqrt{s} = 13$ TeV accumulated with the ATLAS detector. A variety of improvements were introduced in the analysis strategy since the previous analyses [5, 6]. I provided two orthogonal selections targeting each of the ggF and VBF production processes, because their topologies are significantly different. A new method for pairing jets when reconstructing two Higgs boson candidates was prepared for the non-resonant $HH \to b\bar{b}b\bar{b}$ process. To improve the sensitivity, the analysis employed analysis categorizations in the two selections, respectively. The method of QCD multijet background estimation is crucial key in this analysis, because it is hard to model it in simulation and the usual method is found not to work in this analysis. I thus utilized a fully data-driven approach using a novel neural network to properly estimate QCD multijet background.

In addition, I performed a statistical combination using three HH searches in the $b\bar{b}b\bar{b}$, $b\bar{b}\gamma\gamma$ and $b\bar{b}\tau\tau$ final states with up to 139 fb^{-1} of proton-proton collisions at $\sqrt{s} = 13$ TeV in the ATLAS experiment. The $b\bar{b}b\bar{b}$, $b\bar{b}\gamma\gamma$ and $b\bar{b}\tau\tau$ final states have the highest sensitivity for the HH search. The statistical combination of these results improves the constraints on the signal strength, the trilinear Higgs self-coupling and the $HHVV$ coupling, and gives the leading limits for the HH analysis. In this thesis, the results of both non-resonant $HH \to b\bar{b}b\bar{b}$ analysis and the HH statistical combination will be discussed.

This thesis is organized as follows. The first part consists of introductory chapters describing theoretical backgrounds, an overview of experimental apparatus and toolkits used in this analysis:

Chapter 2 describes the theoretical backgrounds that motivate this analysis,

Chapter 3 overviews the Large Hadron Collider and the ATLAS detector,

Chapter 4 describes algorithms used for object reconstructions and particle identifications,

Chapter 5 describes data and simulation samples used in this analysis.

The main descriptions of the non-resonant $HH \to b\bar{b}b\bar{b}$ analysis are given in:

Chapter 6 describes the analysis strategy and selection that enhance non-resonant $HH \to b\bar{b}b\bar{b}$ signal and suppress backgrounds,

Chapter 7 describes the analysis categorizations that enhance the sensitivity,

Chapter 8 shows the background estimation procedure and its validations,

Chapter 9 explains systematic uncertainties associated with the background estimation and signal modelling,

Chapter 10 explains statistical analysis method that tests signal hypotheses and compatibility.

The results and discussions are given in:

Chapter 11 shows the results of the non-resonant $HH \to b\bar{b}b\bar{b}$ analysis,

Chapter 12 discusses the results of the HH statistical combination and the prospects of the HH analysis and the measurement of the trilinear self-coupling for the future experiment.

This analysis has been performed with a lot of cooperation from the ATLAS $HH \to b\bar{b}b\bar{b}$ analysis team, which consists of more than 40 members. My contributions are clarified in the following. My main contributions are validation studies of the background estimation procedure described in Chapter 8 and finalization studies of the non-resonant $HH \to b\bar{b}b\bar{b}$ results described in Chapter 11. In the non-resonant $HH \to b\bar{b}b\bar{b}$ analysis, the most important topic is background estimation. I performed several approaches to validate the background estimation procedure. I also derived the analysis results on behalf of the analysis team. In addition, I also organized the analysis categorization studies, such as a combination of multiple categorizations and the performance test of the low p_{T} category discussed in Chapter 12. In the HH statistical combination, I took a role of a combination liaison on behalf of the $HH \to b\bar{b}b\bar{b}$ analysis team and pushed the study toward the publication.

Chapter 2

Theoretical Background

This chapter provides the theoretical background motivating the analysis described in this thesis. It introduces the current best theory of particle physics and theoretical remaining issues. The approaches of this analysis to these issues are described.

2.1 The Standard Model of Particle Physics

The Standard Model of particle physics (SM), is a theory of particle physics to successfully describe all fundamental particles currently observed and three of the four forces by a Lagrangian. The Lagrangian is constructed to conserve a global Lorentz symmetry, a global translational symmetry and the local gauge symmetries, SU(3) $\times$ SU(2) $\times$ U(1). In the field of particle physics, the theory has achieved a lot of success. The SM theory has established around 1970, and then predictions of the SM have been proven to match the experimental results repeatedly, such as Z-boson [12], W-boson [13], top quark [14] and Higgs boson [1, 2]. The basic descriptions of the SM until the electroweak symmetry breaking, which is the topic of this thesis, are presented in this section.

2.1.1 Elementary Particles

The SM includes several types of *elementary particles*, as shown in Table 2.1,2.2. Each elementary particle has a *spin*, which indicates its intrinsic angular momentum and is related to its behaviour. They are firstly distinguished into three types, *fermions*, *gauge bosons* and *Higgs boson*. Elementary particles with a half-integer spin are called fermions, which are the elementary constituents of *matter*. On the other hand, elementary particles with a spin of 1 are called gauge bosons. Gauge bosons play a role in mediating the fundamental interaction between particles. Higgs boson is a scalar boson with a spin of 0, and plays the special role in feeding masses to fermions and gauge bosons.

There are three types of gauge bosons, *gluon* (g), *weak bosons* ($W^{\pm}, Z$) and *photon* (γ). Three fundamental interactions are defined in each local gauge symmetry as described in Section 2.1.3. The U(1), SU(2) and SU(3) invariants are related to *electromagnetic interaction*, *weak interaction* and *strong interaction*, respectively. The gauge bosons are required by the invariant of the theory in each local gauge symmetry. Photons, weak bosons and gluons mediate respectively the electromagnetic interaction, the weak interaction and the strong interaction.

Fermions can be classified into two classes, *quarks* and *leptons*, according to the interactions. Quarks interact via all three interactions, while leptons interact only via the weak and electromagnetic interactions. They have two types, up-type and down-type, that classify according to its weak isospin charge, and each class is divided into pairs of particles that have the same properties except for its mass, called *generation*. In total six quarks (*up, down, charm, strange, top, bottom*) and six leptons (*electron, electron neutrino, muon, muon neutrino, tau, tau neutrino*) exist. These quarks are referred to as X-quarks by taking the initial letter of its name. For example, up quark is referred to u-quark. Each fermion has the corresponding partner with opposite charge such as electric charge. The partners are called anti-fermions.

Fermion Type	Symbol & Generation 1st	2nd	3rd	S	Q	T^3	Y
Quarks	$\begin{pmatrix} u_L \\ d_L \end{pmatrix}$	$\begin{pmatrix} c_L \\ s_L \end{pmatrix}$	$\begin{pmatrix} t_L \\ b_L \end{pmatrix}$	1/2	$\begin{pmatrix} 2/3 \\ -1/3 \end{pmatrix}$	$\begin{pmatrix} 1/2 \\ -1/2 \end{pmatrix}$	1/3
	u_R	c_R	t_R	1/2	2/3	0	4/3
	d_R	s_R	b_R	1/2	-1/3	0	-2/3
Leptons	$\begin{pmatrix} \nu_{eL} \\ e_L \end{pmatrix}$	$\begin{pmatrix} \nu_{\mu L} \\ \mu_L \end{pmatrix}$	$\begin{pmatrix} \nu_{\tau L} \\ \tau_L \end{pmatrix}$	1/2	$\begin{pmatrix} 0 \\ -1 \end{pmatrix}$	$\begin{pmatrix} 1/2 \\ -1/2 \end{pmatrix}$	-1
	ν_{eR}	$\nu_{\mu R}$	$\nu_{\tau R}$	1/2	0	0	0
	e_R	μ_R	τ_R	1/2	-1	0	-2

Table 2.1 The quantum numbers of fermions in the Standard Model. S, Q, T^3 and Y are respectively the spin, the electric charge from $U(1)_Q$, the third component of week isospin from $\mathrm{SU(2)_L}$ and the weak hypercharge from $\mathrm{U(1)_Y}$. The values for ν_R are shown for the case that they exist.

	Symbol	S	Q	T^3	Y
gluon	g	1	0	0	0
weak bosons	$W^\pm$	1	±1	±1	0
	Z	1	0	0	0
photon	γ	1	0	0	0
Higgs boson	h	0	0	$-1/2$	1

Table 2.2 The quantum numbers of gauge bosons and Higgs boson in the Standard Model. S, Q, T^3 and Y are respectively the spin, the electric charge from $U(1)_Q$, the third component of week isospin from $\mathrm{SU(2)_L}$ and the weak hypercharge from $\mathrm{U(1)_Y}$.

2.1.2 Gauge Principles

The SM is a relativistic quantum field theory, where all terms such as the kinetic term and the mass term of fundamental particles and interactions are described in quantum fields. The Lagrangian for an electrically charged particle (fermion) in free field is given by

$$\mathcal{L} = i\bar{\psi}\gamma^{\mu}\partial_{\mu}\psi - m\bar{\psi}\psi, \tag{2.1}$$

where ψ is a spinor field corresponding to a fermion with the mass of m, and γ^{μ} is the 4-dimensional gamma matrices. In Eq. 2.1, the first term corresponds to the kinetic term which describes the motion of the fermion, and the second term is the mass term.

The Lagrangian should be invariant (symmetric) under a local group transformation, such as a phase transformation and a time-space dependent phase transformation (local U(1) transformation). These transformations are called *gauge transformations*. For example, the local U(1) transformation is given as:

$$\psi \rightarrow e^{i\alpha(x)Q}\psi, \tag{2.2}$$

where $\alpha(x)$ is an arbitrary time-space dependent phase and Q is called the generator of U(1). The generator of U(1) transformation corresponds to electric charge q of the fermion. The Lagrangian is found to be not invariant under local U(1) transformation. However, it is fixable by introducing a covariant derivative D_{μ} as:

$$\partial_{\mu} \rightarrow D_{\mu} = \partial_{\mu} - iqA_{\mu}, \tag{2.3}$$

where A_{μ} is a vector field called a interacting field. It is translated by local U(1) transformation as:

$$A_{\mu} \rightarrow A_{\mu} + \delta A_{\mu} = A_{\mu} + \frac{1}{q}\partial_{\mu}\alpha(x) \tag{2.4}$$

As a result, an extra term is derived. It corresponds to the interaction term between ψ and A_{μ}.

$$\mathcal{L}_{int.} = q\bar{\psi}\gamma^{\mu}\psi A_{\mu} \tag{2.5}$$

This means that fermions interact via the gauge field A_{μ}. Finally, the Lagrangian for a fermion in the gauge field is described by adding a kinetic term $-\frac{1}{4}F_{\mu\nu}F^{\mu\nu}$ of the gauge field A_{μ} with Lorentz and gauge invariances.

$$\mathcal{L} = -\frac{1}{4}F_{\mu\nu}F^{\mu\nu} + i\bar{\psi}\gamma^{\mu}D_{\mu}\psi - m\bar{\psi}\psi, \tag{2.6}$$

where $F_{\mu\nu}$ is defined to satisfy a global Lorentz invariance and gauge invariance as:

$$F_{\mu\nu} = \partial_{\mu}A_{\nu} - \partial_{\nu}A_{\mu} \tag{2.7}$$

We already know something about how electrons interact in the electromagnetic interaction. The A_{μ} field corresponds to the photon field, which carries the electric charge of fermions. This Lagrangian succeeds in describing historical roles of the electromagnetic interaction. The theory describing phenomena involving the electromagnetic interaction is called the Quantum Electromagnetic (QED). The U(1) symmetry in the QED is written as $U(1)_{Q}$ to distinguish the one in the Electroweak Theory. Similarly to the U(1) symmetry, the SM Lagrangian is constructed by the local gauge symmetries and succeeds in

describing the interactions.

2.1.3 Electroweak Theory and QCD

Electroweak Theory

The Electroweak theory [15–17] describes physical phenomena involving the electromagnetic interaction and the weak interaction, expanding the QED theory. The idea of the theory is that the two interactions share a common origin at high energy scale and they are separated from it at that point through a spontaneous symmetry breaking $\mathrm{SU(2)_L} \times \mathrm{U(1)_Y} \rightarrow \mathrm{U(1)_Q}$ (Electroweak Symmetry Breaking, EWSB).

SU(n) is the group of special unitary transformations and is written as Eq. 2.8.

$$\psi \rightarrow e^{i\theta_a(x)T^a}\psi \quad (a = 1, 2, ..., (N^2 - 1)), \tag{2.8}$$

where $a \in \left\{1, 2, ..., (N^2 - 1)\right\}$ are real parameters and T^a is called the generator of the SU(n) group. T^a for SU(2) corresponds to *weak isospin* T, which the third component is labelled as T^3, and for SU(3) corresponds to *colors*. SU(n) transformation is non-abelian, and this means that different elements of the group do not commute with each other on the transformation. This acts on the fermion fields to carries a fermion i to j as:

$$\psi_i \rightarrow \left(e^{i\theta_a(x)T^a}\right)_i^j \psi_j \tag{2.9}$$

$\mathrm{SU(2)_L}$ indicates particularly the left-chirality of the SU(2) gauge transformation and acts only to the left-handed component of fermions. The choice of $\mathrm{SU(2)_L}$ is motivated by the observation of isospin symmetry and the observed phenomenon that parity conservation is violated in the weak interaction [18, 19]. In $\mathrm{U(1)_Y}$, the subscript Y denotes weak hypercharge and is also used to distinguish from $\mathrm{U(1)_Q}$ symmetry after the EWSB described in Section 2.1.2. $\mathrm{SU(2)_L} \times \mathrm{U(1)_Y}$ transformation is given by

$$\psi_L \rightarrow e^{i\theta_3 T^3 + i\alpha Y}\psi_L \tag{2.10}$$

$$\psi_R \rightarrow e^{i\alpha Y}\psi_R, \tag{2.11}$$

where ψ_L and ψ_R are the left-handed and right-handed component of the fermion field *phi*, respectively. Similar to what is done in the QED theory, the Lagrangian for the electroweak theory can be derived by considering to be gauge invariant on the $\mathrm{SU(2)_L} \times \mathrm{U(1)_Y}$ transformation.

$$\mathcal{L}_{EW} = -\frac{1}{4}\mathbf{W}_{\mu\nu}\mathbf{W}^{\mu\nu} - \frac{1}{4}B_{\mu\nu}B^{\mu\nu} + i\bar{\psi}\gamma^\mu D_\mu \psi \tag{2.12}$$

$$D_\mu = \partial_\mu + ig\sum_{a=1}^{3} T^a W_\mu^a + ig'\frac{Y}{2}B_\mu \tag{2.13}$$

$$\mathbf{W}_{\mu\nu} = \partial_\mu W_\nu^a - \partial_\nu W_\mu^a - g\epsilon^{abs}W_\mu^b W_\nu^c \quad (a = 1, 2, 3) \tag{2.14}$$

$$B_{\mu\nu} = \partial_\mu B_\nu - \partial_\nu B_\mu, \tag{2.15}$$

where g and g' are the couplings for $\mathrm{SU(2)_L}$ and $\mathrm{U(1)_Y}$, respectively. The gauge fields W_μ^i and B_μ are the

force carriers of the electroweak theory. W_μ^i can be converted into charge states, W_μ^+, W_μ^0 and W_μ^-.

$$W_\mu^\pm = \frac{W_\mu^1 \mp iW_\mu^2}{\sqrt{2}}, \quad W_\mu^0 = W_\mu^3 \tag{2.16}$$

In addition, we can argue that we should assume the electromagnetic field A_μ is constructed from a combination of B_μ and W_μ^0. They are mixed with a mixing angle (Weinberg angle, θ_W) based on the observed phenomenon that neutrinos have no electromagnetic interaction.

$$\begin{pmatrix} Z_\mu \\ A_\mu \end{pmatrix} = \begin{pmatrix} \cos\theta_W & -\sin\theta_W \\ \sin\theta_W & \cos\theta_W \end{pmatrix} \begin{pmatrix} W_\mu^0 \\ B_\mu \end{pmatrix} \tag{2.17}$$

$$\sin\theta_W = \frac{g'}{\sqrt{g^2 + g'^2}}, \quad \cos\theta_W = \frac{g}{\sqrt{g^2 + g'^2}} \tag{2.18}$$

In Eq. 2.17, the B_μ and W_μ^0 mixing forms not only A_μ but also Z_μ, which is an additional neutral current field interacting with both leptons and neutrinos. Indeed, Z-boson [12] and W-boson [13] have been observed in experiments. This theory well describes the phenomena involving the electroweak interaction. However, in the Lagrangian described in Eq. 2.12, it is impossible to add these particle mass terms with the gauge invariance. The mass terms are indeed obtained via EWSB described in Section 2.1.4.

Quantum Chromodynamics Theory (QCD)

The Quantum Chromodynamics (QCD) theory is the gauge field theory with the SU(3) symmetry describing physical phenomena involving the strong interaction. The SU(3) transformation is the group of all 3×3 unitary matrices with determinant one. This acts on a triplet of fields q, corresponding to *quarks* so that q carries an index i to $j \in 1, 2, 3$. The SU(3) transformation can be written by

$$q_i \to \left(e^{i\theta_a(x)T^a}\right)_i^j q_j \tag{2.19}$$

The quantum number of SU(3) associated with the label i corresponds to *colors*. For the SU(3) invariance, it needs to introduce $3^2 - 1 = 8$ new vector fields, G_μ^a, which correspond to the observed particle called *gluon*. The interaction of the gluons and the quarks is determined by gauge invariance and obtained by replacing the ordinary derivative with the covariant derivative,

$$D_\mu = \partial_\mu + ig_s \sum_{a=1}^{8} \frac{T^a}{2} G_\mu^a \tag{2.20}$$

where g_s is related to the strong coupling constant $\alpha_s = g_s^2/4\pi$. The Lagrangian of the QCD with the SU(3) invariance is then given by

$$\mathcal{L}_{QCD} = -\frac{1}{4}\mathbf{G}_{\mu\nu}\mathbf{G}^{\mu\nu} + i\bar{q}\gamma^\mu D_\mu q \tag{2.21}$$

$$\mathbf{G}_{\mu\nu} = \partial_\mu G_\nu^a - \partial_\nu G_\mu^a - g_s f^{abc} A_\mu^b A_\nu^c \quad (a = 1, 2, ..., 8) \tag{2.22}$$

Similarly to the electroweak theory, the mass terms of quarks, $-i\bar{q}^i m\delta_{ij}\bar{q}^j$, where δ_{ij} is the Kronecker delta, would violate gauge invariance due to the flavor changing currents of SU(2). The quark mass terms are also obtained via EWSB. The summary of fermion contents discussed above, such as its electro charge, is shown in Table 2.1.

2.1.4 Electroweak Symmetry Breaking and Higgs Boson

The final component of the SM is the Higgs field. The problem in the electroweak theory and QCD theory is that the description of these particle mass terms is forbidden. In the SM, the mass terms are provided by the Brout-Englert-Higgs (BEH) mechanism [20, 21]. In the BEH mechanism, a complex scalar field ($\boldsymbol{\phi}$) is introduced. The complex scalar field is a doublet under $SU(2)_L$ and is written as Eq. 2.23.

$$\boldsymbol{\phi} = \begin{pmatrix} \phi_1 + i\phi_2 \\ \phi_3 + i\phi_4 \end{pmatrix} = \begin{pmatrix} \phi^+ \\ \phi^0 \end{pmatrix}, \tag{2.23}$$

where ϕ^+ and ϕ^0 are labelled as their charges before being realized $U(1)_Q$ symmetry. This SU(2) double field is called *Higgs field*. In the SM, the Higgs field forms the following potential.

$$V(\boldsymbol{\phi}) = -\mu^2\boldsymbol{\phi}^\dagger\boldsymbol{\phi} + \lambda\left(\boldsymbol{\phi}^\dagger\boldsymbol{\phi}\right)^2 \tag{2.24}$$

μ and λ are Higgs potential parameters. The Lagrangian related to the Higgs field is then formed by the Higgs potential and a kinetic term of the Higgs field.

$$\mathcal{L}_{Higgs} = \left(D_\mu\boldsymbol{\phi}\right)^\dagger\left(D^\mu\boldsymbol{\phi}\right) + \mu^2\boldsymbol{\phi}^\dagger\boldsymbol{\phi} - \lambda\left(\boldsymbol{\phi}^\dagger\boldsymbol{\phi}\right)^2 \tag{2.25}$$

The minimum of the Higgs potential is related to the vacuum expectation value (v). To ensure that the Higgs potential is bounded below and well explains vacuum state, the parameters must be $\lambda \geq 0$ if $\mu^2 > 0$ else $\lambda > 0$. In the case of $\mu^2 > 0$ and $\lambda \geq 0$, the minimum of the Higgs potential is always located at $\boldsymbol{\phi} = (0, 0)$ in the ϕ_1 - ϕ_2 planes shown in Figure 2.1(a). However, in that case of $\mu^2 < 0$ and $\lambda > 0$, the Higgs potential forms a Mexican hat potential shown in Figure 2.1(b). The minimum of the Higgs potential then shifts into

$$|\boldsymbol{\phi}|^2 = -\frac{\mu^2}{2\lambda}. \tag{2.26}$$

The vacuum expectation value can be defined as Eq. 2.27.

$$v \equiv \sqrt{\frac{\mu^2}{\lambda}} = 246\ \text{GeV} \tag{2.27}$$

This means that the vacuum expectation value is shifted at that point, $v = 0 \rightarrow \sqrt{\mu^2/\lambda}$. This expected phenomenon is referred to as *electroweak symmetry breaking* (EWSB).

The Higgs field in Eq. 2.23 can be parameterized as Eq. 2.28 to describe the Higgs interactions

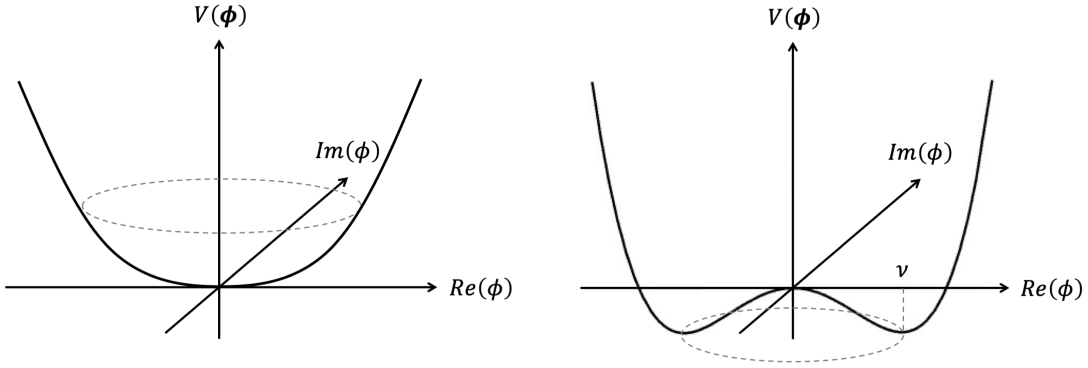

(a) $\mu^2 > 0$ (b) $\mu^2 < 0$

Figure 2.1 Higgs potential for (a) $\mu^2 > 0$ and (b) $\mu^2 < 0$.

around the new vacuum.

$$\boldsymbol{\phi} = \frac{1}{\sqrt{2}} \begin{pmatrix} 0 \\ v + h(x) \end{pmatrix}, \tag{2.28}$$

where h is a real scalar field corresponding to a physical Higgs boson. A fluctuation around the new vacuum spontaneously breaks the rotational symmetry of the Higgs field. A new form of the Higgs potential $V(h)$ in the SM is obtained as Eq. 2.29.

$$\begin{aligned} V(h) &= -\mu^2 h^2 - \lambda v h^3 - \frac{\lambda}{4} h^4 \\ &= \frac{1}{2} m_H^2 h^2 - \lambda_{HHH} v h^3 - \lambda_{HHHH} h^4 \end{aligned} \tag{2.29}$$

The first term corresponds to the mass term of the Higgs field and gives the Higgs boson mass $m_H \equiv \sqrt{-2\mu^2} = \sqrt{2\lambda v^2}$. The second term describes the self-interaction of three Higgs bosons, and the third term is the self-interaction of four Higgs bosons. λ_{HHH} is called the trilinear Higgs self-coupling, and λ_{HHHH} is called the quartic Higgs self-coupling.

$$\lambda_{HHH} = \frac{m_H^2}{2v^2}, \quad \lambda_{HHHH} = \frac{m_H^2}{8v^2} \tag{2.30}$$

The Higgs kinetic term with SU(2) is also redefined to be gauge invariant around the new vacuum as:

$$\left(D_\mu \boldsymbol{\phi}\right)^2 = \frac{1}{2}\left(\partial_\mu h\right)^2 + \frac{g^2 v^2}{4} W_\mu^+ W^{-\mu} \left(1 + \frac{h}{v}\right)^2 + \frac{g^2 v^2}{8\cos^2\theta_W} Z_\mu Z^\mu \left(1 + \frac{h}{v}\right)^2 \tag{2.31}$$

These eigenstates are familiar with photon, $W^\pm$ boson and Z boson. The second term corresponds to the mass terms for $W^\pm$ boson. The third term is the mass term for Z boson. The $W^\pm$ and Z boson masses are

then obtained as

$$m_W = \frac{g v}{2} \tag{2.32}$$

$$m_Z = \frac{g v}{2\cos\theta_W} = \frac{v}{2}\sqrt{g^2 + g'^2} \tag{2.33}$$

The A_μ field corresponding to photon is expressed as a massless field, since the coupling between photon and Higgs boson is zero.

Similar to what is done in the Higgs kinetic term, the interaction term of the Higgs boson with fermions ($\mathcal{L}_{Yukawa}$), known as the Yukawa interaction, can be considered around the new vacuum. The Yukawa Lagrangian is expressed by:

$$\mathcal{L}_{Yukawa} = -\sum_f \left(y_f \bar{\phi}_{fR}\phi_{fL} + y_f \bar{\phi}_{fL}\phi_{fR}\right)\left(\frac{v+h}{\sqrt{2}}\right), \tag{2.34}$$

where f is the index of fermions and y_f is the Yukawa coupling constant. The first term in the Lagrangian corresponds to the fermion mass term, and the fermion mass is obtained as $y_f v/\sqrt{2}$. As described above, the Brout-Englert-Higgs (BEH) mechanism describes successfully the origin of masses for gauge bosons and fermions by the Higgs field.

2.1.5 Successes and Next Quests

The SM is an extremely successful theory to describe physical phenomena in particle physics. The SM theory has been repeatedly verified over several decades. For example, the SM had predicted a new particle that is related to the electroweak symmetry breaking and plays a role in feeding particle masses, as described in Section 2.1.4. Indeed, a new particle with a mass of 125 GeV has been observed in the ATLAS and CMC experiments in 2012 [3, 4]. In addition, several measurements of the new particle properties have been performed in the ATLAS and CMS experiments, and the observed properties such as the Yukawa couplings (Figure 2.2) are found to be consistent with the Higgs boson in the SM predictions. With the Higgs boson discovery, the BEH mechanism has been experimentally proven and all particles predicted in the SM have been discovered. All free parameters in the SM are then known with the measurement of the Higgs boson mass.

However, there are still unknown issues about the Higgs boson, such as the shape of the Higgs potential and the origin of the EWSB. In the SM, the Higgs boson is assumed as an elementary scalar field as described in Eq. 2.28 and the mass parameter μ^2 is then assumed to be negative, which triggers the EWSB. However, this assumption in the SM has not yet been proven by any experiment. This means the Higgs potential can be varied from the SM assumption in new physics scenarios beyond the SM (BSM). In fact, BSM theories predict several different types of the Higgs boson, such as Nambu-Goldstone Higgs [24, 25], Coleman-Weinberg Higgs [26–28] and Tadpole-induced Higgs [29, 30], and several types of the Higgs potential shown in Figure 2.3 are predicted. These issues can be experimentally addressed only by measuring the Higgs self-couplings, because they are only parameters involving the shape of the Higgs potential. Thus the measurement of the Higgs self-couplings is a crucial quest in particle physics in order to clarify the shape of the Higgs potential and the origin of the EWSB.

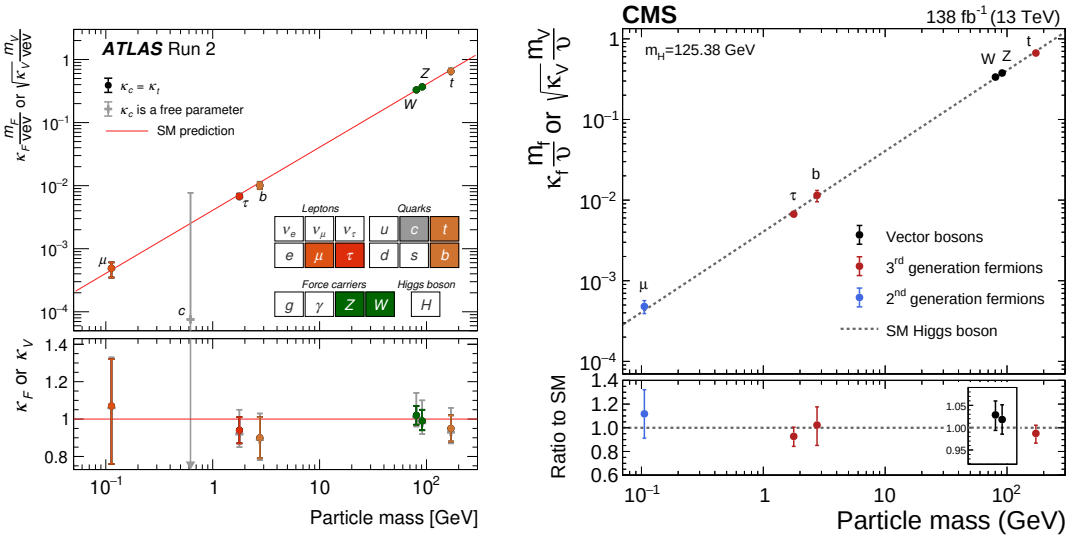

(a) (b)

Figure 2.2 Results of Higgs coupling measurements from the (a) ATLAS [22] and (b) CMS experiment [23]. The experimental results are shown in the colored dots. The SM predictions are shown by the solid red line in (a) and by the dashed black line in (b). The under panel shows the ratio of the experimental results to the SM predictions.

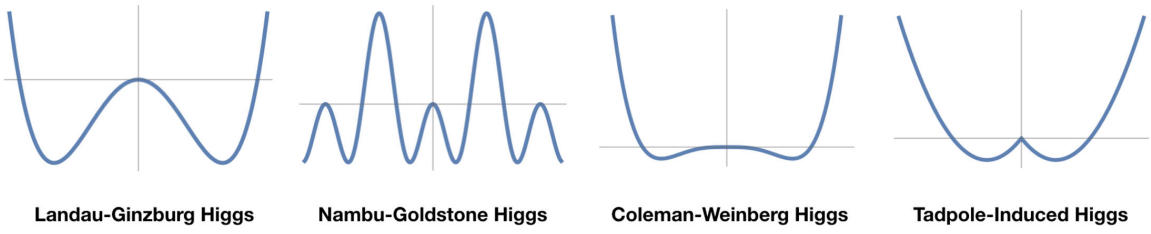

Figure 2.3 The shapes of the Higgs potential in various physics scenarios [31]. Landau-Ginzburg Higgs type corresponds to the Higgs boson predicted in the SM.

2.2 Remaining Problems and Higgs Self-couplings

The SM is a successful theory, but there are several observed phenomena, such as baryon asymmetry of the universe and dark matter, that can not be explained in the SM. To resolve these remained issues, new physics theory beyond the SM (BSM) is needed. Some of new physics theories predict a significant change in the Higgs potential and induce a large modification of the trilinear Higgs self-coupling. In this section, I will discuss possibilities of the modification of the trilinear Higgs self-coupling in new physics models and in more general model (ultraviolet (UV)-completed model).

2.2.1 Baryon Asymmetry of the Universe

One of the remained problems in the SM is the baryon asymmetry of the universe. A baryon refers to a particle with an odd number of quarks at least three [32]. The baryon asymmetry is the imbalance of the baryon number with respect to the anti-baryon number. It must be explained that this has been generated in the early universe after the cosmic inflation, because it is undesirable to consider it as an initial condition of the beginning of the universe. To generate the baryon asymmetry, the following conditions, known as the Sakharov conditions [33], must be satisfied.

1. Baryon number violation
2. C and CP symmetry violations
3. Thermal equilibrium deviation

The electroweak (EW) phase transition described in Section 2.1.4 could provide the baryon asymmetry, only if this is a strongly first-order phase transition. However, in the SM with the Higgs boson mass of 125 GeV, this can not be a strongly first-order phase transition. In order to alter the Higgs potential to it, a significant change in the Higgs potential is needed. The trilinear Higgs self-coupling is predicted to be modified by $O(10)\%$ to satisfy the Sakharov conditions [34–36]. A specific motivation for large modifications of the Higgs potential arises from this idea of electroweak baryogenesis that is expected to resolve the baryon asymmetry problem.

2.2.2 Dark Matter

The other remaining problem is that the SM can not explain the so-called dark matter. Dark matter has been observed through the rotation velocity measurements of galaxies [37, 38]. Dark matter is thought to be a non-baryonic matter that weakly interacts or does not interact. There are no candidates for dark matter in the SM.

The minimal supersymmetric model (MSSM) [39] arises as one of the most attractive candidates that can explain the dark matter problem. New particles predicted in the MSSM are known as supersymmetric (SUSY) particles. In the MSSM, when assuming the R-parity conservation that is new symmetry between the baryon number and the lepton number introduced in the MSSM, the lightest SUSY particle always becomes stable. The lightest SUSY particle thus arises as one of the attractive candidates.

In the MSSM, the trilinear Higgs coupling can be modified. In the MSSM, it is required to introduce two different Higgs double fields to ensure supersymmetry and cancel anomalies [39]. The mixing of the two Higgs fields can lead to modifying the trilinear Higgs coupling by $O(1)\%$ [40]. Additionally in the

next-to-minimal supersymmetric model (NMSSM) which is one of the SUSY models, the change can be $-1.1 < \kappa_\lambda < 2.0$ [40]. This means that all new physics models that need to extend the Higgs field, such as a two double Higgs model (2HDM) [41], can also lead to modifications of the trilinear Higgs coupling. Therefore, the measurement of the trilinear Higgs coupling is motivated not only to understand the origin of the EWSB but also to test new physics scenarios.

2.2.3 Theoretical Constraints and UV-Complete Model

As described above, it is a good way to compute how large the Higgs self-couplings can be in specific new physics models. However, it is difficult to understand how the impact can be induced in a wider class of new physics models with this way. Therefore, this section discusses more general theoretical constraints on the trilinear Higgs self-coupling.

Vacuum stability

Firstly, I will discuss a theoretical constraint of vacuum stability. If one considers a modification to the Higgs potential by introducing a dimension-6 operator given by Eq. 2.35, two kinds of possible cases of different signs for the parameters μ^2, λ and c_6 can be considered (Figure 2.4) [42].

$$V^{(6)}(\boldsymbol{\phi}) = -\mu^2\left(\boldsymbol{\phi}^\dagger\boldsymbol{\phi}\right) - \lambda\left(\boldsymbol{\phi}^\dagger\boldsymbol{\phi}\right)^2 + \frac{c_6}{v^2}\left(\boldsymbol{\phi}^\dagger\boldsymbol{\phi}\right)^3 \tag{2.35}$$

One is the case of $\mu^2 > 0$, $\lambda > 0$ and $c_6 < 0$ which are chosen to make the solution of vacuum expectation value close to the SM. The other one is the case of $\mu^2 < 0$, $\lambda < 0$ and $c_6 > 0$ which can reproduce the SM condition at higher energy scale (Λ). However, as discussed in Ref. [42], a model-independent bound for κ_λ from stability arguments cannot be derived because both instabilities cannot be reliably evaluated in the Effective Field Theory (see Section 2.3.2). Also in UV-complete models, it cannot be derived as discussed later. Thus, the theoretical constraint due to vacuum stability cannot be obtained.

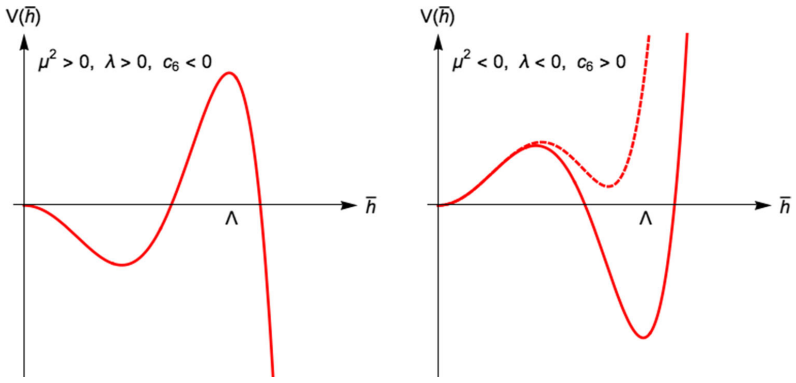

Figure 2.4 Two kinds of the Higgs potential shape with the dimension-6 operator [43].

Perturbativity

The trilinear Higgs self-coupling is constrained by perturbativity. In general, one expects that too large values of the Higgs couplings lead to entering the non-perturbative regime. This is unfavorable from the views of necessities of new phenomena such as strong interactions and new massive particles. The perturbativity range can be estimated by a requirement that the loop-corrected HHH vertex must be smaller than the tree-level vertex [44]. This means the HHH vertex must be perturbative for $\sqrt{\hat{s}} > 2m_H$, where $\hat{s}$ is the parton center of mass energy. This then leads to the κ_λ bound of

$$\kappa_\lambda \leq 6 \tag{2.36}$$

when setting two Higgs bosons on-shell in the HHH vertex. The strong bound is derived from the requirement of $m_{HH} \simeq 2m_H$. It should be noted that this is computed with a simplistic assumption setting two Higgs bosons on-shell and the bound is looser when setting other kinematic configurations, for example of one-loop EW corrections. Therefore, this requirement are not applied to other studies described in the next. However, this bound value helps discuss what constraints are imposed by perturbativity.

UV-complete model

This section turns to how large the Higgs self-couplings can be in renormalizable models (UV-complete models). For simplicity, this section focuses on an extension of the SM with one new particle whose state is above the EW scale. New scalar singlet field (Φ) can couple via several types of tadpole operators (O_Φ) depending on the Φ states. Here concentrate on the simplest case of $O_\Phi = \Phi\boldsymbol{\phi}\boldsymbol{\phi}$. The extended Higgs potential with the scalar singlet field is defined by

$$V(\boldsymbol{\phi}, \Phi) = \mu_1^2|\boldsymbol{\phi}|^2 + \lambda_1|\boldsymbol{\phi}|^4 + \frac{1}{2}\mu_2^2\Phi^2 + \mu_4|\boldsymbol{\phi}|^2\Phi + \frac{1}{2}\lambda_3|\boldsymbol{\phi}|^2\Phi^2 + \frac{1}{3}\mu_3\Phi^3 + \frac{1}{4}\lambda_2\Phi^4, \tag{2.37}$$

where $\boldsymbol{\phi}$ is the doublet field corresponding to the Higgs field, and μ_i and λ_i are parameters. Some of the parameters can be replaced by more familiar phenomenological parameters, such as the mixing angle θ between the singlet field and the doublet field, their vacuum expectation values and the Higgs boson mass. A scan with the input parameters, $m_1 = 125$ GeV, 800 GeV $< m_2 <$ 2000 GeV, $0.9 < \cos\theta < 1.0$, $v_1 = 246$ GeV, $|v_2| < m_2$, $0 < \lambda_2 < 8\pi/3$ and $|\lambda_3| < 16\pi$ assuming a specific UV-complete model, is performed to get the bound of the trilinear Higgs self-coupling. The scan ranges of λ_2 and λ_3 are chosen to satisfy the perturbative regime. The range of the vacuum expectation value v_2 is chosen from a requirement that the potential must be bounded from below.

The result of the parameter scan is shown in Figure 2.5. They are experimentally constrained by the observed phenomena. All points on the left side of the dashed light blue line are excluded by the Higgs coupling measurements. In addition, all points on the left of the dashed dark blue line are also excluded by the W boson mass measurement. As can be seen in Figure 2.5, vacuum stability does not give a constraint because vacuum instability is not directly connected with the modification of the trilinear Higgs self-coupling due to many couplings in the scalar potential. From this result, the maximum possible modifications of the trilinear Higgs self-coupling in the model are

$$-1.5 < \kappa_\lambda < 8.7. \tag{2.38}$$

In this section, I briefly described how large the trilinear Higgs coupling can be in the specific UV-

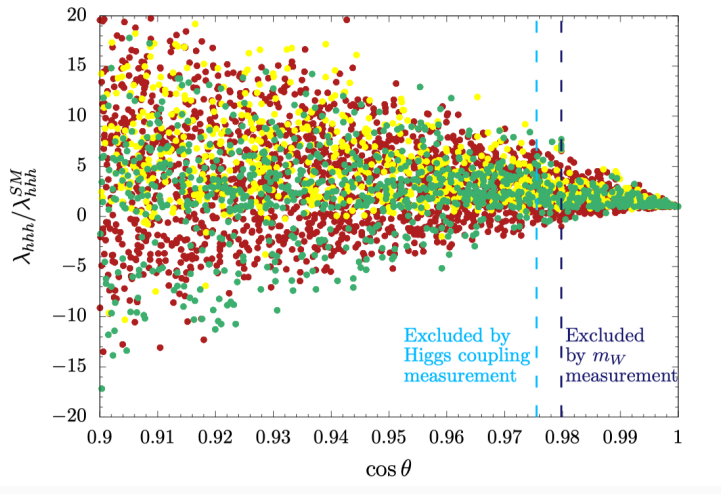

Figure 2.5 Modification of the trilinear Higgs self-coupling from a scan over the singlet model parameters [43,45]. The red, yellow and green points correspond to unstable, metastable and stable vacuum configurations, respectively. The left region from the dashed light blue line is excluded by the Higgs coupling measurements. The left region from the dashed dark blue line is excluded by the W boson mass measurement.

complete model. More detailed descriptions, such as the Φ states, are discussed in Ref. [43,45].

2.2.4 Summary of Possible Modifications of the Trilinear Higgs Self-coupling

I discussed several possible modification ranges of the trilinear Higgs self-coupling and theoretical constraints above. Figure 2.6 illustrates these modification ranges and theoretical constraints. The coloured bands in Figure 2.6 correspond to the regions of interest. However, it should be noted that only a few examples of the BSM scenarios that could modify the trilinear Higgs self-coupling are discussed and shown. Following them, we can give several precision goals for the measurement of the trilinear Higgs self-coupling according to BSM scenarios and can provide the implications of each precision level for the effects due to new physics models. The guidelines are also helpful for future experiments. The general discussion can be found in Ref. [45].

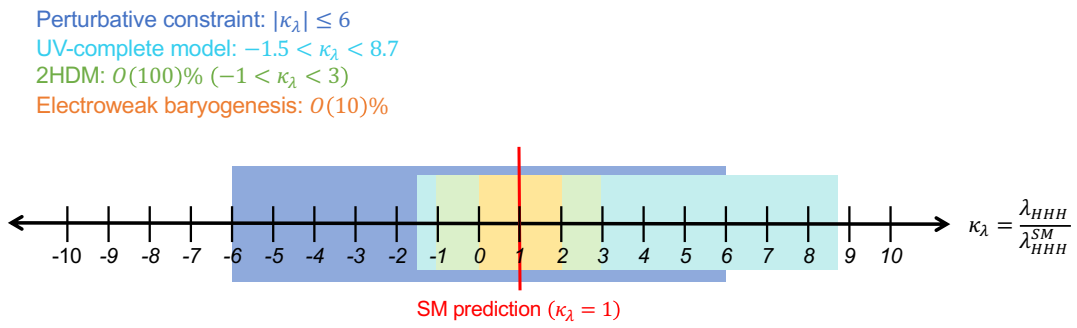

Figure 2.6 Summary of modifications of the trilinear Higgs self-couplings. The SM prediction ($\kappa_\lambda = 1$) is shown by the red line. Perturbative constraint (blue) and a modification value from UV-complete model (turquoise) are obtained from Ref. [43]. A modification value from a two Higgs double model (2HDM) in the Gildener-Weinberg model (green) is taken from Ref. [41]. One from the electroweak baryogenesis (orange) is taken from Ref. [34–36].

2.3 Non-resonant Di-Higgs Production

As described above, the measurement of the trilinear Higgs self-coupling is strongly motivated to test the EWSB and new physics models at higher energy scale. A pair of Higgs boson production (di-Higgs production, HH) is the most promising channel to measure the trilinear Higgs self-coupling. In this section, the phenomenology of HH production is described.

2.3.1 Phenomenology

Non-resonant HH production can be produced by colliding accelerated proton and proton at hadron colliders. The cross-section of the HH process can be described by Eq. 2.39 in the factorization theory [46].

$$\sigma_{pp\to HH} = \sigma_{i,j} \int_0^1 dx_1 \int_0^1 dx_2 \, f_i\left(x_1, \mu_F^2\right) f_j\left(x_2, \mu_F^2\right) \hat{\sigma}_{ij\to HH}\left(\alpha_s, x_1 p_1, x_2 p_2, \mu_F, \mu_R\right), \tag{2.39}$$

where i and j denote a status of the initial partons, x_1 and x_2 are the incoming proton momentum fractions, μ_F is a factorization factor and μ_R is a renormalization scale. $f_{i,j}\left(x_1, \mu_F^2\right)$ is a parton distribution function (PDF) for parton i and j. The PDF distribution of the PDF4LHC PDF sets as a function of the incoming proton momentum fractions $x_{(1,2)}$ are shown in Figure 2.7. $\hat{\sigma}_{ij\to HH}$ denotes the partonic cross-section via an interaction between parton i and j with an interaction energy of partons with a momentum of $x_1 p_1$ and $x_2 p_2$. The total production cross-section can be calculated by integrating the partonic cross-section with the appropriate weight according to the momentum distribution of the incoming partons represented by $f_{i,j}$.

The main production processes are gluon-gluon fusion (ggF), vector-boson fusion (VBF), double Higgs-strahlung (WHH/ZHH) and double Higgs bremsstrahlung off top quarks ($t\bar{t}HH$). The total production cross-sections in the SM are shown in Figure 2.8.

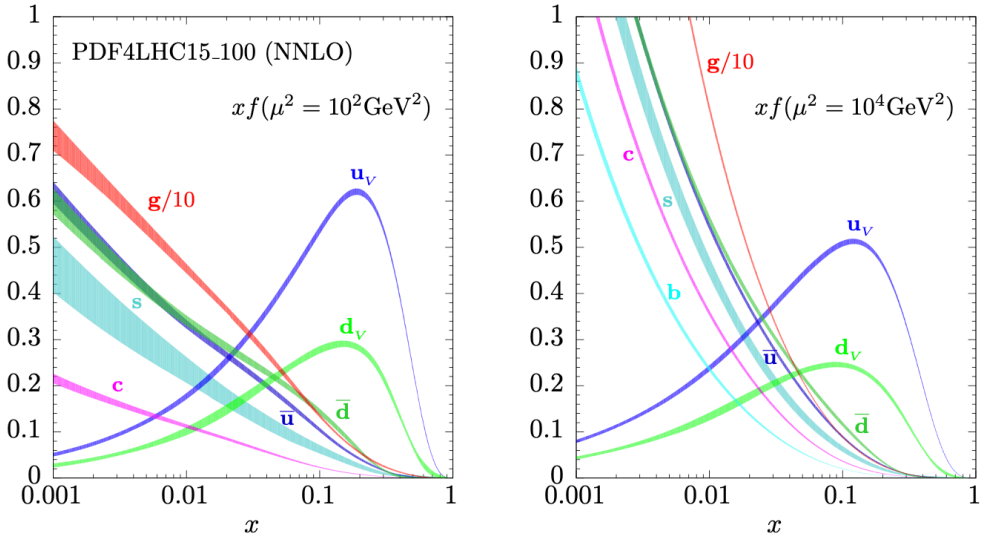

Figure 2.7 The PDF4LHC PDF sets as a function of the incoming proton momentum fractions x with $\mu = 10$ GeV^2 (left) and $\mu = 10^4$ GeV^2 (right), where $\mu = \mu_F = \mu_R$ [47].

Gluon-gluon fusion (ggF)

This analysis focus on only the two leading production processes. The leading production process is the ggF process in the SM. The SM cross-section is $\sigma^{SM}_{ggF} = 31.05$ fb at next-to-next-to-leading order (NNLO) at $\sqrt{s} = 13$ TeV [48]. There are two diagrams, known as a triangle diagram and a box diagram, at the leading order (LO) as shown in Figure 2.9. The triangle diagram involves the trilinear Higgs coupling. κ_λ and k_t are defined as the ratios of the trilinear Higgs coupling and the top quark Yukawa coupling with respect to the SM predictions. Since k_t has been already observed and found to be consistent with the SM prediction [49, 50], it is out of interest in this analysis and fixed to the SM prediction. These contributions destructively interfere, so that the ggF cross-section is reduced (Figure 2.10). The triangle diagram mainly contributes to the invariant mass distribution of di-Higgs (m_{HH}) below 300 GeV, and the dox diagram contributes to the peak around 400 GeV in the SM. These relative contributions can thus be observed in m_{HH}. The ggF production cross-section depends on the trilinear Higgs coupling value, as shown in Figure 2.11. In addition, kinematic properties of the ggF production process also depend on the trilinear Higgs coupling value. As shown in Figure 2.11, a dip around $m_{HH} = 300$ GeV is created around $\kappa_\lambda = 2.4$ due to the maximum destructive interference. Large or small κ_λ values shift the m_{HH} distribution toward lower values, because the contribution of the triangle diagram becomes relativity larger. The trilinear Higgs coupling can thus be measured by investigating the cross-section and the m_{HH} shape of the HH production.

Vector-boson fusion (VBF)

The second largest production process is the VBF process in the SM. The SM cross-section is $\sigma^{SM}_{ggF} = 1.73$ fb at next-to-next-to-next-to-leading order (N3LO) at $\sqrt{s} = 13$ TeV [48]. The leading diagrams in

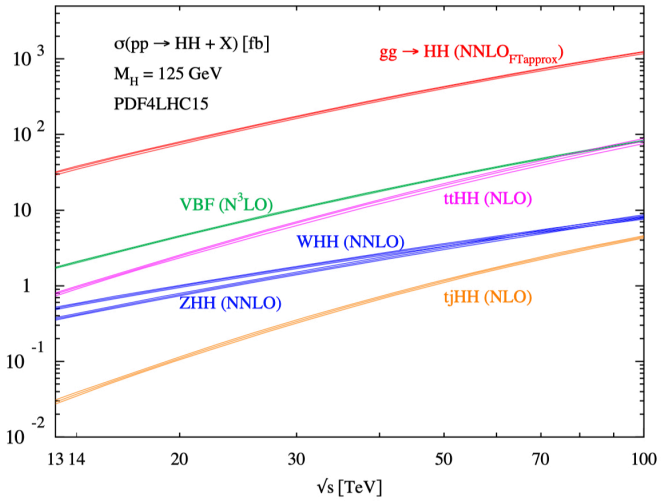

Figure 2.8 Total HH production cross-sections in the SM via each of the four main production processes as a function of a centre-of-mass energy ($\sqrt{s}$) [45]. The ggF cross-section is shown the red line, and the VBF cross-section is shown the green line.

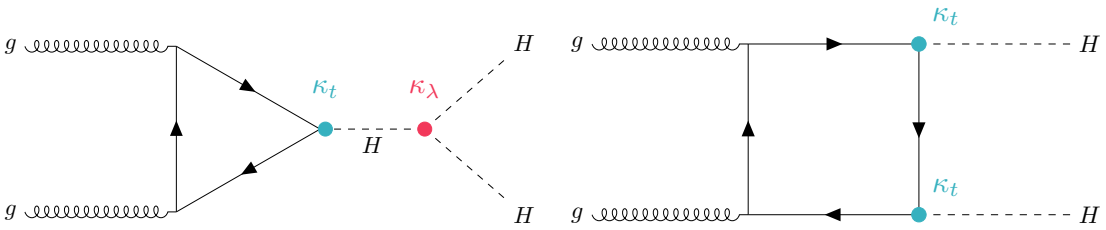

(a) Triangle diagram (b) Box diagram

Figure 2.9 Feynman diagrams of the HH production with gluon-gluon fusion (ggF) in the leading order.

the VBF process are shown in Figure 2.12. The VBF process can provide to access the trilinear Higgs coupling and the Higgs boson and two vector bosons (HVV) coupling in Figure 2.12(a) and 2.12(a) diagrams, and the two Higgs bosons and two vector bosons ($HHVV$) coupling in Figure 2.12(b) diagram. κ_{2V} and κ_V are defined as the ratios of the $HHVV$ coupling and the HVV coupling with respect to the SM predictions, respectively. In this analysis, κ_V is set to the SM prediction to 1, because it can be accessed significantly via $H \to ZZ/WW$ analyses and this analysis focus on only the accessible parameters only via HH analyses. The VBF production cross-section depends on these couplings. In particular, the amplitude involving Figure 2.12(b) diagram and Figure 2.12(c) is given by

$$\mathcal{A} \sim \frac{\hat{s}}{v^2}\left(\kappa_{2V} - \kappa_V^2\right), \tag{2.40}$$

where $\hat{s}$ is the parton center of mass energy. Therefore, in the SM, the diagrams in Figure 2.12(b) and Figure 2.12(c) destructively interfere, so that their contributions are cancelled. If κ_{2V} value deviates from

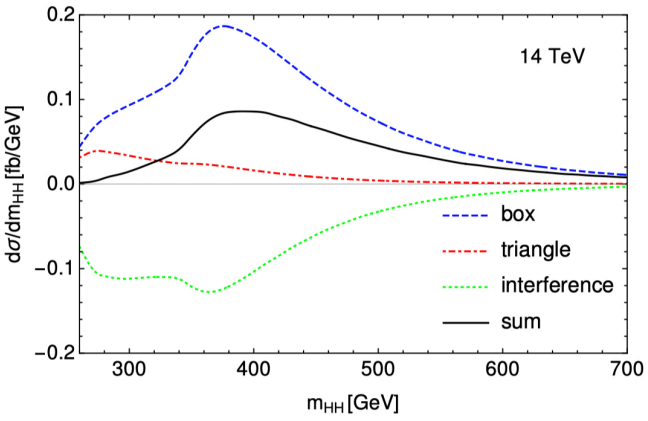

Figure 2.10 The differential cross-sections on m_{HH} distribution for the triangle diagram (dashed red), the box diagram (dashed blue) and their destructive interference (dashed light green) at 14 TeV [45]. The total differential cross-section is shown by the solid black line.

the SM prediction of 1 and then $\kappa_{2V} \neq \kappa_V^2$, the diagram in Figure 2.12(b) becomes to be dominant. As a result, the cross-section is significantly increased and the VBF kinematics become to be harder so that m_{HH} distribution is shifted toward higher value.

Decay Channels

A list of the branching ratios for the HH process is shown in Figure 2.13. A Higgs boson with a mass of 125 GeV can decay into several SM particles. The dominant decay mode is $H \to b\bar{b}$ with a branching ratio of 58%, followed by $H \to W^+W^-$, $H \to gg$ and $H \to \tau^+\tau^-$. Thanks to the highest branching ratio of $H \to b\bar{b}$, the $b\bar{b}b\bar{b}$ final state benefits from the largest signal yield. Thus this thesis focuses on the search for the HH production in the $b\bar{b}b\bar{b}$ final state.

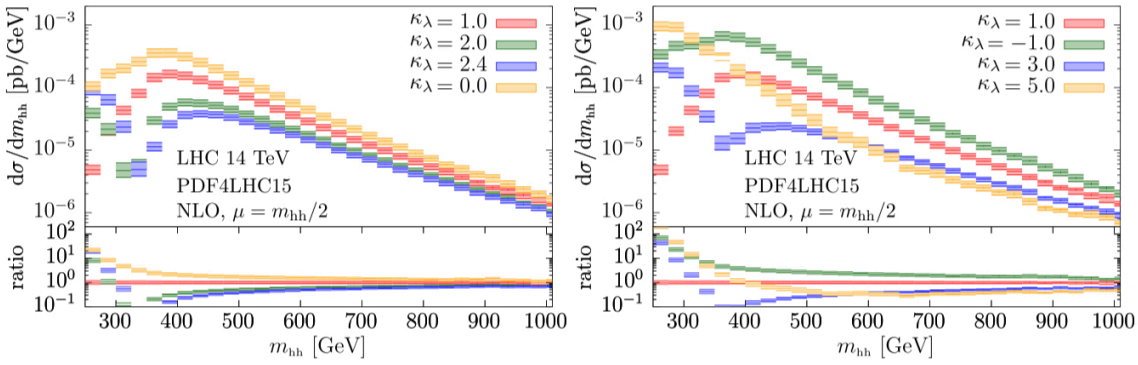

Figure 2.11 Di-Higgs invariant mass (m_{HH}) distribution with various κ_λ values at 14 TeV [45]. The under panel shows the ratios to the SM prediction.

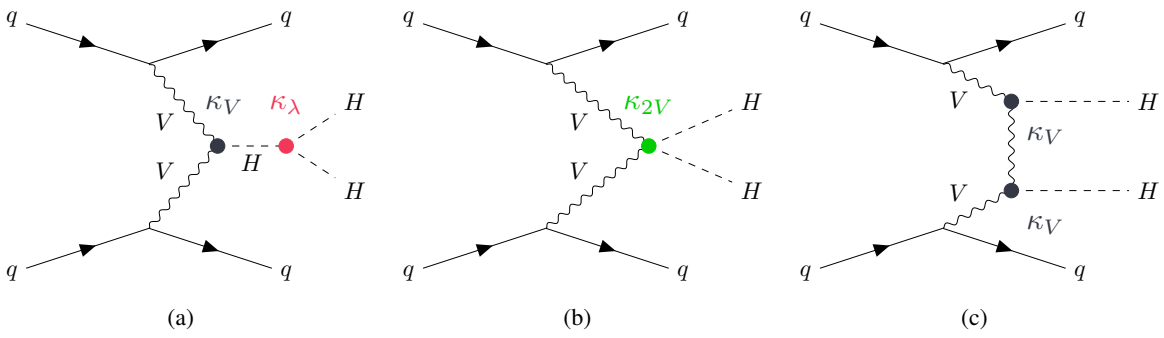

Figure 2.12 Feynman diagrams of the HH production with vector boson fusion (VBF).

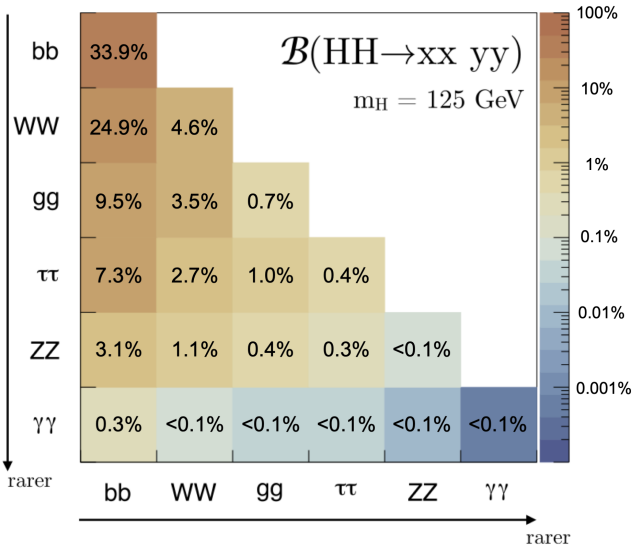

Figure 2.13 Branching ratio for the *HH* process with the Higgs boson mass of 125 GeV. This figure is taken from Ref. [51] and adopted for this thesis.

2.3.2 Phenomenology in Effective Field Theory

As discussed in Section 2.2, it is helpful to understand any effects of new physics in higher energy scale into the low energy of EWSB. Effective Field Theory (EFT) is the current best way to know it. The idea of EFTs is that physics with a small mass scale does not depend on physics with a much larger scale, and then the Lagrangian can be systematically parameterized into components based on the mass dimension. However, it should be noted that EFT Lagrangian can describe only lower energy part of the high energy physics and new Lagrangian that explicitly contains the new particle must be provided to describe the high energy physics itself.

There is no unique way to formulate new physics descriptions in EFTs. In this analysis, two different frameworks called the Standard Model Effective Field Theory (SMEFT) [52–54] and the Higgs Effective Field Theory (HEFT) [55, 56] are thus used to describe new physics descriptions with some simplifying assumptions. This section describes the two EFT frameworks and discusses SMEFT and HEFT coupling modifiers that are accessible via a search of the non-resonant HH production.

Standard Model Effective Field Theory (SMEFT)

The key idea of the SMEFT is to describe a new physics model as additional fields that act on only high energy scale and add them into the SM fields. As the characteristic of the SMEFT, the Higgs field is treated as a component of an SU(2) × U(1) double field as the same as the SM. Thus, the SMEFT Lagrangian can be described by adding higher mass dimensional operators into the SM Lagrangian.

$$\mathcal{L}_{SMEFT} = \mathcal{L}_{SM} + \frac{1}{\Lambda}\sum C_i^{(5)} Q_i^{(5)} + \frac{1}{\Lambda^2}\sum C_j^{(6)} Q_j^{(6)} + ..., \tag{2.41}$$

where the index i and j run over dimension 5 and 6 operators, respectively. Λ indicates the energy scale that new physics exists. $Q_{i,j}^d$ are field operators with the mass dimension d. $C_{i,j}^d$ are coefficients associated with $Q_{i,j}^d$, which are referred to as *Wilson coefficients*.

The operators of odd dimensions (5,7,...) are not considered in this analysis, because they involve lepton number violation. For example, the dimension 5 operators have neutrino mass terms. This analysis focuses only on the dimension 6 operators because other dimension operators should have little sensitivity with respect to the dimension 6 operators. If we consider that new physics is at the energy scale of Λ O(1 TeV) and interacts with the energy scale of the Higgs boson mass O(125 GeV), the dimension 6 operators could provide more than $O(1)\%$ corrections. On the other hand, the dimension 8 operators have only $O(10^{-4})\%$ corrections.

There are 59 independent operators at dimension 6 in the Warsaw basis assuming baryon number conservation [57]. In particular, 6 independent operators involve the ggF HH production in the dimension 6 operators. The Lagrangian involving the ggF HH production can be given by

$$\begin{aligned}\Delta\mathcal{L} = &\frac{\bar{c}_{H\Box}}{\Lambda^2}\left(\boldsymbol{\phi}^\dagger\boldsymbol{\phi}\right)\partial_\mu\left(\boldsymbol{\phi}^\dagger\boldsymbol{\phi}\right) + \frac{\bar{c}_{tH}}{\Lambda^2}\left(\boldsymbol{\phi}^\dagger\boldsymbol{\phi}\right)\bar{Q}_L\widetilde{\boldsymbol{\phi}}t_R + \frac{\bar{c}_H}{\Lambda^2}\left(\boldsymbol{\phi}^\dagger\boldsymbol{\phi}\right)^3 \\ &+ \frac{\bar{c}_{tG}}{\Lambda^2}\bar{Q}_L\sigma^{\mu\nu}G_{\mu\nu}\widetilde{\boldsymbol{\phi}}t_R + \frac{\bar{c}_{HG}}{\Lambda^2}\left(\boldsymbol{\phi}^\dagger\boldsymbol{\phi}\right)G^a_{\mu\nu}G^{a\mu\nu} + \frac{\bar{c}_{H\widetilde{G}}}{\Lambda^2}\left(\boldsymbol{\phi}^\dagger\boldsymbol{\phi}\right)G^a_{\mu\nu}\widetilde{G}^{a\mu\nu},\end{aligned} \tag{2.42}$$

where $\bar{c_H}, \bar{c}_{tH}, \bar{c}_{H\Box}, \bar{c}_{tG}, \bar{c}_{HG}$ and $\bar{c}_{H\widetilde{G}}$ are coefficients for the dimension 6 operators involving the ggF HH production. Q_L indicates the left-handed doublet field for top and b quarks, and $\boldsymbol{\phi}$ is the Higgs

doublet field. This analysis assumes charge conjugation parity (CP) conservation so that the CP-violating operator $O_{H\widetilde{G}}$ is ignored. The Feynman diagrams involving the ggF HH production in the SMEFT dimension 6 operators are shown in Figure 2.14.

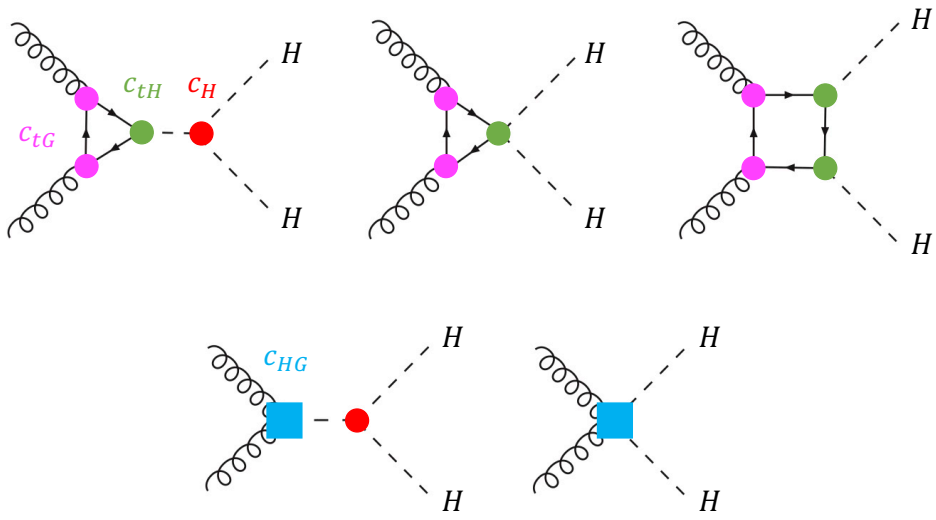

Figure 2.14 Feynman diagrams contributing to the ggF HH production in the SMEFT dimension 6 operators. The operators, c_H, c_{tH}, c_{tG} and c_{HG} are shown in the red circle, the green circle, the pink circle and the turquoise square, respectively. Another operator $c_{H\Box}$ is not shown in the diagrams, but it modifies all Higgs couplings.

In particular, the operators O_H and $O_{H\Box}$ can modify the trilinear Higgs self-couplings as Eq. 2.43.

$$\kappa_\lambda = \frac{\lambda_{HHH}}{\lambda^{SM}_{HHH}} = 1 - \frac{3}{2}c_H + c_{H\Box}, \tag{2.43}$$

where $c_H \equiv 2\bar{c}_H$ and $c_{H\Box} \equiv 2\Lambda^2\bar{c}_{H\Box}/m_H^2$. The c_H corresponds to c_6 discussed in Section 2.2. The $O_{H\Box}$ operator also provides a universal rescaling to all Higgs couplings. The O_{tH} and O_{tG} operators can modify the top quark Yukawa coupling. The O_{tH} also induces a $t\bar{t}$ HH vertex corresponding to the top middle diagram in Figure 2.14. The O_{tG} operator induces an anomalous colour magnetic dipole for the top quark and adds a contact interaction between Higgs boson, gluon and top quark. The O_{HG} operator provides a direct interaction between gluon and Higgs boson, and thus the bottom diagrams in Figure 2.14 are allowed at tree-level. If there is no new physics model, all these coefficients become zero.

The cross-section and kinematics of the ggF HH production depend on these coefficient values. Figure 2.15 shows m_{HH} distributions of the ggF HH production with various values of the SMEFT dimension 6 coefficients. Large kinematic differences on m_{HH} can be seen. These SMEFT dimension 6 coefficients can thus be measured by investigating the cross-section and the m_{HH} shape of the ggF HH production.

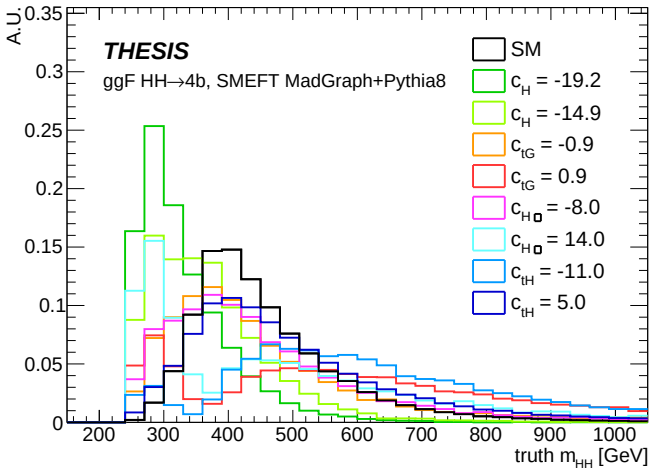

Figure 2.15 Di-Higgs invariant mass (m_{HH}) distributions of the ggF HH production with the SM (black histogram) and various SMEFT coefficient values (colored histograms). The other coefficient values except for one shown in the legend are fixed to the SM values.

Higgs Effective Field Theory (HEFT)

The key idea of the HEFT is the same as the SMEFT but uses a nonlinear realisation of SU(2) × U(1) to describe a new physics model in the low energy scale of the EWSB. This approach is motivated by SU(2) × SU(2) → SU(2) symmetry breaking that is seen in chiral symmetry breaking in the QCD strong interactions. The HEFT thus describes the Higgs field as an SU(2) × U(1) single field. In the concept of the HEFT, new physics is assumed to arise from anomalous couplings of the Higgs boson.

In the HEFT framework, there are 5 relevant operators that involve the ggF HH production in the dimension 6 operators. The Lagrangian involving the ggF HH production can be described as Eq. 2.44.

$$\begin{aligned}\Delta\mathcal{L} = &-m_t\left(c_{t\bar{t}H}\frac{h}{v} + c_{t\bar{t}HH}\frac{h^2}{v^2}\right)\bar{t}t - c_{HHH}\frac{m_H^2}{2v}h^3 \\ &+ \frac{\alpha_s}{8\pi}\left(c_{ggH}\frac{h}{v} + c_{ggHH}\frac{h^2}{v^2}\right)G^a_{\mu\nu}G^{a\mu\nu},\end{aligned} \tag{2.44}$$

where c_i are couplings redefined in the HEFT. The relevant diagrams are shown in Figure 2.16. c_{HHH} modifies the trilinear Higgs self-coupling. $c_{t\bar{t}H}$ modifies the top quark Yukawa coupling. $c_{t\bar{t}HH}$ induces a $t\bar{t}$ HH vertex and allows the top middle diagram in Figure 2.16. c_{ggH} and c_{ggHH} respectively induces a ggH vertex and a $ggHH$ vertex seen in the bottom diagrams in Figure 2.16. In the SM, $c_{t\bar{t}H} = c_{HHH} = 1$ and $c_{t\bar{t}HH} = c_{ggH} = c_{ggHH} = 0$.

In this analysis, 7 HEFT benchmark (BM) models [58] shown in Table 2.3 are defined. They are selected according to their representative shape features of m_{HH}. Figure 2.17 shows these m_{HH} distributions in the HEFT BMs. Using these BMs with a wide variety of characteristic shapes can significantly reduce the number of signal test points, while can explore multiple BSM scenarios.

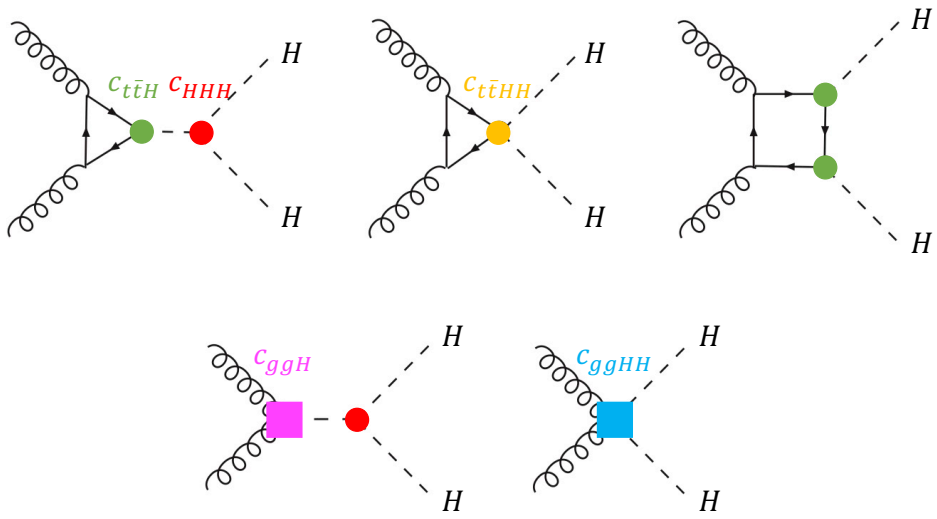

Figure 2.16 Feynman diagrams contributing to the ggF HH production in the HEFT dimension 6 operators. The operators, c_{HHH}, c_t, $c_{t\bar{t}}$, c_{ggH} and c_{ggHH} are shown in the red circle, the green circle, the yellow circle, the pink circle square and the turquoise square, respectively

Benchmark Model	c_{HHH}	$c_{t\bar{t}H}$	c_{ggH}	c_{ggHH}	$c_{t\bar{t}HH}$
SM	1	1	0	0	0
BM 1	3.94	0.94	1/2	1/3	−1/3
BM 2	6.84	0.61	0.0	−1/3	1/3
BM 3	2.21	1.05	1/2	1/2	−1/3
BM 4	2.79	0.61	−1/2	1/6	1/3
BM 5	3.95	1.17	1/6	−1/2	−1/3
BM 6	5.68	0.83	−1/2	1/3	1/3
BM 7	−0.10	0.94	1/6	−1/6	1

Table 2.3 HEFT benchmarks used in this analysis [58].

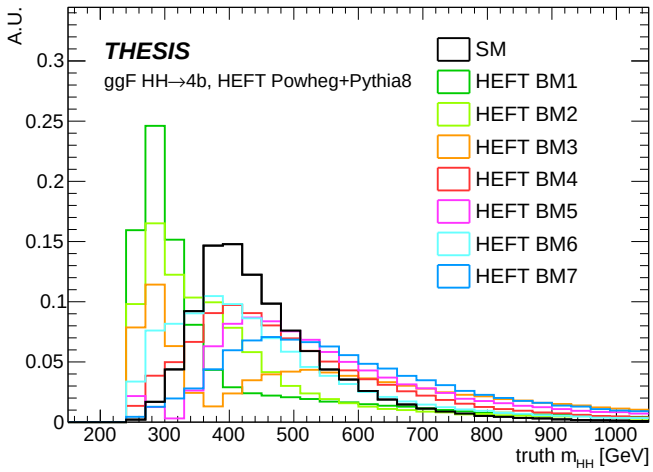

Figure 2.17 Di-Higgs invariant mass distributions of the ggF HH production in the SM (black histogram) and the 7 HEFT benchmark models (colored histograms).

Chapter 3

The ATLAS Experiment at the Large Hadron Collider

HH production is a difficult process to produce sufficient number of events to study its characteristics. The Large Hadron Collider (LHC) [59] is the only accelerator that can provide a large number of HH events thanks to the world's highest collision energy. Data provided by the LHC are accumulated with several detectors. One of the detectors is the ATLAS detector [3]. This analysis relies on the datasets accumulated with the ATLAS detector at the LHC. This chapter describes an overview of the LHC and the ATLAS detector.

3.1 The Large Hadron Collider

The Large Hadron Collider (LHC) is the world's largest circular accelerator with a circumference of 27 km. The goal of the LHC is to provide high-energy and intensity proton-proton collisions to the experiments build on the LHC ring. It is designed to collide protons at a centre-of-mass energy of $\sqrt{s}$ = 14 TeV and a peak luminosity of up to 10^{34} cm^{-2}s^{-1} at the interaction points.

The LHC is the accelerator complex that consists of a series of machines (Figure 3.1). Each machine increases proton energies rather than the previous one and then injects them into the next one. Protons are firstly obtained from hydrogen gas by stripping electrons using electric fields, and their energies are increased up to 50 MeV by the Linear Accelerator 2 (LINAC2). The protons are injected into the Proton Synchrotron Booster (PSB or BOOSTER), Proton Synchrotron (PS) and Super Proton Synchrotron (SPS) in the order. Then they are accelerated up to 1.4 GeV, 25 GeV and 450 GeV by each accelerator. The accelerated protons are split into two portions and injected into the two beam pipes in the LHC. Finally, they can be accelerated up to 7 TeV in opposite directions.

In the LHC, the beams of protons have more than 2000 bunch structures with a spacing of 25 ns. In 2018, 2556 bunches were stored in each beam. Each bunch stores approximately 1×10^{11} protons. Thus multiple proton-proton interactions in the same bunch crossing can take place. Most of these proton-proton interactions are found to be non-interesting inelastic interactions and there are a few interesting hard-scatter interactions. These inelastic interactions are called as *pile-up*. The distributions of the mean number of proton-proton interactions per bunch crossing for data recorded by the ATLAS experiment in a period between 2015 to 2018 are shown in Figure 3.2.

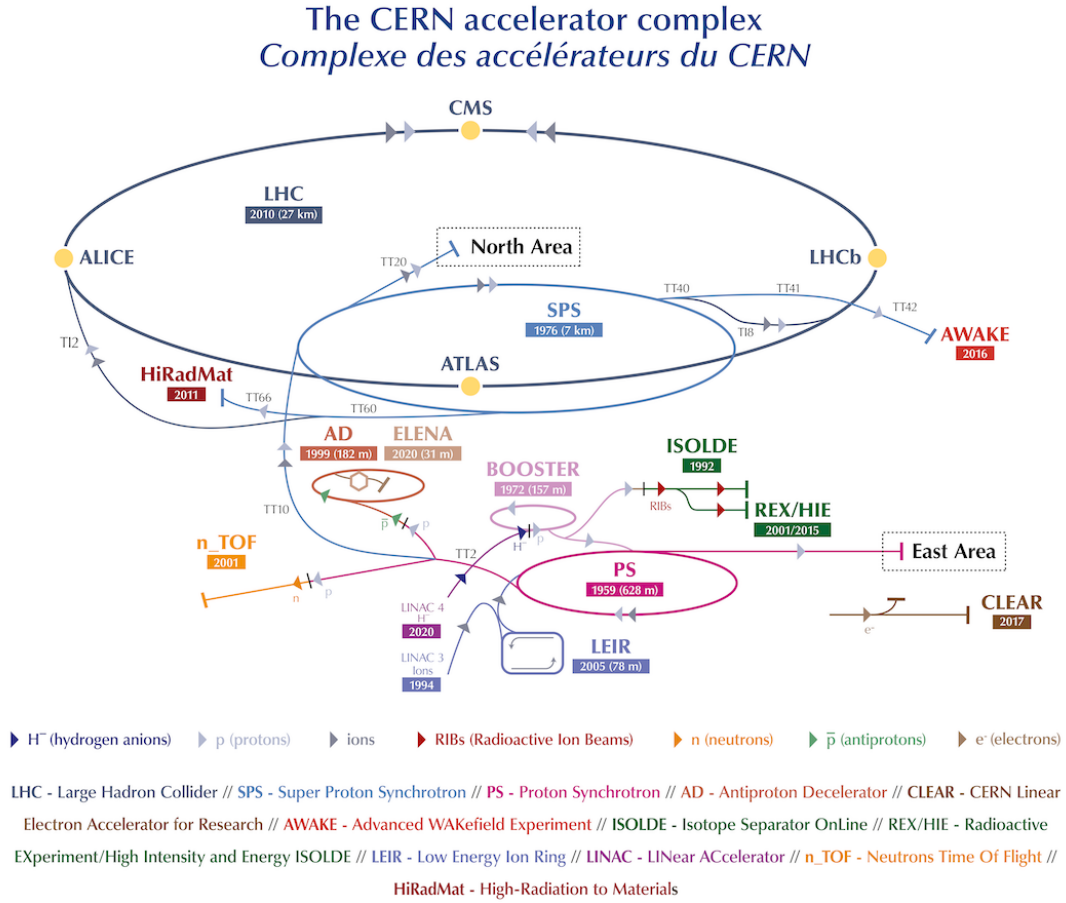

Figure 3.1 Schematic view of the CERN accelerator complex [60]. The LHC is drawn by the last ring (dark blue line) in a complex chain of particle accelerators. The smaller linear and circular accelerators are used to help boost the particles before injecting the LHC.

The LHC has been operated with a centre-of-mass energy of $\sqrt{s}$ = 7 TeV and 8 TeV and a peak luminosity of 0.77×10^{34} cm^{-2}s^{-1} for a period between 2010 to 2012. The first operation is known as Run 1. After a long shutdown between 2013 to 2015 to upgrade the accelerator, the second operation of the LHC has been restarted in 2015 and continued until 2018. The second operation is known as Run 2. In the Run 2, the centre-of-mass energy was increased to 13 TeV and the peak luminosity was achieved to 2.14×10^{34} cm^{-2}s^{-1}. The total integrated luminosity provided during the Run 2 is approximately 156 fb^{-1} thanks to its high peak luminosity (Figure 3.3).

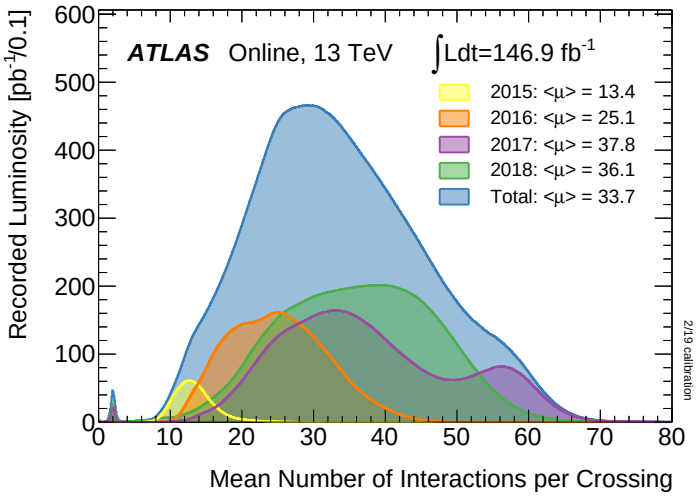

Figure 3.2 Distribution of the mean number of proton-proton interactions per bunch crossing in each year in the LHC [61]. The average numbers, $\langle\mu\rangle$, in each year are shown in the legend.

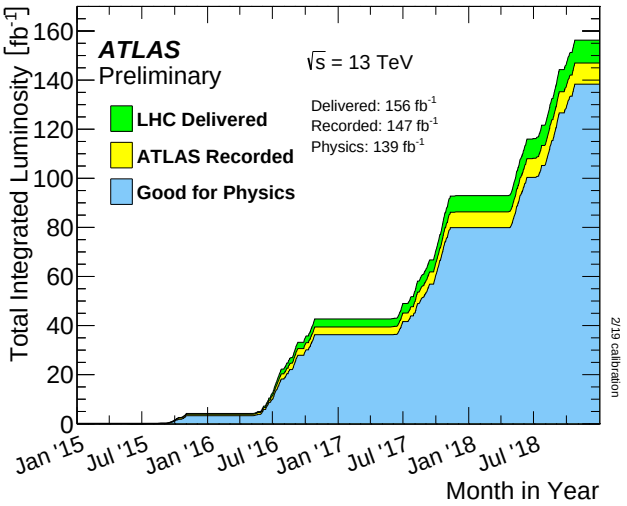

Figure 3.3 Total integrated luminosity delivered by the LHC (green), recorded by the ATLAS experiment (yellow) and certified to be good quality data (blue) in 2015-2018 [61].

3.2 The ATLAS Detector

3.2.1 Overview

The ATLAS detector is a multi-purpose particle detector located at the interaction point 1 (IP1) in the LHC ring (Figure 3.1) [3]. The ATLAS detector is designed to perform a variety of physics programs in a wide range of energies provided by the LHC. It consists of several different detector subsystems, inner detector, calorimeter and muon spectrometer, and three kinds of superconducting magnets, the solenoid and the barrel and end-cap toroids. These detectors cover the interaction point with a cylindrical barrel and two end-caps to avoid missing particles from the interaction point as much as possible. Particles generated by proton-proton collisions at the interaction point are detected as electric signals in these detectors (Figure 3.5). By using these electric signals, the types of particles are identified and these kinematics such as trajectory, mass, charge and momentum are measured. This section presents an overview of the components of the ATLAS detector. The particle reconstructions and identifications will be presented in Chapter 4.

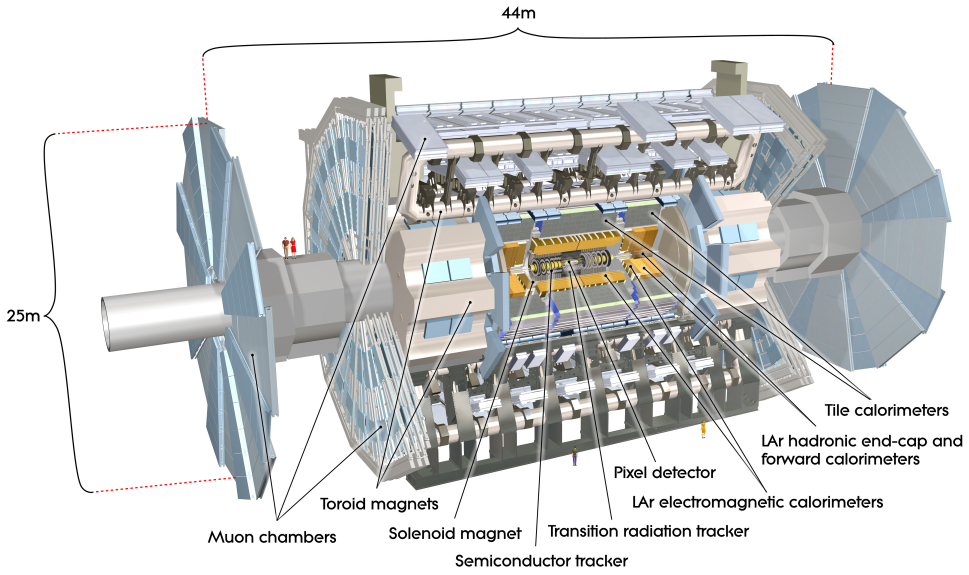

Figure 3.4 Layout of the ATLAS detector [3]. The length of the ATLAS detector is 44 m and the hight is 25 m. The overall weight is approximately 7000 tonnes.

3.2.2 Coordinate system

A right-handed Cartesian coordinate is used to describe the ATLAS detector, as illustrated in Figure 3.6. where the origin is located at the interaction point, the x-axis points to the center of the LHC ring, the y-axis and the z-axis the direction of is defined In the coordinate system, the origin is located at the interaction point. The x-axis points to the center of the LHC ring, the y-axis is the vertically upward direction and the z-axis is the beam direction. A cylindrical coordinate system is also defined, where the

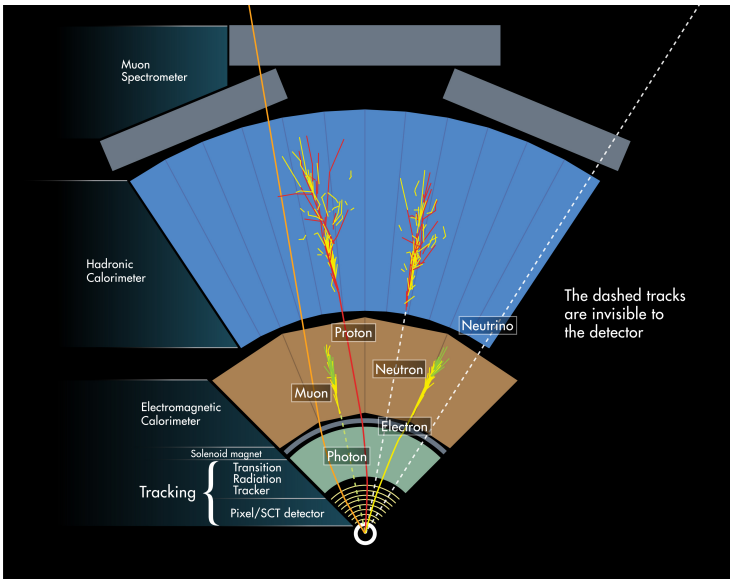

Figure 3.5 Overview of particle interactions within the ATLAS detector [62].

radius distance R is a distance from the beam given by $R = \sqrt{x^2 + y^2}$, and polar angle θ and azimuthal angle ϕ are defined as the angle with respect to the beam and the angle around the beam, respectively.

In hadron colliders, the momentum of particles generated by collisions is varied on the z-axis, because the energies of partons inside the hadrons are asymmetry. It is thus important to ensure that relevant kinematic variables are Lorentz invariant. θ is not Lorentz invariant so that it is parameterized into either rapidity y or pseudo-rapidity η. The rapidity y is defined as:

$$y = \frac{1}{2} \ln \left(\frac{E + p_z}{E - p_z} \right), \tag{3.1}$$

where E and p_z are the energy and the z-component of the momentum of a given object, respectively. The pseudo-rapidity η is defined as:

$$\eta = -\ln \tan \left(\frac{\theta}{2} \right) \tag{3.2}$$

Both of them are Lorentz invariant but the pseudo-rapidity is only true for massless particles. The pseudo-rapidity is well preferred, because it does not rely on the total energy and the z-component of the momentum. Similarly, a set of variables with Lorentz invariant are used. In particular, the transverse component of the momentum is defined as $p_T = \sqrt{p_x^2 + p_y^2}$. The transverse energy is defined as $E_T = \sqrt{m^2 + p_T^2}$. There are the advantages of use of these transverse quantities that they can express the kinematics of relevant particles depending on the collision energy of partons and the vector sum of the transverse components of relevant particles are conserved before and after interactions. The angular distance ΔR between two objects is often used and given by $\Delta R = \sqrt{\Delta\eta^2 + \Delta\phi^2}$.

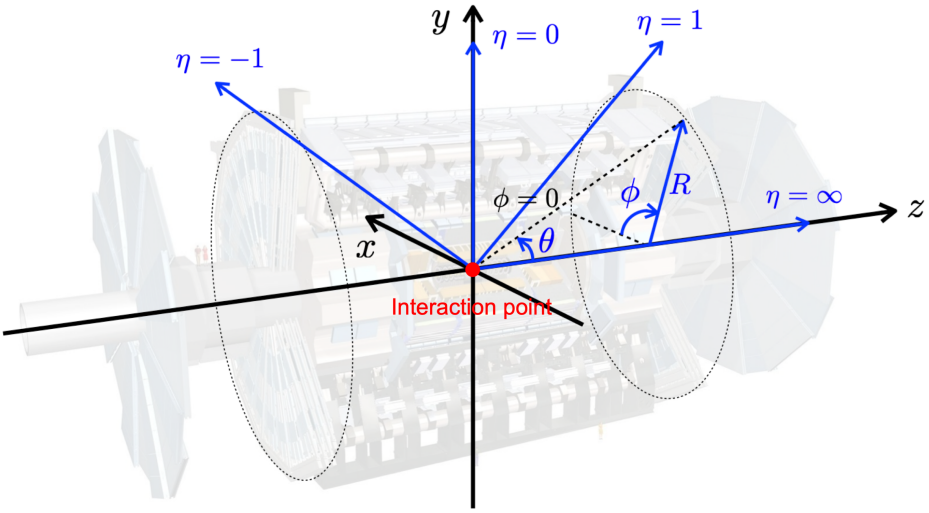

Figure 3.6 Schematic view of the coordinate system used in the ATLAS detector. This figure is taken from Ref. [63] and adopted for this thesis.

3.2.3 Magnet Systems

In the ATLAS detector, three kinds of superconducting magnets, the solenoid, the barrel toroid and the end-cap toroid, are used (Figure 3.7). These superconducting magnets provide magnet fields, which bend the trajectories of charged particles. These curved trajectories are measured by the inner detector or the muon spectrometer. The momentum of charged particles can be then measured.

The solenoid is located between the inner detector and the calorimeter. It provides a magnetic field of 2 T along the beam direction inside the coils for the inner detector, as shown in Figure 3.8(a). In the magnetic field, charged particles are bent in the ϕ direction.

The barrel and end-cap toroid are located outside the calorimeter. Each of them consists of eight toroidal magnets. These toroidal magnets provide magnet fields along the ϕ direction inside the coils. These magnet fields have an 8-fold symmetric structure due to the structure of the toroidal magnets. The integrated magnetic field provided by one component of the toroidal magnets is shown in Figure 3.8(b). The integrated magnetic field in the region of $1.4 < |\eta| < 1.6$ gets small due to the transition region of the barrel coils and the end-cap coils. In the magnetic field, charged particles are bent in the η direction. Full description of these superconducting magnets can be found in Ref. [3, 64].

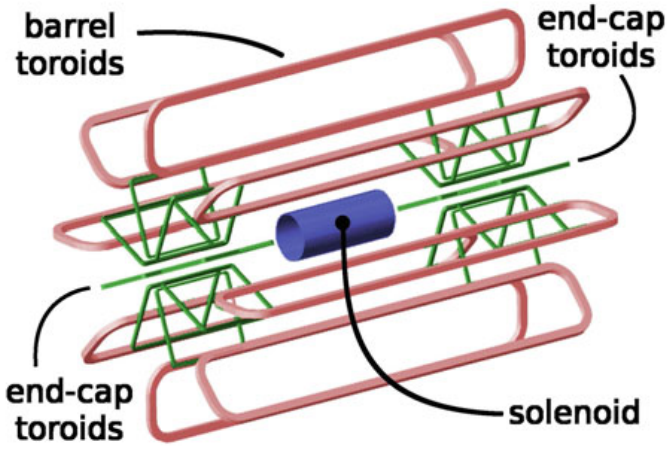

Figure 3.7 Layout of the superconducting magnet system in the ATLAS detector [64].

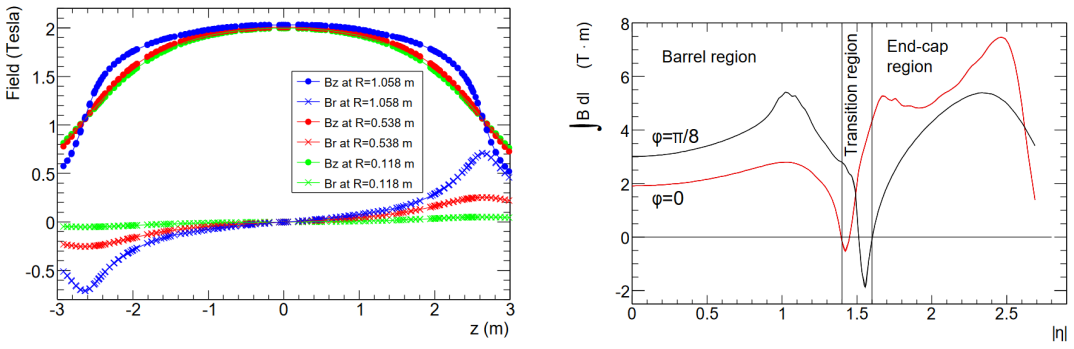

(a) The solenoid

(b) The barrel and end-cap toroids

Figure 3.8 (a) The radial (Br) and axial (Bz) components of the magnetic field provided by the solenoid in the inner detector cavity and (b) the integrated magnetic field provided by the barrel and end-cap toroidal magnets in the muon spectrometer [3]. R- and z-dependence for the solenoid magnetic field and η-dependence for the toroidal magnet fields are shown.

3.2.4 Inner Detector

The inner detector is the innermost subsystem of the ATLAS detector. It is designed to measure the trajectories of charged particles and identify the proton-proton interaction points with their high precisions. It is composed of the pixel detector, the silicon microstrip tracker (SCT) and transition radiation tracker (TRT), as shown in Figure 3.10 from inside to outside.

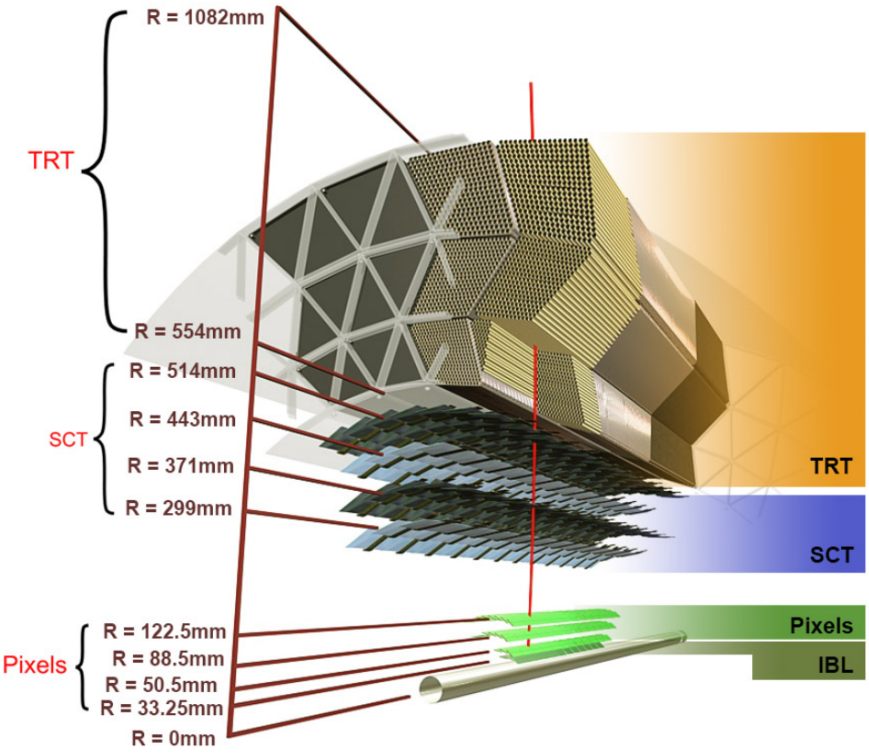

Figure 3.9 Cross-section view of the inner detector [65].

Pixel detector

The pixel detector is made up of four layers of silicon pixel sensor arrays in the barrel and three disks in each side of the end-cap. In particular, the innermost layer in the barrel is called the Insertable B-Layer (IBL), which was newly installed in 2015. The pixel detector has an acceptance of $|\eta| < 2.5$. The detector makes use of the fact that charged particles produce electron-hole pairs when traversing the material. By applying the electric field, these electron-hole pairs are inhaled by the sensors and detected as electric signals. The size of each pixel sensor is 50 μm $\times$ 250 μm in the $\phi - z$ plane (barrel) in the IBL and 50 μm $\times$ 400 μm in both the $\phi - z$ plane (barrel) and the $\phi - R$ plane (end-cap). The position resolution depends on the pixel size, and the intrinsic resolution is shown in Table 3.1.

Silicon Microstrip Tracker

The next layers of the inner detector are the Silicon Microstrip Tracker (SCT). The SCT is composed of four layers of silicon sensor modules in the barrel and nine disks in each side of the end-cap and covers the region of $|\eta| < 2.5$. Each silicon sensor module is made up of one or two pairs of microstrip sensors aligning with a pitch of 80 μm for the barrel and with a pitch of $57-94$ μm for the end-cap. The intrinsic resolution is 17 μm in $R-\phi$ direction for the barrel. However, the intrinsic resolution in z-direction for the barrel and R-direction for the end-cap is a bit worse of 580 μm due to the length of 128 mm. To compensate for the resolution reduction of the individual sensors, the pair of the microstrip sensors is placed with a stereo angle of 40 mrad and provides two-dimensional trajectory information of charged particles.

Transition Radiation Tracker

The final component of the inner detector is the Transition Radiation Tracker (TRT), which provides coverage of the region of $|\eta| < 2.0$. The TRT is composed of straw tubes with a diameter of 4 mm in which xenon-based active gas is filled. Each of the straw tubes contains a central anode wire of gold-plated tungsten-rhenium with a diameter of 30 μm. The straw tubes make use of the fact that charged particles induce electron cascades when passing the gas mixture by the ionization and collect the secondary electrons with the central wire. The intrinsic position resolution per straw tube is approximately 130 μm.

The TRT is also designed to distinguish electrons from other heavier charged particles such as pions. The spaces between these straw tube are filled with polypropylene fibers for the barrel and polypropylene radiator foils for the end-cap. When particles cross the boundaries between the straw tube and the polypropylene, they emit transition radiation due to the large difference in their indices of refraction. The amount of transition radiation produced by a particle with a given energy depends on its mass. The TRT also detects the electric signal of transition radiation and allows electrons to be distinguished from other heavier charged particles.

Subdetector	Element size	Intrinsic resolution [μm]	Radius of the barrel layers [mm]
Pixel (IBL)	50×250 μm^2	8×40	33.2
Pixel (Other layers)	50×400 μm^2	10×115	50.5, 88.5 and 122.5
SCT	80 μm	17	299, 371, 443 and 514
TRT	4 mm	130	554 – 1082

Table 3.1 Summary of the main characteristics of the subdetectors of the inner detector [66]. The intrinsic resolutions along the $R-\phi$ and z-direction for the pixels and along the $R-\phi$ for the SCT and TRT are shown The element sizes for the SCT and TRT present the spacing of the readout strips and the diameter of the straw tubes, respectively.

3.2.5 Calorimeters

The calorimeter system surrounds the solenoid magnet and the inner detector, covering the region of $|\eta| < 4.9$. It is composed of three different calorimeters, the electromagnetic calorimeter (ECAL), the hadronic calorimeter (HCAL) and forward calorimeter (FCAL). The ECAL is further divided into barrel ($|\eta| < 1.475$) and end-cap ($1.375 < |\eta| < 3.2$) regions. The HCAL is also divided into barrel ($|\eta| < 1.7$) and end-cap ($1.5 < |\eta| < 3.2$) regions. The whole view of the calorimeter system is shown in Figure 3.10. All of them are sampling calorimeters, which are composed of alternating layers of absorbing and sensing materials. They are designed to contain and measure the energy of electrons, photons and hadrons.

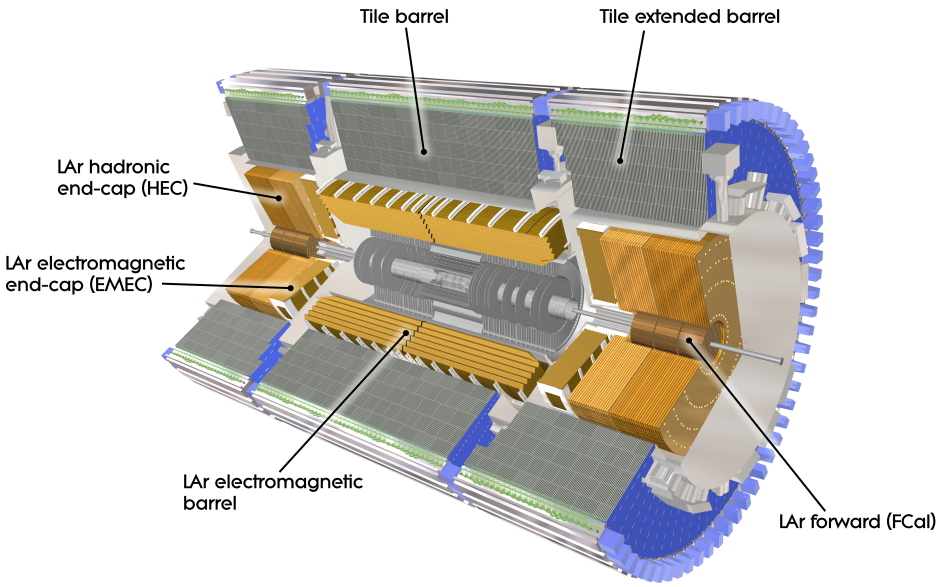

Figure 3.10 Cut-away view of the calorimeters [65].

Electromagnetic Calorimeter

The electromagnetic calorimeter (ECAL) is designed to measure the absorbing energy of electrons, photons and hadrons via their electromagnetic (EM) showers. The ECAL consists of lead layers, liquid argon (LAr) layers and copper-kapton electrodes. They play the role of the absorbing material, the active material and the sensing materials, respectively. The EM showers are developed in the absorbing material via bremsstrahlung radiation of incoming particles. The EM showers produce ionized electrons in the active material and then they are collected as electrical signals by the sensors. Since the collection of the ionized energies is related to the energy of the original particle, the ECAL can measure the energy of the incoming particle.

The ECAL is sub-divided into three layers in the depth direction. To distinguish the energies from multiple particles in the event, the ECAL is further sub-divided into many segments, also known as *cells*. The geometry and segment of the ECAL vary between the barrel and the end-cap. Figure 3.11 schematics

the barrel module of the ECAL. The segment of the barrel module is $\Delta\eta \times \Delta\phi = 0.0031 \times 0.098$ in the first layer, 0.025×0.0245 in the second layer and 0.05×0.0245 in the third layer. The energy resolution of the barrel module for a particle with a given energy E is given by [67]:

$$\frac{\sigma_E}{E} = \frac{10\%}{\sqrt{E}} \oplus \frac{17\%}{E} \oplus 0.7\%. \tag{3.3}$$

The first term corresponds to the sampling term, the second term is the electronics and pile-up noise term and the third term is the constant term.

The ECAL is sufficiently effective to collect the energy of electrons and photons, but it is not as effective for hadrons due to their longer radiation length of the material. The energy of hadrons is thus collected by the HCAL as well as the ECAL. It is described in the next selection.

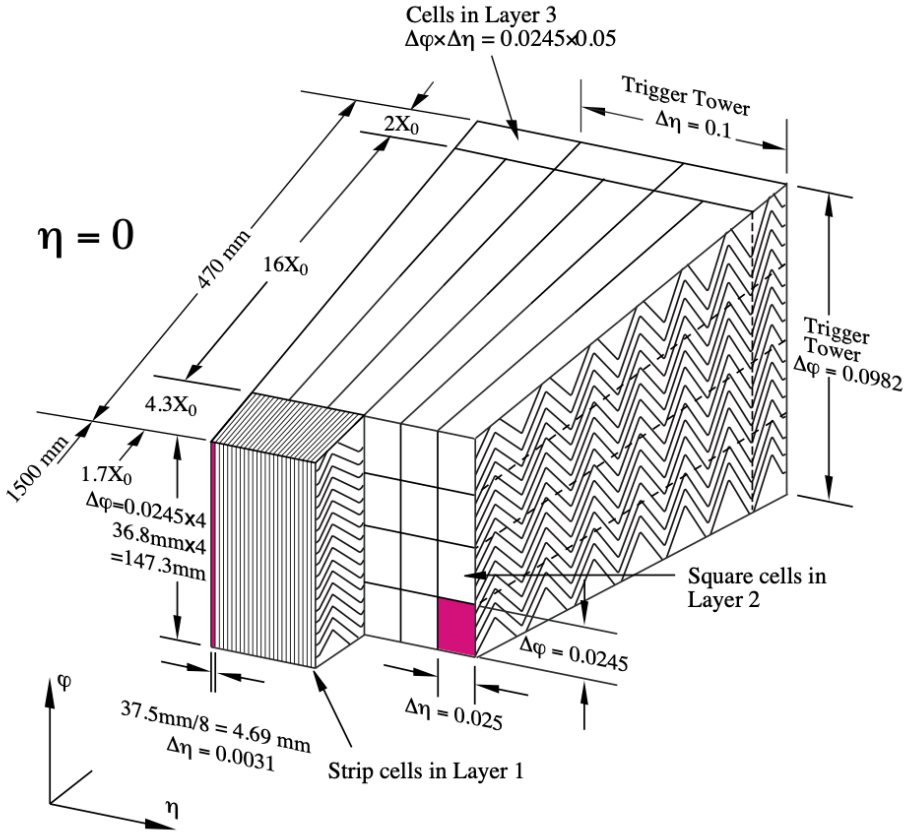

Figure 3.11 Sketch of the barrel module of the electromagnetic calorimeter [3], where three different layers are visible in the depth direction. The segments in each layer are also shown.

Hadronic Calorimeter

The hadronic calorimeter (HCAL) is designed to measure the absorbing energy of hadrons exploiting the fact that they interact with atomic nuclei and produce a shower. The detection principle of the HCAL is the same as the ECAL, but the HCAL is optimized to generate the hadronic showers via the interaction with atomic nuclei and ionization. The HCAL is composed of two different calorimeters where different combinations of absorber and active material are used.

One is the tile hadronic calorimeter (Tile HCAL), which covers the barrel region of $|\eta| < 1.7$. The Tile HCAL is composed of steel layers as the absorber and plastic scintillation tiles as the active material. Similarly with the ECAL, the Tile HCAL is sub-divided into three layers in the depth direction and many segments in the $\eta - \phi$ plane (Figure 3.12(a)). The segment is $\Delta\eta \times \Delta\phi = 0.1 \times 0.1$ in both first and second layers and 0.2×0.1 in the third layer. The intrinsic resolution of the Tile HCAL for a particle with a given energy E is given by:

$$\frac{\sigma_E}{E} = \frac{50\%}{\sqrt{E}} \oplus 3\%. \tag{3.4}$$

The other one is end-cap hadronic calorimeter (End-cap HCAL), which covers the end-cap region of $1.5 < |\eta| < 3.2$. The End-cap HCAL uses copper layers as the absorber and LAr layers as the active material. The End-cap HCAL is also segmented into four layers in the depth direction and segments in the $\eta - \phi$ plane (Figure 3.12(b)). The size of the segment is $\Delta\eta \times \Delta\phi = 0.1 \times 0.1$ in the range of $1.5 < |\eta| < 2.5$ and 0.2×0.2 in the range of $2.5 < |\eta| < 3.2$. The intrinsic resolution of the End-cap HCAL is given by:

$$\frac{\sigma_E}{E} = \frac{100\%}{\sqrt{E}} \oplus 10\%. \tag{3.5}$$

Forward Calorimeter

The forward calorimeter (FCAL) is designed to detect particles originating from hard-scatter interactions with extreme boosted to the beam direction. The FCAL is made up of three sampling calorimeters where both functions of the ECAL and the HCAL are integrated as shown in Figure 3.13, and provides coverage over the forward region of $3.1 < |\eta| < 4.9$. The first layer uses copper absorbers for EM showers, and the other two layers use tungsten absorbers for hadronic showers. All of them use LAr as the active material. The FCAL thus allows the energies of electrons, photons and hadrons to be measured in the forward region with the same detection principle as the ECAL and HCAL.

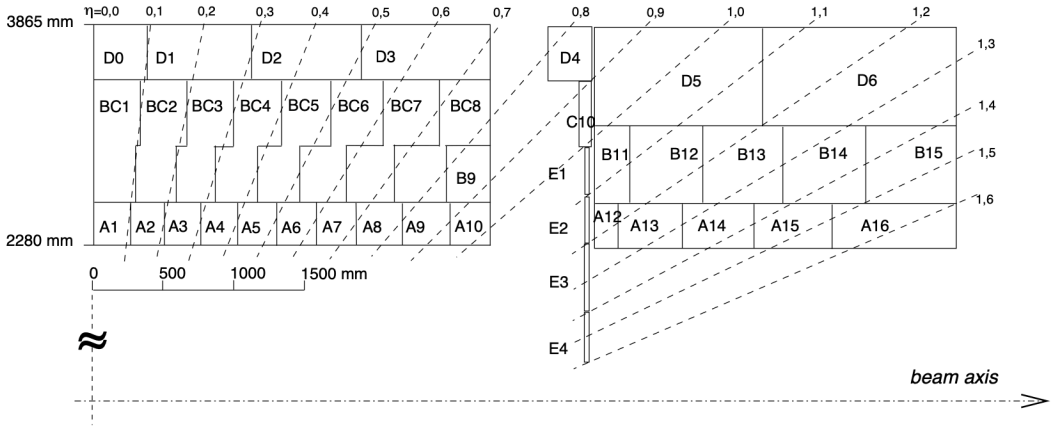

(a) Tile Hadronic Calorimeter

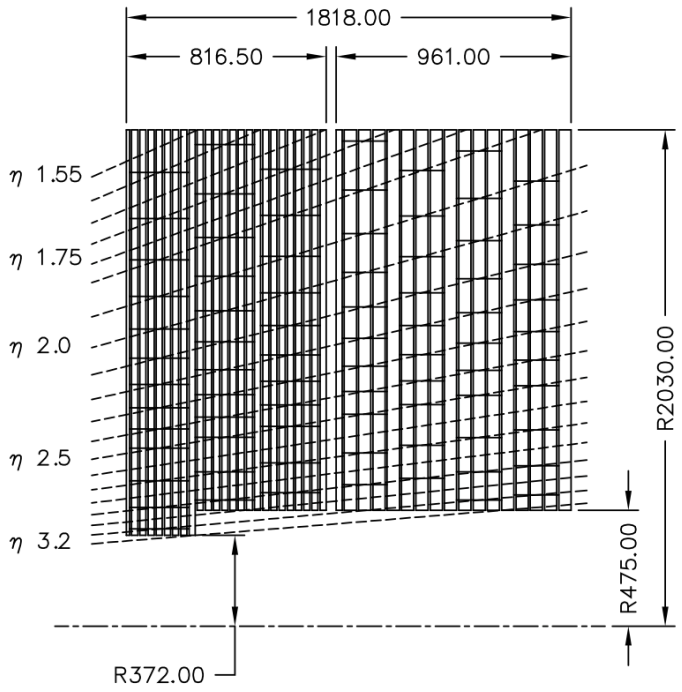

(b) End-cap Hadronic Calorimeter

Figure 3.12 Schematic views of (a) the Tile Hadronic Calorimeter and (b) the End-cap Hadronic Calorimeter in the depth and R plane [3]

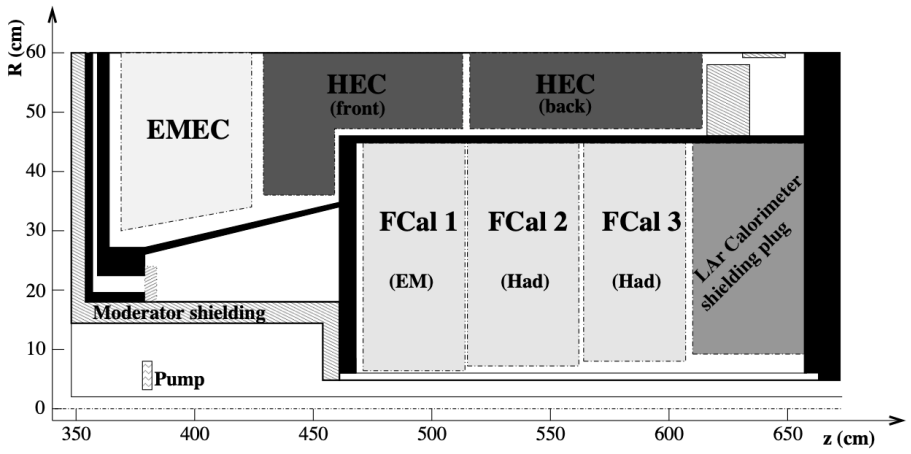

Figure 3.13 Schematic diagram of the forward calorimeter [3]

3.2.6 Muon Spectrometer

The muon spectrometer (MS) is the outermost subsystem of the ATLAS detector (Figure 3.14). Muons typically pass through the inner detector and the calorimeter. The amount of bremsstrahlung radiation in the ECAL is inversely proportional to the square of incoming particle mass, and thus muons, which are much heavier than electrons, deposit relatively few fractions of their energy. In addition, muons deposit only the energy of a few GeV in the HCAL following the Bethe-Bloch equation [68]. Therefore, the MS allows the trajectory of muons to be measured with high precision. Since the trajectory of muons is bent by magnetic fields of the toroidal magnets, the momentum can be measured with the MS.

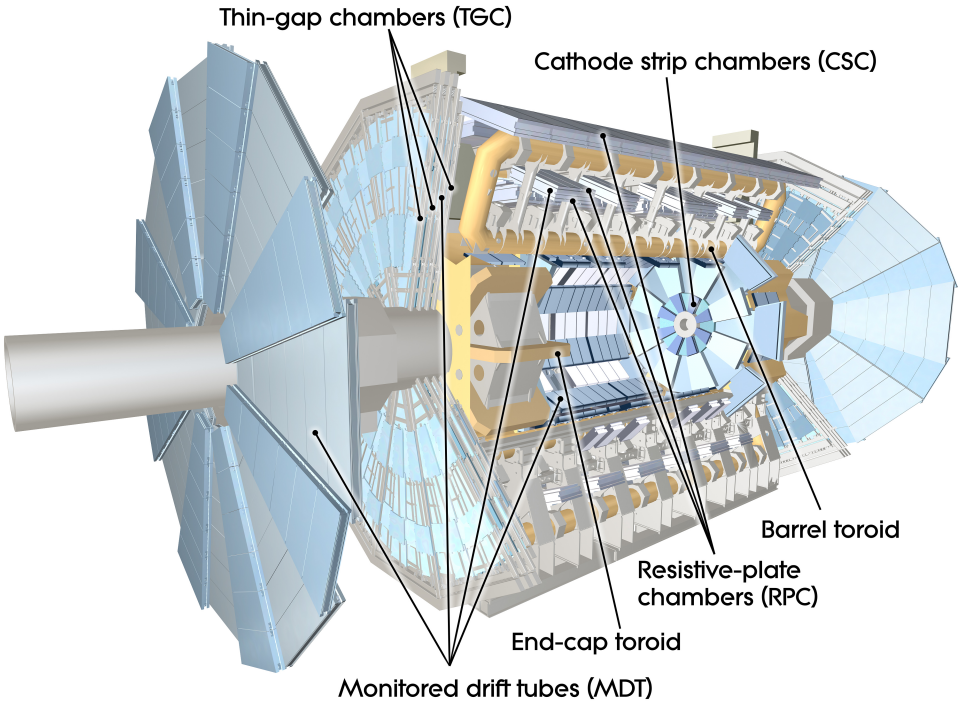

Figure 3.14 Cut-away view of the muon spectrometer [3]

The MS is divided into two types according to the purposes. One is precision chambers, which are designed to measure the trajectories of muons with high precision. The precision chambers are Monitored Drift Tubes (MDTs) and Cathode Strip Chambers (CSCs). The other one is trigger chambers, which are designed to provide a fast response of electric signals within 25 ns for the trigger system described in Section 3.3. The trigger chambers are Resistive Plate Chambers (RPCs) and Thin Gap Chambers (TGCs). All of these detectors work on similar detection principle to the TRT drift tubes but without the component of transition radiation.

Monitored Drift Tubes

The Monitored Drift Tubes (MDTs) are cylindrical drift tubes with a diameter of 30 mm. The tubes are filled with a gas mixture of Ar (93%) and CO_2 (7%). Drifting electrons are collected by a gold-plated

tungsten-rhenium wire with a diameter of 50 μm in the center of a tube, where a bias voltage of 3080 V is applied. The maximum drift time is approximately 700 ns, and the position resolution per drift tube is 80 μm. There are three layers of the MDT chambers as shown in Figure 3.15. They are additionally divided into the barrel and end-cap regions according to the structure and totally provide coverage over $|\eta| < 2.7$. However, the innermost layer in the region of $2.0 < |\eta| < 2.7$ is not placed because the rate of incoming particles exceeds the limitation of MDTs (150 Hz/cm^2).

Cathode Strip Chambers

The Cathode Strip Chambers (CSCs) are multiwire proportional chambers with cathode strips. The cathode strips are oriented in the ϕ direction and the anode wires are oriented in the R direction. Since they are perpendicular, the CSCs provide two position coordinates for incoming particles. The chambers are operated with a gas mixture of Ar (80%) and CO_2 (20%) and with a bias voltage of 1900 V. The position resolution per chamber is 5 mm in the ϕ direction and 60 μm in the R direction. The CSCs are used in the innermost layer where the MDTs are not able to cover due to the higher rate thanks to the relatively short drift time of < 40 ns.

Resistive Plate Chambers

The Resistive Plate Chambers (RPCs) are designed to provide a fast response for the trigger system. Three layers of the RPC chambers are placed in the barrel region of $|\eta| < 1.05$ as shown in Figure 3.15. The RPCs are made from two parallel electrode plates with metal strips on their outer surfaces. The gap between these plates is 2 mm, where is filled with a gas mixture of $C_2H_2F_4$ (94.7%), Iso-C_4H_{10} (5%) and SF_6 (0.3%). A uniform high electric field of approximately 4900 V/mm is applied. When charged particles pass through the gas mixture, they produce ionization electrons from it and then the high electric field immediately leads to an avalanche growth of these electrons. A short electric signal obtained by the avalanche provides a high time resolution of approximately 1 ns. The RPCs are thus used for the trigger system. Since the metal strips of each RPC are placed to be perpendicular, the RPCs provide two position coordinates in the $z - \phi$ plane with a position resolution of 10 mm.

Thin Gap Chambers

The Thin Gap Chambers (TGCs) are multi-wire proportional chambers covering the end-cap region of $1.05 < |\eta| < 2.4$. They are placed in the innermost layer and the middle layers as shown in Figure 3.15. The TGCs are characterized that a distance of 1.4 mm between the anode wire and the cathode strip being smaller than that of 1.8 mm between the anode wires. They are operated with a highly quenching gas mixture of CO_2 (55%) and n-C_5H_{12} (45%) and with a high voltage of 2900 $\pm$ 100 V applied to the anode wires. The thinner distance and the high voltage lead to a fast response with a high time resolution of approximately 4 ns. The cathode strips are segmented in the ϕ direction to provide ϕ coordinate, complementing the measurement of the MDTs in the R direction. On the other hand, the anode wires are arranged to be parallel to the MDT tubes in the ϕ direction. The TGCs thus provide two position coordinates in the $R - \phi$ plane with a position resolution of 2-6 mm and 3-7 mm, respectively.

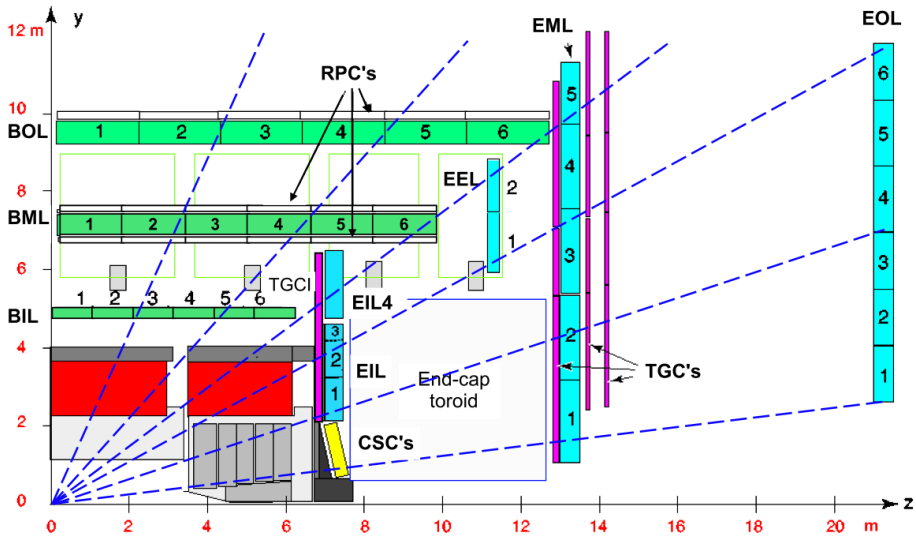

Figure 3.15 Layout of the muon spectrometer at $\phi = \pi/2$ in the $R - z$ plane [3]. The MDT, CSC, RPC and TGC layers are shown in the blue and green boxes, the yellow box, the gray lines and the magenta lines, respectively.

3.3 Trigger and Data Acquisition System

Due to buffer bandwidth limitation of 4 GB/s, it is impossible to record all collision data provided by the LHC within the ATLAS detector with a bunch crossing rate of over 40 MHz and an event read-out size of approximately 1 MHz. In addition, most of the collision events originate from non-interesting inelastic scattering. The Higgs boson production cross-section is $O(10)$ pb, while the cross-section of the total inelastic scattering is $O(10^{10})$ pb. Therefore, the ATLAS Trigger and Data Acquisition (TDAQ) system [69] is used to select only events that are likely to be relevant to interesting hard-scatter interactions during data taking (online). Then, it suppresses the average data rate to be approximately 1 kHz. The online process is called a *trigger*.

The ATLAS TDAQ system is designed to reduce the data rate in two stages gradually: the hardware-based Level-1 (L1) trigger and the software-based High-Level Trigger (HLT), as shown in Figure 3.16. The p_{T} of particles originating from a hard-scatter interaction is typically higher than that of particles originating from an inelastic scatter interaction. The ATLAS TDAQ system thus selects such events with higher-p_{T} objects such as leptons, photons or jets, exploiting these kinematical and topological differences. The average output data rate is 100 kHz for the L1 trigger and 1 kHz for the HLT.

3.3.1 Hardware-based Level-1 Trigger

The L1 trigger is allocated 2.5 μs to reconstruct objects and make a decision if passing the event to the HLT or discarding it per bunch crossing. The L1 trigger consists of three trigger systems, L1Calo, L1Muon and L1Topo, and a Central Trigger Processor (CTP).

The L1Calo trigger system makes decisions for electron, photon, tau lepton, jet and missing trans-

verse energy ($E_{\mathrm{T}}^{\mathrm{miss}}$) in the event using the calorimeter. Since jets and the other objects except $E_{\mathrm{T}}^{\mathrm{miss}}$ have the different shapes of energy deposits in the calorimeter, they are reconstructed separately in the Cluster Processor (CP) and the Jet/Energy-sum Processor (JEP) [70]. The calorimeter regions, where these objects passing L1 trigger selections exist, are considered as *Regions-of-Interest* (RoIs). The $E_{\mathrm{T}}^{\mathrm{miss}}$ for an event is produced by the vector sum of the energy deposits in the JEP and then similarly considered. The L1Muon trigger system reconstructs muons using the RPC and TGC trigger chambers [69]. Similarly to the L1Calo trigger system, the MS regions with muons passing L1 trigger selections are considered as RoIs. After these processes, the decision information in each trigger system is passed on to the L1Topo and the CTP. The L1Topo trigger system receives the decision information of per object from the L1Calo and L1Muon trigger systems. In the L1Topo trigger system, topological variables, such as angular separation and invariant mass of objects, in the event are calculated. Then, the decision information is passed on to the CTP. The CTP receives the decision information from the L1Calo, L1Muon and L1Topo trigger systems. The CTP controls the average data rate to be 1 kHz and makes a final decision in the event. The L1 trigger system also provides RoIs to the HLT.

3.3.2 Software-based High-Level Trigger

After events are accepted in the L1 trigger, they are buffered in the Read-Out System (ROS) and processed by the HLT. The HLT is limited to an average time of 500 ms to reconstruct objects and make a decision in the event with 50,000 processing units in 2018. The HLT receives the RoIs from the L1 trigger and refine the L1 objects using more precious detector information. This process is performed using partial detector information based on the RoIs to meet the CPU limitation. However, objects can be missed or misidentified in the L1 trigger due to the detector structure and resolution and they are not processed by the HLT in the RoI-based partial reconstruction. The HLT thus reconstructs objects by scanning over the whole detector according to the trigger selections to recover missing objects in the L1 trigger. It finally reduces the average data rate to approximately 1 kHz. The events accepted by the HLT are stored in the data storage and used in physics analyses.

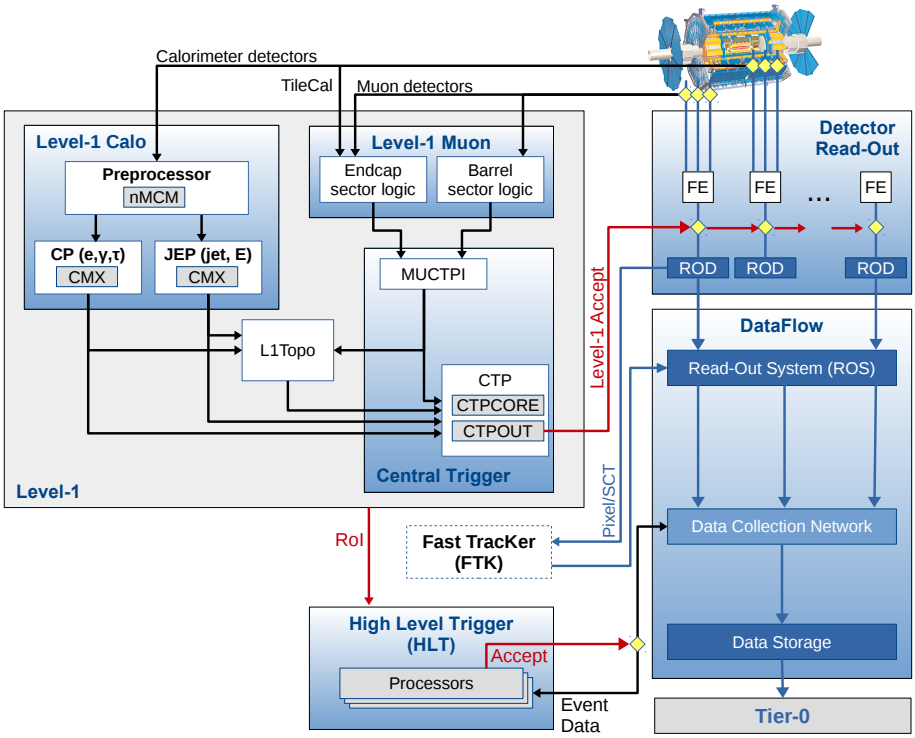

Figure 3.16 Schematic of the ATLAS Trigger and Data Acquisition system [69]. Read-out lines of trigger detectors are input separately into L1Calo and L1Muon trigger systems.

Chapter 4

Object Reconstruction and Identification

Electric signals of the events detected in the ATLAS detector need to be converted to physics objects to use in the analysis. A series of processes is known as object reconstruction. This chapter describes an overview of the reconstruction procedures. In particular, the jet reconstruction and the jet flavour identification procedures are provided because this analysis deeply relies on jet objects containing b-hadrons.

4.1 Fundamental Units of Physics Objects

4.1.1 Tracks

Charged particles such as electron, muon and so on, are detected in the inner detector as *hits*. A trajectory of the charged particle, referred to as a *track*, is reconstructed by connecting these hits. Tracks are used in many places such as the primary vertex reconstruction, the jet reconstruction and the b-jet identification. I will summarize the track reconstruction in this section. The detail of the track reconstruction used in this analysis is given in Ref. [71].

A charged particle often lefts the charge in multiple adjacent pixels as multiple hits in a pixel sensor, as illustrated in Figure 4.1. A group of the hits, referred to as a *cluster*, is thus assembled by a connected component analysis [72], where common edges or corners of the charge above the threshold are grouped into the cluster. Three-dimensional measurements referred to as *space-points* are created from these clusters. The space-points denote the points that the charged particle traversed in the inner detector. A combinatorial Kalman filter [73] is then used to form track candidates. The algorithm uses *track seeds* formed from sets of three space-points and incorporates additional space-points in the different layers of the detector, where compatible ones with the trajectory are selected. It is allowed to create multiple track candidates per track seed if there are more than one compatible space-points on the same layer, to account for merged clusters due to very collimated charged particles as illustrated in Figure 4.1(b). However, this allows some track candidates to have overlapping space-points and be incorrectly assigned. *Track scores* that denote the track quality are thus calculated per track candidate, and the-low quality candidates under the threshold are rejected. In addition, the basic quality criteria described in Ref. [71] are applied to keep track quality.

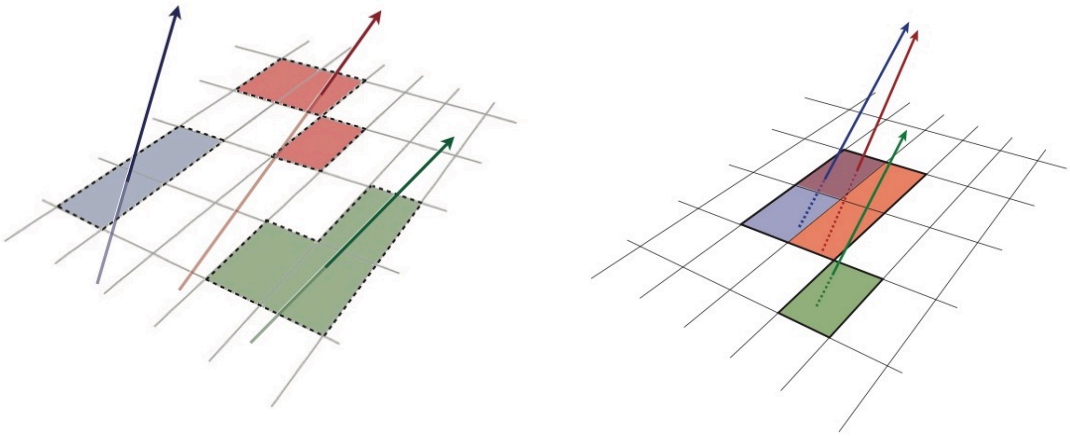

(a) Single-particle pixel clusters (b) Merged pixel clusters

Figure 4.1 Illustration of (a) single-particle pixel clusters and (b) merged pixel clusters on a pixel sensor [71]. Different colours indicates energy deposits from different charged particles and the arrows shows the trajectories.

4.1.2 Topological Clusters

A topological cluster of calorimeter cells (*topo-cluster*) is the basic unit of energy measurement in the calorimeter detector. In the topological clustering algorithm [74] used in this analysis, seed cells are firstly defined as cells in which absolute energy deposits exceed 4σ of the expected noise level including electronic noise and the average contribution from pile-up. All neighboring cells with energy deposits exceeding 2σ of the noise level are iteratively collected into the corresponding seed cell. If there are two or more local maxima with energies over 500 MeV in the cluster, they are split between the corresponding signal peaks in all three spatial dimensions. The clusters with one local maximum are then defined as *topo-cluster*. These topo-clusters are used as one of the inputs for the jet reconstruction as described later.

4.1.3 Primary Vertices

Multiple proton-proton interactions take place in the same bunch crossing in the LHC. The positions in space where proton-proton interactions have occurred are referred to as *vertices*. These vertices are identified by a vertex reconstruction algorithm [75] using the tracks reconstructed in the inner detector. The procedure can be divided into two steps. The first step is vertex finding, which creates vertex candidates from the tracks based on pattern recognition. The next step is vertex fitting, where the actual vertex positions are reconstructed from vertex candidates. In particular, the vertex in which the sum of p_{T} of the associated tracks is highest in the bunch crossing is defined as a *primary vertex* and used to reconstruct the full kinematic properties of the event and calibrate the objects.

4.2 Jets

A quark in the final state of the event generated by proton-proton collisions produces particles by hadronizations and then constructs a collimated shower. The collection of particles is called a *jet*, as illustrated in Figure 4.2.

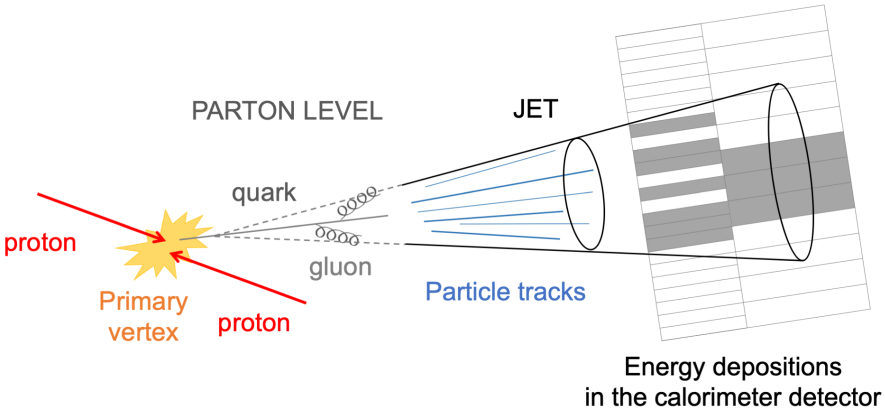

Figure 4.2 A scheme of jet interaction in the detector.

4.2.1 Reconstruction

Firstly, particle flow objects (PFlow objects) are provided by the particle flow algorithm [76]. This algorithm is based on the fact that jets produce both tracks in the inner detector and topo-clusters in the calorimeter detector and takes advantage of the unique feature that tracks have better energy resolution in low energies, while topo-clusters have better energy resolution in high energies. The particle flow algorithm firstly attempts to match each selected track that is matched to the primary vertex to a single topo-cluster. However, a single particle often deposits its energy in multiple topo-clusters. The expected energy deposited in the calorimeter detector is thus computed from the track momentum and the topo-cluster position. If the corresponding topo-cluster energy is less than the expected energy, different topo-clusters that do not match any other track and are compatible with the track are combined until the set of topo-cluster energies is consistent with the expected one. The procedure can improve the energy resolution in particular of low p_{T} jets. These selected tracks and the corresponding sets of topo-clusters are considered as PFlow objects.

The anti-k_t jet clustering algorithm [77] is then employed to reconstruct jets from PFlow objects. The basic step of the anti-k_t jet clustering algorithm is merging the proximate two objects. The distance d_{ij} between two objects i and j and the distance d_{iB} between i and the beam (B) are given by:

$$d_{ij} = \min\left(k_{t,i}^{2p}, k_{t,j}^{2p}\right)\frac{\Delta_{ij}^2}{R^2}, \tag{4.1}$$

$$d_{iB} = k_{t,i}^{2p}, \tag{4.2}$$

where $\Delta_{ij} = \sqrt{\left(y_i^2 - y_j^2\right) + \left(\phi_i^2 - \phi_j^2\right)}$ is the angler distance between two objects , and $y_{i,j}$, $\phi_{i,j}$ and $k_{t,i,j}$ are the rapidity, the azimuthal angle and the transverse momentum. R is a radium parameter providing the typical size of the reconstructed jet and is set to 0.4 in this analysis. p is set to -1 in the anti-k_t jet clustering algorithm. The distances for all the relevant objects are calculated. The two objects with the smallest distance are merged into one if their distance is less than d_{iB}, and the distances are then recalculated. This process is repeated until no pair of two objects that satisfy $d_{ij} < d_{iB}$ is found. A collection of jets is finally obtained. The anti-k_t jet clustering algorithm plays clustering soft-objects with hard-objects before clustering them with each other. This is well-motivated to reduces the loss of momentum resolution due to pile-up.

4.2.2 Calibration

Energies of reconstructed jets are measured at the scale of the detector not the scale of the truth particle. The deferences are primarily caused by the fact that the detectors only measure the energy deposits due to the interaction of the jet with the active materials. Therefore, several jet calibrations are applied to obtain the truth particle energy for a given jet. The procedure used in this analysis follows Ref. [78].

Pile-up correction

Jet energies measured in the calorimeter detectors often include contributions of particles from pile-up jets. It thus needs to well-understand and account for the pile-up contribution to the p_{T} of the reconstructed jet. The k_t jet clustering algorithm with $R = 0.4$, where $p = 1$ is set in Eq. 4.1 and 4.3, is used to form a set of k_t jets from positive energy topo-clusters in the range of $|\eta| < 2$. The k_t jet clustering algorithm can naturally reconstruct jets including an uniform soft background in contrast to the anti-k_t jet clustering algorithm. After that, the jet area A, which denotes a measure of the susceptibility of the jet to pile-up, is calculated by a ghost-association algorithm [79], and the median p_{T} density (ρ) of these k_t jets is derived in the $y - \phi$ plane, $\langle p_{\mathrm{T}}/A \rangle$. The pile-up contribution is then estimated by $\rho \times A$.

In addition, a residual correction is applied because some dependences of the anti-k_t jet p_{T} on pile-up conditions are also observed. The residual correction is given as a function of the number of reconstructed primary vertices in the event (N_{PV}) and pile-up (μ). Therefore, the pile-up correction function is given by:

$$p_{\mathrm{T}}^{\mathrm{corr}} = p_{\mathrm{T}}^{\mathrm{reco}} - \rho \times A - \alpha \times (N_{PV} - 1) - \beta \times \mu, \tag{4.3}$$

where $p_{\mathrm{T}}^{\mathrm{reco}}$ is the p_{T} of the reconstructed jet before the pile-up correction is applied, and $p_{\mathrm{T}}^{\mathrm{corr}}$ is the p_{T} of the corrected jet. α and β are differential coefficients derived in bins of truth particle p_{T} and reconstructed jet $|\eta|$.

Jet energy scale and η calibration

The jet energy scale and η calibration are applied to correct differences on the jet four-momentum between the reconstruction level and the truth particle level due to the incomplete and varying response of the detector. Figure 4.3 shows the average jet energy response (R), which is defined as the average ratio of the reconstructed jet and truth particle energies, as a function of the reconstructed jet energy (E^{reco}) and $\eta\left(\eta^{\mathrm{det}}\right)$. As can be seen, there are significant differences in the jet energy between the reconstruction

level and the truth particle level, and the average jet energy response significantly varies depending on E^{reco} and η^{det}. These differences and variations are primarily made by the increased fraction of the jet energy deposits for high-energy particles, the transition regions between different calorimeter detectors and the differences in calorimeter granularity. To account for these differences, the jet calibration factors are derived as the inverse of the average jet energy response in bins of E^{reco} and η^{det} and are applied.

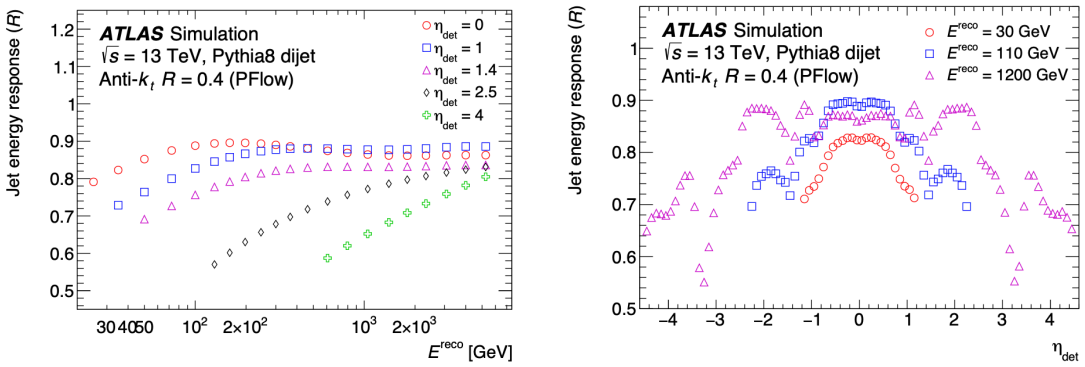

(a) (b)

Figure 4.3 The average jet energy response R as a function of (a) the reconstructed jet energy (E^{reco}) and (b) η $\left(\eta^{\text{det}}\right)$ [78].

Global sequential calibration

Even after the previous calibrations are applied, the jet response is found to still vary jet-by-jet depending on their initial particles and their flavors as well as other factors such as energy distributions of the constituent particles. The variation can be observed most notably between quark- and gluon-initial jets. A quark-initial jet often contains hadrons with a higher fraction of the jet energy and penetrates deeply into the calorimeter detectors. On the other hand, a gluon-initial jet typically includes more particles with lower energy, resulting in a lower response and a wider jet shower shape. A series of multiplicative corrections is thus applied to reduce these impacts and improve the jet resolution. These corrections are based on the information of jet energy deposits measured in each detector, such as the fraction of jet energy measured in the first layer of the HCAL and the fraction of jet energy measured in the last layer of the ECAL, and information about constituent particles, such as the fraction of the jet p_{T} measured by constituent tracks. The series of these corrections is called the global sequential calibration [76].

In situ jet calibration

Following the previous calibrations, jets have been calibrated to the truth particle level. However, there are still differences in the jet response between data and simulation due to imperfect modellings of the detector materials and the physics processes in simulation. Therefore, *In situ* jet calibration [76] is used to correct the differences. The jet response must be calculated in data to measure the differences between data and simulation. Therefore, jets from $Z + jet$, $\gamma + jet$ and multi-jet processes are selected and used as well-calibrated reference objects. The jet response R_{insitu} is then obtained as the average ratio of the jet

to the reference object p_{T}, and the correction factors are derived as the double ratio of the jet responses in data and simulation as given by:

$$c = \frac{R^{data}_{in\ situ}}{R^{sim}_{in\ situ}} \tag{4.4}$$

This provides a reliable measure of the difference on the jet energy scale between data and simulation so long as the reference objects are well-modelled in simulation. Finally, the correction factor are applied to reconstructed jets in data.

4.2.3 Jet-vertex-tagger

Many of the reconstructed jets are found to come from pile-up processes, not from the hard-scatter primary vertex. The suppression of these pile-up jets is important to focus on a hard-scatter event.

The Jet Vertex Tagger (JVT) cut [80] is used in this analysis to suppress the contribution. The discriminant formula that denotes a probability of a jet to be formed by hard-scatter processes than pile-up processes is derived from two variables: a corrected jet vertex fraction (corrJVF) and a variable $R_{p_{\mathrm{T}}}$. Jet vertex fraction (JVF) is defined as the scalar sum of the track p_{T} associated with the jet from the primary vertex, $\sum_k p_{\mathrm{T}}^{\mathrm{trk}_k}(\mathrm{PV}_0)$, divided by the scalar sum of p_{T} of all associated tracks, $\sum_l p_{\mathrm{T}}^{\mathrm{trk}_l}(\mathrm{PV}_0) + \sum_{n\geq 1}\sum_l p_{\mathrm{T}}^{\mathrm{trk}_l}(\mathrm{PV}_{\mathrm{n}})$. The corrJVF is a corrected form of the JVF to add a correlation that takes into account a dependence of the scalar p_{T} sum from pile-up tracks associated with the jet on the number of the pile-up tracks including in the event, $n^{\mathrm{PU}}_{\mathrm{trk}}$. It is defined by:

$$\mathrm{corrJVF} = \frac{\sum_k p_{\mathrm{T}}^{\mathrm{trk}_k}(\mathrm{PV}_0)}{\sum_l p_{\mathrm{T}}^{\mathrm{trk}_l}(\mathrm{PV}_0) + \frac{\sum_{n\geq 1}\sum_l p_{\mathrm{T}}^{\mathrm{trk}_l}(\mathrm{PV}_{\mathrm{n}})}{k\cdot n^{\mathrm{PU}}_{\mathrm{trk}}}}, \tag{4.5}$$

where PV_0 and PV_{n} denote the primary vertex and the other vertex. k is a scaling fator defined the pile-up conditions such as the number of pile-up tracks. $R_{p_{\mathrm{T}}}$ is defined as the scalar sum of p_{T} of the tracks associated with the jet from the primary vertex, $\sum_k p_{\mathrm{T}}^{\mathrm{trk}_k}(\mathrm{PV}_0)$, divided by p_{T} of the fully calibrated jet, p_{T}^{jet}. It is defined by:

$$R_{p_{\mathrm{T}}} = \frac{\sum_k p_{\mathrm{T}}^{\mathrm{trk}_k}(\mathrm{PV}_0)}{p_{\mathrm{T}}^{jet}} \tag{4.6}$$

They have strong discriminant between hard-scatter jets and pile-up jets, as shown in Figure 4.4. The JVT discriminant is constructed as a 2-dimensional likelihood based on a k-nearest neighbor algorithm [81] using both of these two variables. The distributions of the JVT discriminant for hard-scatter jets and pile-up jets are shown in Figure 4.4(c). In this analysis, the threshold value that keeps 96% efficient for hard-scatter jets is used.

4.2.4 Jets in this analysis

In this analysis, jets are classified into two groups based on their kinematics. *Central* jets are used to form *Higgs candidates*. *Forward* jets are used to identify jets produced in the VBF production process. They are also used to separate events into two channels, ggF channel and VBF channel (described in Section 6.4.2), targeting the different HH production processes.

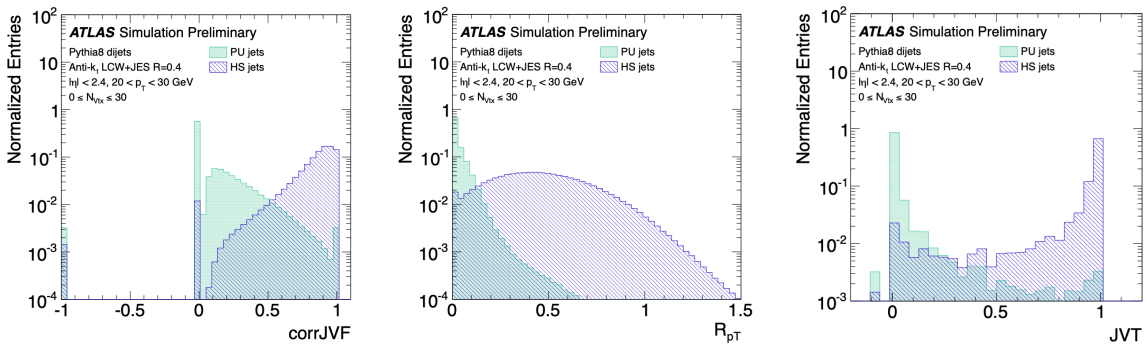

(a) (b) (c)

Figure 4.4 (a) corrJVF, (b) $R_{p_{\mathrm{T}}}$ and (c) JVT discriminant distributions of hard-scatter jets (purple) and pile-up jets (green) [80]. Jets with no associated tracks are located at a bin of corrJVF= 1, and jets with no associated hard-scatter tracks are at a bin of corrJVF= 0.

***Central* jets:** Jets with $p_{\mathrm{T}} \geq 40$ GeV and $|\eta| < 2.5$.

***Forward* jets:** Jets with $p_{\mathrm{T}} \geq 30$ GeV and $|\eta| \geq 2.5$.

4.3 *b*-jets

It is useful to identify the flavor of the initial particle that originates the jet. Jets originating from *b*-quarks are called *b*-jets. The procedure of the *b*-jet identification is called *b*-tagging. Since the *HH* production decays to two pairs of *b*-quarks with the highest branching ratio of approximately 34%, the *b*-tagging is crucial to select the signals and reduce backgrounds. This section presents the *b*-tagging procedure.

4.3.1 *b*-jet Identification

b-hadrons produced by the hadronization of *b*-quarks have longer lifetimes of approximately 1.5 ps, corresponding to a proper decay length of $c\tau \approx 450\mu$m, than other hadrons originating from the other quarks. This feature of *b*-hadrons produces a distinctive trajectory whose length typically gets a few millimetres before its decays. Thus, *b*-jets typically have a secondary vertex, as shown in Figure 4.5. The *b*-tagging is performed by exploiting the features of *b*-jets such as the long lifetime, high mass and high multiplicity of *b*-hadron decays. The *b*-tagging procedure consists of five low-level algorithms (IP2D, IP3D, RNNIP, SV1 and JetFitter) and one high-level algorithm (DL1r). The low-level algorithms provides discriminating variables that indicate topological and kinematical differences between *b*-jet and other flavor jet, and then the high-level algorithm makes use of these discriminating variables and outputs the final discriminant that denotes a probability of a jet to be a *b*-jet. The *b*-tagging is performed using a cut of the final discriminant.

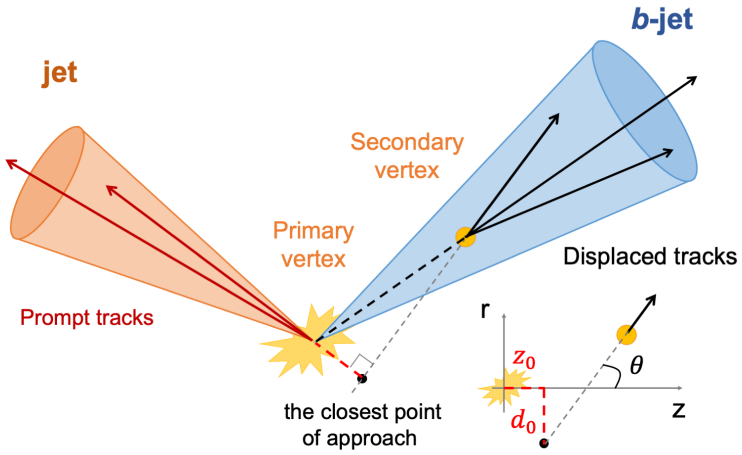

Figure 4.5 Illustration of an interaction producing a b-jet and other flavor jet. d_0, z_0 and θ indicate the transverse and longitudinal impact parameters and the polar angle between the track and the beam pipe.

Impact parameter based algorithm: IP2D, IP3D and RNNIP

Two complementary impact parameter-based algorithms called IP2D and IP3D [82], which exploit the impact parameters of tracks associated with the jet, are used. The Impact parameter is defined as the distance of the closest approach of the track to the primary vertex [83]. The transverse and longitudinal impact parameters are referred to as d_0 and z_0, and the resolutions are referred to as σ_{d_0} and σ_{z_0}, respectively. These impact parameters for b-jets typically become large due to its long lifetime. The IP2D thus makes use of the transverse impact parameter significance, d_0/σ_{d_0}, and the IP3D makes use of both the transverse and longitudinal impact parameter significance, $z_0 \sin\theta/\sigma_{z_0 \sin\theta}$, where θ is the polar angle between the track and the beam pipe. These algorithms compute probability density functions (pdfs) of the transverse and longitudinal impact parameter significances of tracks associated with b-jets, c-jets and other light-flavor jets using simulation. The ratios of b-jet, c-jet and other light-flavor jets probabilities per track associated with the jet are calculated using the probability density functions. Log-likelihood ratio (LLR) discriminants are then derived as the sum of the probability ratios of the tracks. These algorithms finally output three discriminants for the b-tagging: $\sum_{i=1}^{N} \log(p_b/p_c)$, $\sum_{i=1}^{N} \log(p_b/p_u)$ and $\sum_{i=1}^{N} \log(p_c/p_u)$, where $p_{b,c,u}$ are the b-jet, c-jet and the other light-flavor jet probabilities of a track i and N is the number of tracks associated with the jet.

An impact parameter-based algorithm based on a recurrent neural network (RNN), which algorithm is called RNNIP [84], is also used to take into account the flavor-dependent correlations between tracks associated with the jet. In the IP2D and IP3D, the discriminants are derived without considering any correlations between tracks associated with the jet. However, they can be correlated depending on the jet flavor. For a b-jet, multiple charged tracks are produced from the b-hadron decay so that they should be correlated. On the other hand, for a light-flavor jet such as a u-jet, such correlation is not observed due to no such decay. The RNNIP thus makes use of the flavor-dependent correlations between tracks in the jet using RNN and then provides the flavor probabilities for each jet. Full details such as the input variables

and the structure of RNN can be found in Ref. [84].

Secondary vertex finding algorithm: SV1

The secondary vertex finding algorithm called SV1 [82] is used to reconstruct a single secondary vertex using tracks associated with the jet. After a set of qualification requirements is applied to tracks in the jet, all pairs of two tracks in these tracks are formed and the two-track vertex consistency of each pair is tested. This procedure is based on the fact that all tracks originating from the vertex are close to the vertex built by any two of these tracks. However, tracks originating from the primary vertex often get close enough to form a secondary vertex candidate in such a simple algorithm. Extra requirements, such as the vertex invariant mass less than 6 GeV, are thus applied to further reduce such fake vertices that are not likely to originate from $b-$ and c-hadrons. If there are multiple candidates, the vertex with the highest invariant mass is selected as the secondary vertex in the jet. The SV1 finally outputs eight variables for the b-tagging, such as the invariant mass of the secondary vertex, the energy fraction of tracks associated with the secondary vertex to all tracks associated with the jet and the number of two-track vertices. A full list of the output variables can be found in Ref. [82].

Topological multi-vertex finding algorithm: JetFitter

The topological multi-vertex finding algorithm called JetFitter [85] is also used to provide topological information of the jet. The JetFitter makes use of the topological differences on the inside structures of b-hadrons and the other flavor jets, and attempts to reconstruct the full b-hadron decay chain. A modified Kalman filter [86] is adopted to find a common line between the primary vertex and b-hadron (c-hadron) vertex, corresponding to the flight direction. The JetFitter then outputs eight variables for the b-tagging, such as the fight length and the invariant mass of tracks associated with the b-hadron (c-hadron) vertex. A full list of the output variables can be found in Ref. [82].

High-level tagging algorithm: DL1r

The high-level tagging algorithm, DL1r [82], is based on a deep neural network. The DL1r outputs three different probabilities of a given jet to be a b-jet (p_b), c-jet (p_c) or the other light-flavor jet (p_u) using output variables from the IP2, IP3, RNNIP, SV1 and JetFitter. Then a discriminant score is provided from the three probabilities as given by:

$$D_{DL1r} = \log \frac{p_b}{f_c \times p_c + (1 - f_c) \times p_u}, \tag{4.7}$$

where f_c is a parameter to control the importance of c-jet discrimination and is set to 0.018 in the DL1r algorithm. However, the DL1r algorithm does not make the decision which the jet is a b-jet, c-jet or the other light-flavor jet, and it needs to assign a cut on the discriminant score to label that. Four cuts on the discriminant score are thus supported so that the b-tagging efficiency to truth b-jets becomes 60%, 70%, 77% and 85%. These criteria are known as *working points* (WP). In this analysis, the 77% and 85% WPs are used, as discussed in Section 6.4.1. The b-tagging performance at 77% WP are shown in Figure 4.6.

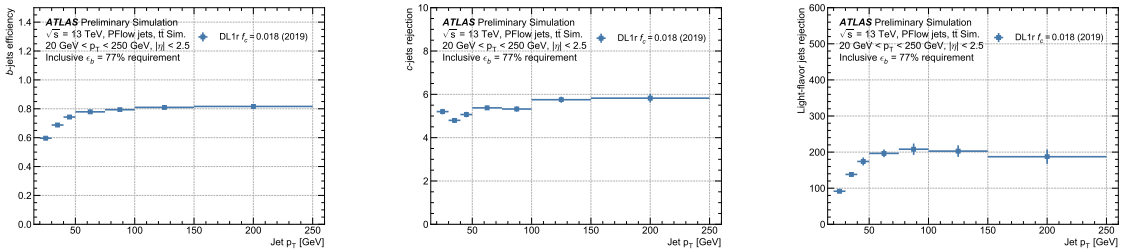

(a) (b) (c)

Figure 4.6 (a) Efficiency of b-jet identification and the rejection rates of (b) c-jets and (c) the other light-flavor jets as a function of jet p_{T} in the b-tagging 77% WP. The rejection rate is defined as the inverse of mis-identification efficiency ($1/\epsilon$). These plots are taken from Ref. [87] and adopted for this thesis.

4.3.2 b-tagging Calibration

There are differences in the b-tagging performances between data and simulation. The b-tagging calibration [88] is thus applied to ensure that the b-tagging performance is consistent between data and simulation. The b-tagging efficiencies are derived on both data and simulation using b-jet enriched data samples obtained mostly from $t\bar{t}$ process. The ratio of these efficiencies is then computed and used as the calibration factor, also known as the scale factor. Since the scale factors are found to vary for jet p_{T} and η, they are supported in bins of these variables.

4.3.3 b-jet Calibration

The jet energy calibrations described in Section 4.2.2 focus on the corrections for all relevant jets originating from quarks and gluons. For b-jets, additional energy calibrations are needed because their energy is underestimated due to two main effects:

1. When the b-hadron decays semi-leptonically with $W \to \mu\nu_{\mu}$, the neutrino energy is not captured in the detectors and the muon energy is only partially added in the jet reconstruction because it does not typically stop in the calorimeter detector.
2. Some of the particles originating from the b-hadron decay are missed in the jet clustering algorithm due to the b-jet feature that the fragmentation is typically wider than the other flavor jets. It is known as *out-of-cone effect*.

Therefore, b-jet energy is calibrated by two steps in this analysis.

The first step is simply adding the four-momentum of a single muon into the jet to account for missing muon energy. Muons are reconstructed from tracks in the inner detector and the muon spectrometer and selected to be $p_{\mathrm{T}} > 4$ GeV and $|\eta| < 2.5$. These muons are additionally selected by a variable radius cone $\Delta R\,(\mathrm{jet}, \mu) < \min\left(0.4,\ 0.04 + 10/p_{\mathrm{T}}^{\mu}\ \mathrm{GeV}\right)$ from the jet axis, where p_{T}^{μ} is the muon p_{T}, to ensure that it originates from the b-hadron decay. If there are multiple candidates, the closest one of the selected muons is chosen and its four-momentum is combined into the jet four-momentum.

The second step account for missing neutrino energy and the out-of-cone effect. The correction factor is defined as the mean of the ratio of reconstructed b-jet p_{T} to truth b-jet p_{T} in bins of logarithmic reconstructed b-jet p_{T}. Since the correction for b-jets with semi-leptonically decay is typically larger than that for b-jets with hadronically due to missing neutrino energy, these correction factors are derived separately for b-jets with muon and no muon.

Figure 4.7 shows the b-jet correction effect on the invariant masses of the leading Higgs boson (m_{H1}) and the sub-leading Higgs boson (m_{H2}) for the SM ggF HH production process. The b-jet correction performance is evaluated by the Bukin function fitting [89]. The m_{H1} and m_{H2} resolutions are found to be improved by approximately 5% and 20% by the b-jet correction, respectively.

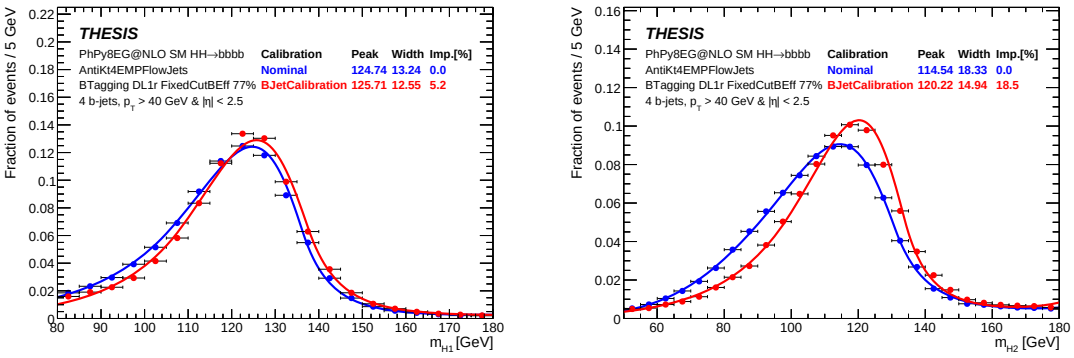

(a) m_{H1} (b) m_{H2}

Figure 4.7 Comparisons of m_{H1} and m_{H2} distributions before the b-jet calibration (blue) and after the b-jet calibration (red) for the SM ggF HH production process. These distributions are fitted using the Bukin function, and the peak, the peak resolution and the relative improvement are shown in the legend.

Chapter 5

Dataset and Monte Carlo Samples

This analysis uses both data and simulation samples. The data samples corresponding to the ATLAS Run-2 dataset of proton-proton collisions at $\sqrt{s} = 13$ TeV are described in Section 5.1. The simulation samples for non-resonant $HH \to b\bar{b}b\bar{b}$ signals are described in Section 5.2.

5.1 Dataset

This analysis uses the ATLAS Run-2 datasets, corresponding to 126 fb^{-1}, of proton-proton collisions at $\sqrt{s} = 13$ TeV taken from 2016 to 2018. In particular, the datasets collected by multi b-jet triggers listed in Table 5.1 are used. As this analysis use multi b-jet triggers, the integrated luminosity is lower than the full Run-2 dataset corresponding to 139 fb^{-1} shown in Figure 3.3. The reason is that the 2015 dataset and the beginning of the 2016 data are not used in this analysis. In the 2015 dataset, there was a bug in the online jet information, which causes the matching efficiency between online and offline jets to be 0%. The matching is necessary for the analysis and required in the analysis selection described in Section 6.3. This bug is fixable, but there is little gain from the 2015 dataset because it is only 2.5% of the total datasets and multi b-jet triggers in 2015 have low efficiency. Therefore, the 2015 dataset is removed from this analysis. During the beginning of the 2016 data taking, an inefficiency of the online primary vertex reconstruction due to a bug in the algorithm was observed. b-jet triggers need the primary vertex information for the b-jet identification, so the issue lowers the data quality. In the ATLAS experiment, in order to avoid using such low-quality datasets, *Good Run List* (GRL) that guarantees the data quality on each period of data taking is provided. Due to the issue, the beginning of the 2016 datasets are removed from GRL for analyses using b-jet triggers and are not used in this analysis. The integrated luminosities used in this analysis are ultimately:

- 2016: 24.56 fb^{-1}
- 2017: 43.65 fb^{-1}
- 2018: 57.70 fb^{-1}

Year	Requirement	ATLAS Terminology	Type
2016	Two b-jet (60% eff. WP) with $E_{\mathrm{T}} > 55$ GeV and one extra jet with $E_{\mathrm{T}} > 100$ GeV	HLT_j100_2j55_bmv2c2060_split	2b1j
	Two b-jet (60% eff. WP) with $E_{\mathrm{T}} > 35$ GeV and two extra jet with $E_{\mathrm{T}} > 35$ GeV	HLT_2j35_bmv2c2060_split_2j35_ L14J15.0ETA25	2b2j
2017	Two b-jet (70% eff. WP) with $E_{\mathrm{T}} > 55$ GeV and one extra jet with $E_{\mathrm{T}} > 150$ GeV	HLT_j110_gsc150_boffperf_split_ 2j35_gsc55_bmv2c1070_split_L1J85_3J30	2b1j
	Two b-jet (40% eff. WP) with $E_{\mathrm{T}} > 35$ GeV and two extra jet with $E_{\mathrm{T}} > 35$ GeV	HLT_2j15_gsc35_bmv2c1040_split_ 2j15_gsc35_boffperf_split_L14J15.0ETA25	2b2j
2018	Two b-jet (70% eff. WP) with $E_{\mathrm{T}} > 55$ GeV and one extra jet with $E_{\mathrm{T}} > 150$ GeV	HLT_j110_gsc150_boffperf_split_ 2j45_gsc55_bmv2c1070_split_L1J85_3J30	2b1j
	Two b-jet (60% eff. WP) with $E_{\mathrm{T}} > 35$ GeV and two extra jet with $E_{\mathrm{T}} > 35$ GeV	HLT_2j35_bmv2c1060_split_2j35_ L14J15.0ETA25	2b2j

Table 5.1 List of multi b-jet triggers used for this analysis.

5.2 Monte Carlo Samples

Monte-Carlo (MC) simulation is the current best toolkit to provide theoretical predictions on the topology and kinematics of event process and also the detector responses. I use the EvtGen (v.1.7,0) program [90] that is used to prepare simulated events. Generators and parton shower simulators used for each signal sample are described in Section 5.2.1. A full simulation of the ATLAS detector responses is performed by the ATLAS detector simulation software [91] based on Geant4 [92].

These generators typically provide theoretical predictions at next-to-leading-order (NLO) due to theoretical limits on perturbative calculation in QCD. However, total cross-sections are often available at more leading order, typically next-to-next-to- leading-order (NNLO). In that case, simulation samples are normalized by the best available theoretical prediction. The signal samples used in this analysis are generated based on NLO and normalized by the NNLO cross-section.

5.2.1 HH Signal Samples

ggF HH samples

HH signal samples via the ggF process are generated using Powheg Box v2 generator [93–95] at NLO with full NLO correlations with finite top mass. Parton distribution function (PDF) refers to the PDF4LHC [96] PDF set. Parton shower and hadronization are simulated with Pythia 8.244 [97] with the A14 set of tuned parameters [98] and the NNPDF2.3lo PDF set [99]. The Higgs boson mass is set to 125 GeV. The SM ggF HH cross-section is taken as $\sigma_{ggF} = 31.05$ fb, which is calculated at NNLO including finite top-quark mass effects [48], and the $4b$ branching ratio is $B(4b) = 0.3392$. Therefore the normalization for the SM process is set to the cross-section times the $4b$ branching ratio $\sigma_{ggF} \times B(4b) = 10.53$ fb.

Alternative ggF HH samples are generated with the same Powheg Box v2 generator but simulated

with HERWIG 7 (v.7.1.6p3) [100] with the H7.1-default set of tuned parameters [101] and MMHT2014LO PDF set [102]. The alternative samples are used only to derive the parton shower uncertainty, in order to assess a systematic bias on the parton showering and hadronization simulator by using the two different simulators.

In this analysis, only SM and $\kappa_\lambda = 10$ ggF HH samples are explicitly generated with the above configurations and in general, only the SM sample is used. A reweighting method with the SM sample is used to describe the distributions and yields with other modifier values of κ_λ. The details are discussed in Section A.1. The $\kappa_\lambda = 10$ sample is used just to validate the reweighting performance as described in Section 9.2.3.

VBF HH samples

HH signal samples via VBF process are generated using MADGRAPH (v.2.7.3p3.atlas6) [103] at leading order (LO) with NNPDF3.0NLO PDF set. The parton shower and hadronization are simulated using the same simulator as the ggF HH sample. The Higgs boson mass is set to 125 GeV. The SM VBF HH cross-section is taken as $\sigma_{VBF} = 1.726$ fb, which is calculated at N3LO QCD [104–107].

Alternative VBF HH samples are generated using MADGRAPH (v.2.7.3p3.atlas6) generator and HERWIG 7 (v.7.1.6p3) for the parton showering and hadronization. The alternative samples are used for the parton shower uncertainty as same as the alternative ggF HH samples.

In this analysis, VBF HH samples with coupling modifier values of $(\kappa_\lambda, \kappa_{2V}, \kappa_V) = (1, 1, 1), (1, 1.5, 1), (2, 1, 1), (10, 1, 1), (1, 1, 0.5), (-5, 1, 0.5), (0, 1, 1), (1, 0, 1)$ and $(1, 3, 1)$ are generated. Other coupling modifier samples are derived by a reweighting method using some of these samples as same as the ggF reweighting. The details are discussed in Section A.2. The $(\kappa_\lambda, \kappa_{2V}, \kappa_V) = (0, 1, 1), (1, 0, 1)$ and $(1, 3, 1)$ samples are used only to validate the reweighting performance, as described in Section 9.2.3.

HEFT HH samples

As described in Section A.3, this analysis uses the reweighting method to model HH signals with various HEFT coefficient values. HEFT HH samples are used only to validate the consistency of the reweighting method after the analysis selections. POWHEG BOX v2 generator is used to generate HEFT HH samples, and then PYTHIA 8.244 is used to simulate parton showering and hadronization with the same setup as the ggF HH samples. In this analysis, the samples with different HEFT coefficient values in Table 2.3 and 5.2 are generated and used in the reweighting validation.

SMEFT HH samples

Similarly to the HEFT HH samples, SMEFT HH samples are used only to validate the reweighting method described in Section A.3. SMEFT HH samples are generated and simulated by MADGRAPH (v.2.7.3p3.atlas6) with the SMEFT@NLO model [108] and PYTHIA 8.244. The reason why MADGRAPH is used for SMEFT not POWHEG BOX is that all SMEFT coefficient modifiers are not available in POWHEG BOX v2. Some of SMEFT coefficients in POWHEG BOX v2 have been recently available, but all couplings that are of interest in HH analyses such as c_{tG} are not available. Therefore, MADGRAPH that is the common generator for SMEFT variations in the ATLAS experiment is used. In this analysis, the

c_{HHH}	$c_{t\bar{t}H}$	c_{ggH}	c_{ggHH}	$c_{t\bar{t}HH}$	Usage in the reweighting validation
1.0	1.0	0	−0.5	0	HEFT c_{ggHH} 1D
1,0	1.0	0	0.5	0	HEFT c_{ggHH} 1D
1,0	1.0	0	1.0	0	HEFT c_{ggHH} 1D
1,0	1.0	0	0.0	−0.5	HEFT $c_{t\bar{t}HH}$ 1D
1,0	1.0	0	0.0	0.5	HEFT $c_{t\bar{t}HH}$ 1D
1,0	1.0	0	0.0	1.0	HEFT $c_{t\bar{t}HH}$ 1D

Table 5.2 HEFT coefficient values used to generate MC samples in this analysis.

samples with different SMEFT coefficient values in Table 5.3 are generated and used in the reweighting validation.

5.2.2 QCD multijet and $t\bar{t}$ Samples

The main backgrounds in this analysis are QCD multijet processes and $t\bar{t}$ processes. These MC samples are used only to validate the background estimation procedure described in Chapter 8 because this analysis uses a fully data-driven approach to estimate these background distributions. QCD multijet samples are generated and simulated by Pythia 8.244 at LO with the A14 set of tuned parameters and the NNPDF2.3LO PDF set. $t\bar{t}$ samples are generated by Powheg Box v2 at NLO with NNPDF3.0NLO and simulated by Pythia 8.230 with the A14 set of tuned parameters and the NNPDF2.3LO PDF set. a

5.3 HH Signal Reweighting

It is not easy to produce all signal samples with a wide range of κ_λ and κ_{2V} coupling values and varied HEFT and SMEFT coefficients, because MC production is computationally expensive and takes a lot of time. Therefore, this analysis employs a reweighting method to model the cross-section and kinematic distributions of HH signals across the wide parameter space. The reweighting method makes use of the fact that the cross-section and kinematic distributions of the HH production processes fundamentally depend on the relevant coupling values.

The ggF HH production cross-section and kinematics depend on κ_λ and k_t, as can be seen in Figure 2.9(b). The differential ggF HH cross-section on m_{HH} can be expressed as a function of κ_λ and k_t:

$$\frac{d\sigma_{ggF}(\kappa_\lambda, k_t)}{dm_{HH}} = |A(\kappa_\lambda, k_t)|^2 = \left|\kappa_\lambda k_t M_\triangle(m_{HH}) + k_t^2 M_\square(m_{HH})\right|^2 \tag{5.1}$$

$$= \kappa_\lambda^2 k_t^2 |M_\triangle(m_{HH})|^2 + \kappa_\lambda k_t^3 \left[M_\triangle^*(m_{HH}) M_\square(m_{HH}) + M_\square^*(m_{HH}) M_\triangle(m_{HH})\right] + k_t^4 |M_\square(m_{HH})|^2 \tag{5.2}$$

$$= \kappa_\lambda^2 k_t^2 a_1(m_{HH}) + \kappa_\lambda k_t^3 a_2(m_{HH}) + k_t^4 a_3(m_{HH}), \tag{5.3}$$

where $M_\triangle(m_{HH})$ indicates a contribution of the triangle diagram shown in Figure 2.9(a) and $M_\square(m_{HH})$

c_H	c_{tG}	$c_{H\Box}$	c_{tH}	c_{HG}	Usage in the reweighting validation
−19.20	0	0	0	0	SMEFT c_H 1D
14.93	0	0	0	0	SMEFT c_H 1D
0	−0.9	0	0	0	SMEFT c_{tG} 1D
0	0.9	0	0	0	SMEFT c_{tG} 1D
0	0	−8.0	0	0	SMEFT $c_{H\Box}$ 1D
0	0	14.0	0	0	SMEFT $c_{H\Box}$ 1D
0	0	0	−11.0	0	SMEFT c_{tH} 1D
0	0	0	5.0	0	SMEFT c_{tH} 1D
0	0	0	0	−0.5	SMEFT c_{HG} 1D
0	0	0	0	0.5	SMEFT c_{HG} 1D
−2.5	0.15	0	0	0	SMEFT c_H −c_{tG} 2D
2.5	0.15	0	0	0	SMEFT c_H −c_{tG} 2D
−1.0	0	−1.0	0	0	SMEFT c_H −$c_{H\Box}$ 2D
1.0	0	−1.0	0	0	SMEFT c_H −$c_{H\Box}$ 2D
−2.0	0	0	−1.5	0	SMEFT c_H −c_{tH} 2D
2.0	0	0	−1.5	0	SMEFT c_H −c_{tH} 2D
1.0	0	0	0	−1.0	SMEFT c_H −c_{HG} 2D
1.0	0	0	0	1.0	SMEFT c_H −c_{HG} 2D

Table 5.3 SMEFT coefficient values used to generate MC samples in this analysis.

is of the box diagram shown in Figure 2.9(b) as a function of m_{HH}. In this analysis, the k_t coupling is set to the SM value of 1 and Eq. A.3 is thus simplified to an equation depending on only the κ_λ coupling value. The differential ggF HH cross-section on m_{HH} as a function of κ_λ can be then given by:

$$\frac{d\sigma_{ggF}(\kappa_\lambda)}{dm_{HH}} = \kappa_\lambda^2 a_1(m_{HH}) + \kappa_\lambda a_2(m_{HH}) + a_3(m_{HH}) \tag{5.4}$$

where a_1, a_2 and a_3 have a dependence on m_{HH}. The reweighting function used in this analysis is based on Eq. A.4. a_1, a_2 and a_3 in Eq. A.4 can not be trivially derived for a given κ_λ, but they can be mathematically determined by solving a set of linear equations using three different κ_λ samples in each m_{HH} bin. Therefore, the values of a_i are solved using three ggF HH samples with $\kappa_\lambda = 0, 1$ and 20, where no decays and cuts are applied to be common to all HH analyses [109]. Weights for every κ_λ value are then derived in each m_{HH} bin of 10 GeV by taking the ratio between the target κ_λ coupling and

the SM. To model kinematic distributions of the target κ_λ coupling, these weights are applied to the SM ggF HH samples based on their truth m_{HH} values. Truth m_{HH} is selected here based on the assumption that signal kinematics vary coherently with m_{HH} and signal acceptance times efficiency on the analysis selections only depends on m_{HH}. The reweighting procedure is only used to model the signal shapes. Therefore, these reweighted samples are normalized by their cross-section predictions [48].

Figure 5.1 shows truth level m_{HH} distributions comparing the reweighted and generated samples for $\kappa_\lambda = 2$ and 10 without any decays and analysis selections. As can be seen, the reweighting procedure works well. I also validated the reweighting procedure after the analysis selections described in Chapter 6. The details are described in Chapter 9.

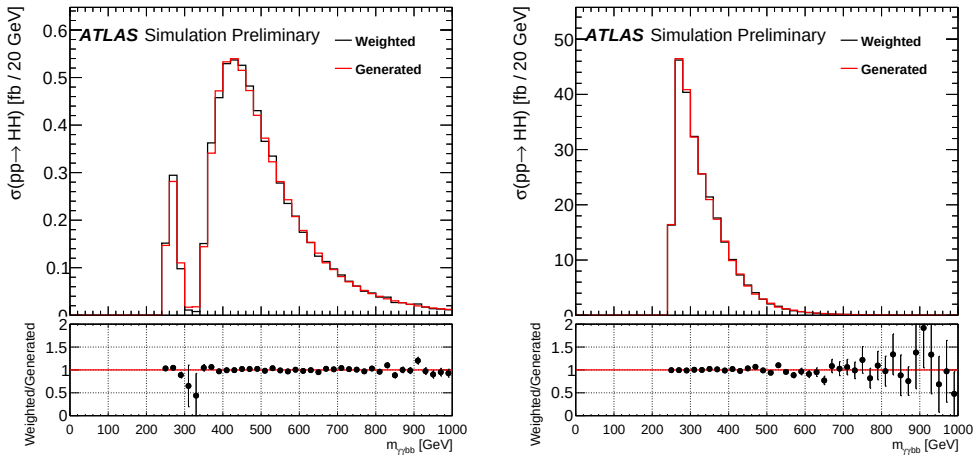

(a) $\kappa_\lambda = 2$ (b) $\kappa_\lambda = 10$

Figure 5.1 Truth m_{HH} distribution of generated (red) and reweighted (black) ggF HH samples with (a) $\kappa_\lambda = 2$ and (b) $\kappa_\lambda = 10$ to validate the ggF reweighting procedure [109]. The under panel shows the ratio of the reweighted distribution to the generated distribution. $m_{\gamma\gamma bb}$ in the x-label is exactly the same as m_{HH}.

Similarly to the ggF reweighting, the VBF HH samples with a wide range of κ_λ and κ_{2V}, the HEFT HH samples and the SMEFT HH samples with varied these coefficients are also modelled by the same reweighting procedure. The details can be found in Appendix A.

Chapter 6

Analysis Selection

The goal of this chapter is to define *signal regions*, where the signal hypotheses and the compatibility between data and backgrounds are tested. A significance is given by $\sigma = \sqrt{(S+B)\ln(1+\mathrm{S/B}) - \mathrm{S}} \simeq S/\sqrt{B}$, where S and B are the expected yields of signal and background. This means that it's important to discriminate signal and background effectively by analysis selections in order to obtain better significance. In this analysis, two main selections for the ggF process and the VBF process are provided (Figure 6.1). The ggF selection is optimized to set a limit on the HH cross-section and to give a constraint on κ_λ. The VBF selection is optimized to give a constraint on κ_{2V}. The steps of the event selections are the following:

Step (1) Events must pass a combination of multi b-jet triggers and trigger bucket selection.

Step (2) Events must have at least 4 *central* jets.

Step (3) Events must pass a b-tagging criterion within all *central* jets. Three different b-tagging criteria are used in this analysis and described in Section 6.4.1.

Step (4) This step aims to categorize events into two orthogonal selections called the ggF selection and the VBF selection. Three cuts detailed in Section 6.4.2 are used. If events pass all three cuts, they go to the VBF selection. If events fail any of the three cuts, they go to the ggF selection.

Step (5) Two *Higgs candidates* are reconstructed using the four *Higgs candidate jets*.

Step (6 Events must pass QCD background veto cut for only ggF selection.

Step (7) Events must pass $t\bar{t}$ background veto cut.

Step (8) Three kinematic regions, *signal region*, *control region 1* and *control region 2* are defined in the m_{H1} and m_{H2} planes, and events must be located in the *signal region*.

The details are described in the following sections.

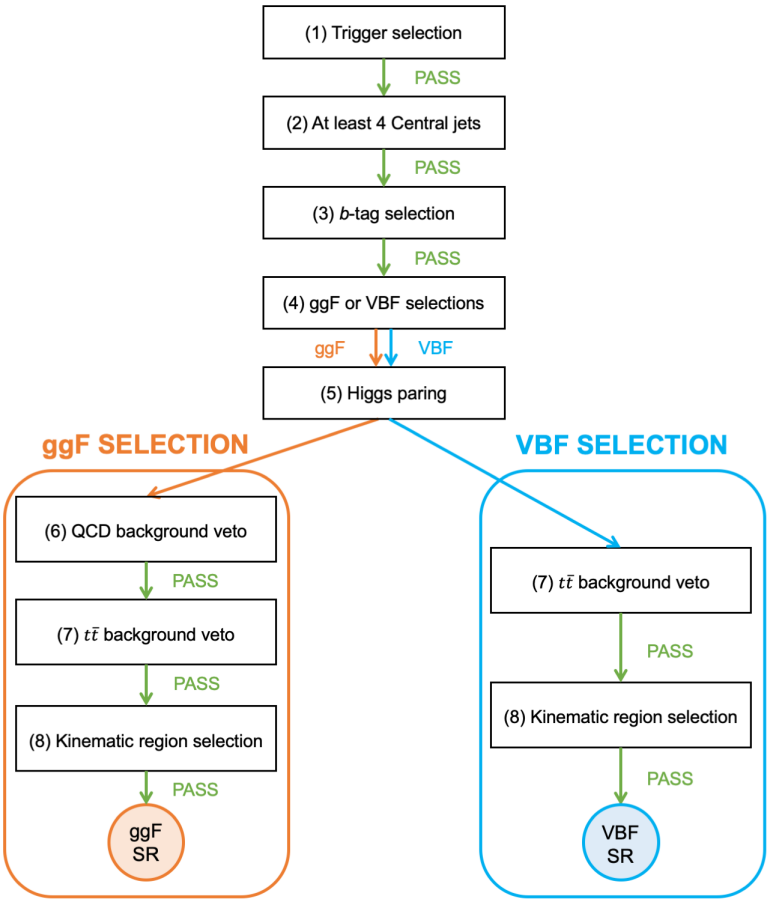

Figure 6.1 Analysis selection flowchart.

6.1 Pre-selection

The dataset and MC samples described in Chapter 5 are skimmed to reduce a file size so that they are more manageable by this analysis. Table 6.1 shows the pre-selection used in this analysis. Events must contain at least objects defined in Table 6.1. No impact of this stage is for events passing the analysis selection.

6.2 Trigger Selection

This analysis uses a combination of multi b-jet triggers. The multi b-jet triggers are listed in Table 5.1. The number of b-jets and jets required by the trigger is referred to as *Type*, either 2b1j or 2b2j. This abbreviated name is used henceforth for ease of writing and reading. In each trigger, events passing through the selection shown in *Requirement* in Table 5.1 are selected. For example for the 2b1j trigger in 2016, events must have at least two b-jet identified on 60% eff. WP with $E_{\mathrm{T}} > 55$ GeV and one extra jet with $E_{\mathrm{T}} > 100$ GeV.

Figure 6.2 and 6.3 show the individual trigger efficiencies of the 2b1j and 2b2j triggers for the SM ggF

0 lepton	
Lepton	No lepton: no tight electron and good muon with $p_{\mathrm{T}} > 25$ GeV
Jet	Two loosely b-tagged jets (77% eff. WP) with $p_{\mathrm{T}} > 25$ GeV, and two extra jets with $p_{\mathrm{T}} > 25$ GeV

1 lepton	
Lepton	One lepton: one tight electron or good muon with $p_{\mathrm{T}} > 25$ GeV
Jet	Two loosely b-tagged jets (77% eff. WP) with $p_{\mathrm{T}} > 25$ GeV

Table 6.1 Summary of pre-selection used in this analysis.

HH signal after the pre-selection described in Section 6.1 as a function of m_{HH} which is reconstructed from the four-momentum of generated Higgs bosons at truth level (truth m_{HH}). The 2b1j trigger has high signal acceptance in the high m_{HH} spectrum since the jet E_{T} requirement is tight but the requirement for the number of jets is loose. The 2b2j trigger can enhance signal acceptances in the low m_{HH} spectrum. The lower signal acceptance in the 2b2j trigger in 2017 is due to the tighter b-tagging requirement.

Figure 6.4 show the combined trigger efficiencies for the SM ggF HH signal as a function of truth m_{HH}. The combination of 2b1j and 2b2j triggers can improve signal acceptance across all m_{HH} spectrums.

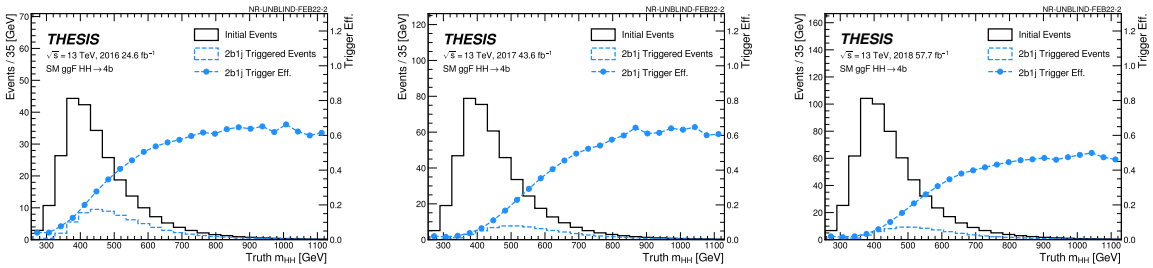

(a) 2016 (b) 2017 (c) 2018

Figure 6.2 Trigger efficiencies of 2b1j trigger for each year for SM ggF HH signal as a function of truth m_{HH}. The black histogram shows the truth m_{HH} distribution of the initial events, and the dashed blue histogram shows one of the triggered events. The blue line graph shows the trigger efficiency corresponding to the ratio of the initial events and the triggered events.

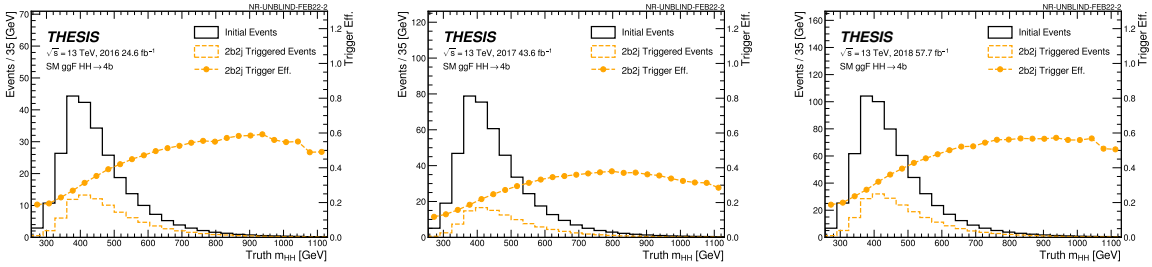

(a) 2016 (b) 2017 (c) 2018

Figure 6.3 Trigger efficiencies of 2b2j trigger for all years for SM *gg*F *HH* signal as a function of truth m_{HH}. The black histogram shows the truth m_{HH} distribution of the initial events, and the dashed orange histogram shows one of the triggered events. The orange line graph shows the trigger efficiency corresponding to the ratio of the initial events and the triggered events.

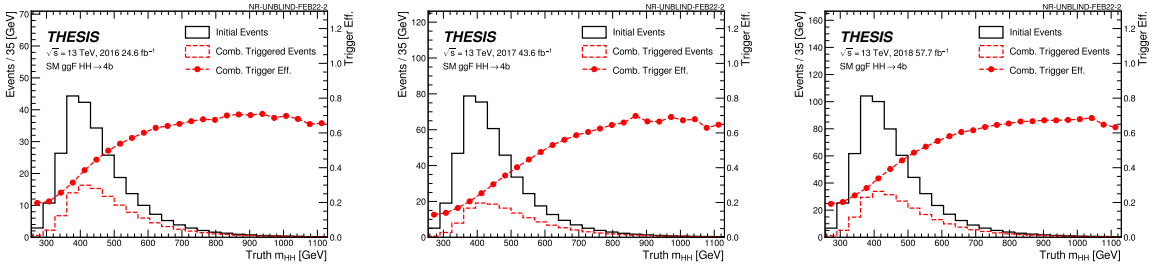

(a) 2016 (b) 2017 (c) 2018

Figure 6.4 Trigger efficiencies of 2b1j and 2b2j triggers for all years for SM *gg*F *HH* signal as a function of truth m_{HH}. The black histogram shows the truth m_{HH} distribution of the initial events, and the dashed red histogram shows one of the triggered events. The red line graph shows the trigger efficiency corresponding to the ratio of the initial events and the triggered events.

6.3 Trigger Bucket Selection

The trigger bucket strategy is used to apply the trigger scale factors that is used to correct a difference on the trigger efficiency between MC simulation and data to MC samples in this analysis. Since this analysis uses a combination of multi *b*-jet triggers, the calculation of the trigger scale factor is complicated. The trigger bucket strategy simplifies it as only one multi *b*-jet trigger is considered in each *Bucket*.

Figure 6.5 shows a flowchart of the trigger bucket selection. It splits up events into two different categories, *Bucket 1* and *Bucket 2*, by applying cuts using fully reconstructed variables. The bucket selection is motivated by the characteristics of the trigger that the jet E_{T} requirement of 2b1j trigger is tighter than one of 2b2j trigger. The bucket selection is that the leading jet p_{T} must be greater than 170 GeV and the third leading jet p_{T} must be greater than 70 GeV. The latter cut is used to reduce the amount of events passed and discarded in *Bucket 1*. Those cuts are optimized so that the number of discarded SM *gg*F *HH* signals is minimized. Then, only a multi *b*-jet trigger is used to determine if the

event is kept or discarded in each category, where it is also required to match all online jets fired by the multi b-jet trigger to corresponding offline jets. *Bucket 1* is corresponding to 2b1j trigger, and *Bucket 2* is corresponding to 2b2j trigger. Finally, events kept in either *Bucket 1* or *Bucket 2* are passed to the next selection.

Figure 6.6 shows the trigger bucket composition of m_{HH} distribution for the SM ggF HH signal after the trigger selection described in Section 6.2. The two *Buckets* enhance our sensitivity to different parts of the m_{HH} spectrum. *Bucket 1* targets events in the high m_{HH} spectrum. On the other hand, *Bucket 2* can enhance our sensitivity to the low m_{HH} spectrum. The total acceptance of the SM HH signal is 85-90%. The loss of events affects background as well as signal. The change in our sensitivity is negligible.

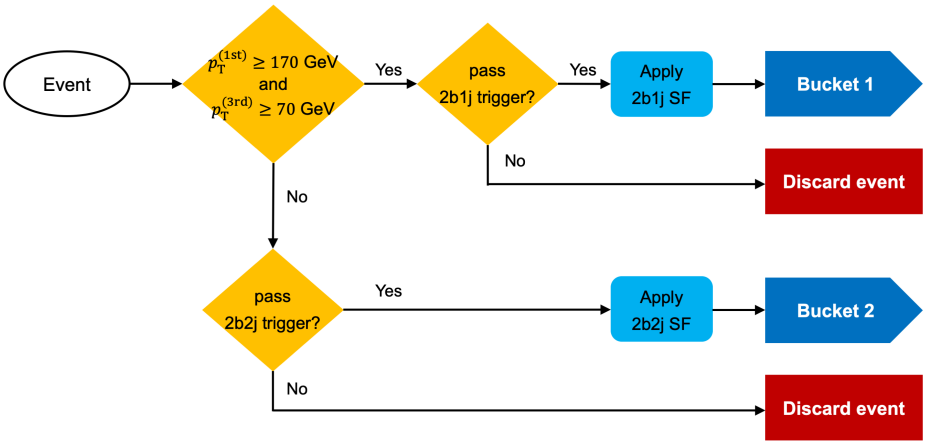

Figure 6.5 A flowchart of the trigger bucket selection.

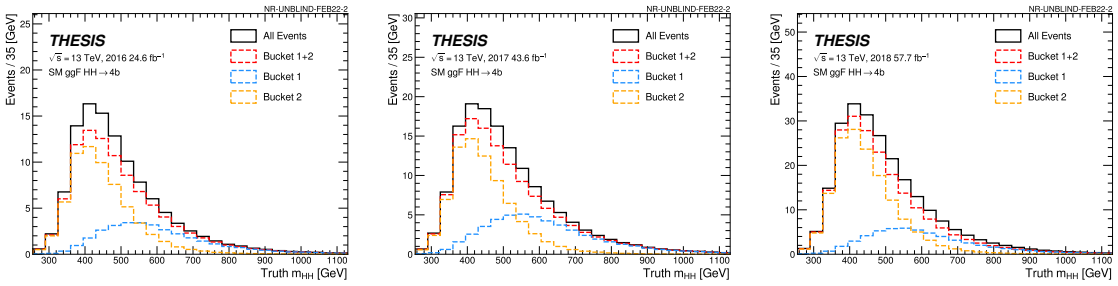

Figure 6.6 The bucket composition of m_{HH} distribution for the SM ggF HH signal. Events that pass the trigger selection are indicated in black histogram. Events that pass *Bucket 1*, corresponding to the 2b1j trigger, are indicated in blue histogram. Events that pass *Bucket 2*, corresponding to the 2b2j trigger, are indicated in orange histogram. Events that pass either *Bucket 1* or *Bucket 2* are indicated in red histogram.

6.4 Event Selections

6.4.1 *b*-tag Selection

Events are categorized based on the number of *b*-tagged *central* jets. The summary can be found in Table 6.2. The main *b*-tag criteria for the *signal region* requires at least four *b*-tagged jets with 77% WP (4b events) to increase our sensitivity. Events with exactly two *b*-tagged jets are classified as 2b events and used for the background estimation described in Section 8.1. Events with exactly three *b*-tagged jets and one failed loosely *b*-tagged jet with 85% WP are classified as 3b1f events and used for one of the background validation described in Chapter 8.

Notation	Definition	Usage
2b	Exactly two central jets *b*-tagged with 77% WP	Background Estimation
3b1f	Exactly three central jets *b*-tagged with 77% WP and one central jet failed 85% WP	Background Validation
4b	At least four central jets *b*-tagged with 77% WP	Signal Region

Table 6.2 Different *b*-tagging criteria based on the number of *b*-tagged *central* jets.

6.4.2 *gg*F and VBF Channel Definition

In this analysis, two main channels targeting different HH production processes are provided. One is optimized for the *gg*F process and the other one is for the VBF process. They are designed to be orthogonal in order to statistically combine them when deriving results. To belong events to either the *gg*F channel or the VBF channel, the selection consists of three steps in the Step (4) shown in Figure 6.1. The cuts are based on whether it contains any characteristic of VBF *jets* that they are well-separated and have high energy. The three steps are the following:

Step (4.1) Events have at least six *central* or *forward* jets, which are defined in Section 4.2.4.

Step (4.2) Events have VBF *jets* with $m_{jj} > 1$ TeV and $|\Delta\eta_{jj}| > 3.0$.

Step (4.3) Events meet that the p_{T} of the vector sum of 4-momenta of VBF *jets* and jets forming the *Higgs candidates* (described in Section 6.4.3) be less than 65 GeV.

First, events must have at least six jets to belong to the VBF channel, since the $HH \to b\bar{b}b\bar{b}$ events with the VBF process have four jets decaying from the two Higgs and two associated jets (Figure 2.12). VBF *jets* are selected as the two jets with the maximal di-jet invariant mass (m_{jj}) from a pool of *central* jets and *forward* jets, where only non-*b*-tagged jets with 77% are considered. If there is no such pair of jets, the event is passed in the *gg*F channel.

Three cuts are then applied to reduce the number of the *gg*F signal and background passed in the VBF channel. The first two cuts require the VBF *jets* to have the invariant mass of $m_{jj} > 1$ TeV and the

rapidity gap of $|\Delta\eta_{jj}| > 3.0$. Finally, the six four-vectors of the VBF *jets* and *Higgs candidates* jets are summed, and a cut of the p_{T} of the vector sum of 65 GeV is applied. If an event passes all three cuts, it is passed in the VBF selection. On the other hand, if it fails any of the three cuts, it is passed in the *gg*F selection.

As also shown in Table 6.3, the yield of the SM *gg*F *HH* production in the VBF signal region is only 1.5% with respect to that in either signal region. On the other hand, SM VBF *HH* events are well-separated into the VBF channel and the yield in the VBF signal region is about 60% with respect to that in either signal region.

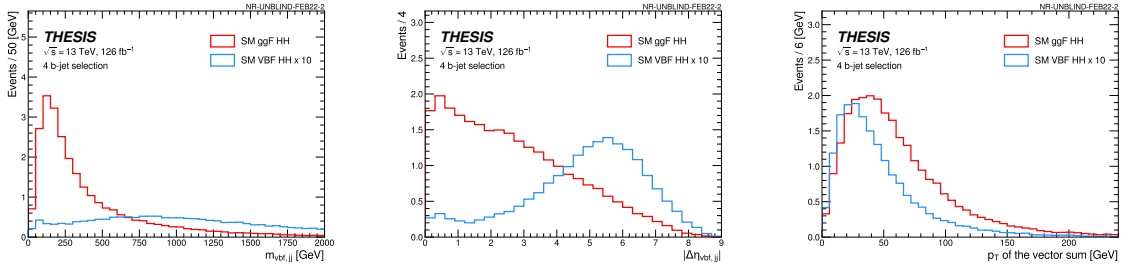

(a) m_{jj} (b) $|\Delta\eta_{jj}|$ (c) p_{T} of the combined four-vector

Figure 6.7 Kinematic distributions used in the *gg*F and VBF channel definition for SM *gg*F *HH* signal (red) and SM VBF *HH* signal (blue), where events pass through Section 6.1-6.4.1 and are required to have at least six *central* or *forward* jets.

6.4.3 Higgs Candidate Pairing

The $HH \rightarrow b\bar{b}b\bar{b}$ system is reconstructed from two *Higgs candidates*, which are themselves reconstructed from two *b*-jets. In total, four *Higgs candidates jets* are needed. *Higgs candidates jets* are selected from the pool of *central* jets. *b*-jets are selected first as *Higgs candidates jets*. If the event is classified as a 4b event, the leading four *b*-jets in p_{T} are selected. If the event is classified as a 2b or 3b1f event, the other two or one *Higgs candidates jets* are filled by the leading non-*b*-tagged jets in p_{T}.

Figure 6.8 shows the accuracy of the *Higgs candidates jets* selection as a function of κ_λ and κ_{2V}. The Higgs jet selection accuracy is defined as the probability that all *Higgs candidates jets* in the event are matched to the truth *b*-quarks decayed from Higgs bosons within $\Delta R < 0.3$ between *Higgs candidates jet* and truth *b*-quark. The Higgs jet selection accuracy is 75% for the *gg*F signal in the *gg*F selection with a few % variations across the κ_λ values. The accuracy loss is mostly caused by events where one of the four *b*-quarks is out of the *b*-jet acceptance. The average of Higgs jet selection accuracy for the VBF signal in the VBF selection is 85% and 90% across the κ_λ and κ_{2V} values. The dependence on κ_λ and κ_{2V} is due to the positive dependence of *b*-tagging efficiency on *b*-jet p_{T}. Harder signals are likely to have higher *b*-tagging efficiency therefore higher accuracy of the *Higgs candidates jets* selection.

From the four *Higgs candidates jets*, in total three possible pairings can be defined as illustrated in Figure 6.9. In this analysis, the best pairing from the three possible ones is defined by the opening angle ($\Delta R_{leading}$) between the jets in the leading *Higgs candidate*. It is based on the principle that the decay products of the Higgs bosons are usually collimated due to the Higgs's initial momentum. Of

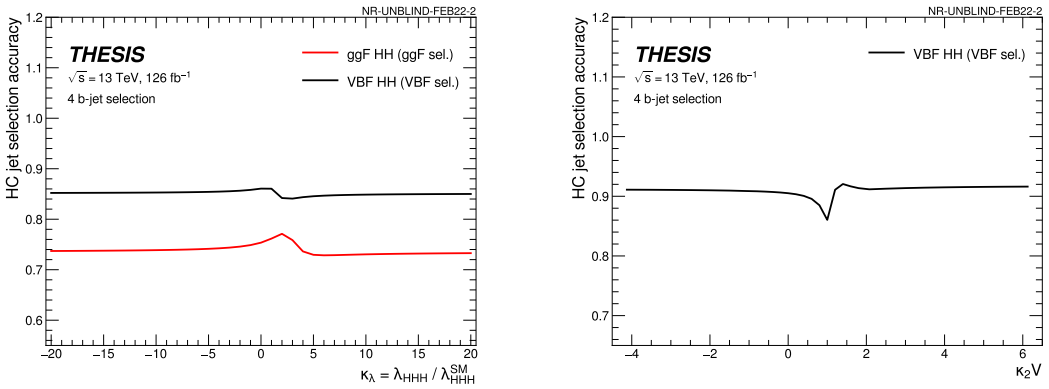

(a) κ_λ (b) κ_{2V}

Figure 6.8 Accuracy of the *Higgs candidates jets* selection for ggF HH signal in the ggF selection (red) and VBF HH signal in the VBF selection (black) as a function of (a) κ_λ and (b) κ_{2V}.

the two *Higgs candidates*, the *leading* Higgs candidate is defined as the one with the highest p_{T} and the *sub-leading* Higgs candidate is defined as the other one, for every three possible pairings. Then, the opening angle ($\Delta R_{leading}$) between the jets in the leading *Higgs candidate* is calculated. The pairing with the smallest $\Delta R_{leading}$ is selected as the best pairing candidate.

Figure 6.10 shows the pairing accuracy using the smallest $\Delta R_{leading}$ selection for ggF and VBF signals as a function of κ_λ and κ_{2V}. Figure 6.11 shows the same information for SM ggF and VBF signals as a function of m_{HH}. The pairing accuracy is defined as the fraction of correctly paired events to the events where the four *Higgs candidates jets* are correctly selected in the jet selection. The pairing accuracy is 88% for the SM ggF signal in the ggF selection and 77% for the SM VBF signal in the VBF selection. Signals with higher p_{T} Higgs boson tend to have more collimated decay products, so that the pairing accuracies on SM-like κ_λ signals, non-SM κ_{2V} signals and higher m_{HH} signals are higher. On the other hand, the pairing accuracies on non-SM κ_λ, SM-like κ_{2V} and lower m_{HH} signals are dropped due to their soft kinematics. Their accuracy losses can be acceptable because most backgrounds are distributed at low m_{HH} and they don't affect on the sensitivity.

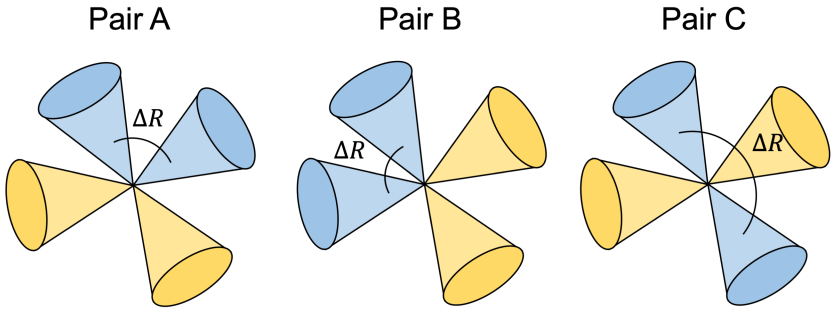

Figure 6.9 Three possible HH pairing from the four *Higgs candidates jets*. Blue cones indicate jets of the leading *Higgs candidate* and yellow cones indicate jets of the sub-leading *Higgs candidate*. The opening angle ΔR between the jets in the leading *Higgs candidate* are also shown.

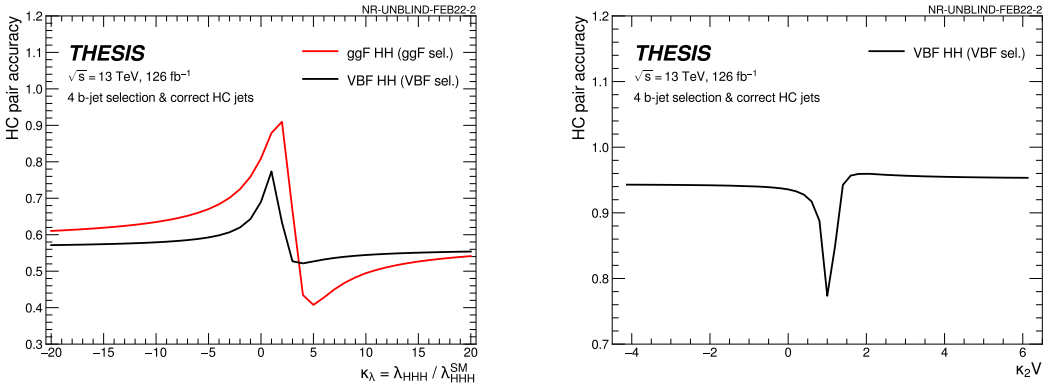

(a) κ_λ (b) κ_{2V}

Figure 6.10 Accuracy of Higgs candidate pairing for ggF HH signal in the ggF selection (red) and VBF HH signal in the VBF selection (black) as a function of (a) κ_λ and (b) κ_{2V}. The pairing with the smallest $\Delta R_{leading}$ is selected.

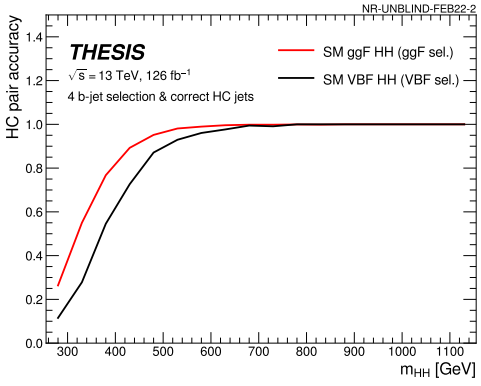

Figure 6.11 Accuracy of Higgs candidate pairing for SM ggF signal (red) and SM VBF signal (black) as a function of m_{HH}. The pairing with the smallest $\Delta R_{leading}$ is selected.

6.4.4 QCD and $t\bar{t}$ Background Reduction

After the ggF and VBF selection described in Section 6.4.2, QCD multijet and $t\bar{t}$ backgrounds are dominated in the both ggF and VBF channels. To suppress QCD backgrounds, a pseudorapidity separation between the two *Higgs candidates* described in Eq. 6.1 is required in the ggF channel.

$$|\Delta\eta_{HH}| < 1.5 \tag{6.1}$$

Figure 6.12 shows $|\Delta\eta_{HH}|$ distributions of SM ggF, SM VBF HH signals and blinded 4b data, where the signal region's events described in Section 6.5 are excluded, in the ggF and VBF channels. This cut is not used for the VBF selection due to it having the high sensitivity to the SM VBF HH signal in $|\Delta\eta_{HH}| >$ 1.5 region. The $|\Delta\eta_{HH}|$ cut reduces approximately 40% of QCD multijet background with keeping 85% of SM ggF HH signal.

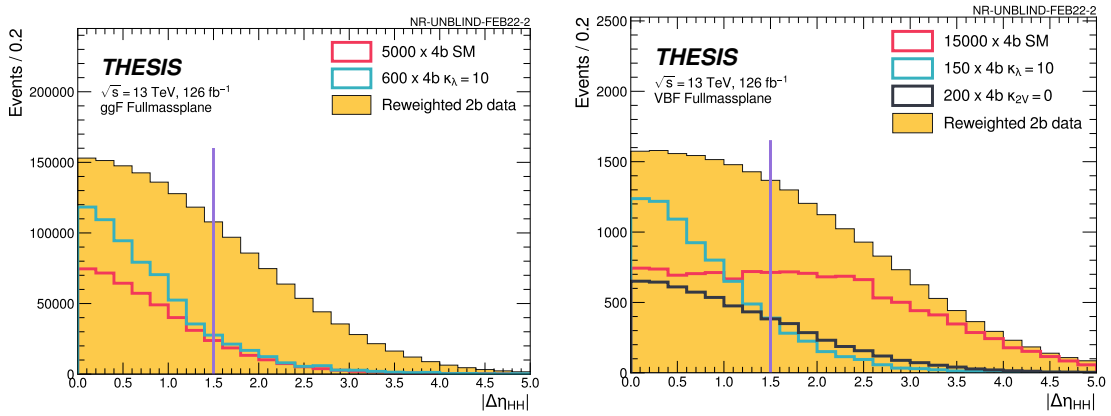

(a) ggF channel (b) VBF channel

Figure 6.12 $|\Delta\eta_{HH}|$ distributions of SM ggF, SM VBF HH signals and QCD background in (a) the ggF channel and (b) VBF channel. Events on the right of $|\Delta\eta_{HH}| = 1.5$ are discarded in the ggF channel.

Additionally, a top veto cut is applied to suppress backgrounds from top-quark hadronic decays, such as $t\bar{t}$ background. A discriminant, X_{wt}, that is constructed to measure compatibility that an event contains a hadronically decaying top-quark ($t \to bW \to bq\bar{q}$), is defined as:

$$X_{wt} = \min\left[\sqrt{\left(\frac{m_W - 80.4\text{GeV}}{0.1\, m_W}\right)^2 + \left(\frac{m_t - 172.5\text{GeV}}{0.1\, m_t}\right)^2}\right], \tag{6.2}$$

where m_W and m_t indicate the invariant mass of W boson and top-quark candidate formed from jet combinations in each event. W boson candidate is formed from any pair of *central jets* including those that were not selected for *Higgs candidate jets* and VBF *jets*. top-quark candidate is formed from the W boson candidate and any remaining b-jet that were selected for *Higgs candidate jets*. All possible candidates are considered, and the minimum X_{wt} is obtained in each event. Figure 6.13 shows X_{wt} distributions of SM ggF, SM VBF HH signals and $t\bar{t}$ background in the ggF and VBF channels. Events are discarded

if the minimum X_{wt} is less than 1.5 in both channels. The top veto cut reduces approximately 55% of $t\bar{t}$ background with keeping 85% of SM ggF HH signal in the ggF channel, and reduces 45% of $t\bar{t}$ background with keeping 90% of SM VBF HH signal in the VBF channel.

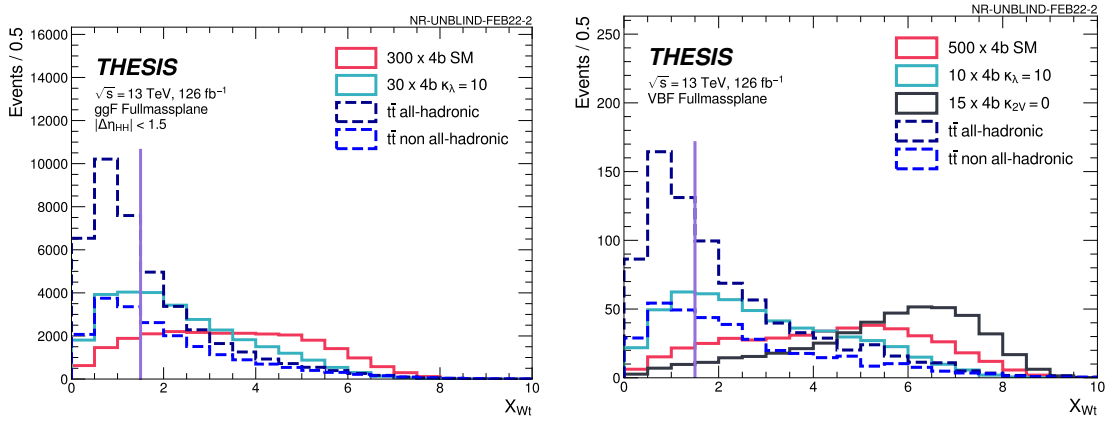

(a) ggF channel (b) VBF channel

Figure 6.13 Xwt distributions of SM ggF, SM VBF HH signals and $t\bar{t}$ background in (a) the ggF channel and (b) VBF channel. Events on the left of $X_{wt} = 1.5$ are discarded in both channels. $|\Delta\eta_{HH}| < 1.5$ is applied only to the ggF channel,

6.5 Kinematic Region Selection

The final cut using X_{HH} as given Eq. 6.3 is applied to events passing the event selections described in Section 6.4 to define a *signal region* (SR). The functional form is similar to an ellipse equation, but the radius is formed to be a function of the invariant masses of Higgs candidates, m_{H1} and m_{H2}, to make the cut harsher for the higher mass spaces where the jet resolution is better.

$$X_{HH} = \sqrt{\left(\frac{m_{H1} - 124\ \text{GeV}}{0.1\ m_{H1}}\right)^2 + \left(\frac{m_{H2} - 117\ \text{GeV}}{0.1\ m_{H2}}\right)^2}. \tag{6.3}$$

The m_{H1} and m_{H2} centers (124, 117) in Eq. 6.3 are chosen to approximately match the centers of the m_{H1} and m_{H2} distributions for correctly paired signal events (Figure 6.14). The SR is defined in Eq. 6.4. The cut value of 1.6 is defined so that maximizes our sensitivity to the measurement of the SM HH cross-section. The visualization of the SR can be found in the red line in Figure 6.15. As Figure 6.15(a) shows, SM ggF HH events are nicely peaking into the SR.

$$\text{SR} \quad : \quad X_{HH} < 1.6 \tag{6.4}$$

$$\text{CR Inner Edge} \quad : \quad X_{HH} = 1.6 \tag{6.5}$$

$$\text{CR Outer Edge} \quad : \quad \sqrt{(m_{H1} - 1.05 \times 124\ \text{GeV})^2 + (m_{H2} - 1.05 \times 117\ \text{GeV})^2} = 45\ \text{GeV} \tag{6.6}$$

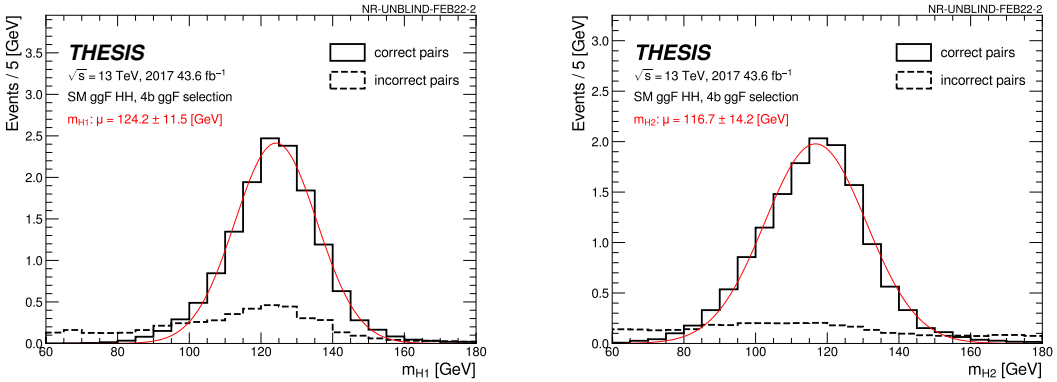

(a) m_{H1} (b) m_{H2}

Figure 6.14 m_{H1} and m_{H2} distributions for correctly paired events (solid black) and incorrectly paired events (dashed black) after the event selections described in Section 6.4 for SM ggF HH signal. The red line shows the gaussian function fitted in the correctly paired distribution.

Additionally, I defined two *control regions* (CR), CR1 and CR2, for the background estimation described in Section 8. The key task in this analysis is to accurately estimate QCD background in the SR. To achieve it, I utilized a fully data-driven method, which uses events in kinematically similar CRs to the SR. The CRs are defined to locate into the band as given by Eq. 6.5 and Eq. 6.6. The band is split into four quadrants. CR1 and CR2 are each defined as a pair of quadrants such that the quadrants are on opposite sides of the band. The angle between the x-axis and the closest CR1 and CR2 boundary above the x-axis is 45°. The $t\bar{t}$ veto cut described in Section 6.4.4 drops in the number of events with m_{H1} or m_{H2} equal to about 80 GeV. The impacts can be observed in Figures 6.15(b) and Figure 6.15(c) as the two straight bands centred about 80 GeV on the x-axis and y-axis. The angle of 45°is chosen to make the impacts of the $t\bar{t}$ background reduction approximately equal in both CR1 and CR2. I tested the background estimation on several difference angles, 0°, 30°and 45°. Then, 45°was found to give better agreements on the 3b1f validation described in Section 8.2.2. The CR1 and CR2 are visualized as the dashed black lines and the dashed light-blue lines in Figure 6.15.

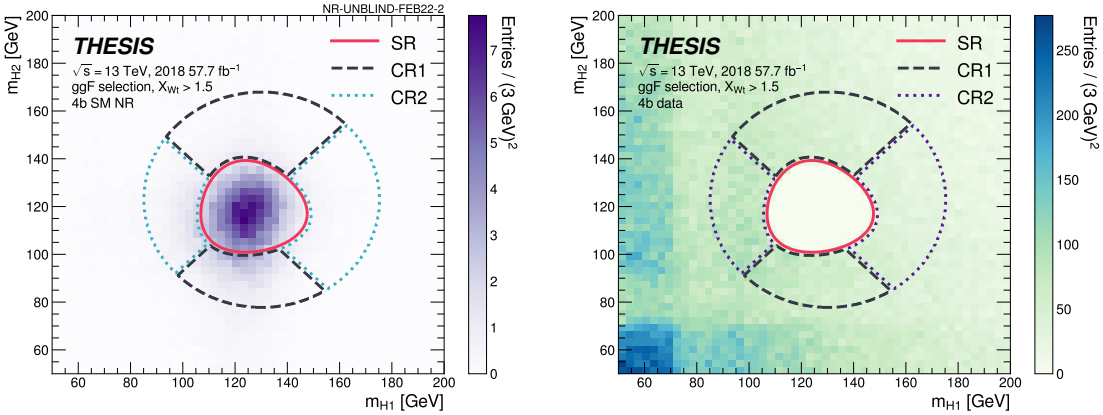

(a) 2018: 4b SM ggF HH Signal

(b) 2018: 4b Data

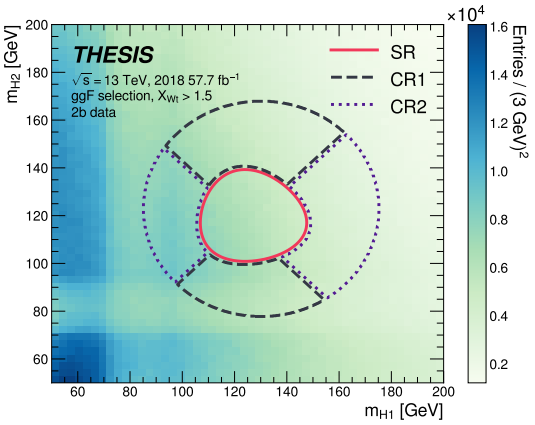

(c) 2018: 2b Data

Figure 6.15 Kinematic region definitions superimposed on (a) 4b SM ggF HH signal, (b) 4b data and (c) 2b data. The red line indicates the Signal Region (SR), the dashed black lines indicate the Control Region 1 (CR1) and the dotted turquoise or purple lines indicate the Control Region 2 (CR2). 4b data in the SR is blinded. Two straight bands around 80 GeV in the x-axis and y-axis are due to the $t\bar{t}$ veto cut.

6.6 Signal Acceptances and Cutflows

The signal acceptance times efficiency at each step in the analysis selection with respect to events after the preselection as a function of κ_λ and κ_{2V} is shown in Figure 6.16. The yields (*cutflow*) of data, SM and κ_λ =+10 ggF signals, SM and κ_{2V} =0 VBF signals are shown in Table 6.3. The signal loss is mainly caused by the trigger selection, because the decay products of non-resonant HH signals tend to have lower p_{T} and it's difficult to pass the trigger p_{T} selections. In the 4 b-tagging selection, we used the b-tagging algorithm with the efficiency of 77%, so that the signal acceptance in this step is less than 35% depending on jet p_{T}. The acceptance times efficiency on SM-like κ_λ ggF signals and non-SM κ_{2V} ggF signals is higher, because they are the hardest productions in non-resonant HH production. On the other hand, the acceptance times efficiency on no-SM κ_λ ggF signals and SM-like κ_{2V} ggF signals is lower due to their soft kinematics.

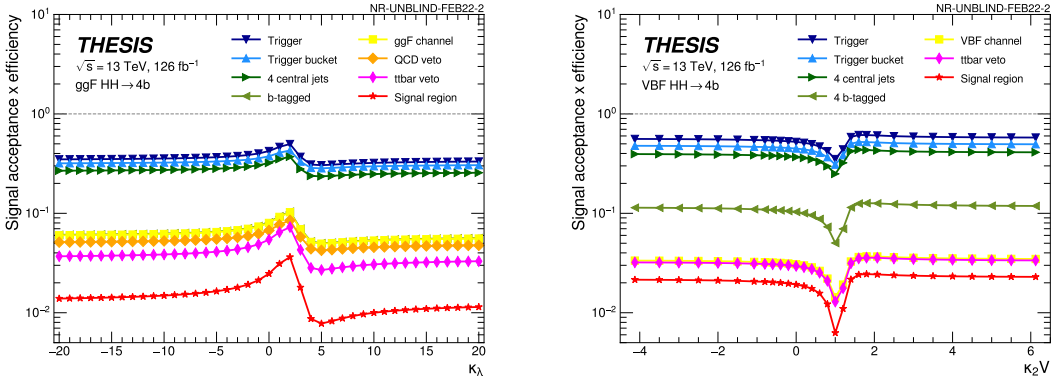

(a) ggF HH signal: κ_λ variation

(b) VBF HH signal: κ_{2V} variation

Figure 6.16 Signal acceptance times efficiency with respect to events after the preselection as a function of κ_λ and κ_{2V}. (a) ggF HH signal in the ggF selection and (b) VBF HH signal in the VBF selection are shown.

	Data	**ggF Signal**		**VBF Signal**		
		SM	$\kappa_\lambda = 10$	SM	$\kappa_{2V} = 0$	$\kappa_\lambda = 10$
Common selection						
Preselection	5.70×10^8	934.4	18095.9	52.2	901.7	3120.3
Trigger selection	2.81×10^8	435.3	5819.1	18.4	471.5	1285.5
Trigger bucket	2.49×10^8	380.4	5374.7	16.1	404.1	1126.2
4 central jets	1.84×10^8	327.5	4494.6	13.0	331.9	930.2
At least 4 b-tagged central jets	1.91×10^6	87.1	972.9	2.63	93.2	185.2
ggF selection						
Pass ggF selection	1.89×10^6	86.0	962.4	1.88	65.4	139.1
$\lvert\Delta\eta_{HH}\rvert < 1.5$	1.03×10^6	71.6	824.4	0.95	46.5	114.4
$X_{wt} > 1.5$	7.51×10^5	60.4	554.3	0.74	43.2	78.8
$X_{HH} < 1.6$ (ggF signal region)	1.62×10^4	29.1	181.0	0.24	23.0	25.5
VBF selection						
Pass VBF selection	2.71×10^4	1.14	10.53	0.75	27.7	46.1
$X_{wt} > 1.5$	2.18×10^4	1.01	7.57	0.68	26.6	33.9
$X_{HH} < 1.6$	5.02×10^2	0.48	2.57	0.33	17.3	13.7

Table 6.3 Data and HH MC simulation yields at each step in this analysis.

Chapter 7

Sensitivity Improvements with Analysis Categorizations

To maximize the analysis sensitivity, I adopt analysis categorizations in both ggF and VBF channels. Total sensitivity σ_{total} in the analysis depends on the quadratic sum of a sensitivity σ_i in a given signal region i, and so depends on the signal yield S_i and the background yield B_i, as shown in Eq. 7.1.

$$\sigma_{\text{total}} = \sqrt{\sum_i \sigma_i^2} = \sqrt{\sum_i \{(S_i + B_i)\ln(1 + \mathrm{S_i}/\mathrm{B_i}) - \mathrm{S_i}\}} \simeq \sqrt{\sum_i S_i^2/B_i} \tag{7.1}$$

This indicates that we can statistically improve the total sensitivity if we further discriminate signal and background events in the signal region into *categories*. Therefore, I use two discriminating variables, $|\Delta\eta_{HH}|$ and X_{HH}, and provide 6 categories for the ggF channel and 2 categories for the VBF channel. In this chapter, the analysis categorizations in the ggF and VBF channels will be discussed.

7.1 ggF Categories

Events in the ggF channel are categorized by two variables, X_{HH} and $|\Delta\eta_{HH}|$. These variables are already used in the analysis selection described in Chapter 6. $|\Delta\eta_{HH}| < 1.5$ is to suppress QCD multijet background, and $X_{HH} < 1.6$ is to define the *signal region* (SR). The X_{HH} and $|\Delta\eta_{HH}|$ distributions of SM and $\kappa_\lambda = 10$ ggF HH signals and background prediction in the ggF SR are shown in Figure 7.1. As can be seen in Figure 7.1, these two variable distributions of the HH signals and background are significantly different. The X_{HH} distribution of background goes up as larger X_{HH}, but the signal distributions have a peak around 0.95. The $|\Delta\eta_{HH}|$ distribution of background is mostly flat, but the signal distributions go down as larger $|\Delta\eta_{HH}|$. It means they are helpful to further discriminate between signals and background. Therefore, I set three $|\Delta\eta_{HH}|$ bins with an equal space of 0.5 between 0 and 1.5 and two X_{HH} bins with a boundary of 0.95. The boundaries are optimized to get the highest sensitivity for the SM ggF signal. To summarize, in total 6 categories are defined for the ggF channel as below:

- $|\Delta\eta_{HH}| < 0.5$ & $X_{HH} < 0.95$
- $0.5 \leq |\Delta\eta_{HH}| < 1.0$ & $X_{HH} < 0.95$

- $|\Delta\eta_{HH}| \geq 1.0$ & $X_{HH} < 0.95$
- $|\Delta\eta_{HH}| < 0.5$ & $X_{HH} \geq 0.95$
- $0.5 \leq |\Delta\eta_{HH}| < 1.0$ & $X_{HH} \geq 0.95$
- $|\Delta\eta_{HH}| \geq 1.0$ & $X_{HH} \geq 0.95$

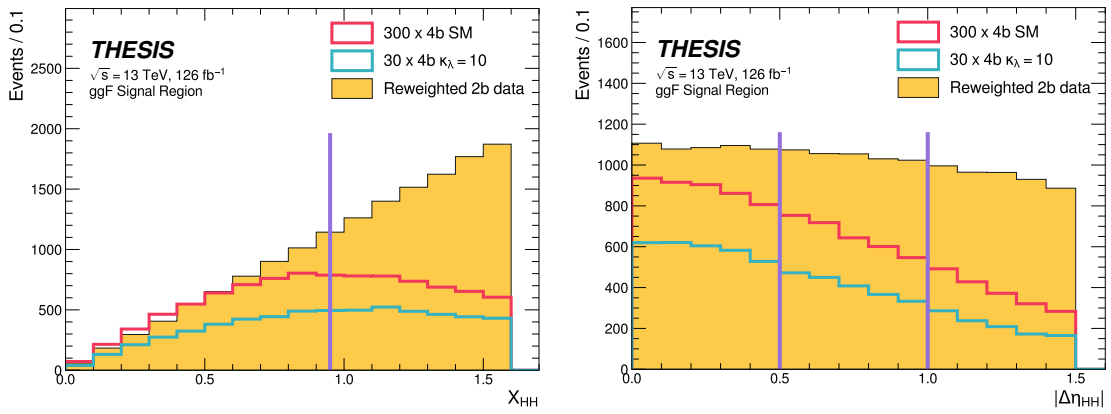

(a) X_{HH} (b) $|\Delta\eta_{HH}|$

Figure 7.1 X_{HH} and $|\Delta\eta_{HH}|$ distributions of SM (red) and $\kappa_\lambda = 10$ (blue) ggF HH signals and background estimation (yellow) in the ggF signal region. The purple lines indicate the boundaries used for the ggF categorization.

Figure 7.2 shows m_{HH} distributions of the ggF HH signals and background estimation in the ggF signal region with the X_{HH} and $|\Delta\eta_{HH}|$ categorization. The under panels on these plots show the $S/\sqrt{B}$ sensitivity to visualize which categories have the sensitivity. Since the signals have peaks of lower $|\Delta\eta_{HH}|$ and X_{HH}, the $|\Delta\eta_{HH}| < 0.5$ & $X_{HH} < 0.95$ category is the most sensitive category.

The sensitivity improvement of the X_{HH} and $|\Delta\eta_{HH}|$ categorization can be found in Figure 7.3, where only background modelling uncertainties described in Chapter 9 are considered. As can be seen in Figure 7.3, the ggF categorization improves the sensitivity by 35% across κ_λ.

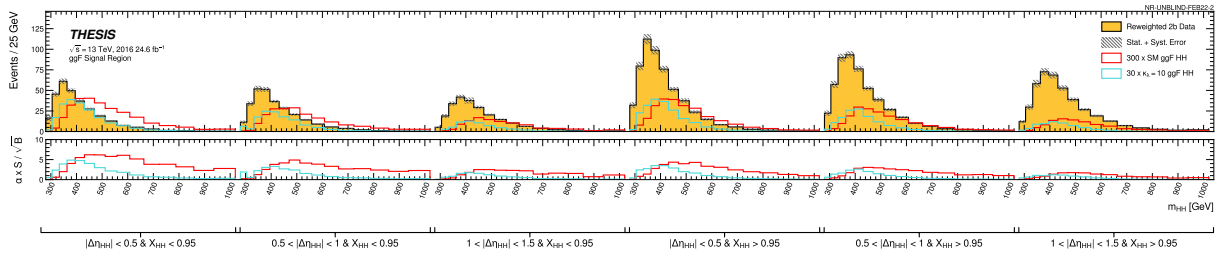

(a) 2016

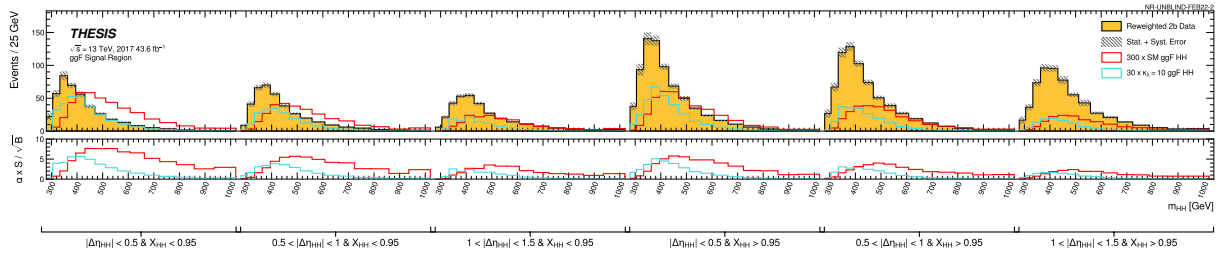

(b) 2017

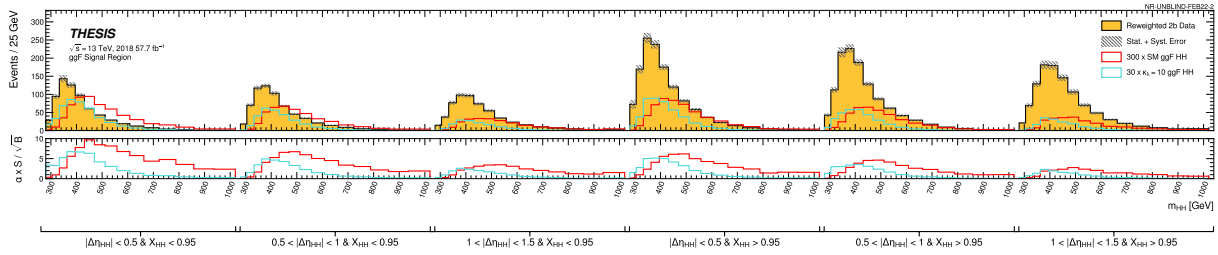

(c) 2018

Figure 7.2 m_{HH} distribution of SM and $\kappa_\lambda = 10$ ggF HH signals (shown by the red and blue histograms) and background estimation (shown by the yellow histogram) in the ggF signal regions with the ggF categorization. The under panel shows the $S/\sqrt{B}$ sensitivities for SM and $\kappa_\lambda = 10$ ggF HH signals in each m_{HH} bins.

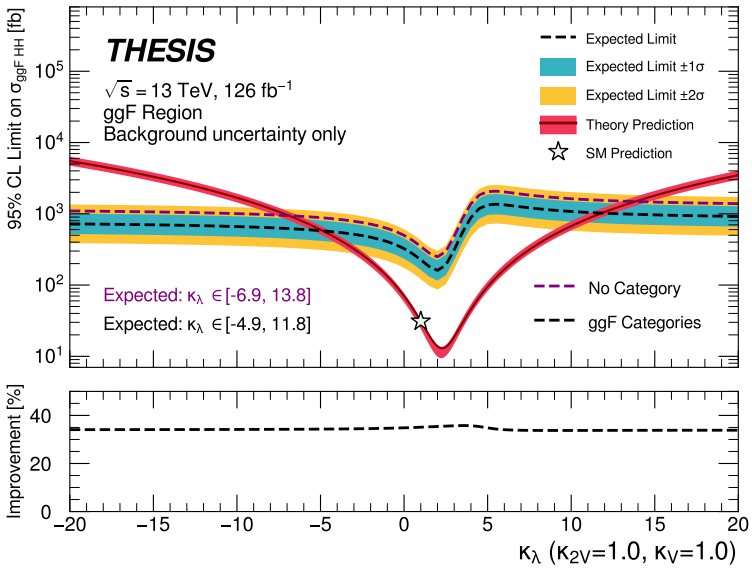

Figure 7.3 Sensitivity improvements on κ_λ scan in the ggF channel with the X_{HH} and $|\Delta\eta_{HH}|$ categorization. The dashed purple and black lines indicate the expected 95% CL upper limits on the ggF HH cross-section with no categorization and the ggF categorization, respectively. The inner blue band and outer yellow band indicate the $\pm1\sigma$ and $\pm2\sigma$ uncertainty ranges for the expected upper limits with the ggF categorization. Only background modelling uncertainties described in Chapter 9 are considered.

7.2 VBF Categories

In the VBF channel, events are categorized in $|\Delta\eta_{HH}|$. Figure 7.4 shows $|\Delta\eta_{HH}|$ distributions of the SM, $\kappa_\lambda = 10$ and $\kappa_{2V} = 0$ VBF HH signals and background prediction in the VBF SR. As shown in Figure 7.4, the $|\Delta\eta_{HH}|$ peak of the non-SM HH signals is close to $|\Delta\eta_{HH}| = 0$. On the other hand, the peak of the SM HH signal is close to $|\Delta\eta_{HH}| = 2$. The boundary of 1.5 for $|\Delta\eta_{HH}|$ categorization is chosen to maximize the sensitivity and keep the accuracy of background modelling in the VBF categories when taking into account the statistics.

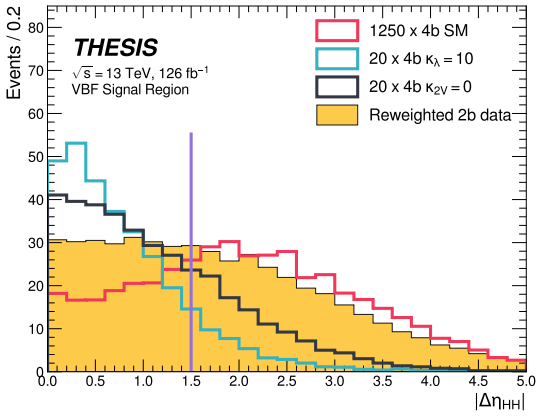

Figure 7.4 $|\Delta\eta_{HH}|$ distributions of the SM (red), $\kappa_\lambda = 10$ (blue) and $\kappa_{2V} = 0$ (black) VBF HH signals and background estimation (yellow) in the VBF signal region. The purple line indicates the boundary used for the VBF categorization.

Figure 7.5 shows m_{HH} distributions of the VBF HH signals and background estimation in the VBF signal region with the VBF categorization. The $|\Delta\eta_{HH}| < 1.5$ category derives the sensitivity to non-SM signals and the $|\Delta\eta_{HH}| > 1.5$ category is more sensitive to the SM HH signal.

The sensitivity improvement of the $|\Delta\eta_{HH}|$ categorization can be found in Figure 7.6, where only background modelling uncertainties described in Chapter 9 are considered. As can be seen in Figure 7.6, the VBF categorization improves the sensitivity by 30% across κ_λ and by 40% for BSM κ_{2V}.

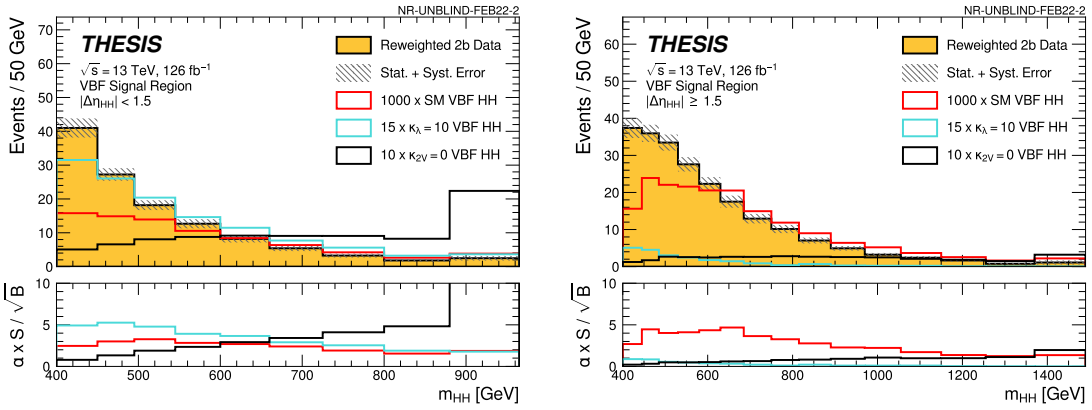

(a) $|\Delta\eta_{HH}| < 1.5$ (b) $|\Delta\eta_{HH}| > 1.5$

Figure 7.5 m_{HH} distribution of SM, $\kappa_\lambda = 10$ and $\kappa_{2V} = 0$ VBF HH signals (shown by the red, blue and black histograms) and background estimation (shown by the yellow histogram) in the VBF signal regions with the VBF categorization. The under panel shows the $S/\sqrt{B}$ sensitivities for the VBF HH signals in each m_{HH} bins.

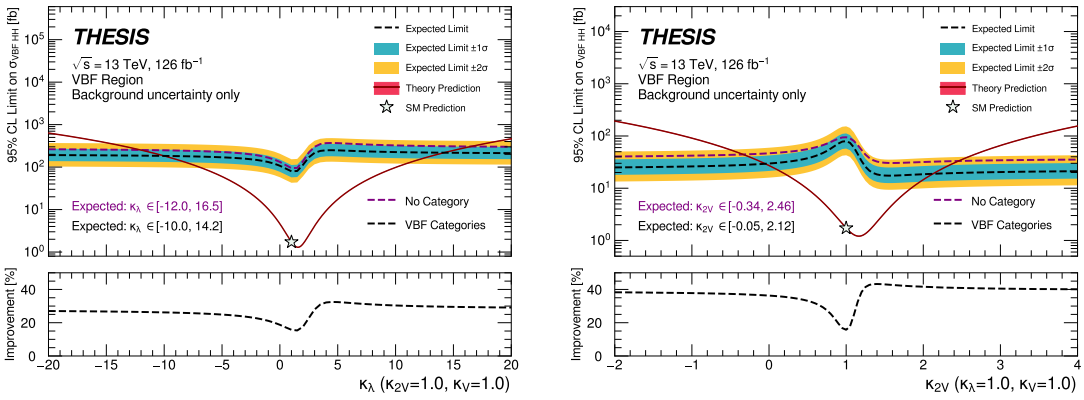

(a) κ_λ (b) κ_{2V}

Figure 7.6 Sensitivity improvements on (a) κ_λ and (b) κ_{2V} scans in the VBF channel with the $|\Delta\eta_{HH}|$ categorization. The dashed purple and black lines indicate the expected 95% CL upper limits on the VBF HH cross-section with no categorization and the VBF categorization, respectively. The inner blue band and outer yellow band indicate the $\pm1\sigma$ and $\pm2\sigma$ uncertainty ranges for the expected upper limits with the VBF categorization. Only background modelling uncertainties described in Chapter 9 are considered.

7.3 Combined ggF and VBF Categories

Finally, the ggF and VBF categories are combined to futher improve the sensitivity when performing the fits. Figure 7.7 shows the exclusion limits on the HH production cross-section as a function of κ_λ and κ_{2V} in the ggF category, the VBF category and the combiend ggF and VBF categories. For the κ_λ limit, the combined ggF and VBF categories can improve the constraints by approximately 5% due to the contribution of the VBF HH process. For the κ_{2V} limit, the ggF HH process has no dependency on κ_{2V} and no contribution. However, since 40% of the VBF HH process with respect to that in either channel are located in in the ggF channel. the combined ggF and VBF categories can improve the κ_{2V} constraint by a few %, where the SM ggF HH process is treated as background.

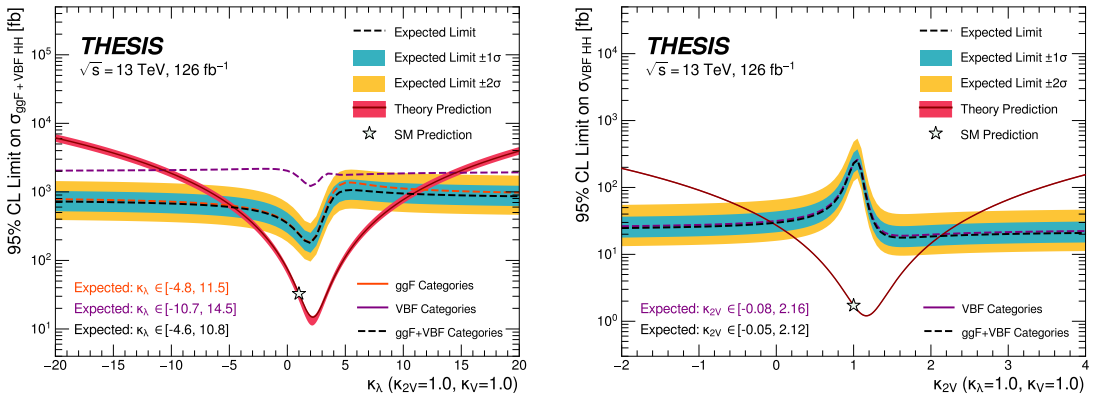

(a) κ_λ (b) κ_{2V}

Figure 7.7 The 95% CL expected limit on (a) κ_λ and (b) κ_{2V} scans in the combined ggF and VBF categories. The dashed orange line denotes the expected 95% CL upper limit in the ggF category, the dashed purple line denotes that in the VBF category and the dashed black line denotes that in the combined ggF and VBF categories. The inner blue band and outer yellow band indicate the $\pm1\sigma$ and $\pm2\sigma$ uncertainty ranges for the expected upper limits with the combined ggF and VBF categories. All systematic uncertainties discussed in Chapter 9 are included.

7.4 m_{HH} Binning

This analysis uses the invariant mass of the di-Higgs system (m_{HH}) as the final discriminating variable for the fit. The binning of m_{HH} is also important to maximize the sensitivity following Eq. 7.1.

This analysis chooses a logical binning scheme. In the scheme, after setting the lowest bin edge, the second bin edge is defined at $(100 + X\%) \times$ the lowest bin edge. X is the specified percentage parameter. The third bin edge is then also defined at $(100 + X\%) \times$ the second bin edge. This step is repeated until the predefined upper threshold is surpassed. The bin widths are thus increased by a constant $X\%$ with respect to the previous bin.

The binning parameters for the ggF categories and the VBF categories are shown in Table 7.1. These parameters are optimized to keep the statistical uncertainty of the background estimation described in

Section 9.1 less than 30%. For the ggF categories, the same binning is used, because the m_{HH} distributions differs little across the categories. For the VBF categories, because the tails of the m_{HH} distributions differs significantly, the different binnings are used. Overflow events are included into the highest bin in both channels. Underflow events are included in the lowest bin in the ggF channel, but not included in the VBF channel. The reason is that $m_{HH} < 400$ GeV events are not used in the VBF channel due to poor background modelling, as described in Section 8.1. The lowest bin edge is redefined to 400 GeV after setting all bin edges.

	Lowest bin edge [GeV]	Highest bin edge [GeV]	Percentage X [%]	Round off [GeV]
All ggF categories	280	950	9	1
VBF $\lvert\Delta\eta_{HH}\rvert < 1.5$	280	890	10	5
VBF $\lvert\Delta\eta_{HH}\rvert < 1.5$	290	1470	9	5

Table 7.1 Parameters used in the logical binning scheme. However, $m_{HH} < 400$ GeV bins are not used in the VBF categories due to poor background modelling. The lowest bin edge is redefined to 400 GeV after setting all bin edges.

Chapter 8

Background Estimation and Validation

Following the analysis selections described in Chapter 6, there are two major sources of background: QCD multijet and $t\bar{t}$ processes. Approximately 90% of background events come from QCD multijet processes, which originate from non-resonant QCD production with multiple heavy quarks (b and t quarks) or mis-identified light quarks, and the remaining 10% are $t\bar{t}$ processes. Other background contributions such as single Higgs processes (VH and ttH etc) were studied and found to be negligible.

For analyses using a fully hadronic channel, the background estimation of QCD multijet processes is the most important issue. To test the compatibility between observed data and background estimation in the signal regions, we need a good estimate of the background distribution. Though the nominal approach to estimate backgrounds is to use simulation samples in High Energy Physics (HEP) experiments, QCD multijet processes are hard to model in simulation. The approach using simulation samples doesn't work in this analysis. Therefore, I utilize a fully data-driven background estimation using an artificial neural network. In this chapter, the background estimation procedure and validations are discussed.

8.1 Background Estimation using Neural Network

8.1.1 Background Estimation Procedure

In this analysis, a fully data-driven approach is used to estimate kinematic distributions of QCD multijet and $t\bar{t}$ backgrounds, because it is difficult to model QCD multijet background in simulation. This approach is motivated by the high relative population of QCD multijet backgrounds and the flexibilities of machine learning methods.

Events in data with exactly two b-tagged jets, referred to as 2b events, are used to estimate 4b backgrounds. It is assumed here that the kinematics of 2b events are similar to the kinematics of events with more b-tagged jets such as three and four b-tagged jets, due to presenting multiple b-tagged jets. The same analysis selections as 4b data are applied to 2b data, except for the b-tagged selection. Of course, we could use other data, such as events with exactly three b-tagged jets (referred to 3b data) and reversed-$|\Delta\eta_{HH}|$ data in which inverted QCD veto cut ($|\Delta\eta_{HH}| > 1.5$) is applied, instead of 2b data, but 2b data is preferred in this analysis because of having more statistics and similar kinematics to 4b data. However, there is a bit difference between 2b data and 4b data on the selection of Higgs candidate jets. For 4b data, these jets are the four leading b-tagged jets in p_{T} to form two Higgs candidates. For 2b data,

the two b-tagged jets and two highest p_{T} jets are used. Due to the bias of the analysis selections and different processes contributing to 2b and 4b data, the kinematic shapes of 2b and 4b data are not exactly identical. Therefore, a kinematic reweighting is applied to 2b data to make it have the same kinematic distributions as 4b data.

The reweighting procedure used in this analysis is based on the traditional data-driven ABCD method as shown in Figure 8.1. In the ABCD method, four regions, A, B, C and D, are defined. A, B and C are the unblinded regions in which we can open data, and D is the blinded region corresponding to the signal region. In the method, it is assumed that a reweighting function or weights derived in A and C are the same as ones derived in B and D ($C/A = D/B$). With the assumption, the blinded region D can be estimated from the unblinded regions A, B and C with the equation $D = B \times C/A$. Kinematically similar regions with the blinded region are provided as A, B and C. The regions, A, B, C and D, correspond to CR2b, SR2b, CR4b and SR4b in this analysis, respectively. CR2b and CR4b indicate 2b data and 4b data in the control region, and SR2b and SR4b indicate 2b data and 4b data in the signal region, respectively. The reweighting procedure for SR4b can be roughly written as SR4b = SR2b (CR4b/CR2b). Validation studies for the assumption are discussed in Section 8.2.

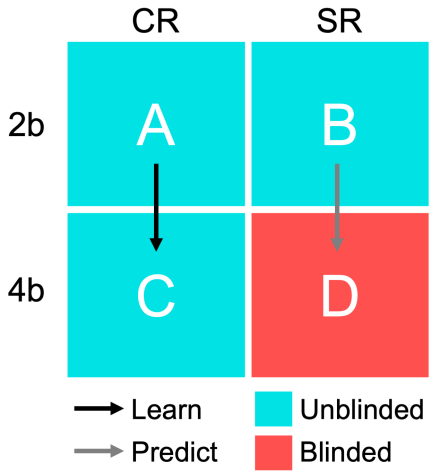

Figure 8.1 Illustration of the reweighting procedure, represented as a traditional data-driven ABCD method. The turquoise squares indicate the unblinded regions corresponding to A: CR2b, B: SR2b and C: CR4b, while the red square indicates the blinded region corresponding to D: SR4b. The black arrow indicates that a reweighting function from A to B is derived as the density ratio of A to C. The gray arrow indicates that the function is applied to B in order to D.

8.1.2 Neural Network Reweighting

As described above, the background estimation in this analysis works by correcting kinematic differences between 2b and 4b data by the kinematic reweighting. Firstly, some binned approaches that simply derive weights in bins of the relevant kinematic variables have been considered [5]. However, such an approach was found to be limited for background estimation in their handling of correlations between kinematic

variables and in the "curse-of-dimensionality". The relation between 2b and 4b data is not simple, so that we need to see differences and correlations in many variables. We could attempt to bin further in additional variables to account for correlations. However, the dataset becomes sparser and sparser, as the number of dimensions increases. This forces us to choose either a lower quality fit using more coarse bins due to the low resolution or an unstable fit using finely grained bins due to the low statistics. Consequently, binned approaches can not provide better background modelling due to these problems.

To resolve these problems and archive better background modelling, I utilized a machine learning approach using a neural network to derive the reweighting function. Neural network performs a truly multivariate approach, allowing for proper treatment of variable correlations. It further resolves the problems associated with binned approaches by learning the reweighting function directly. It provides greater sensitivity to local differences and can help avoid the curse of dimensionality.

The reweighting function $w(x)$, corresponding to weights, used in this analysis is defined using the probability density functions, $p_{4b}(x)$ and $p_{2b}(x)$, for 4b and 2b data respectively across some input variables x as:

$$p_{2b}(x) \cdot w(x) = p_{4b}(x) \tag{8.1}$$

$$w(x) = \frac{p_{4b}(x)}{p_{2b}(x)}. \tag{8.2}$$

To learn the reweighting function directly in a neural network, the approach used here is based on those described in Ref. [110, 111] and the following loss function:

$$\mathcal{L}(R(x)) = \mathbb{E}_{x\sim p_{2b}}\left[\sqrt{R(x)}\right] + \mathbb{E}_{x\sim p_{4b}}\left[\frac{1}{\sqrt{R(x)}}\right], \tag{8.3}$$

where $R(x)$ is an estimator dependent on input variables x and $\mathbb{E}_{x\sim p_{2b}}$ and $\mathbb{E}_{x\sim p_{4b}}$ are the expectation values with respect to the 2b and 4b probability densities. A neural network with such a loss function has an objective of finding the estimator, $R(x)$, that minimizes this loss function by training on input variables x.

$$R_{\min}(x) \equiv \arg\min_{R} \mathcal{L}(R(x)) = \frac{p_{4b}(x)}{p_{2b}(x)} \tag{8.4}$$

This is exactly the form of the reweighting function.

However, negative weights could be derived by a neural network with the loss function. They are undesirable for background estimation because they could lead to unphysical negative background predictions. Therefore, to avoid imposing any direct constraint on the positivity of weights, an exponential encoding $Q(x) \equiv \log R(x)$ is adopted and the loss function is modified as described in Eq. 8.5.

$$\mathcal{L}(Q(x)) = \mathbb{E}_{x\sim p_{2b}}\left[\sqrt{e^{Q(x)}}\right] + \mathbb{E}_{x\sim p_{4b}}\left[\frac{1}{\sqrt{e^{Q(x)}}}\right] \tag{8.5}$$

$$Q_{\min}(x) \equiv \arg\min_{Q} \mathcal{L}(Q(x)) = \log\frac{p_{4b}(x)}{p_{2b}(x)} \tag{8.6}$$

Finally, the reweighting function can be obtained as $e^{Q_{\min}(x)}$.

The neural networks with the loss function defined at Eq. 8.5 are trained on a set of input variables. Kinematic variables that are sensitive to the difference between 2b and 4b data are selected as the input variables, except for the discriminant variables, m_{HH}. $|\Delta\eta_{HH}|$ and X_{HH}, to avoid potential biases. These

input variables are optimized for each *gg*F and VBF channel, and are listed in Table 8.1. The natural logarithm of some of the variables is used to help bring out these differences. One-hot encoding is a process to translate categorical variables to a group of binary variables, where only one of them will be true to represent the state. This is often used for machine learning because it makes it easier to deal with categorical variables and improves the performance. In this analysis, the trigger bucket index and the year index are encoded to one-hot. For example, *Bucket 1* is translated to 01 and *Bucket 2* is 10. The number of jets is added to deal with the analytic bias of the *Higgs candidate jet* selection. All input variables are standardized by subtracting the mean in the training sample and dividing it by the standard deviation.

The neural networks used for the *gg*F channel consist of one input layer, three densely connected hidden layers of 50 nodes each with Rectified-Linear-Unit (ReLU) activation functions and a single node linear output. The same architecture is used for the VBF channel, except for the number of nodes in the hidden layers. Only 20 nodes are set in the three hidden layers, because of the lower statistics in the VBF channel. These configurations are optimized to get better reweighting performance in the background modelling of a variety of input and non-input variables. The neural network architectures for the *gg*F and VBF reweighting are visualized in Figure 8.2.

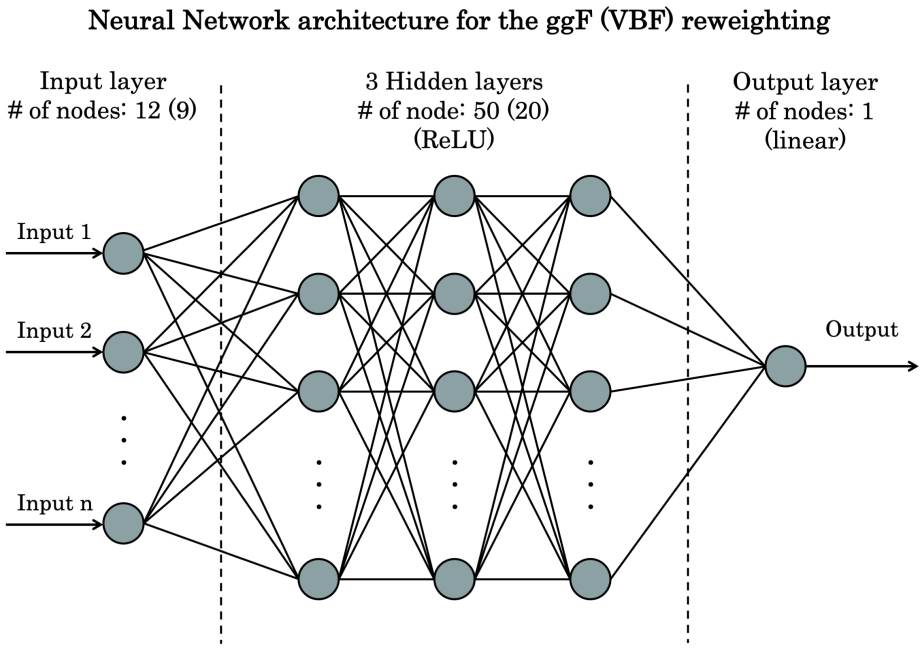

Figure 8.2 A visualization of the neural network architecture for the *gg*F and VBF reweighting.

Even though the same architecture is used, the reweighting performance can be fluctuated due to the training statistics and the initial conditions. To increase the stability of the reweighting performance and take into account the variations between a set of neural network trainings, an ensemble of 100 neural networks is prepared in this analysis. To generate a different training sample for each neural network training, the bootstrap resampling technique [112] is used. In each training sample, 2b sample is the full set of 2b data in the Control Region (CR2b) and 4b sample is constructed by sampling with

replacement from the original 4b data in the CR (CR4b), where the words in parentheses correspond to the regions described in Figure 8.1. Then, the ensemble of 100 neural networks is trained with each different training sample. These neural networks are used to derive a weight for each 2b event in the signal region (SR2b). 2b events in the SR are reweighted to predict 4b background distribution in the SR (SR4b). A normalization factor is derived such that the yield of reweighted 2b data in the CR matches the yield of each 4b data in the CR. Each reweighted 2b data in the SR is normalized by the normalization factor. Consequently, a set of 100 background estimations is provided. To account for the variations, the mean of 100 background estimations is taken as the baseline of background estimation. This approach achieved improving the stability of background estimation. The standard deviation of 100 background estimations is taken as the bootstrap statistic uncertainty. Further details are described in Chapter 9.

As described in Section 6.5, two control regions, CR1 and CR2 are defined in order to take into account a systematic bias in deriving weights in the CR and extrapolating to the SR. One ensemble of neural networks is trained in the CR1. The background estimation derived by these neural networks is then used as the nominal background estimation. In addition, a different ensemble of neural networks is trained in the CR2 independently. The background estimation from the CR2-derived neural networks can play a role in the alternative background estimation, since the CR1 and CR2 are located to surround the SR. The difference between the nominal and the alternative is used to assign a systematic uncertainty to account for the systematic bias. Further details are discussed in Chapter 9.

Due to the difference in the trigger selection such as jet p_{T} threshold and b-tagging efficiency, kinematic differences on data exist between years. Therefore, the neural networks are trained separately on the years for the ggF channel. This means that the background estimation and the corresponding uncertainties are derived individually for each year. On the other hand, for the VBF channel, the neural network trainings are performed inclusively in the years because the statistics are more limited than the ggF channel. For this reason, it is motivated to add the year index information into input variables for the VBF channel.

Table 8.1 Set of input variables used for the neural network reweighting in the ggF and VBF channels.

ggF channel	VBF channel
1. $\log(p_{\mathrm{T}})$ of the 4th leading *Higgs candidate jet*	1. Maximum di-jet mass out of passible pairing of the four *Higgs candidate jets*
2. $\log(p_{\mathrm{T}})$ of the 2nd leading *Higgs candidate jet*	2. Minimum di-jet mass out of passible pairing of the four *Higgs candidate jets*
3. $\log\Delta R_{jj}$ between the closest two *Higgs candidate jets*	3. Energy of the leading Higgs candidate
4. $\log\Delta R_{jj}$ between the other two *Higgs candidate jets*	4. Energy of the subleading Higgs candidate
5. Average absolute value of *Higgs candidate jet* η	5. Second smallest ΔR_{jj} between the jets in the leading Higgs candidate (out of the three possible pairings for the leading Higgs candidate)
6. $\log(p_{\mathrm{T}})$ of the di-Higgs system	6. Average absolute value of *Higgs candidate jet* η
7. ΔR between the two Higgs candidates	7. $\log(X_{wt})$, where X_{wt} is the discriminant variable used for the top veto
8. $\Delta\Phi$ between the jets in the leading Higgs candidate	8. Trigger bucket index as one hot encoder
9. $\Delta\Phi$ between the jets in the subleading Higgs candidate	9. Year index as one hot encoder (for the years inclusive training)
10. $\log(X_{wt})$, where X_{wt} is the discriminant variable used for the top veto	
11. Number of jets in the event	
12. Trigger bucket index as one hot encoder (*Bucket 1*: 10, *Bucket 2*: 01)	

8.1.3 Neural Network Reweighting Performance

Figure 8.3 and 8.4 show m_{HH} distributions of 4b data, normalized 2b data and reweighted 2b data in the CR1 for the ggF and VBF channel, respectively. The normalized 2b data refers to 2b data normalized to match the yield of 4b data in the CR1 without the neural network reweighting. The reweighted 2b data corresponds to the background estimation. As can be seen, there is a significant difference between 2b and 4b data before the reweighting, but the reweighting well performs to correct the difference. However, for the VBF channel, poor background modelling on m_{HH} below 400 GeV is observed. Because the sensitivity below 400 GeV is low, I decided to drop the bins of $m_{HH} < 400$ GeV in the fit described in Chapter 10 in the VBF channel. Other kinematic variable distributions are shown in Appendix C.

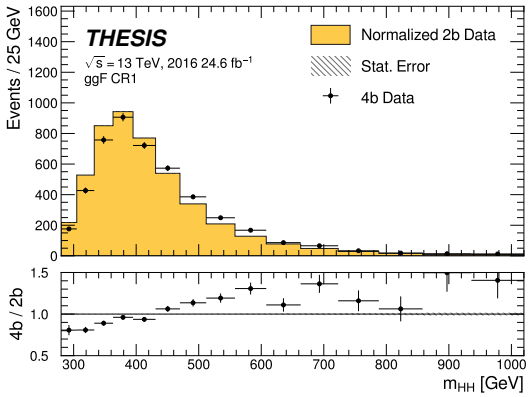

(a) m_{HH} before reweighting in 2016

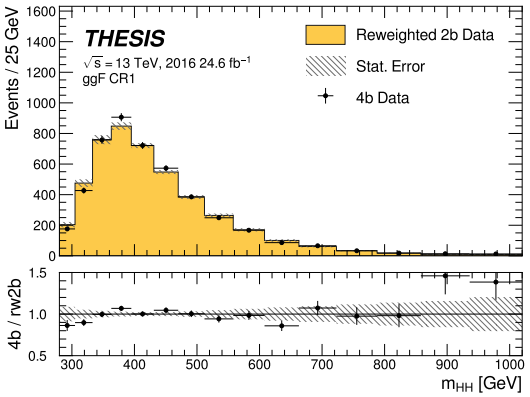

(b) m_{HH} after reweighting in 2016

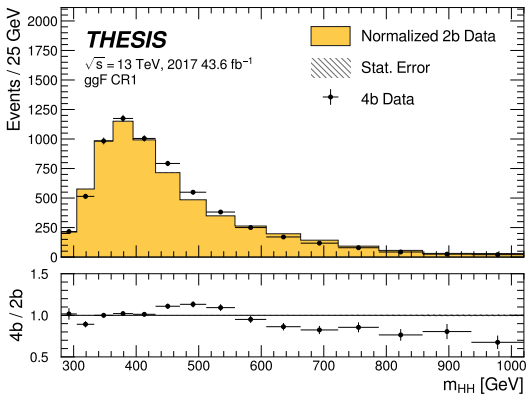

(c) m_{HH} before reweighting in 2017

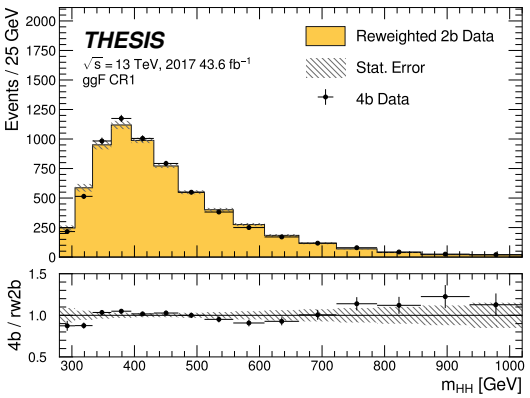

(d) m_{HH} after reweighting in 2017

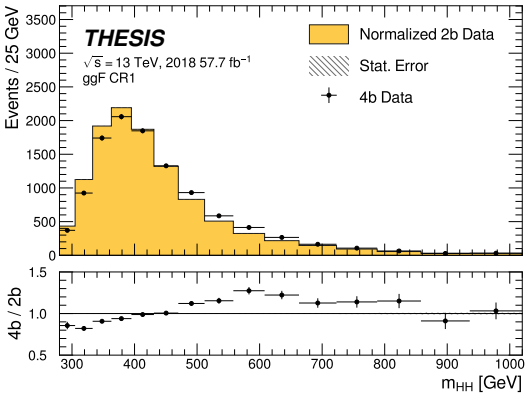

(e) m_{HH} before reweighting in 2018

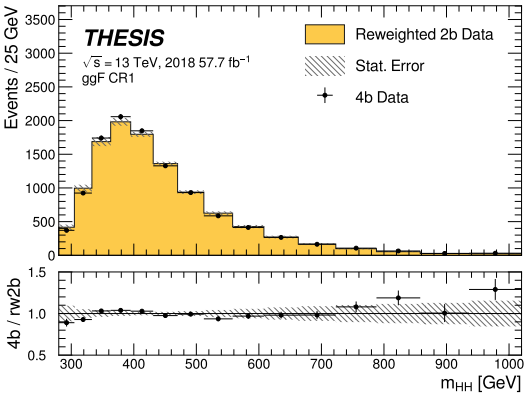

(f) m_{HH} after reweighting in 2018

Figure 8.3 m_{HH} distributions of normalized 2b data, reweighted 2b data and 4b data in the ggF control region 1. For the normalized 2b data, the statistic uncertainty includes only 2b poisson uncertainty. For the reweighted 2b data, the statistic uncertainty includes 2b poisson uncertainty and the bootstrap statistic uncertainty.

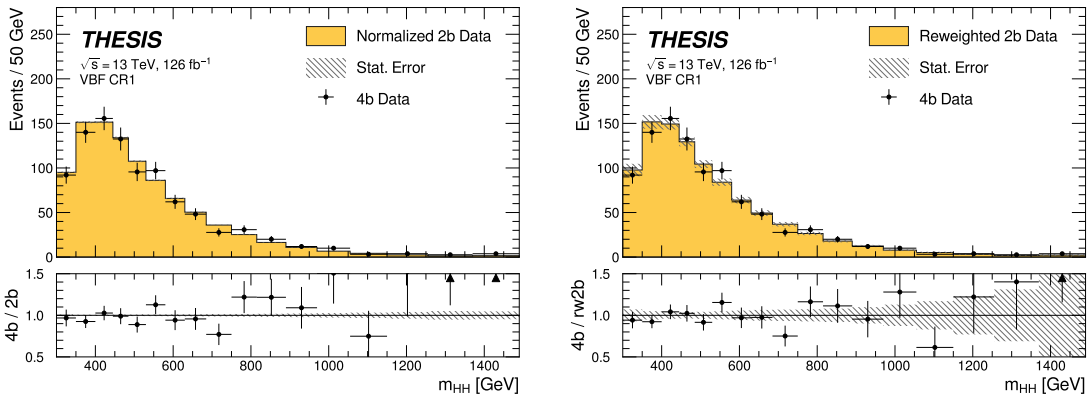

(a) m_{HH} before reweighting

(b) m_{HH} after reweighting

Figure 8.4 m_{HH} distributions of normalized 2b data, reweighted 2b data and 4b data in the VBF control region 1. For the normalized 2b data, the statistic uncertainty includes only 2b poisson uncertainty. For the reweighted 2b data, the statistic uncertainty includes 2b poisson uncertainty and the bootstrap statistic uncertainty.

8.2 Background Validation

In this background estimation procedure, it is assumed that weights derived in CR2b and CR4b are similar to ones derived in SR2b and SR4b as discussed in Section 8.1, and then SR4b can be estimated by the reweighting with the equation SR4b = SR2b (CR4b/CR2b). To confirm that the neural network reweighting works in the signal regions with this assumption, I performed four validation studies. *Significace* defined in Appendix B is used henceforth to check consistency between observed data and the background estimation and shown in the under pannel in the plots.

8.2.1 Shifted Regions

Shifted Region Definitions

The shifted region strategy relies on defining several regions identical to the true signal and control regions but in a distinct position in the m_{H1}-m_{H2} plane. These alternative regions are each referred to as a *shifted region*. The positions are chosen such that they are close to the true signal region but do not overlap it. In total five shifted regions are defined. The SR of each shifted region is defined using X_{HH}^{shift} as given by Eq. 8.7, instead of the nominal X_{HH}.

$$X_{HH}^{\text{shift}} = \sqrt{\left(\frac{m_{H1} - m_{H1}^{\text{center}}}{\sigma_{m_{H1}} \cdot m_{H1}}\right)^2 + \left(\frac{m_{H2} - m_{H2}^{\text{center}}}{\sigma_{m_{H2}} \cdot m_{H2}}\right)^2} \tag{8.7}$$

The functional form is the same as Eq. 6.3 for the true SR definition, but the center values and the resolutions of m_{H1} and m_{H2} are adjusted to avoid overlapping with the true SR. The center values, m_{H1}^{center} and m_{H2}^{center}, shown in Table 8.2 are the centers of the five shifted regions. The resolutions, $\sigma_{m_{H1}}$ and $\sigma_{m_{H2}}$, are given in Eq. 8.8. The SR definition cut value is 1.6, same as the true SR.

$$\sigma_{m_{H1}} = 0.1 \times \frac{124}{m_{H1}^{\text{center}}}, \quad \sigma_{m_{H2}} = 0.1 \times \frac{117}{m_{H1}^{\text{center}}} \tag{8.8}$$

Table 8.2 m_{H1} and m_{H2} centers for the five shifted regions. The shifted regions are named according to their position relative to the true signal region in the m_{H1}-m_{H2} plane.

Shifted Region	m_{H1}^{center} [GeV]	m_{H2}^{center} [GeV]
Upper Left	78	166
Upper Center	124	180
Upper Right	170	166
Center Right	188	117
Lower Right	170	68

Each shifted region's CR1 and CR2 are also defined similarly to the true CR1 and CR2, as described in Section 6.5, but using the center values of m_{H1} and m_{H2} as shown in Table 8.2. Figure 8.5 displays

the boundaries of the five shifted regions. As Figure 8.5 shows, the true SR does not overlap with any of the regions. In the lower right region, CR2 is used for the true estimate instead of CR1, because CR1 extends below the acceptance threshold for m_{H2}, resulting in distinct kinematic differences. CR1 is used to derive the shape systematic uncertainty. Due to the acceptance threshold for m_{H1} and m_{H2}, the shape systematic uncertainties in the lower right region and the upper right region are larger than other regions.

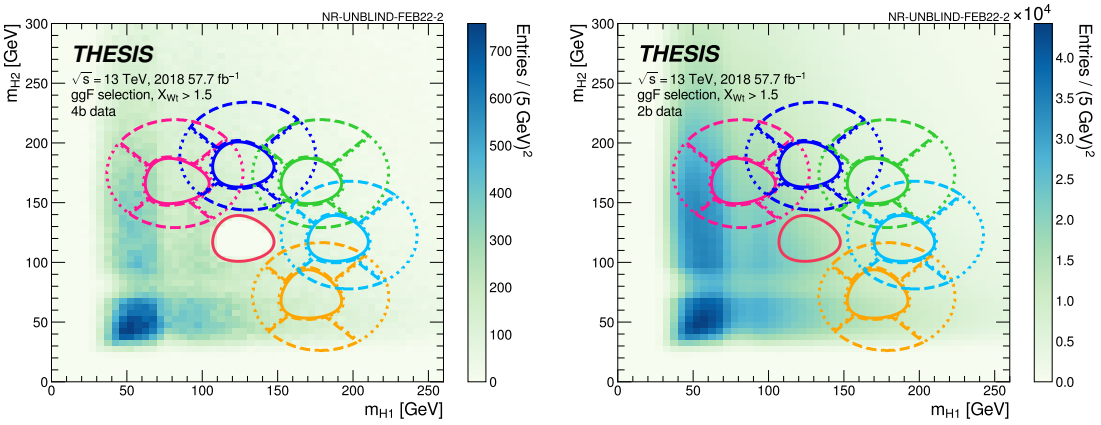

(a) 2018: 4b Data

(b) 2018: 2b Data

Figure 8.5 Shifted regions superimposed on (a) 4b data and (b) 2b data. The red solid closed curve in the center indicates the true SR described in Section 6.5. In clockwise order: upper left (pink), upper center (blue), upper right (green), center right (light-blue), lower right (orange).

Shifted Region's ggF Results

Since the SRs of the shifted regions contain negligible signal events and can be unblinded, the background estimate can be validated directly by comparing with the data in the SRs. The same standard background estimation procedure is still conducted, including same training variables, neural network architecture and statistic and systematic uncertainties estimates.

Figure 8.6, 8.7 and 8.8 show the 4b background estimation results in the shifted regions with the ggF selection. As can be seen, the m_{HH} shape of background estimation is consistent with 4b data in all shifted regions. The background estimation yield is also consistent with the 4b yield within 1 σ.

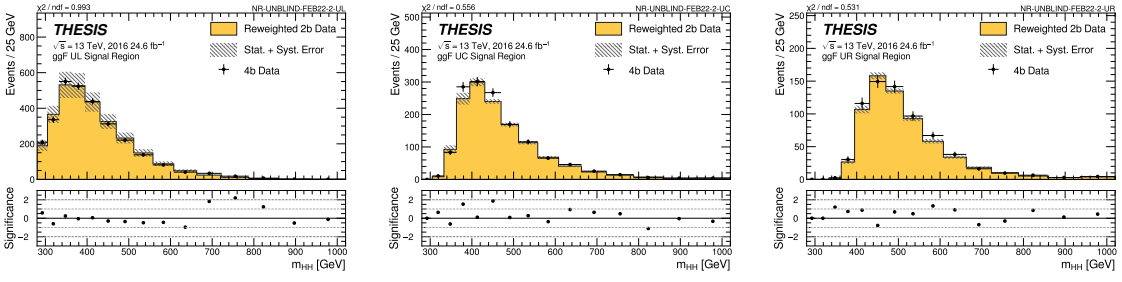

(a) Upper Left (b) Upper Center (c) Upper Right

(d) Center Right (e) Lower Right

Figure 8.6 m_{HH} distributions of reweighted 2b data and 4b data in the ggF signal region in the shifted regions in 2016. Upper left, upper center, upper right and center right regions use CR1 derived weights, but lower right region uses CR2 derived weights. The error of background includes the 2b poisson statistic error, the bootstrap error and the shape systematic error.

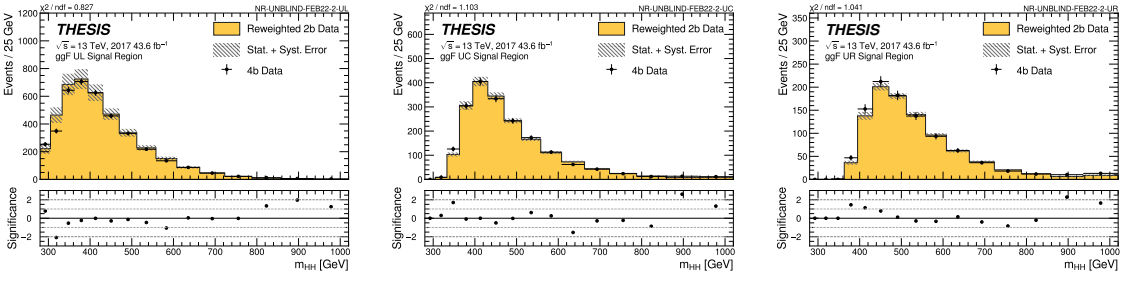

(a) Upper Left (b) Upper Center (c) Upper Right

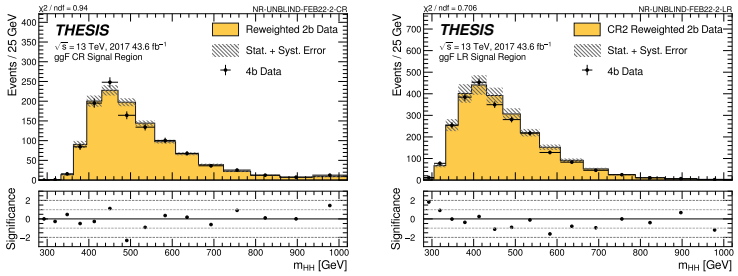

(d) Center Right (e) Lower Right

Figure 8.7 m_{HH} distributions of reweighted 2b data and 4b data in the ggF signal region in the shifted regions in 2017. Upper left, upper center, upper right and center right regions use CR1 derived weights, but lower right region uses CR2 derived weights. The error of background includes the 2b poisson statistic error, the bootstrap error and the shape systematic error.

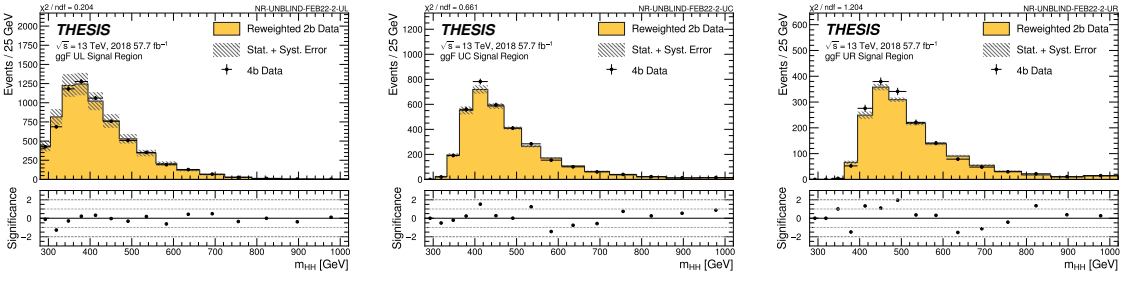

(a) Upper Left (b) Upper Center (c) Upper Right

(d) Center Right (e) Lower Right

Figure 8.8 m_{HH} distributions of reweighted 2b data and 4b data in the ggF signal region in the shifted regions in 2018. Upper left, upper center, upper right and center right regions use CR1 derived weights, but lower right region uses CR2 derived weights. The error of background includes the 2b poisson statistic error, the bootstrap error and the shape systematic error.

Shifted Region's VBF **Results**

Figure 8.9 shows the same information for the VBF selection. The conclusion is the same as that for the ggF selection. Good closure is observed.

The results of this shifted region study suggest that weights derived in the CR1 can be successfully extrapolated into the SR, resulting in well-modelled background estimates.

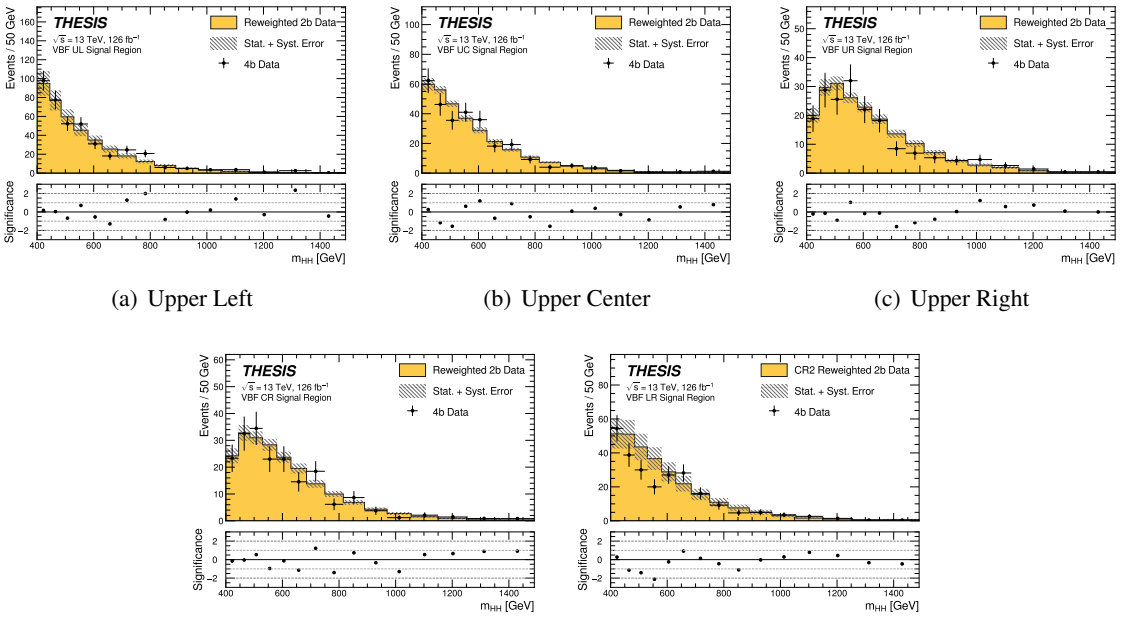

(a) Upper Left (b) Upper Center (c) Upper Right

(d) Center Right (e) Lower Right

Figure 8.9 m_{HH} distributions of reweighted 2b data and 4b data in the VBF signal region in the shifted regions. Upper left, upper center, upper right and center right regions use CR1 derived weights, but lower right region uses CR2 derived weights. The error of background includes the 2b poisson statistic error, the bootstrap error and the shape systematic error.

8.2.2 3b + 1 fail (3b1f) data

The 3b1f (3 b-tagged + 1 failed) region, where events with three jets that are b-tagged at the 77% working point but all other jets failed to be b-tagged at even the loosest 85% working point are contained, is used to validate the background estimation procedure. The background yields in the 3b1f region are expected to be approximately 10 times larger than the 4b region, and the signal yields are negligible with respect to the background as shown in Table 8.3. This analysis doesn't gain any additional sensitivity from the 3b1f region. It allows assessing the background modelling using the neural network reweighting described in Section 8.1 in the 3b1f signal region. This is a nice way to validate the interpolation of the background estimation into the signal region.

The question is, whether the 3b1f validation uses the full statistics or the available 4b statistics. The 3b1f region has approximately 10 times larger events than the 4b region. This means we can assess

Table 8.3 Signal and 3b1f data yields in 3b1f ggF and VBF signal regions.

Year	SM ggF HH	SM VBF HH	3b1f data
ggF Signal Region			
16	4.30	0.03	41945
17	6.26	0.04	44648
18	9.08	0.06	93451
VBF Signal Region			
All	0.27	0.17	7080

the background modelling either by using the full statistics or downsampling the statistics to mimic the available 4b statistics. In general, it is expected that using the full statistics gives better performance.

To test the impact of the statistical limit on the background modelling, the reweighting performances using the full 3b1f statistics and downsampled statistics are compared. The standard methodology of the background estimation is performed with 4b events replaced by 3b1f events. It means a neural network is trained with 2b events and 3b1f events to capture their differences, and then 2b events are reweighted by the weights to predict 3b1f distributions. However, in the downsampled statistics, the 3b1f events in the control region 1 are split into 10 downsamples. Each downsample is trained with the 2b events and the standard methodology. Therefore, ten different predictions are derived and the medium of the ten background predictions is approximately 10 times smaller than the full statistics one.

Figure 8.10 compares the background prediction using the full statistics and the background prediction using downsampled statistics in m_{HH} distribution in the 3b1f ggF signal region with the ggF categorization. In the distributions using downsampled statistics, the medians of the ten predictions and 3b1f data are shown. The error band indicates the standard deviation of the ten predictions. Figure 8.11 shows the same information in the 3b1f VBF signal region with the VBF categorization. In both ggF region and VBF region, it can be seen that the impact due to the statistical limit is small, because the ratio of 3b1f data and background prediction is similar between the full statistics and downsampled statistics and the standard deviation covers the background prediction using the full statistics even without other uncertainties. Therefore, I decided to use the median of the ten predictions using downsampled statistics to validate the background modelling, in order to test with the available 4b statistics.

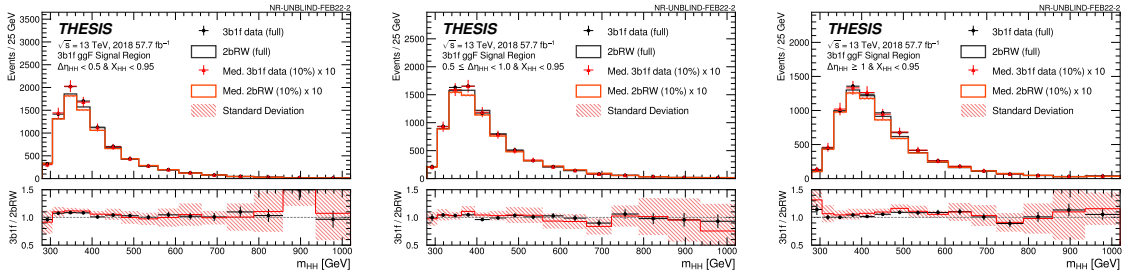

(a) $|\Delta\eta_{HH}| < 0.5$ & $X_{HH} < 0.95$ (b) $0.5 \leq |\Delta\eta_{HH}| < 1.0$ & $X_{HH} < 0.95$ (c) $|\Delta\eta_{HH}| \geq 1.0$ & $X_{HH} < 0.95$

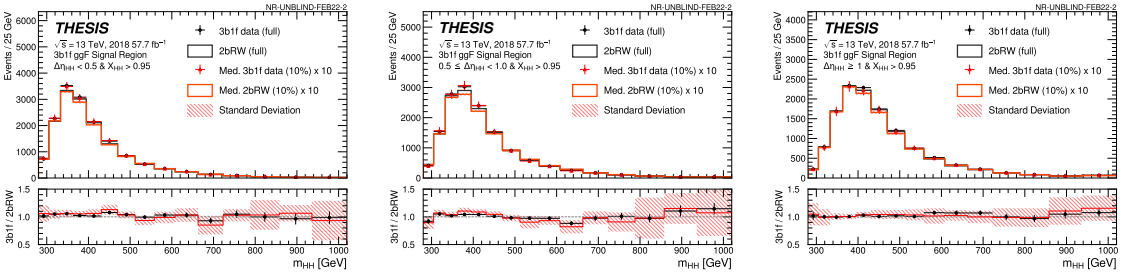

(d) $|\Delta\eta_{HH}| < 0.5$ & $X_{HH} \geq 0.95$ (e) $0.5 \leq |\Delta\eta_{HH}| < 1.0$ & $X_{HH} \geq 0.95$ (f) $|\Delta\eta_{HH}| \geq 1.0$ & $X_{HH} \geq 0.95$

Figure 8.10 Comparison of the background estimations with the full statistics (shown in the black histogram) and the downsampled statistics (shown in the red histogram) in m_{HH} distribution in the 3b1f ggF signal region with the X_{HH} and $|\Delta\eta_{HH}|$ categorization in 2018. The black (red) dots show m_{HH} distributions of full (downsampled) 3b1f data. The under panel shows the ratio of the 3b1f data to the background estimation. The downsampled distributions are scaled by a factor of 10.

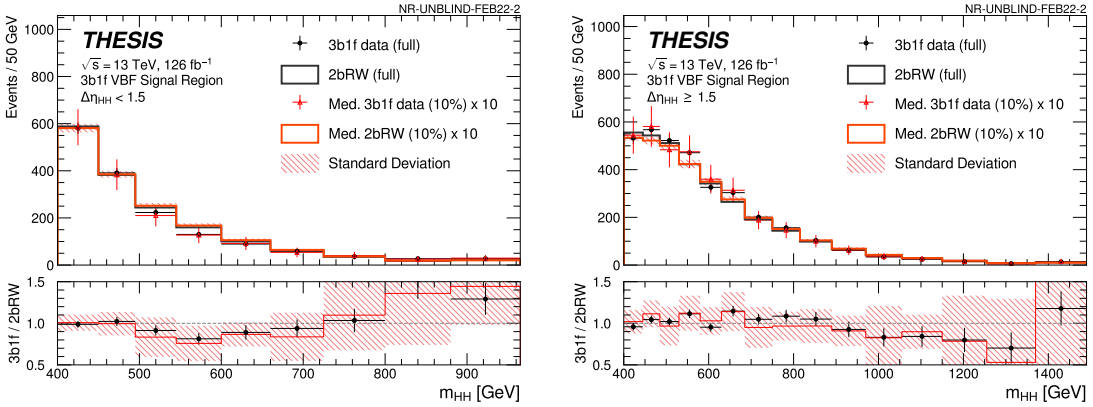

(a) $|\Delta\eta_{HH}| < 1.5$ (b) $1.5 \leq |\Delta\eta_{HH}|$

Figure 8.11 Comparison of the background estimations with the full statistics (shown in the black histogram) and the downsampled statistics (shown in the red histogram) in m_{HH} distribution in the 3b1f VBF signal region with the $|\Delta\eta_{HH}|$ categorization. The black (red) dots show m_{HH} distributions of full (downsampled) 3b1f data. The under panel shows the ratio of the 3b1f data to the background estimation. The downsampled distributions are scaled by a factor of 10.

3b1f's ggF Results

Figure 8.12, 8.13 and 8.14 show the 3b1f validation results in the ggF signal region with the ggF categorization. The thick-red line indicates the median of ten 3b1f downsampled data and the thick-green line indicates the median of ten background predictions using downsampled statistics. The thin-red lines show the ten 3b1f downsampled data and the thin-green lines show the ten background predictions. Pulls of the medians of the 3b1f downsampled data and the background predictions with 2b poison uncertainty, bootstrap uncertainty and shape systematic uncertainty are shown in the lower panels. In general, good closure is observed in the ggF region. However, as can be seen in the lower panels, slightly non-closure is observed around the peak of m_{HH} distribution across the ggF categories. The non-closure is observed in the background prediction using the full statistics too, as can be seen in Appendix D. Therefore, I decided to add an additional uncertainty for the 3b1f non-closure for the ggF channel. The details of the 3b1f non-closure uncertainty are described in Section 9.1.3.

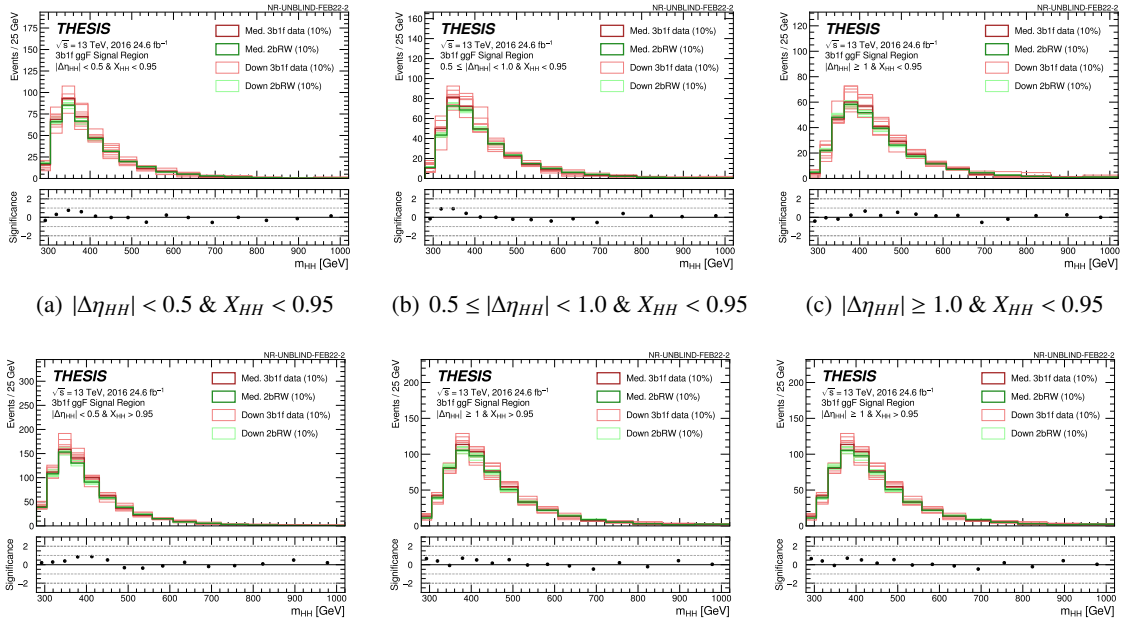

(a) $|\Delta\eta_{HH}| < 0.5$ & $X_{HH} < 0.95$ (b) $0.5 \leq |\Delta\eta_{HH}| < 1.0$ & $X_{HH} < 0.95$ (c) $|\Delta\eta_{HH}| \geq 1.0$ & $X_{HH} < 0.95$

(d) $|\Delta\eta_{HH}| < 0.5$ & $X_{HH} \geq 0.95$ (e) $0.5 \leq |\Delta\eta_{HH}| < 1.0$ & $X_{HH} \geq 0.95$ (f) $|\Delta\eta_{HH}| \geq 1.0$ & $X_{HH} \geq 0.95$

Figure 8.12 m_{HH} distributions of 3b1f (red) and the background estimation (green) in the ggF signal region with the X_{HH} and $|\Delta\eta_{HH}|$ categorization in 2016. The thin lines show the 10 downsampled distributions and the thick lines show the median of the 10 downsampled distributions. The under panel shows *significaces* defined in Appendix B from the median distributions.

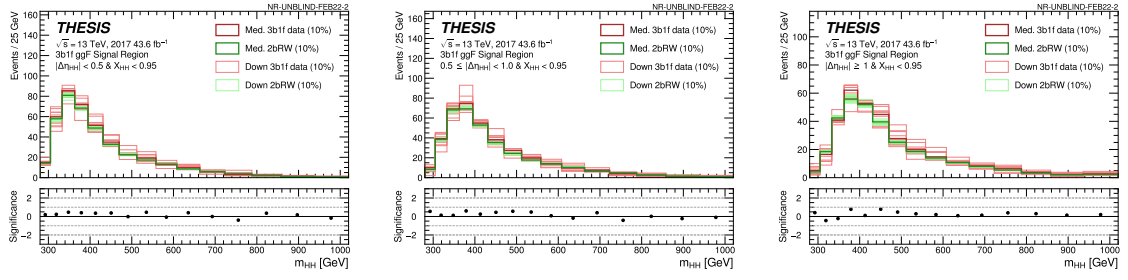

(a) $|\Delta\eta_{HH}| < 0.5$ & $X_{HH} < 0.95$ (b) $0.5 \leq |\Delta\eta_{HH}| < 1.0$ & $X_{HH} < 0.95$ (c) $|\Delta\eta_{HH}| \geq 1.0$ & $X_{HH} < 0.95$

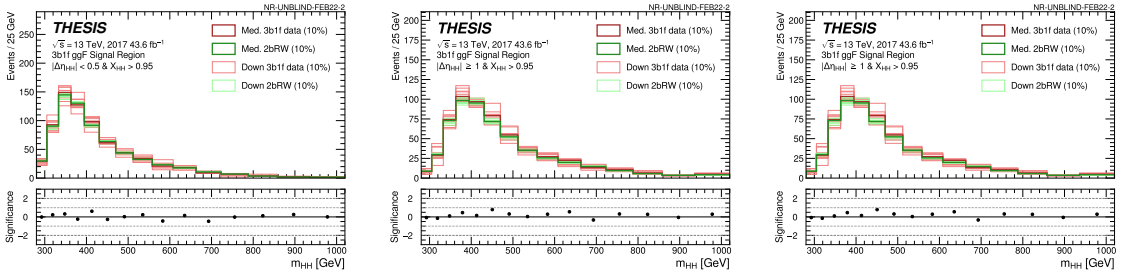

(d) $|\Delta\eta_{HH}| < 0.5$ & $X_{HH} \geq 0.95$ (e) $0.5 \leq |\Delta\eta_{HH}| < 1.0$ & $X_{HH} \geq 0.95$ (f) $|\Delta\eta_{HH}| \geq 1.0$ & $X_{HH} \geq 0.95$

Figure 8.13 m_{HH} distributions of 3b1f data (red) and the background estimation (green) in the ggF signal region with the X_{HH} and $|\Delta\eta_{HH}|$ categorization in 2017. The thin lines show the 10 downsampled distributions and the thick lines show the median of the 10 downsampled distributions. The under panel shows *significaces* defined in Appendix B from the median distributions.

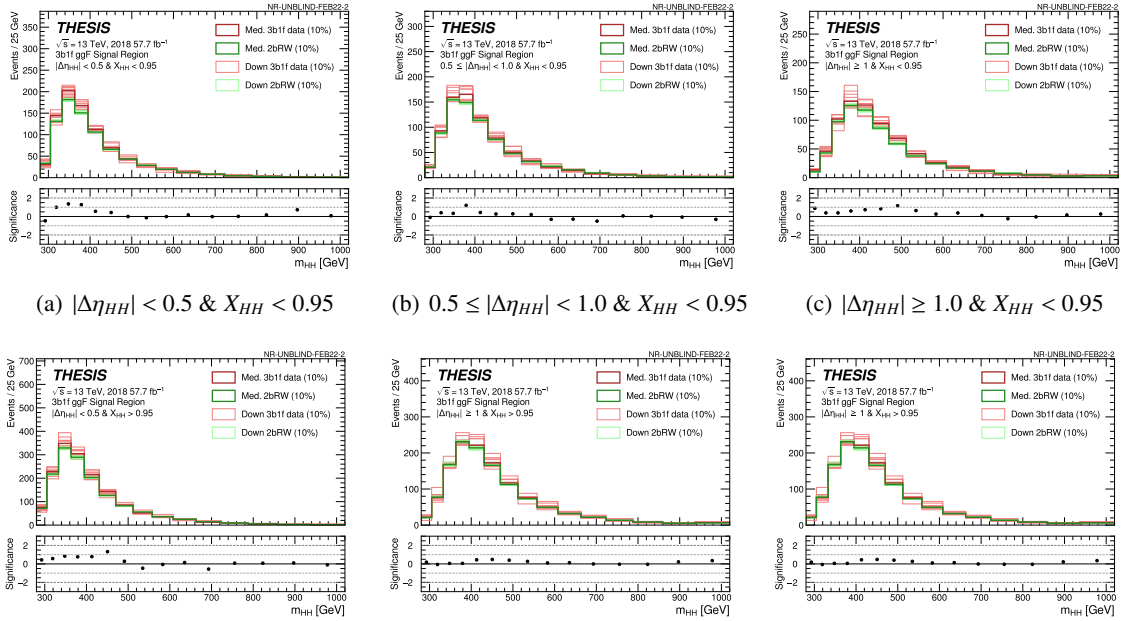

(a) $|\Delta\eta_{HH}| < 0.5$ & $X_{HH} < 0.95$ (b) $0.5 \leq |\Delta\eta_{HH}| < 1.0$ & $X_{HH} < 0.95$ (c) $|\Delta\eta_{HH}| \geq 1.0$ & $X_{HH} < 0.95$

(d) $|\Delta\eta_{HH}| < 0.5$ & $X_{HH} \geq 0.95$ (e) $0.5 \leq |\Delta\eta_{HH}| < 1.0$ & $X_{HH} \geq 0.95$ (f) $|\Delta\eta_{HH}| \geq 1.0$ & $X_{HH} \geq 0.95$

Figure 8.14 m_{HH} distributions of 3b1f data (red) and the background estimation (green) in the ggF signal region with the X_{HH} and $|\Delta\eta_{HH}|$ categorization in 2018. The thin lines show the 10 downsampled distributions and the thick lines show the median of the 10 downsampled distributions. The under panel shows *significaces* defined in Appendix B from the median distributions.

3b1f's VBF Results

Figure 8.15 shows the same information in the VBF signal region with the VBF categorization. In the VBF region, very good closure is observed. Therefore, no additional uncertainty is added for the VBF channel.

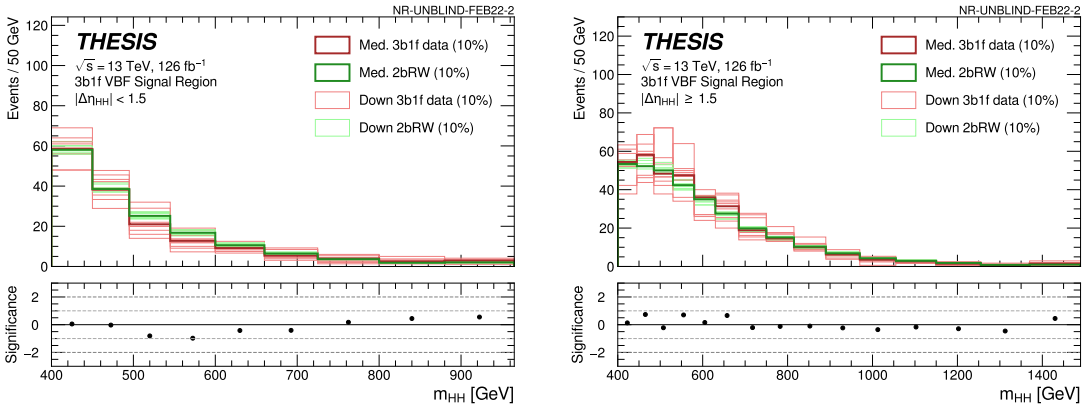

(a) $|\Delta\eta_{HH}| < 1.5$ (b) $1.5 \leq |\Delta\eta_{HH}|$

Figure 8.15 m_{HH} distributions of 3b1f data (red) and the background estimation (green) in the VBF signal region with the $|\Delta\eta_{HH}|$ categorization. The thin lines show the 10 downsampled distributions and the thick lines show the median of the 10 downsampled distributions. The under panel shows *significaces* defined in Appendix B from the median distributions.

8.2.3 Reversed-$\Delta\eta$ data

The reversed-$|\Delta\eta_{HH}|$ region, where inverted QCD veto cut ($|\Delta\eta_{HH}| > 1.5$) is applied instead of the nominal cut, is also useful to validate the background modelling for the ggF channel. As described in Section 6.4.4, the ggF selection imposes a $|\Delta\eta_{HH}| < 1.5$ cut to suppress QCD multijet background. On the other hand, the reversed-$|\Delta\eta_{HH}|$ region has enriched QCD multijet background events as described in Table 8.4. It allows assessing the background modelling as same as the 3b1f region. However, this validation can not be performed in the VBF channel, because the VBF selection doesn't impose the QCD veto cut.

Table 8.4 Signal and data yields in reversed-$|\Delta\eta_{HH}|$ ggF signal regions.

Year	SM ggF HH	SM VBF HH	4b reversed-$|\Delta\eta_{HH}|$ data
16	1.19	0.09	4424
17	1.92	0.13	5692
18	2.80	0.20	10421

In this reversed-$|\Delta\eta_{HH}|$ validation, the standard methodology of the background estimation is performed with 4b events replaced by 4b reversed-$|\Delta\eta_{HH}|$ events. The distributions of 4b reversed-$|\Delta\eta_{HH}|$ data and the background estimation for the variables used to discriminate the ggF channel are shown in Figure 8.16. To validate the background modelling with the ggF categorization, I choose the $|\Delta\eta_{HH}|$ boundary for the reversed-$|\Delta\eta_{HH}|$ validation to keep equal statistics between the categories as below:

- $1.5 \leq |\Delta\eta_{HH}| < 2.5$
- $2.5 \leq |\Delta\eta_{HH}| < 3.6$
- $3.6 \leq |\Delta\eta_{HH}|$

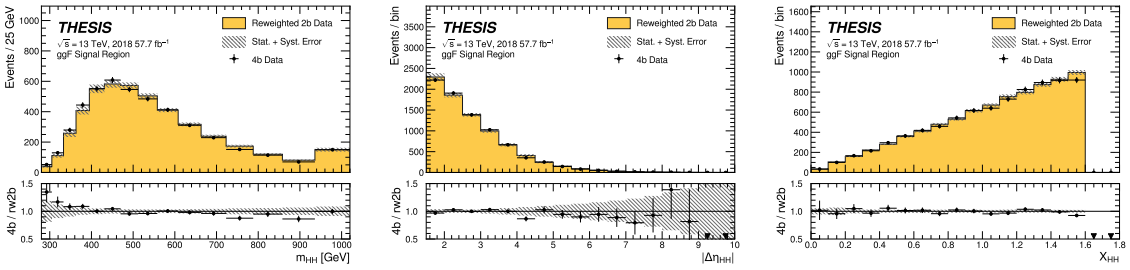

(a) m_{HH} (b) $|\Delta\eta_{HH}|$ (c) X_{HH}

Figure 8.16 The discriminating variables, (a) m_{HH}, (b) $|\Delta\eta_{HH}|$ and (c) X_{HH}, distributions of 4b reversed-$|\Delta\eta_{HH}|$ data (black dots) and the background estimation (yellow histograms) for the ggF channel in 2018.

Reversed-$|\Delta\eta_{HH}|$ ggF Results

Figure 8.17, 8.18 and 8.19 show the m_{HH} distributions of 4b reversed-$|\Delta\eta_{HH}|$ data and the background estimation in the reversed-$|\Delta\eta_{HH}|$ signal regions with the tentative $|\Delta\eta_{HH}|$ and X_{HH} categorization. The background estimation uncertainties include 2b poisson statistic uncertainty, bootstrap uncertainty, and CR1 versus CR2 shape uncertainty (see Section 9). As can be seen, the background estimation is consistent with the 4b reversed-$|\Delta\eta_{HH}|$ data, and the uncertainties fully cover any differences between them. Therefore, good closure is observed and the background modelling performance is validated in the reversed-$|\Delta\eta_{HH}|$ validation.

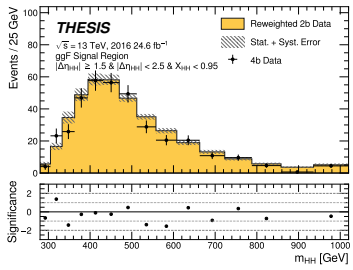

(a) $1.5 \leq |\Delta\eta_{HH}| < 2.5$ & $X_{HH} < 0.95$

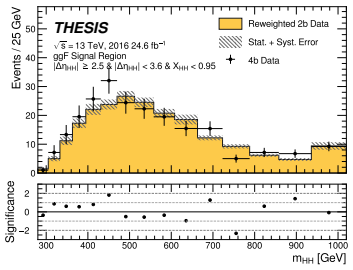

(b) $2.5 \leq |\Delta\eta_{HH}| < 3.6$ & $X_{HH} < 0.95$

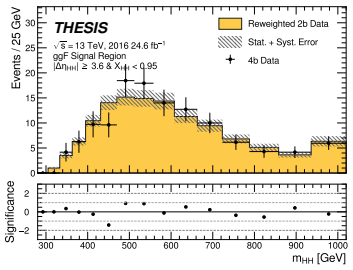

(c) $3.6 \leq |\Delta\eta_{HH}|$ & $X_{HH} < 0.95$

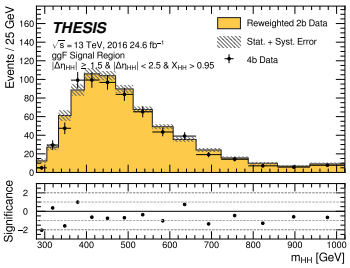

(d) $1.5 \leq |\Delta\eta_{HH}| < 2.5$ & $X_{HH} \geq 0.95$

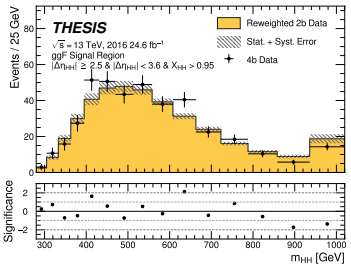

(e) $2.5 \leq |\Delta\eta_{HH}| < 3.6$ & $X_{HH} \geq 0.95$

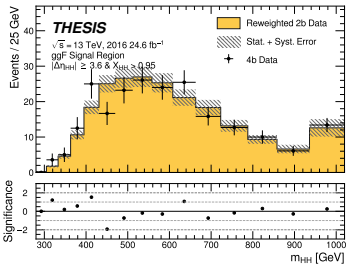

(f) $3.6 \leq |\Delta\eta_{HH}|$ & $X_{HH} \geq 0.95$

Figure 8.17 m_{HH} distributions of 4b reversed-$|\Delta\eta_{HH}|$ data (shown by the black dots) and the background estimation (shown by the yellow histograms) in the ggF signal region in 2016.

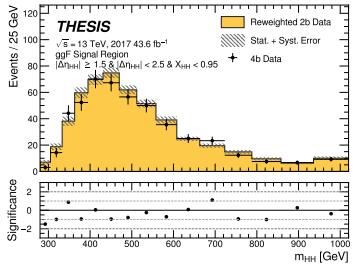

(a) $1.5 \leq |\Delta\eta_{HH}| < 2.5$ & $X_{HH} < 0.95$

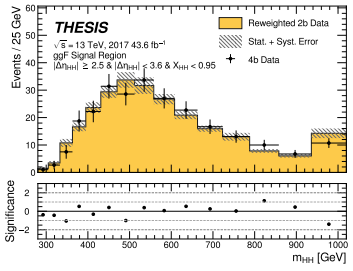

(b) $2.5 \leq |\Delta\eta_{HH}| < 3.6$ & $X_{HH} < 0.95$

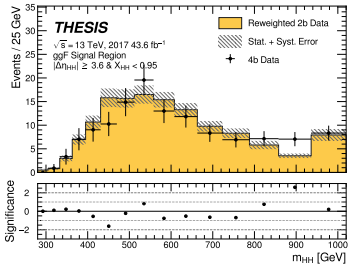

(c) $3.6 \leq |\Delta\eta_{HH}|$ & $X_{HH} < 0.95$

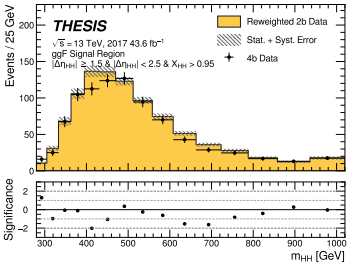

(d) $1.5 \leq |\Delta\eta_{HH}| < 2.5$ & $X_{HH} \geq 0.95$

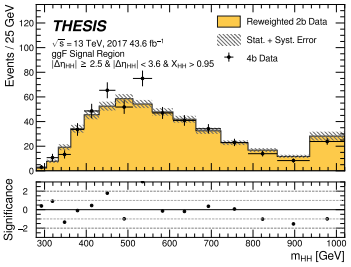

(e) $2.5 \leq |\Delta\eta_{HH}| < 3.6$ & $X_{HH} \geq 0.95$

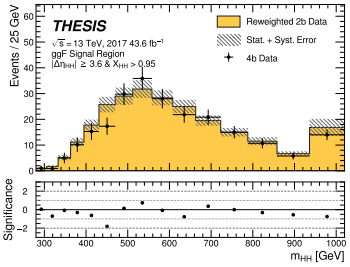

(f) $3.6 \leq |\Delta\eta_{HH}|$ & $X_{HH} \geq 0.95$

Figure 8.18 m_{HH} distributions of 4b reversed-$|\Delta\eta_{HH}|$ data (shown by the black dots) and the background estimation (shown by the yellow histograms) in the ggF signal region in 2017.

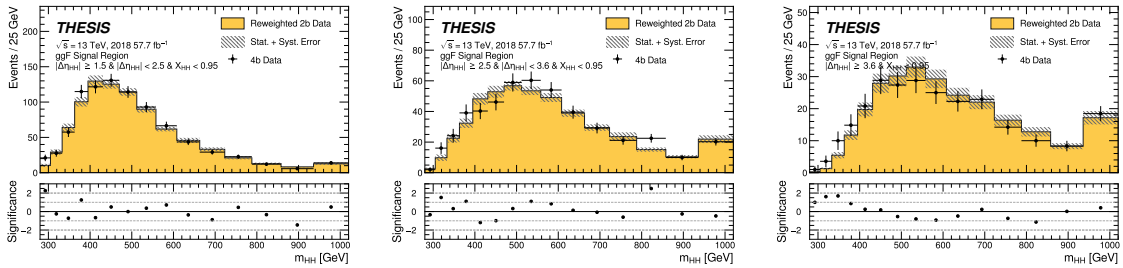

(a) $1.5 \leq |\Delta\eta_{HH}| < 2.5$ & $X_{HH} < 0.95$ (b) $2.5 \leq |\Delta\eta_{HH}| < 3.6$ & $X_{HH} < 0.95$ (c) $3.6 \leq |\Delta\eta_{HH}|$ & $X_{HH} < 0.95$

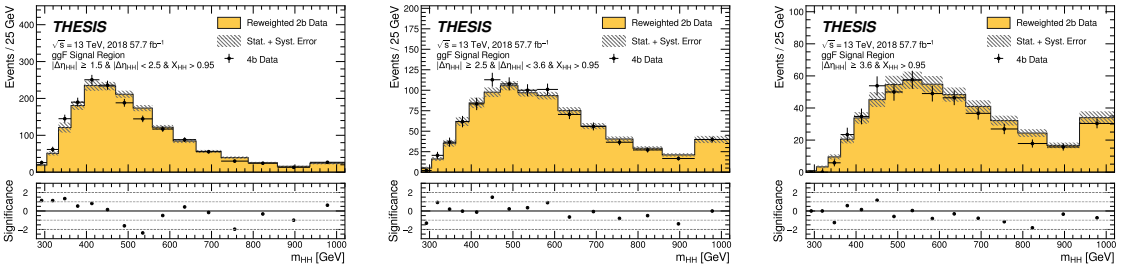

(d) $1.5 \leq |\Delta\eta_{HH}| < 2.5$ & $X_{HH} \geq 0.95$ (e) $2.5 \leq |\Delta\eta_{HH}| < 3.6$ & $X_{HH} \geq 0.95$ (f) $3.6 \leq |\Delta\eta_{HH}|$ & $X_{HH} \geq 0.95$

Figure 8.19 m_{HH} distributions of 4b reversed-$|\Delta\eta_{HH}|$ data (shown by the black dots) and the background estimation (shown by the yellow histograms) in the ggF signal region in 2018.

8.2.4 Monte Carlo Samples

The two primary sources of background in this analysis are QCD multijet and $t\bar{t}$. To ensure that the Neural Network used to derive the data-driven background estimate was accurately modelling these background contributions, QCD multijet and $t\bar{t}$ MC simulation was supplied in place of the data when assessing the neural network model. The neural network used in this validation was trained on data. Although the MC modelling is poor, this is a nice way to check that the neural network model trained on data and actually used in the signal region properly works. This validation is performed only on the ggF channel without the ggF categorization because of the statistical limitations of the MC samples.

MC's ggF Results

Figure 8.20 shows the m_{HH} distributions of 4b simulated events and the reweighted 2b simulated events in the inclusive ggF signal region. The error band shows 2b poisson statistic uncertainty, bootstrap uncertainty, and the CR12 shape uncertainty. Instead of applying the ggF categorization, the discriminant variables $|\Delta\eta_{HH}|$ and X_{HH} are also checked, as can be seen in Figure 8.20. Though there is a bit of fluctuation of the 4b events due to the poor statistic, good agreements between 4b simulated events and reweighted 2b simulated events on these kinematic variables in the signal regions are observed.

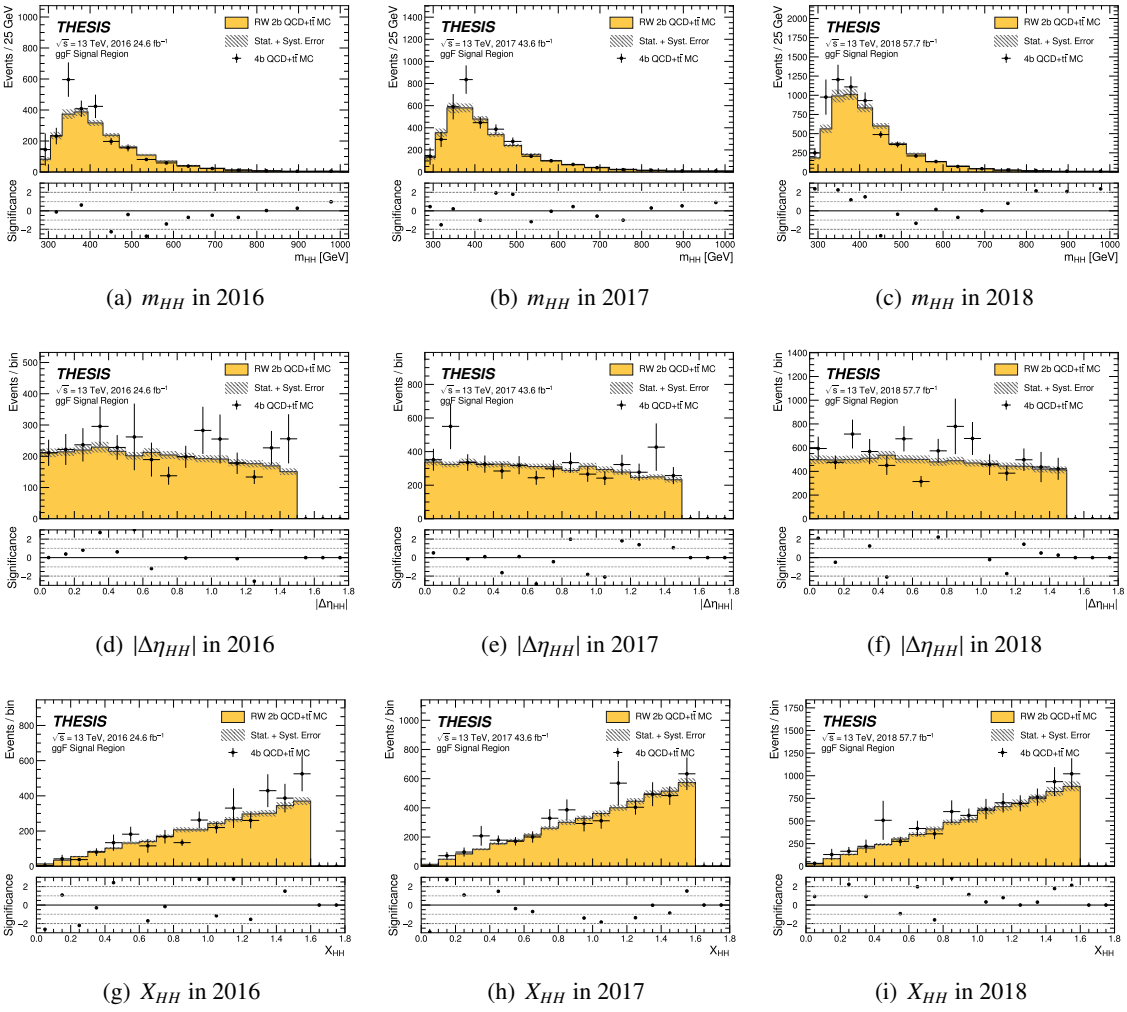

(a) m_{HH} in 2016 (b) m_{HH} in 2017 (c) m_{HH} in 2018

(d) $|\Delta\eta_{HH}|$ in 2016 (e) $|\Delta\eta_{HH}|$ in 2017 (f) $|\Delta\eta_{HH}|$ in 2018

(g) X_{HH} in 2016 (h) X_{HH} in 2017 (i) X_{HH} in 2018

Figure 8.20 m_{HH}, $|\Delta\eta_{HH}|$ and X_{HH} distributions of $4b$ events (shown by the black dots) and the background estimation (shown by the yellow histograms) in Monte Carlo simulation in the ggF signal region in 2016.

Following these validation studies, I confirmed that the fully data-driven background estimation using the neural network reweighting works well in this analysis. Consequently, the most important issue in this analysis is resolved.

Chapter 9

Systematic Uncertainties

There are systematic biases in the background modelling and the signal modelling in the analysis. These known biases are accounted for as systematic uncertainties. In this section, systematic uncertainties for the background modelling and the signal modelling are discussed.

9.1 Background Modelling Uncertainties

For the background estimation described in Section 8, I assess several background modelling uncertainties to consider any impacts of neural network training and reweighting conditions:

- Standard poisson error of 2b data in the signal region
- Initial conditions of neural networks and limited size of the training samples
- Kinematic differences between the control region 1 and signal region
- Extrapolation from 2b events to another b-tagged events discussed in Section 8.2.2.

In this section, the background modelling uncertainties are described.

9.1.1 2b Poisson and Bootstrap Statistic Uncertainty

There are two components to the statistical error for the neural network background estimation. The first one is standard poisson error of the 2b data in the signal region. The 2b poisson error Δn_i is calculated by

$$\Delta n_i = \sqrt{\sum_{j \in i} w_j^2}, \tag{9.1}$$

where i indicates a given bin in the background histogram and w_j is the weight for an event j which is located at bin i.

However, this does not take into account the statistical uncertainty for w_j itself. w_j should be also fluctuated due to neural network initial conditions and the training samples in the control region 1 (CR1). Due to the large size different between the 2b data and 4b data, the impact of the 4b statistics dominates on it.

The bootstrap resampling technique [112] is used to estimate this uncertainty. In the technique, a set of statistically equivalent training samples is constructed by sampling with replacement from the original

training sample. A set of neural networks is trained on each of the bootstrapped samples, resulting in a set of background predictions being provided. In this analysis, total 100 bootstrapped samples are constructed and 100 background predictions are provided. Figure 9.1, 9.2, 9.3 and 9.4 show the ratio of a background prediction with each single bootstrapped sample to the nominal background prediction in the ggF and VBF signal regions. As described in Section 8, the nominal background prediction uses the mean of 100 background predictions. To take into account the statistical uncertainty for the weights, the standard deviation of 100 background predictions is obtained as the bootstrap statistical uncertainty. The bootstrap statistical uncertainty in m_{HH} distribution is shown in Figure 9.1, 9.2 and 9.3 for the ggF signal regions and in Figure 9.4 for the VBF signal regions. These two uncertainties are combined quadratically at bin-by-bin.

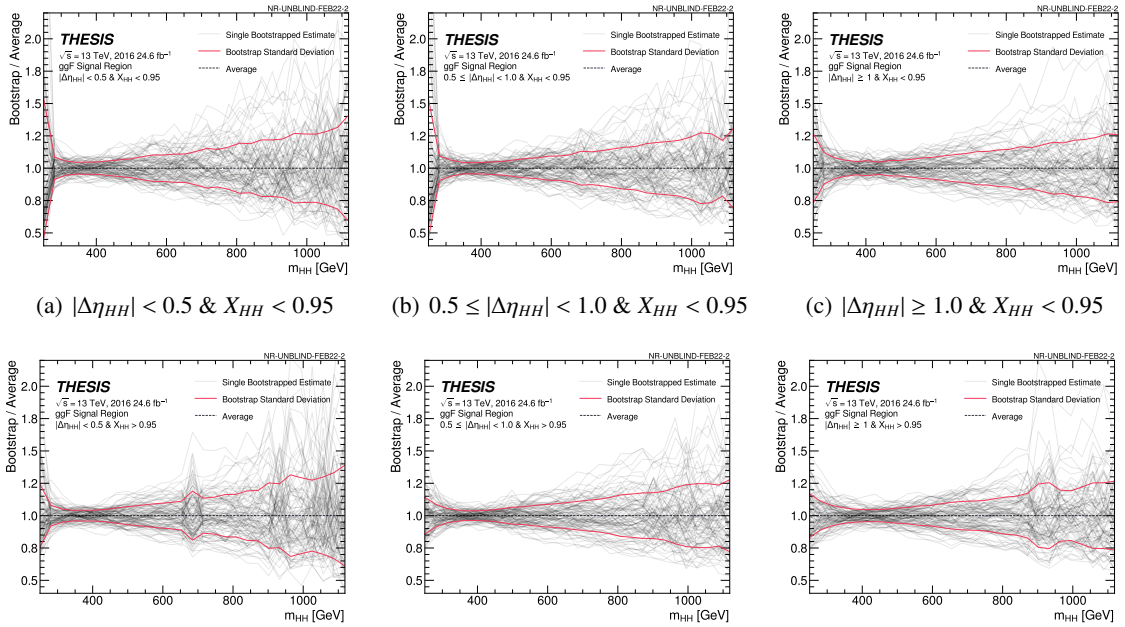

(a) $|\Delta\eta_{HH}| < 0.5$ & $X_{HH} < 0.95$ (b) $0.5 \leq |\Delta\eta_{HH}| < 1.0$ & $X_{HH} < 0.95$ (c) $|\Delta\eta_{HH}| \geq 1.0$ & $X_{HH} < 0.95$

(d) $|\Delta\eta_{HH}| < 0.5$ & $X_{HH} \geq 0.95$ (e) $0.5 \leq |\Delta\eta_{HH}| < 1.0$ & $X_{HH} \geq 0.95$ (f) $|\Delta\eta_{HH}| \geq 1.0$ & $X_{HH} \geq 0.95$

Figure 9.1 Bootstrap statistical uncertainty in m_{HH} distribution in the ggF signal region with the ggF categorization in 2016. Each gray line is the ratio of a background prediction with a single bootstrapped sample and the nominal background prediction, and the red line shows the standard deviation of 100 bootstrapped background predictions.

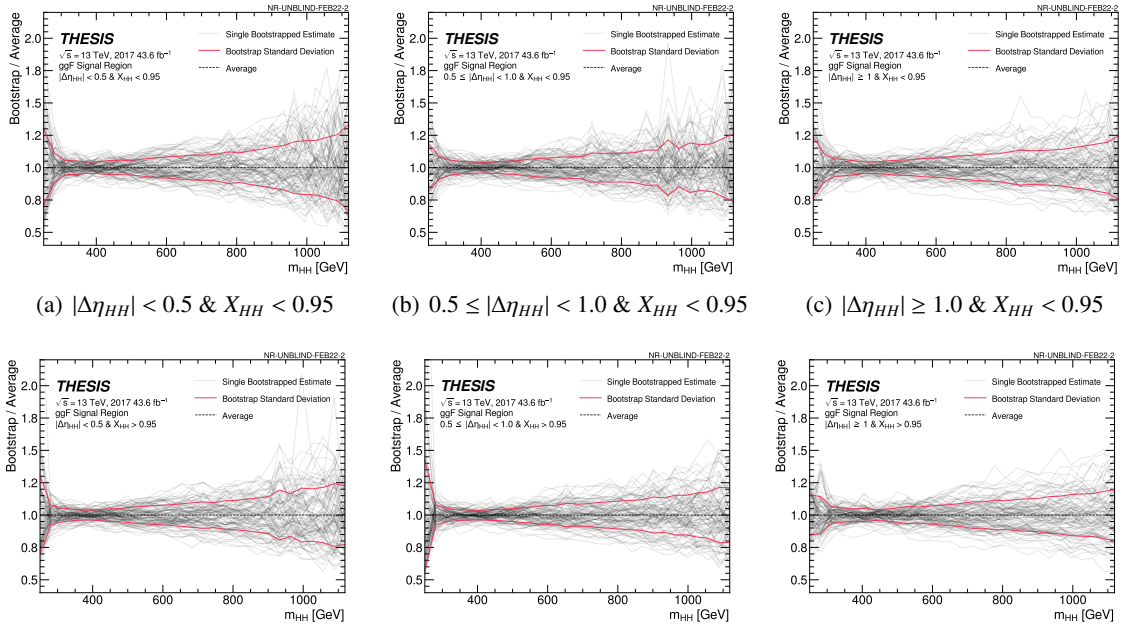

(a) $|\Delta\eta_{HH}| < 0.5$ & $X_{HH} < 0.95$ (b) $0.5 \leq |\Delta\eta_{HH}| < 1.0$ & $X_{HH} < 0.95$ (c) $|\Delta\eta_{HH}| \geq 1.0$ & $X_{HH} < 0.95$

(d) $|\Delta\eta_{HH}| < 0.5$ & $X_{HH} \geq 0.95$ (e) $0.5 \leq |\Delta\eta_{HH}| < 1.0$ & $X_{HH} \geq 0.95$ (f) $|\Delta\eta_{HH}| \geq 1.0$ & $X_{HH} \geq 0.95$

Figure 9.2 Bootstrap statistical uncertainty in m_{HH} distribution in the ggF signal region with the ggF categorization in 2017. Each gray line is the ratio of a background prediction with a single bootstrapped sample and the nominal background prediction, and the red line shows the standard deviation of 100 bootstrapped background predictions.

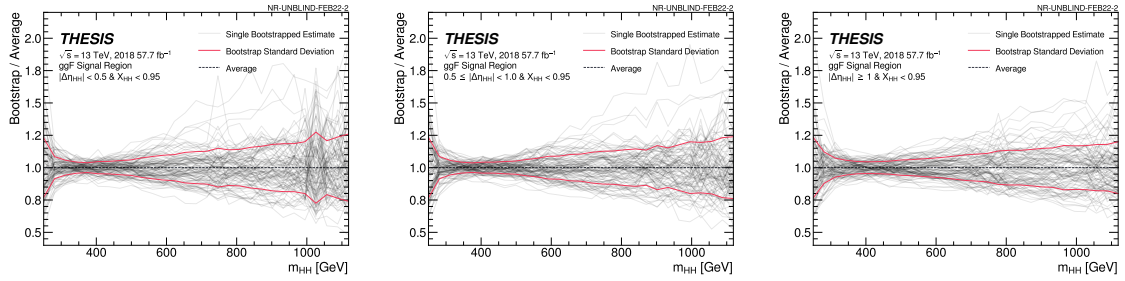

(a) $|\Delta\eta_{HH}| < 0.5$ & $X_{HH} < 0.95$ (b) $0.5 \leq |\Delta\eta_{HH}| < 1.0$ & $X_{HH} < 0.95$ (c) $|\Delta\eta_{HH}| \geq 1.0$ & $X_{HH} < 0.95$

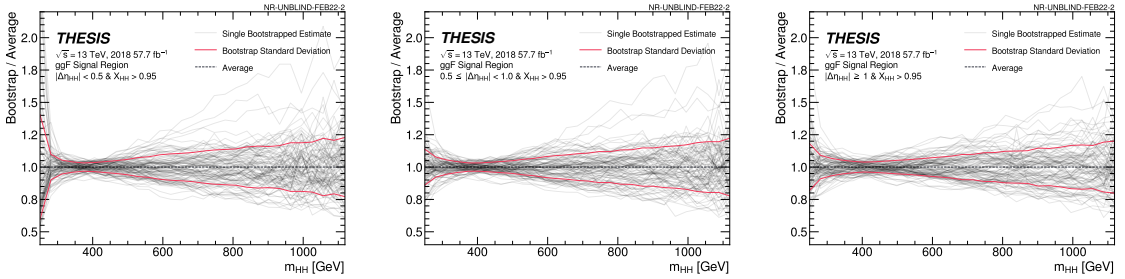

(d) $|\Delta\eta_{HH}| < 0.5$ & $X_{HH} \geq 0.95$ (e) $0.5 \leq |\Delta\eta_{HH}| < 1.0$ & $X_{HH} \geq 0.95$ (f) $|\Delta\eta_{HH}| \geq 1.0$ & $X_{HH} \geq 0.95$

Figure 9.3 Bootstrap statistical uncertainty in m_{HH} distribution in the ggF signal region with the ggF categorization in 2018. Each gray line is the ratio of a background prediction with a single bootstrapped sample and the nominal background prediction, and the red line shows the standard deviation of 100 bootstrapped background predictions.

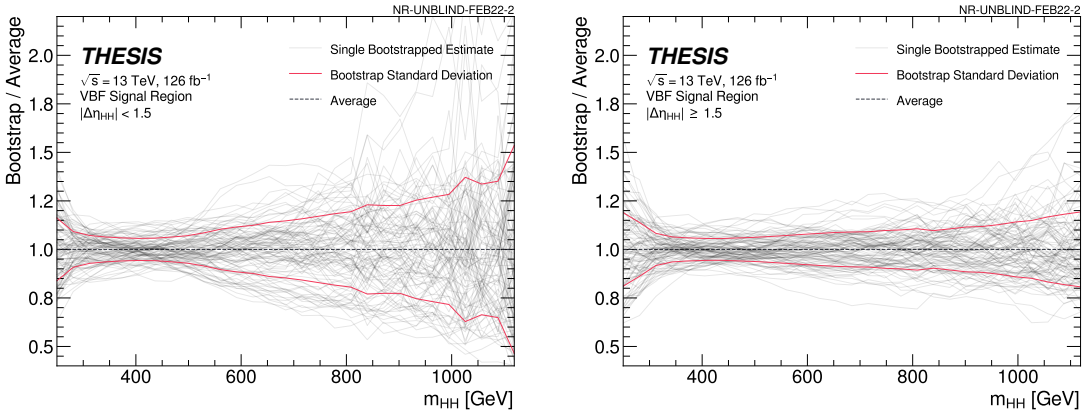

(a) $|\Delta\eta_{HH}| < 1.5$ (b) $1.5 \leq |\Delta\eta_{HH}|$

Figure 9.4 Bootstrap statistical uncertainty in m_{HH} distribution in the VBF signal region with the VBF categorization. Each gray line is the ratio of a background prediction with a single bootstrapped sample and the nominal background prediction, and the red line shows the standard deviation of 100 bootstrapped background predictions.

9.1.2 CR12 Shape Systematic Uncertainty

There is a systematic bias in deriving the reweighting function in Control Region 1 (CR1) and extrapolating to Signal Region (SR). To take into account the systematic bias, an alternative background model is derived in Control Region 2 (CR2). CR2 is the other pair of quadrants defined around the SR. To aid in deriving an uncertainty, the SR is split into quadrants as shown in Figure 9.5. The four sectors are defined to be approximately equal area, and the angle of alignment is set to match the one used to define the quadrants for CR1 and CR2. The four SR quadrants are referred to as Q_N (north), Q_S (south), Q_E (east) and Q_W (west), where Q is the short name of quadrant and cardinal points are their relative positions in the m_{H1} and m_{H2} plane. The way of splitting into the four quadrants allows the systematic uncertainty to naturally follow the kinematic similarity of the adjacent CR quadrant. In addition, it can introduce more degrees of freedom to the fit for the final results described in Chapter 10.

The systematic uncertainty, referred to as the CR12 shape systematic uncertainty, is derived by taking a difference between the nominal background estimation and the alternative background estimation. The nominal background estimation is derived by applying weights derived in CR1 to all four SR quadrants. The alternative background estimation is derived by applying weights in CR1 to three SR quadrants and weights in CR2 to the other one. For example, an alternative background estimation for Q_N is derived by applying CR1-derived weights to Q_S, Q_E and Q_W and CR2-derived weights to Q_N. The CR12 shape systematic uncertainty is made two-sided by symmetrizing the difference around the nominal background estimation. The symmetrized difference between the nominal and alternative background estimation, which corresponds to the CR12 shape systematic uncertainty, in the ggF channel is shown in Figure 9.6, 9.8 and 9.8. The same information in the VBF channel is shown in Figure 9.9. Nuisance parameters for the background shape systematic uncertainties are labeled as *alpha_CR12_shape_{E,N,S,W}_{ggf,vbf}_{16,17,18}*. For example, *alpha_CR12_shape_E_ggf_16* stands

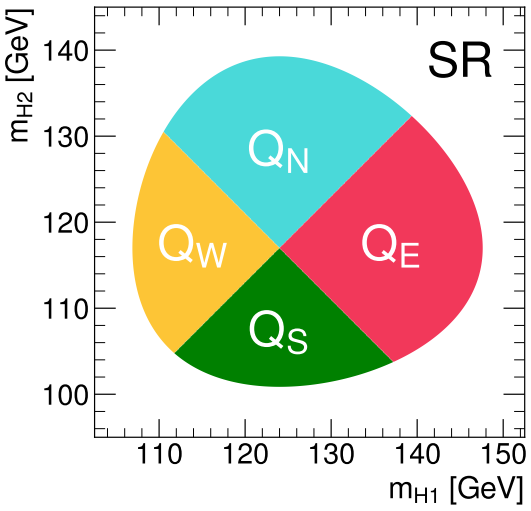

Figure 9.5 A visualization of the signal region quadrants to derive four nuisance parameters of background estimation variation in the m_{H1} and m_{H2} plane.

for the background shape systematic uncertainty on the east quad in 2016 for the ggF channel.

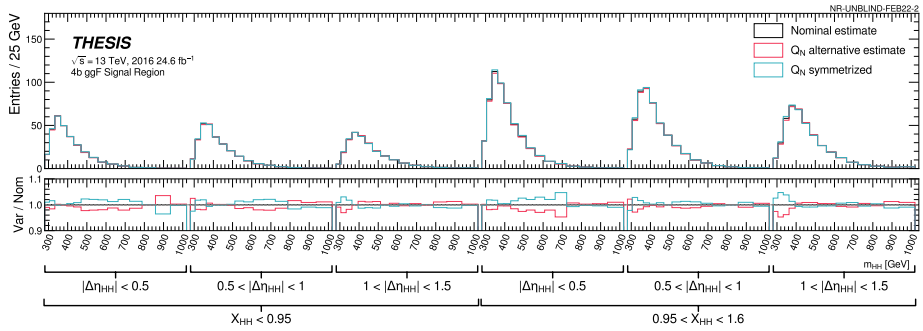

(a) Q_N

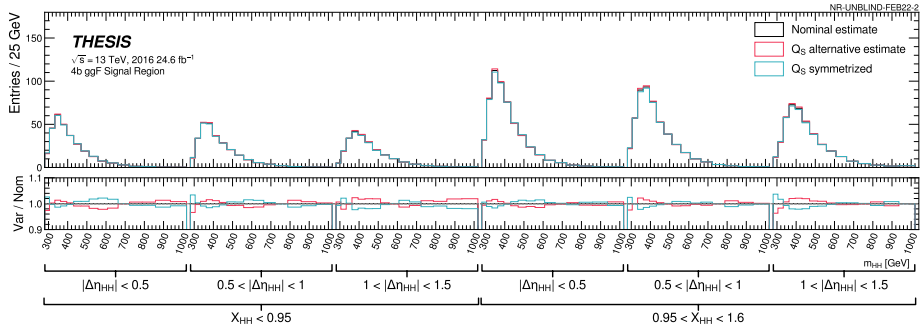

(b) Q_S

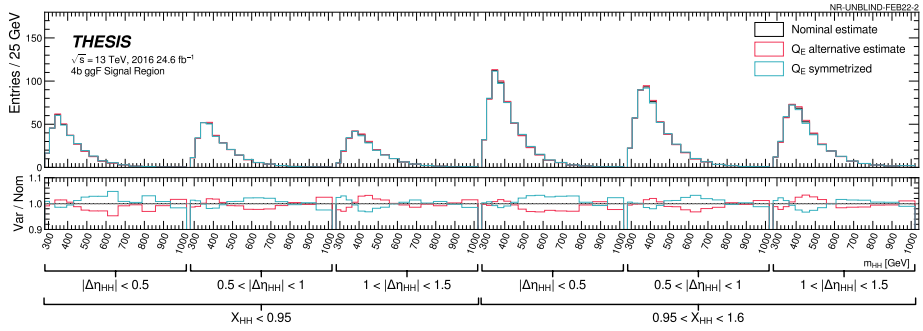

(c) Q_E

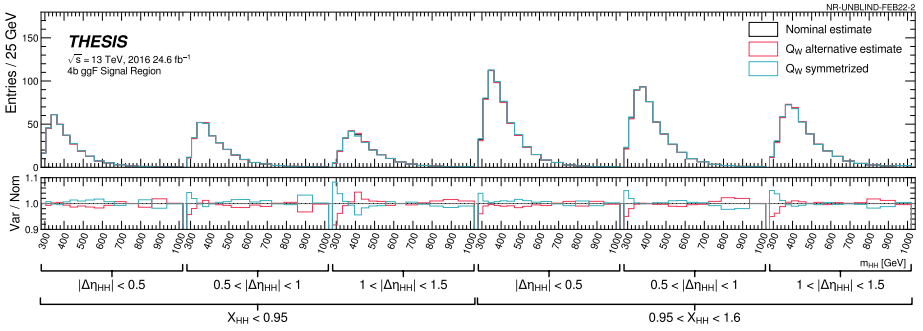

(d) Q_W

Figure 9.6 Quadrant decompositions of the CR12 shape systematic uncertainty in the ggF signal regions in 2016. The black, red and blue histograms indicate the nominal, alternative and symmetrized alternative background estimations, respectively. The under panel shows the ratio of the alternative background estimation to the nominal background estimation. Q_N (north), Q_S (south), Q_E (east) and Q_W (west) indicate the SR quadrants with their relative positions.

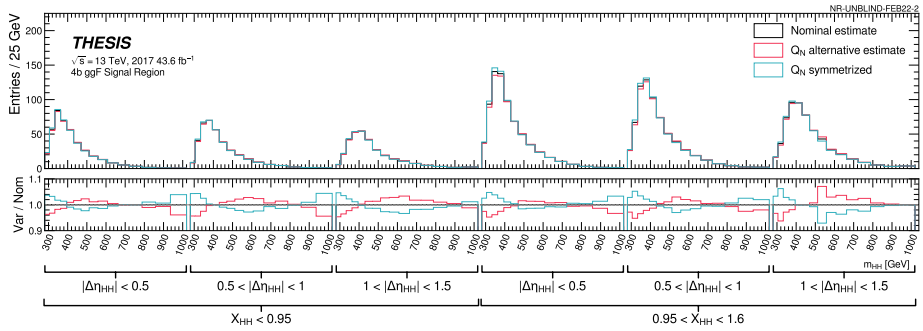

(a) Q_N

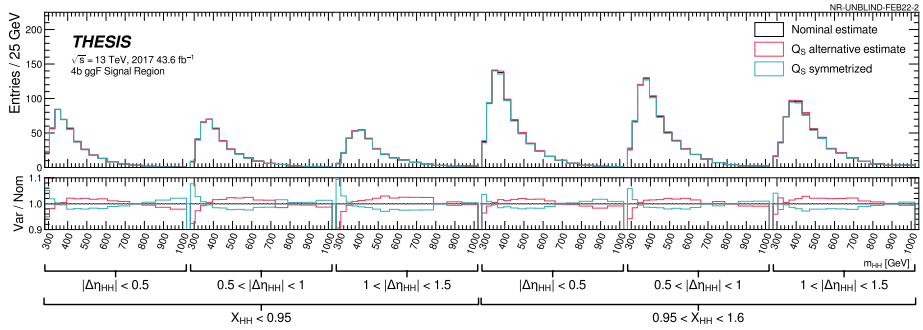

(b) Q_S

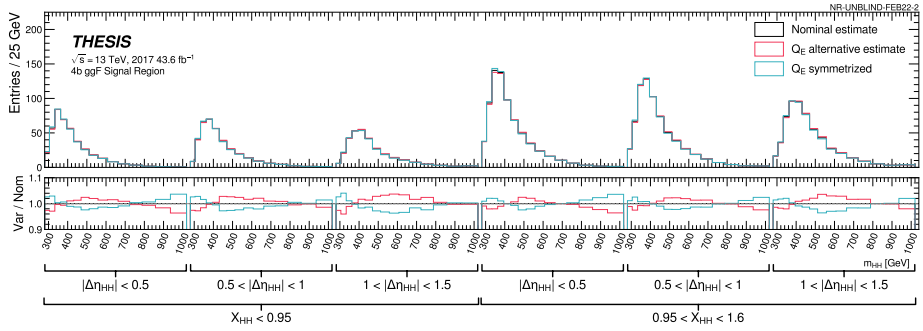

(c) Q_E

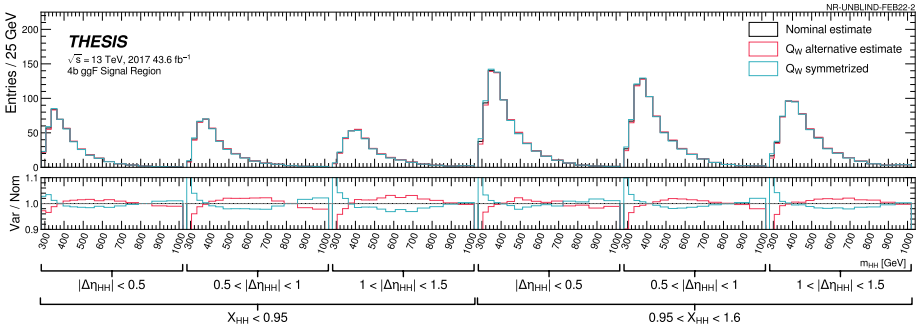

(d) Q_W

Figure 9.7 Quadrant decompositions of the CR12 shape systematic uncertainty in the ggF signal regions in 2017. The black, red and blue histograms indicate the nominal, alternative and symmetrized alternative background estimations, respectively. The under panel shows the ratio of the alternative background estimation to the nominal background estimation.. Q_N (north), Q_S (south), Q_E (east) and Q_W (west) indicate the SR quadrants with their relative positions.

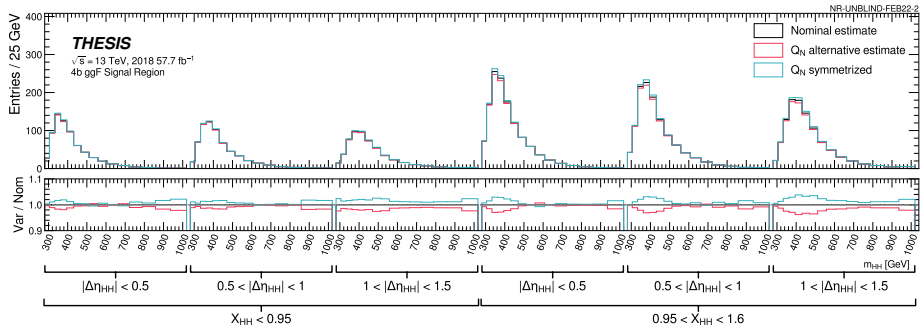

(a) Q_N

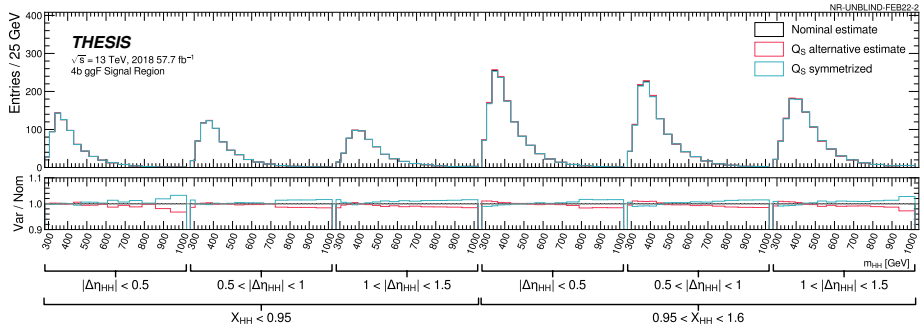

(b) Q_S

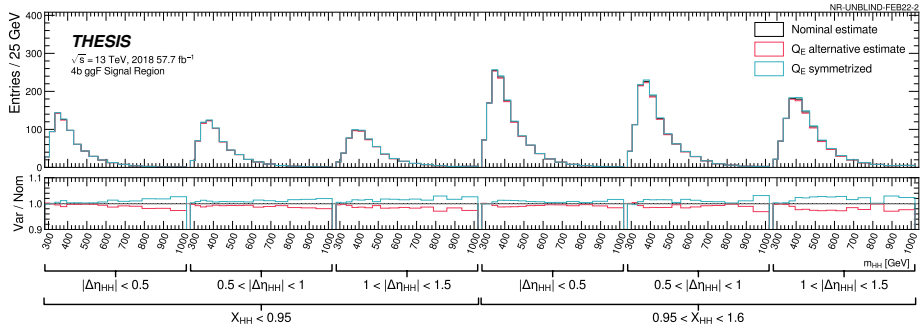

(c) Q_E

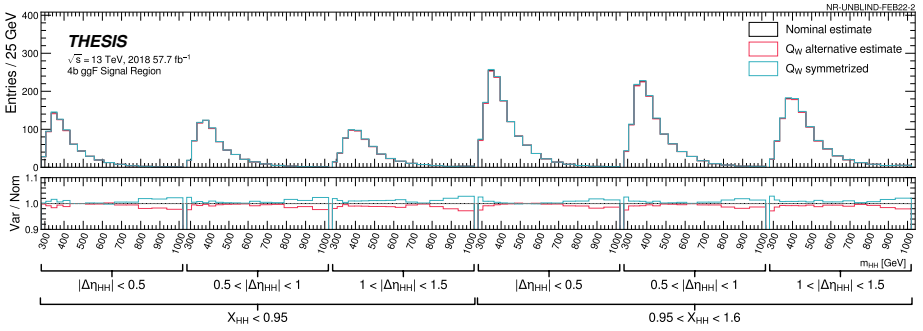

(d) Q_W

Figure 9.8 Quadrant decompositions of the CR12 shape systematic uncertainty in the ggF signal regions in 2018. The black, red and blue histograms indicate the nominal, alternative and symmetrized alternative background estimations, respectively. The under panel shows the ratio of the alternative background estimation to the nominal background estimation. Q_N (north), Q_S (south), Q_E (east) and Q_W (west) indicate the SR quadrants with their relative positions.

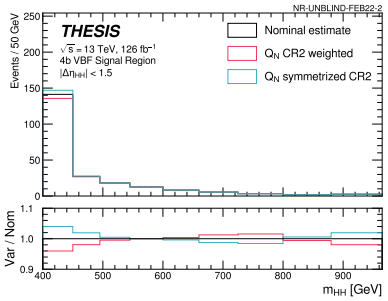

(a) Q_N in $|\Delta\eta_{HH}| < 1.5$

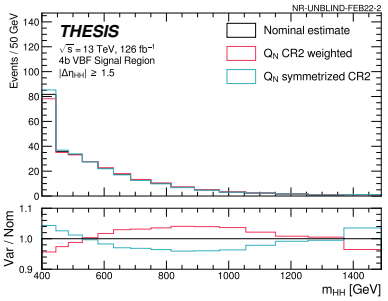

(b) Q_N in $|\Delta\eta_{HH}| \geq 1.5$

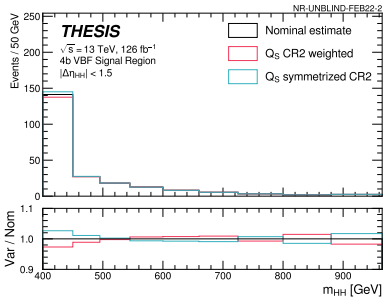

(c) Q_S in $|\Delta\eta_{HH}| < 1.5$

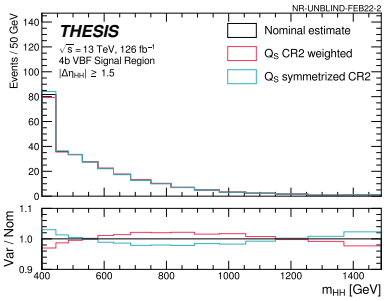

(d) Q_S in $|\Delta\eta_{HH}| \geq 1.5$

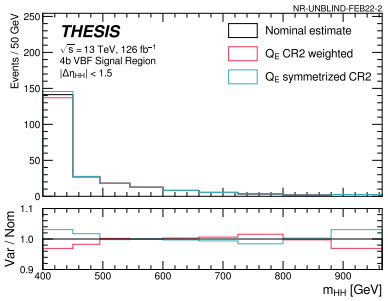

(e) Q_E in $|\Delta\eta_{HH}| < 1.5$

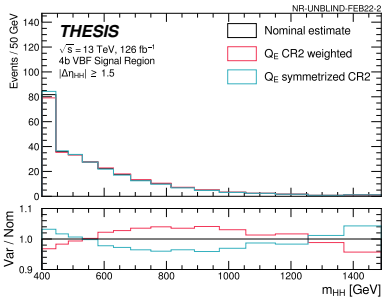

(f) Q_E in $|\Delta\eta_{HH}| \geq 1.5$

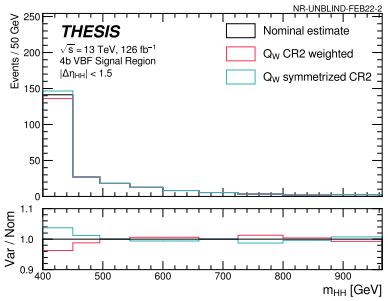

(g) Q_W in $|\Delta\eta_{HH}| < 1.5$

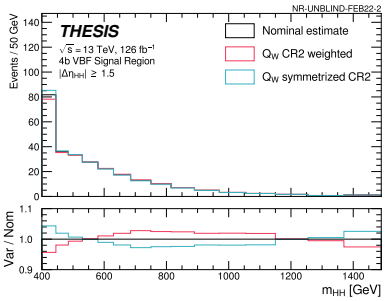

(h) Q_W in $|\Delta\eta_{HH}| \geq 1.5$

Figure 9.9 Quadrant decompositions of the CR12 shape systematic uncertainty in the VBF signal regions. The black, red and blue histograms indicate the nominal, alternative and symmetrized alternative background estimations, respectively. The under panel shows the ratio of the alternative background estimation to the nominal background estimation. Q_N (north), Q_S (south), Q_E (east) and Q_W (west) indicate the SR quadrants with their relative positions.

9.1.3 3b1f Non-Closure Systematic Uncertainty

An additional systematic uncertainty due to the 3b1f non-closure is added for the ggF channel. As discussed in Section 8.2.2, a small deviation between the 3b1f data and the background estimation is observed in the ggF channel in the 3b1f validation. To take into account the non-closure, the 3b1f non-closure systematic uncertainty is derived as follows:

1. Take a ratio of the 3b1f data and the background estimation at bin-by-bin of m_{HH} distribution.
2. If the deviation is not covered by the quadratic sum of the background estimation uncertainties (the 2b poisson statistical uncertainty, the bootstrap statistical uncertainty and the CR12 shape systematic uncertainty) and the 3b1f statistical uncertainty in the bin, the residual is taken.
3. To reduce the statistical fluctuations in bins, the residuals are smoothed by averaging each bin with its neighboring bins.
4. The smoothed residuals are taken as the 3b1f non-closure systematic uncertainty.

In the 3b1f validation, the downsampled background estimations were used. On the other hand, the full statistics background estimation is used to derive the 3b1f non-closure systematic uncertainty, because it's more straightforward than using the downsamples. The difference between the full statistics background estimation and the downsampled background estimation is much smaller so that we can obtain reasonable values in either way. Nuisance parameters for the 3b1f non-closure systematic uncertainty are labeled as *alpha_NC_3b1f_ggf_{16,17,18}*.

Figure 9.10 shows the 3b1f non-closure systematic uncertainty in the ggF signal regions. The impact of the 3b1f non-closure systematic uncertainty is much smaller on the sensitivity than the other background uncertainties.

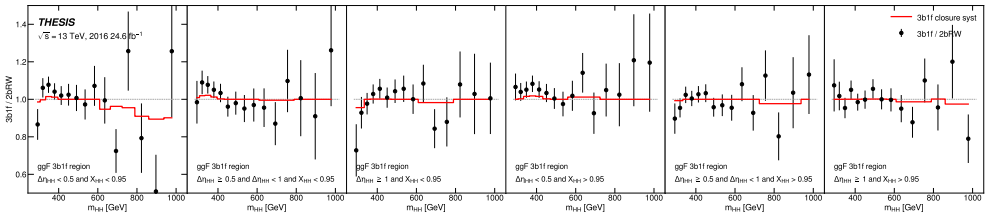

(a) 2016

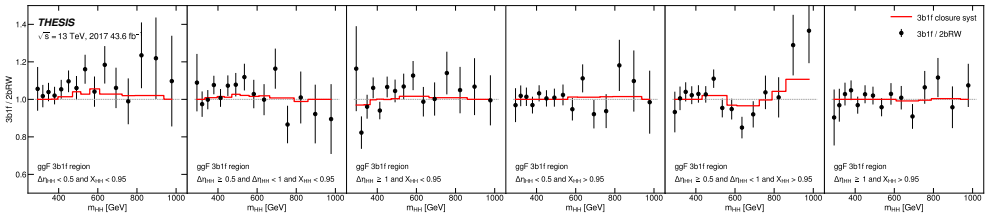

(b) 2017

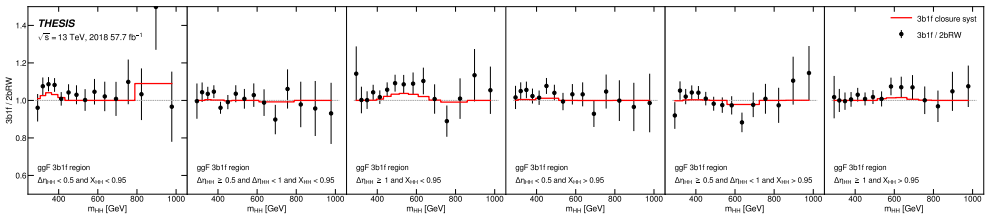

(c) 2018

Figure 9.10 Raio of 3b1f and background estimation (shown by the black points) and the 3b1f non-closure systematic uncertainty (shown by the red line) at m_{HH} distribution in the ggF signal region with the ggF categorization.

9.1.4 Summary of Background Modelling Uncertainties

Figure 9.11 and 9.12 show the magnitudes of the background modelling uncertainties in the ggF channel and in the VBF channel. The 2b poisson uncertainty is negligible relative to the bootstrap statistical uncertainty, and the statistical uncertainty dominates for higher m_{HH} region. The CR12 shape systematic uncertainty contributes more in the m_{HH} region that derives the sensitivity.

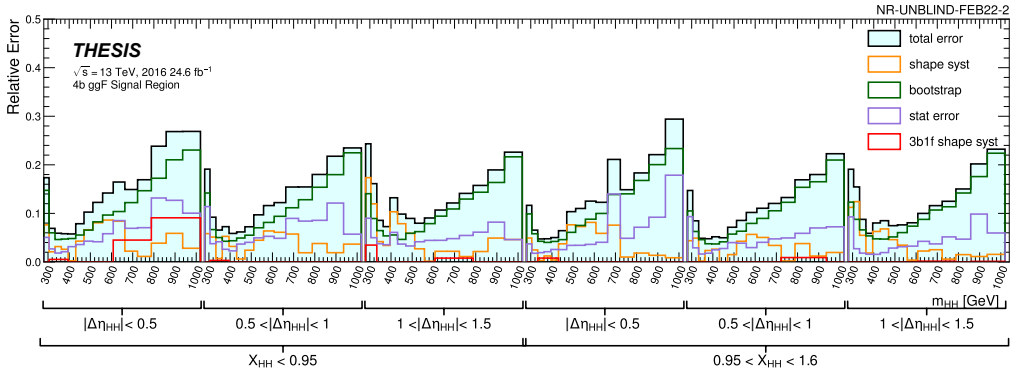

(a) 2016

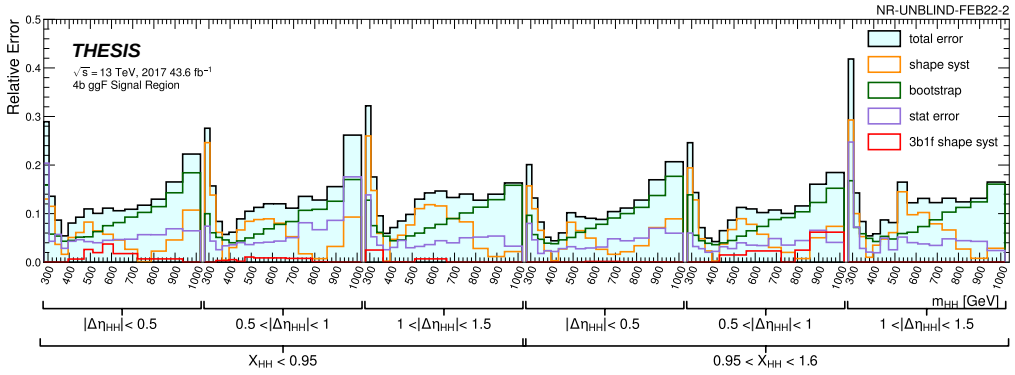

(b) 2017

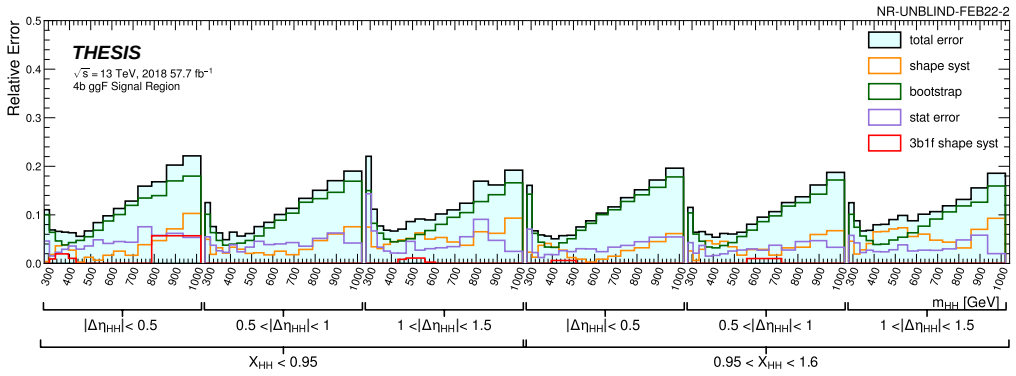

(c) 2018

Figure 9.11 Summary of the background modelling relative uncertainties in the *gg*F channel. The 2b poisson and bootstrap statistic uncertainties are shown by the green and purple histograms, respectively. The CR12 shape systematic uncertainty is shown by the orange histogram. The 3b1f non-closure systematic uncertainty is shown by the red histogram. The total background modelling uncertainty is shown by the light blue histogram.

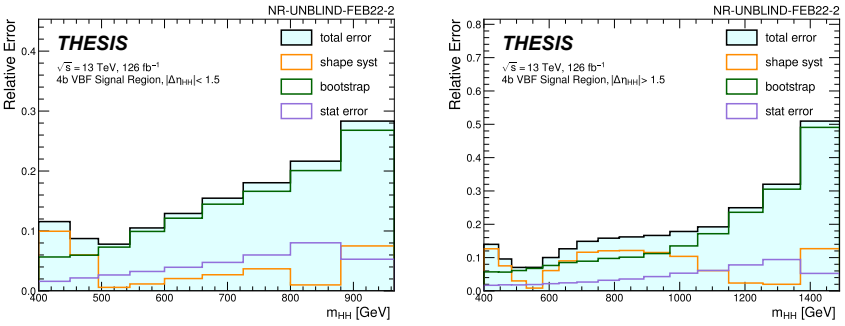

(a) $|\Delta\eta_{HH}| < 1.5$ (b) $|\Delta\eta_{HH}| \geq 1.5$

Figure 9.12 Summary of the background modelling relative uncertainties in the VBF channel. The 2b poisson and bootstrap statistic uncertainties are shown by the green and purple histograms, respectively. The CR12 shape systematic uncertainty is shown by the orange histogram. The total background modelling uncertainty is shown by the light blue histogram.

9.2 Signal Modelling Uncertaities

There are many systematic biases due to mismodellings in simulation. These systematic biases are accounted as systematic uncertainties. Since the backgrounds are estimated by the fully data-driven approach, these systematic uncertainties are considered only in the signal models. These systematic uncertainties can be divided into two categories. One is the experimental uncertainty that is associated with the detector modelling and the object reconstruction. The other one is the theoretical uncertainty arising from the theoretical predictions.

9.2.1 Experimental Uncertainties

The experimental uncertainty takes into account differences between MC simulation and data due to the detector mismodellings and inconsistent performances of the object reconstructions between MC simulation and data. The relevant uncertainties in this analysis are the luminosity uncertainty, the jet-related uncertainties, the b-jet tagging efficiency uncertainty, the b-jet energy correction uncertainty and the trigger uncertainty.

Luminosity uncertainty

The integrated luminosity values are used to scale the signal cross-sections to obtain the expected signal yields in data. An uncertainty of 1.7% is considered to take into account the potential inaccuracy in the integrated luminosity measurement. The uncertainty is derived from the calibration of the luminosity scale using x-y beam-separation scans. This detailed methodology is found in Ref. [113]. The luminosity uncertainty is labelled as *alpha_ATLAS_LUMI_**.

Jet-related uncertainty

Systematic uncertainties associated with the jet reconstruction and calibration are important because of the fully hadronic analysis. There are many jet-related uncertainties. The leading jet-related uncertainty is the jet energy scale (JES) uncertainty. The energy scale of jets is corrected by the dedicated calibration procedure described in Section 4.2. The potential biases of the calibration procedure due to analysis selection, event topology dependence and differences between MC simulation and data are assigned as the JES uncertainties according to Ref. [78].

The second-leading jet-related uncertainty is the jet energy resolution (JER) uncertainty. Since the residual calibration is applied to ensure that the jet energy resolutions between MC simulation and data match, the relevant systematic uncertainties are accounted for. The main sources of the systematic uncertainties come from a potential bias of the detector noise evaluation due to our imperfect understanding and differences between MC simulation and data [78]. They are assigned as the JER uncertainties.

The other one is the jet vertex tagger (JVT) uncertainty. Since the jet vertex tagger is used to discriminate hard scatter jets from pile-up jets, the relevant systematic uncertainties are considered. The main sources are a potential mismodelling of hard scatter jet kinematics and a difference of hard scatter jet modelling between the different MC generators [80]. These systematic uncertainties are assigned as the JVT uncertainties. These jet-related uncertainties are labelled as *alpha_JET_**.

Flavor tagging uncertainty

Systematic uncertainties associated with the flavor tagging are also important since this analysis relies on the b-tagging performance. The flavor tagging uncertainties take into account a systematic bias of the calibration of the flavor tagging efficiency applied to correct the performance difference between MC simulation and data. The uncertainties on the b-tagging efficiency, the c-tagging efficiency and the light-flavor tagging efficiency are evaluated separately. These uncertainties originate from the statistical sources, the detector calibration and physics modelling [82], and are assigned as the b-tagging uncertainty, the c-tagging uncertainty and the light-flavor tagging uncertainty separately. They are labelled as *alpha_FT_EFF_*_{B,C,Light}_*, respectively.

b-jet energy correction uncertainty

An additional uncertainty from the b-jet energy correction described in Section 4.3.3 arises. The magnitude of the b-jet energy correction uncertainty is found to be smaller than 0.1%, and therefore it is neglected in this analysis.

Trigger uncertainty

As a trigger uncertainty, the mismodelling of the trigger efficiency in simulation is accounted for. This systematic uncertainty is associated with the calculation method of trigger scale factors. Since the trigger scale factors for the hardware (L1) trigger and the software trigger (HLT) are provided separately, the uncertainties are also evaluated separately. The trigger scale factors are derived from $t\bar{t}$ MC samples and the data. A difference between $t\bar{t}$ MC samples and HH samples on the trigger efficiency is observed to be up to 10%. The difference is assigned as a systematic uncertainty. Furthermore, differences stemming from the matrix element and the parton shower generators of the $t\bar{t}$ process are also taken as systematic uncertainties. The trigger uncertainty corresponds to the quadrature sum of these systematic uncertainties. They are labelled as *alpha_TRIG_{L1,HLT}_*.

9.2.2 Theoretical Uncertainties

Systematic uncertainties due to theoretical predictions are referred to theoretical uncertainties. When generating and simulating MC samples, several approximations and assumptions, such as PDF, parton shower and hadronization, due to theoretical limits are adopted. Systematic uncertainties of the simulations are thus assigned. They can be broken down into the HH cross-section uncertainty, the Higgs branching ratio uncertainty, the modelling uncertainty of parton shower and hadronization and the acceptance uncertainties on the PDF, α_s and the renormalisation and factorisation scales.

HH cross-section uncertainty

The theoretical uncertainty on the HH cross-section arises from choices of the PDF, α_s, the renormalisation and factorisation scales and the scale of the top-quark mass. These systematic biases on the HH cross-section calculation are considered. For the ggF HH cross-section, the PDF + α_s uncertainty is $\pm 3.0\%$ and the scale uncertainty is $^{+6\%}_{-23\%}$. For the VBF HH cross-section, the PDF + α_s uncertainty is

$\pm 2.1\%$ and the scale uncertainty is $^{+0.03\%}_{-0.04\%}$. These values are taken from Ref. [48, 114, 115]. They are labelled as *alpha_THEO_XS_{PDFalphas,SCALEMTop}_**. It should be noted that the HH cross-section uncertainty is included only when evaluating the limit on the signal strength, while is excluded when evaluating the limits on the cross-section.

Higgs branching ratio uncertainty

An uncertainty on the $H \to b\bar{b}$ branching ratio (BR) is considered with $m_H = 125$ GeV. The Higgs branching ratio uncertainty is derived by linearly adding the total parametric uncertainty (PU) and the total theoretical uncertainty (TU) taking into account that both Higgs boson decay to a pair of b-quarks [114, 116].

$$\Delta\text{BR} = 2 \times \left(\Delta\text{BR(TU)} + \sqrt{\Delta\text{BR}(\text{PU}_{\text{m}_\text{q}})^2 + \Delta\text{BR}(\text{PU}_{\alpha_\text{s}})^2}\right), \tag{9.2}$$

where ΔBR(TU) is $\pm 0.65\%$, $\Delta\text{BR}(\text{PU}_{\text{m}_\text{q}})$ is a parametric uncertainty due to the quark mass parameters of $\pm 0.72\%$ and $\Delta\text{BR}(\text{PU}_{\alpha_\text{s}})$ is that due to the α_s parameter of $^{+0.77\%}_{-0.79\%}$ in this analysis. The Higgs branching ratio uncertainty is approximately 3.5%. A dependence of the Higgs branching ratio uncertainty on κ_λ values is neglected. It is labelled as *alpha_THEO_BR_Hbb*.

Parton shower and hadronization uncertainty

Uncertainties due to the parton shower and hadronization modelling are evaluated by comparing two different samples generated with Pythia and Herwig described in Section 5.2. For the ggF HH samples, the differences on the m_{HH} shape between the two generators are derived on the SM and $\kappa_\lambda = 10$ ggF HH samples in each category. Since no significant difference between the m_{HH} bins is observed, normalization uncertainties are derived. The worst case of the values is applied to the ggF HH samples for the limit on HH cross-section as the parton shower and hadronization (PS) uncertainty. On the other hand, the value derived on the SM ggF HH sample is applied for the limit on the signal strength. For the VBF HH samples, normalization uncertainties are derived on the SM, $\kappa_\lambda = 10$ and $\kappa_{2V} = 0$ VBF HH samples in each category, and the same strategy as the ggF samples is used. A summary of the normalization uncertainties for the ggF and VBF samples is shown in Appendix E. The PS uncertainty is labelled as *alpha_THEO_ACC_PS_**.

PDF and α_s uncertainty

Systematic biases arising from the PDF and α_s choices on the shape of m_{HH} distribution are also considered following Ref. [96]. PDF uncertainties are evaluated with alternative weights using the PDF4LHC_NLO_MC set [96]. Standard deviations of the signal distributions for each replica on each m_{HH} bin and category are assigned as PDF uncertainties. α_s uncertainties are evaluated using the nominal PDF set and different α_s values. The central value of the variations is taken as α_s uncertainty. These two uncertainties are combined quadratically in each m_{HH} bin and the combined values are assigned as the PDF and α_s uncertainty. They are evaluated with the SM and BSM samples, and the same procedure as the PS uncertainty is then applied. The magnitudes are typically less than 1% in both ggF and VBF

HH signals and the maximum magnitude is approximately 2%. The PDF and α_s uncertainty is labelled as *alpha_THEO_ACC_PDFalphas_**.

Uncertainty of the renormalisation and factorisation scales

A systematic uncertainty due to missing higher order corrections is accounted for. The uncertainty is derived by taking an envelope of variations with the 7 point scale variations in each m_{HH} bin and category. This approach follows Ref. [96]. This is also evaluated with the SM and BSM samples, and the same procedure as the PS uncertainty is then applied. The typical magnitudes are approximately 2% in both ggF and VBF HH signals. The maximum magnitude is approximately 5% in the ggF signals, and 6% in the VBF signal. The uncertainty of the renormalisation and factorisation scales is labelled as *alpha_THEO_ACC_SCALE_**.

9.2.3 Reweighting Uncertainties

In this analysis, the reweighting method is used to model the BSM signal distributions, as described in Chapter 5. We already know that the reweighting method works well on m_{HH} distribution before the analysis selections. However, the modelling performance could be affected by the analysis selection because it deeply relies on the assumption that the signal acceptances of the HH productions on the analysis selections only depend on m_{HH}. Therefore, I validated the modelling performances on m_{HH} after the analysis selection and categorizations.

κ_λ and κ_{2V} reweighting uncertainty

For the κ_λ and κ_{2V} reweighting, m_{HH} distributions taken directly from MC simulation and modelled by the reweighting method after the analysis selection and categorization are compared. The comparisons are performed on $\kappa_\lambda = 10$ ggF and $\kappa_\lambda = 0$ and $\kappa_{2V} = 0$ VBF HH samples, and then good agreements are then observed as can be seen in Figure 9.13 and 9.14. To ensure that these disagreements have no impact on the results of this analysis, additional comparisons of the cross-section limits using the two distributions is performed. The differences in the expected limits on $\kappa_\lambda = 10$ ggF and $\kappa_\lambda = 0$ and $\kappa_{2V} = 0$ VBF HH cross-sections are found to be less than 1%. Therefore, no additional uncertainty for the kl and κ_{2V} reweighting is assigned.

SMEFT and HEFT reweighting uncertainty

Similarly, m_{HH} distributions with different SMEFT and HEFT coefficienct obtained from MC simulation and the reweighting method are compared. However, the comparisons are evaluated in the inclusive signal region without the ggF categorization due to the statistical limitations of the MC simulation samples. For the SMEFT reweighting, the SMEFT samples described in Table 5.3 are used. Non-negligible differences between the two distributions are observed as can be seen in Figure 9.15. In particular in the last two m_{HH} bins, the large discrepancies are observed due to the poor modelling over $m_{HH} = 1040$ GeV, the maximum bin used in the reweighting method (Appendix A). Therefore, they are split into two components, one for the last two bins and one for the previous bins, and assigned normalization uncertainties in each component as the SMEFT reweighting uncertainty to consider the large discrepancies in the last

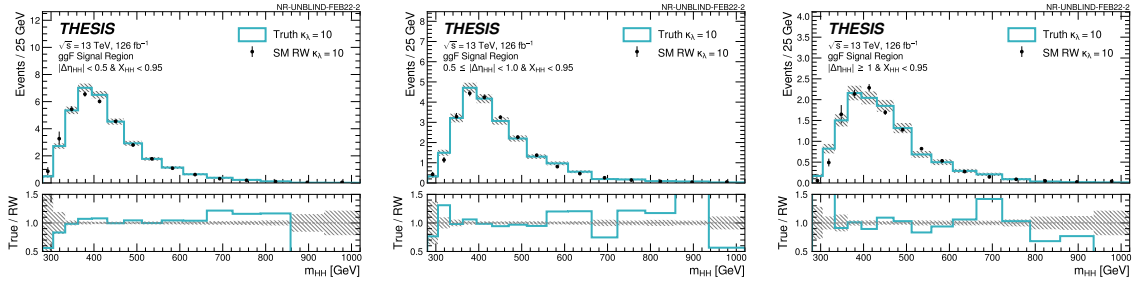

(a) $|\Delta\eta_{HH}| < 0.5$ & $X_{HH} < 0.95$ (b) $0.5 \leq |\Delta\eta_{HH}| < 1.0$ & $X_{HH} < 0.95$ (c) $|\Delta\eta_{HH}| \geq 1.0$ & $X_{HH} < 0.95$

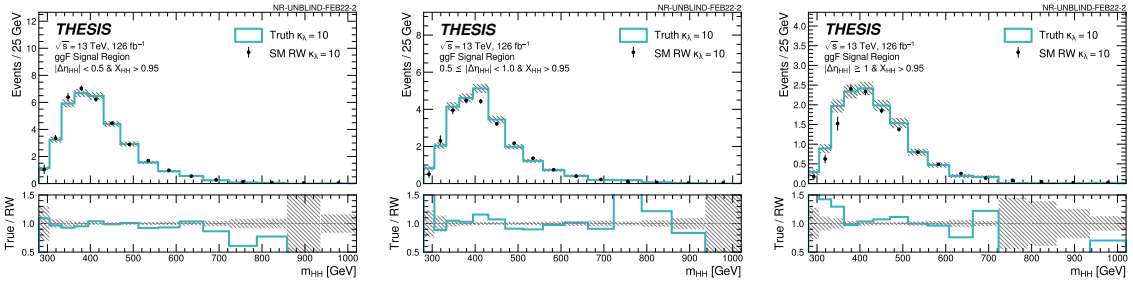

(d) $|\Delta\eta_{HH}| < 0.5$ & $X_{HH} \geq 0.95$ (e) $0.5 \leq |\Delta\eta_{HH}| < 1.0$ & $X_{HH} \geq 0.95$ (f) $|\Delta\eta_{HH}| \geq 1.0$ & $X_{HH} \geq 0.95$

Figure 9.13 m_{HH} distributions of $\kappa_\lambda = 10$ ggF HH signals taken from MC simulation (shown by the turquoise histogram) and generated by the κ_λ reweighting (shown by the black dots) in the ggF categories. The under panel shows the ratio of the MC simulation to the reweighted one.

two bins. For each SMEFT 1-D and 2-D limit, the worst case of the relevant samples is used and applied to all categories. For example for the SMEFT c_{tG} 1-D limit, $c_{tG} = -0.9$ and 0.9 samples are used to compute the SMEFT reweighting uncertainty and the worst values of them are applied into the SMEFT c_{tG} 1-D limit. The magnitudes of the SMEFT reweighting uncertainties used in this analysis are shown in Appendix F.

For the HEFT reweighting, the HEFT samples described in Table 2.3 and 5.2 are used. Similarly to the SMEFT reweighting, non-negligible differences are observed in particular the last two bins. Therefore, the HEFT reweighting uncertainties are derived by the same procedure as the SMEFT reweighting uncertainty. For the 7 HEFT BMs, the difference observed in the corresponding sample is assigned. For the HEFT c_{ggHH} and $c_{t\bar{t}HH}$ 1-D limits, the worst case of three relevant samples is assigned. The magnitudes of the HEFT reweighting uncertainties used in this analysis are also summarised in Appendix F.

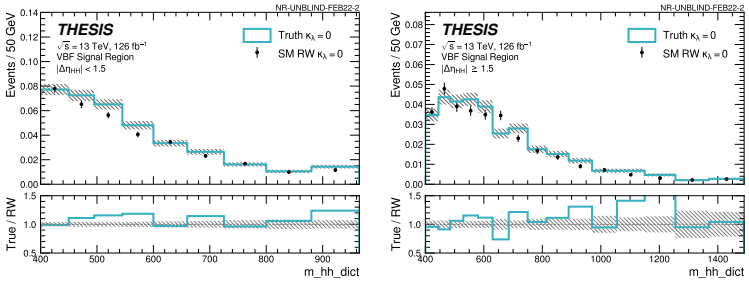

(a) $|\Delta\eta_{HH}| < 1.5$

(b) $|\Delta\eta_{HH}| \geq 1.5$

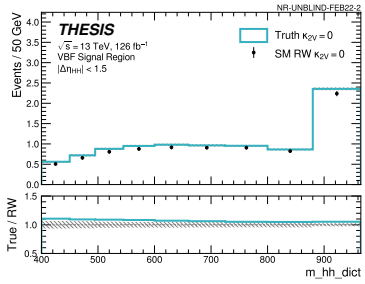

(c) $|\Delta\eta_{HH}| < 1.5$

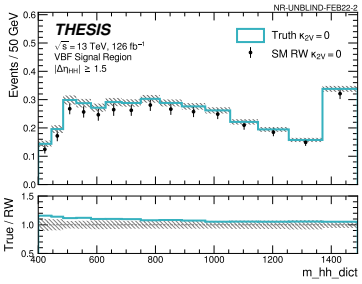

(d) $|\Delta\eta_{HH}| \geq 1.5$

Figure 9.14 m_{HH} distributions of $\kappa_\lambda = 0$ and $\kappa_{2V} = 0$ VBF HH signals taken from MC simulation (shown by the turquoise histogram) and generated by the κ_λ and κ_{2V} reweighting (shown by the black dots) in the VBF categories. The under panel shows the ratio of the MC simulation to the reweighted one.

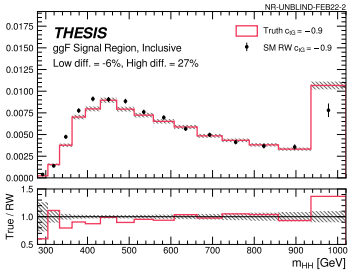

(a) $c_{tG} = -0.9$

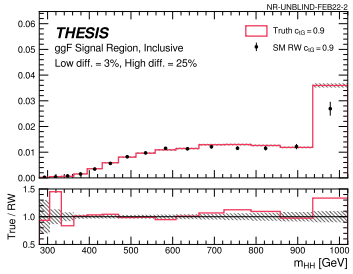

(b) $c_{tG} = 0.9$

Figure 9.15 m_{HH} distributions of SMEFT signals with $c_{tG} = -0.9$ and 0.9taken from MC simulation (shown by the red histogram) and generated by the SMEFT reweighting (shown by the black dots) in the ggF categories. The under panel shows the ratio of the MC simulation to the reweighted one.

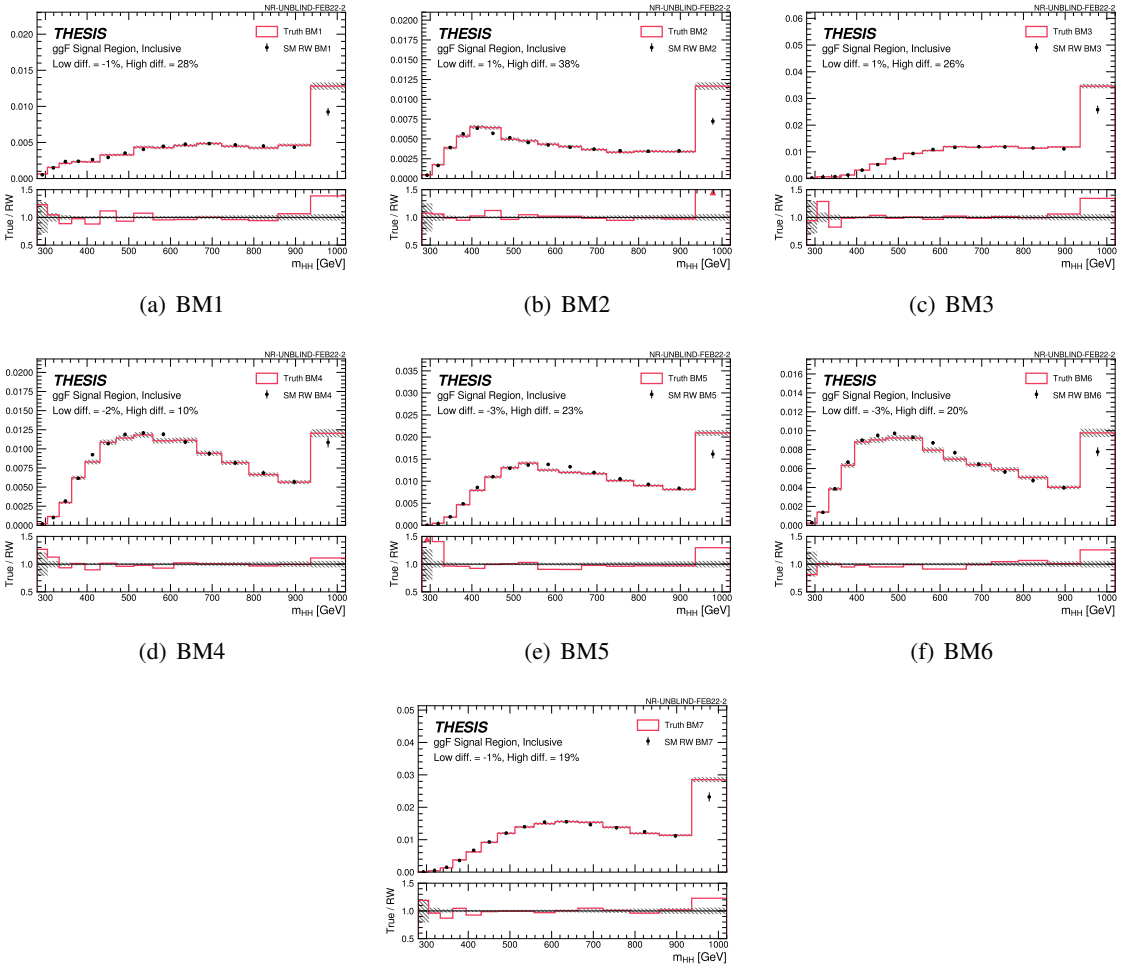

(a) BM1 (b) BM2 (c) BM3

(d) BM4 (e) BM5 (f) BM6

(g) BM7

Figure 9.16 m_{HH} distributions of HEFT signals in the 7 BMs taken from MC simulation (shown by the red histogram) and generated by the HEFT reweighting (shown by the black dots) in the inclusive ggF signal region. The under panel shows the ratio of the MC simulation to the reweighted one.

9.3 Summary of Systematic Uncertainties

Table 9.1 shows the impacts of these systematic uncertainties on the expected upper limit on the signal strength of the SM ggF +VBF HH production ($\mu_{ggF+VBF}$). They are derived by taking a relative difference between the expected upper limits including all systematic uncertainty and fixing the group of systematic uncertainty. Only groups of the dominant systematic uncertainty that have an impact of at least 1% are shown. As can be seen in Table 9.1, the background modelling uncertainties and the theoretical uncertainties are dominant in the upper limit on the signal strength. For the cross-section limits on κ_λ, κ_{2V} and so on, the background modelling uncertainties dominate since the HH cross-section uncertainty is excluded.

Source of uncertainty	$\lvert\Delta\mu\rvert/\mu$
Background Modeling Uncertainties	
2b poisson and bootstrap statistical uncertainty	7.1%
CR12 shape systematic uncertainty	7.5%
3b1f non-closure systematic uncertainty	2.0%
Experimental Uncertainties	< 1.0%
Theoretical Uncertainties	
HH cross-section uncertainty	9.0%
All other theoretical uncertainty	1.4%

Table 9.1 Summary of the impacts of the dominanl uncertainties on the expected upper limit on the signal strength $\mu_{ggF+VBF}$. Only groups of the systematic uncertainties that have at least 1% impact are shown.

Chapter 10

Statistical Analysis

The exclusion limits discussed in the next chapter are derived with a hypothesis testing procedure using a profile likelihood test statistic and performed using the standard asymptotic formulas [117]. In this analysis, m_{HH} distributions with the systematic uncertainties described in Chapter 9 are used in the profile likelihood fit as the discriminant variable. The likelihood describing the agreement between observed data and background prediction can be summarized as follows:

$$\mathcal{L}(\mu, \boldsymbol{\theta}) = \prod_{c \in \text{categories}} \prod_{b \in \text{bins}} \text{Pois}(n_{c,b} | \lambda_{c,b}(\hat{\mu}, \hat{\boldsymbol{\theta}})) \cdot \prod_{s \in \text{systematics}} \text{Gaus}(\hat{\theta}_s | \theta_s). \tag{10.1}$$

μ is the parameter of interest (POI), also known as the signal strength. $\mu = 0$ corresponds to the background-only model and $\mu = 1$ corresponds to the background and the predicted signal. θ_s are nuisance parameters that parametrize the effects of systematic uncertainties assigned in the analysis, and $\boldsymbol{\theta}$ is the ensemble of all nuisance parameters. It is needed to interpolate and extrapolate θ_s in order to evaluate the likelihood. In this analysis, the default setup of HistFactory [118] that performs a 6th-order polynomial interpolation and a linear extrapolation is used. The $\boldsymbol{\theta}$ also alters the poisson expectation $\lambda_{r,b}(\hat{\mu}, \hat{\boldsymbol{\theta}})$ and needs to be determined, but are of minor interest.

A profile likelihood ratio test statistic given by Eq. 10.2 is used in hypothesis testing following the Neyman-Pearson lemma [119].

$$\tilde{\lambda}(\mu) = \begin{cases} \frac{\mathcal{L}(\mu, \hat{\hat{\boldsymbol{\theta}}}(\mu))}{\mathcal{L}(\hat{\mu}, \hat{\boldsymbol{\theta}})} & \hat{\mu} \geq 0, \\ \frac{\mathcal{L}(\mu, \hat{\hat{\boldsymbol{\theta}}}(\mu))}{\mathcal{L}(0, \hat{\boldsymbol{\theta}}(0))} & \hat{\mu} < 0, \end{cases} \tag{10.2}$$

where $\hat{\hat{\boldsymbol{\theta}}}(\mu)$ denotes the maximum likelihood estimates of the NPs for a given value μ, while $\hat{\mu}$ and $\hat{\boldsymbol{\theta}}$ are the maximum likelihood estimates corresponding to the best fit values. The tilde ($\sim$) on λ is placed to emphasize the boundary at $\mu = 0$ for the differing definition for the $\hat{\mu} < 0$ case. The test statistic, $\tilde{q}_\mu$, considered for limit setting is defined by

$$\tilde{q}_\mu = \begin{cases} -2 \ln \tilde{\lambda}(\mu) & \hat{\mu} \leq \mu \\ 0 & \hat{\mu} > \mu \end{cases} = \begin{cases} -2 \ln \frac{\mathcal{L}(\mu, \hat{\hat{\boldsymbol{\theta}}}(\mu))}{\mathcal{L}(0, \hat{\hat{\boldsymbol{\theta}}}(0))} & \hat{\mu} \leq 0, \\ -2 \ln \frac{\mathcal{L}(\mu, \hat{\hat{\boldsymbol{\theta}}}(\mu))}{\mathcal{L}(\hat{\mu}, \hat{\boldsymbol{\theta}})} & 0 \leq \hat{\mu} \leq \mu, \\ 0 & \hat{\mu} > \mu. \end{cases} \tag{10.3}$$

The distributions of the test statistics, $f(\tilde{q}_\mu)$, for a given μ hypothesis are given by the asymptotic formulas [117, 120]. The p-value can be then calculated as follows:

$$p_\mu = \int_{\tilde{q}_{\mu,\text{obs}}}^{\infty} f(\tilde{q}_\mu|\mu, \boldsymbol{\theta}(\mu))d\tilde{q}_\mu,$$

$$p_0 = 1 - \int_{\tilde{q}_{\mu,\text{obs}}}^{\infty} f(\tilde{q}_\mu|\mu = 0, \boldsymbol{\theta}(\mu = 0))d\tilde{q}_\mu.$$

The 95% confidence level (CL) exclusion limit, μ_{up}, is obtained by solving:

$$p'_\mu = \frac{p_\mu}{1 - p_0} \leq 5\%.$$

The error bands for the one and two standard deviation ($\pm 1\sigma$ and $\pm 2\sigma$) on the limits are derived using the following formula with some fine-tunings, known as `betterBand` option.

$$\mu_{\text{up}+N} = \mu_{\text{up}} \left(\Phi^{-1}(1 - 0.05\Phi(\pm N)) \pm N\right),$$

where Φ^{-1} is the quantile function of a standard Gaussian distribution. To take into account uncertainties coming from limited statistics, a poisson constraint is applied in each bin. A pruning threshold of 0.5% is set to stabilize the fitting, while no pruning is applied for the systematics.

Chapter 11

Results

I performed the non-resonant $HH \to b\bar{b}b\bar{b}$ analysis strategy described above with the Run-2 datasets corresponding to 126 fb^{-1} at $\sqrt{s}$ = 13 TeV accumulated with the ATLAS detector. The results are discussed in this section.

11.1 Results of the Trilinear Higgs Self-coupling and $HHVV$ Coupling

11.1.1 ggF Channel Results

The observed data and the background prediction before fitting in the ggF signal regions with the ggF categorization are shown in Figure 11.1, 11.2 and 11.3. Firstly, in order to check if the observed data is consistent with our background estimation, a fit with no signal hypothesis (background-only fit) is performed. The background shape systematic uncertainties are treated as correlated across the ggF categories and as uncorrelated across the years, because the background estimation is derived inclusively for the categories and separately for each year. The 3b1f non-closure systematic uncertainty is treated the same as the background shape systematic uncertainties. The signal modelling uncertainties are treated as correlated across the ggF categories and years. The pulls associated with the background modelling uncertainties from the background-only fit are shown in Figure 11.4. The pulls of *alpha_CR12_shape_E_ggf_16* and *alpha_CR12_shape_S_ggf_16* become approximately 2 σ to cover an excess at the lower m_{HH} regions across the ggF categories in 2016. No other large pull is observed. The corresponding correlation matrices associated with the background modelling uncertainties are shown in Figure 11.5. All pulls and correlation matrices including the signal modelling uncertainties are shown in Appendix G and H. The observed data and the background prediction after the background-only fitting are shown in Figure 11.6, 11.7 and 11.8. The yields of the observed data and the expected background are shown in Table 11.1. I also tested several signal hypotheses with various κ_λ values in the ggF signal regions. The observed data are then found to be well consistent with the background prediction. Consequently, no evidence for the ggF HH production is observed.

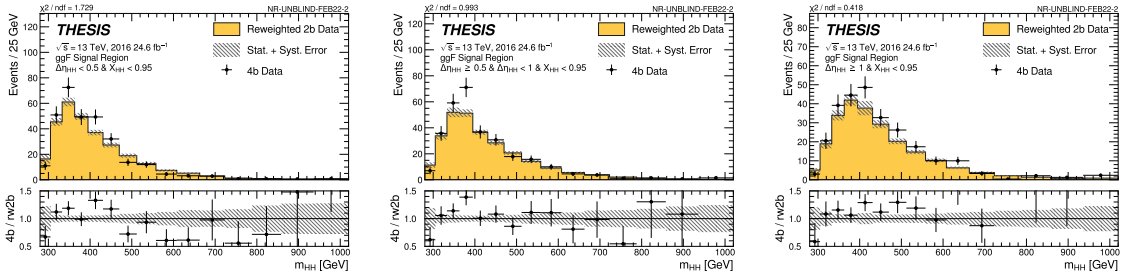

(a) $|\Delta\eta_{HH}| < 0.5$ & $X_{HH} < 0.95$ (b) $0.5 \leq |\Delta\eta_{HH}| < 1.0$ & $X_{HH} < 0.95$ (c) $|\Delta\eta_{HH}| \geq 1.0$ & $X_{HH} < 0.95$

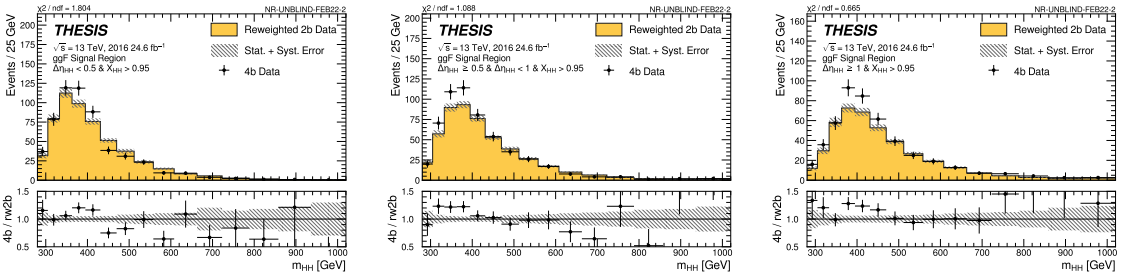

(d) $|\Delta\eta_{HH}| < 0.5$ & $X_{HH} \geq 0.95$ (e) $0.5 \leq |\Delta\eta_{HH}| < 1.0$ & $X_{HH} \geq 0.95$ (f) $|\Delta\eta_{HH}| \geq 1.0$ & $X_{HH} \geq 0.95$

Figure 11.1 m_{HH} distribution of unblinded 4b data (shown by the black points) and background estimation (shown by the yellow histogram) before fitting in the signal regions with the ggF selection and the $|\Delta\eta_{HH}|$ and X_{HH} categorization in 2016.

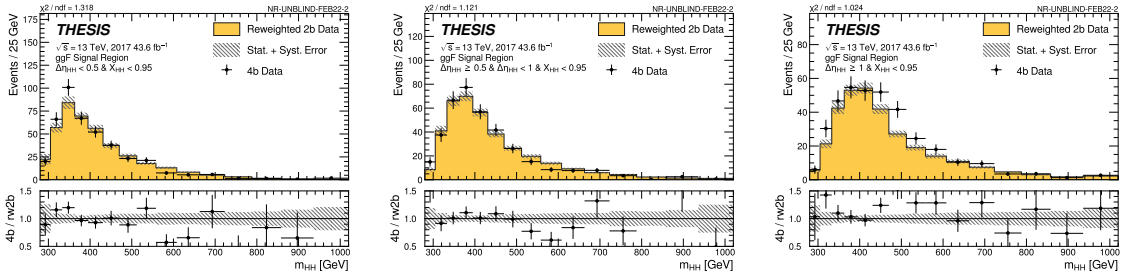

(a) $|\Delta\eta_{HH}| < 0.5$ & $X_{HH} < 0.95$ (b) $0.5 \leq |\Delta\eta_{HH}| < 1.0$ & $X_{HH} < 0.95$ (c) $|\Delta\eta_{HH}| \geq 1.0$ & $X_{HH} < 0.95$

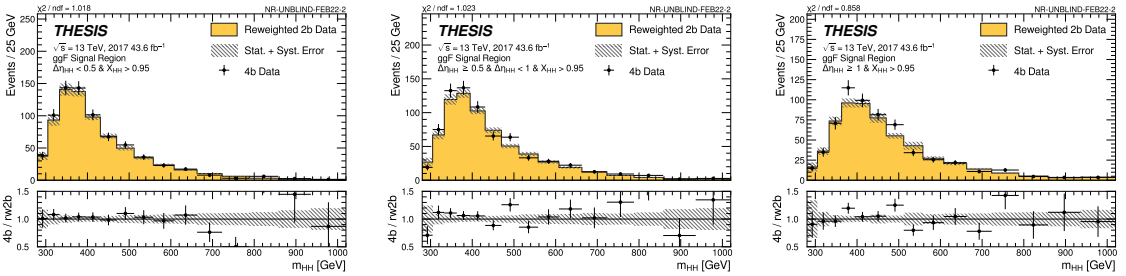

(d) $|\Delta\eta_{HH}| < 0.5$ & $X_{HH} \geq 0.95$ (e) $0.5 \leq |\Delta\eta_{HH}| < 1.0$ & $X_{HH} \geq 0.95$ (f) $|\Delta\eta_{HH}| \geq 1.0$ & $X_{HH} \geq 0.95$

Figure 11.2 m_{HH} distribution of unblinded 4b data (shown by the black points) and background estimation (shown by the yellow histogram) before fitting in the signal regions with the ggF selection and the $|\Delta\eta_{HH}|$ and X_{HH} categorization in 2017.

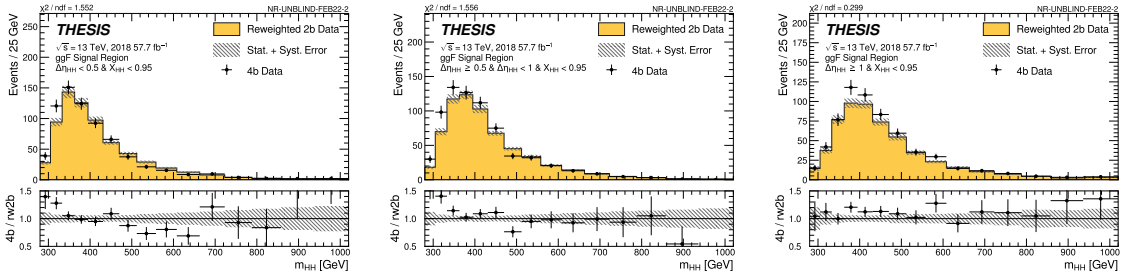

(a) $|\Delta\eta_{HH}| < 0.5$ & $X_{HH} < 0.95$ (b) $0.5 \leq |\Delta\eta_{HH}| < 1.0$ & $X_{HH} < 0.95$ (c) $|\Delta\eta_{HH}| \geq 1.0$ & $X_{HH} < 0.95$

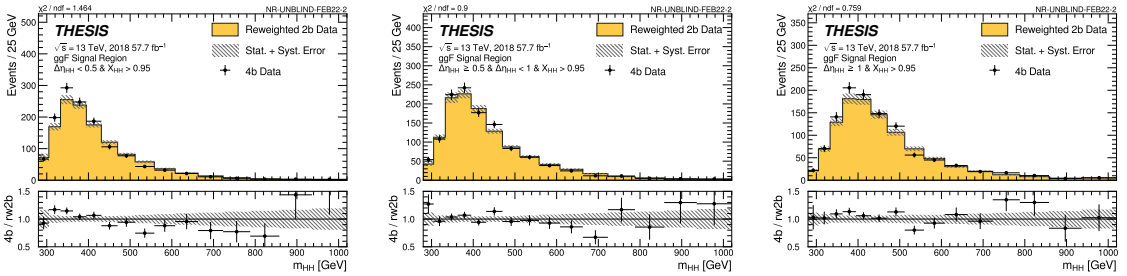

(d) $|\Delta\eta_{HH}| < 0.5$ & $X_{HH} \geq 0.95$ (e) $0.5 \leq |\Delta\eta_{HH}| < 1.0$ & $X_{HH} \geq 0.95$ (f) $|\Delta\eta_{HH}| \geq 1.0$ & $X_{HH} \geq 0.95$

Figure 11.3 m_{HH} distribution of unblinded 4b data (shown by the black points) and background estimation (shown by the yellow histogram) before fitting in the signal regions with the ggF selection and the $|\Delta\eta_{HH}|$ and X_{HH} categorization in 2018.

Table 11.1 The yields of the observed data, expected background, and expected SM ggF and VBF signals in each ggF category. The expected background yields are obtained using a background-only fit to the observed data. The expected signal yields are obtained from MC simulations.

Category	**Observed Data**	**Expected Background**	**ggF Signal SM**	**VBF Signal SM**
$\lvert\Delta\eta_{HH}\rvert < 0.5$ & $X_{HH} < 0.95$	1940	1935 ± 25	7.0	0.038
$\lvert\Delta\eta_{HH}\rvert < 0.5$ & $X_{HH} > 0.95$	3602	3618 ± 37	6.5	0.036
$0.5 < \lvert\Delta\eta_{HH}\rvert < 1.0$ & $X_{HH} < 0.95$	1924	1874 ± 21	5.1	0.037
$0.5 < \lvert\Delta\eta_{HH}\rvert < 1.0$ & $X_{HH} > 0.95$	3540	3492 ± 35	4.7	0.040
$\lvert\Delta\eta_{HH}\rvert > 1.0$ & $X_{HH} < 0.95$	1880	1739 ± 22	2.9	0.043
$\lvert\Delta\eta_{HH}\rvert > 1.0$ & $X_{HH} > 0.95$	3285	3212 ± 37	2.8	0.041

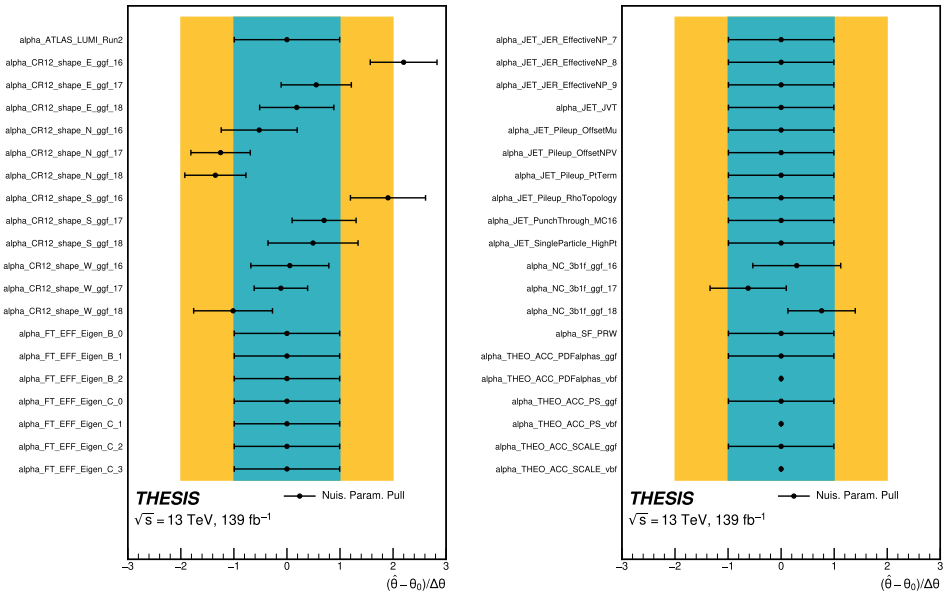

(a) CR12 shape pulls in *gg*F channel (b) NC 3b1f pulls in *gg*F channel

Figure 11.4 Pulls associated with the background systematic uncertainties when performing the background-only fit in the *gg*F channel. (a) describes the pulls of the background shape systematic uncertainties, *alpha_CR12_shape_{E,N,S,W}_ggf_{16,17,18}* and (b) describes the pulls of the 3b1f non-closure systematic uncertainty, *alpha_NC_3b1f_ggf_{16,17,18}*.

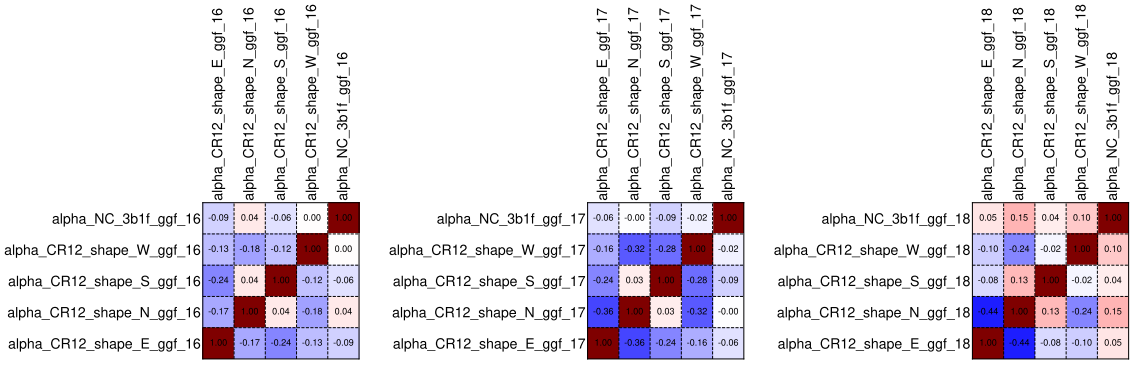

(a) 2016 (b) 2017 (c) 2018

Figure 11.5 Correlation matrix associated with the background systematic uncertainty from the background-only fit in the *gg*F channel.

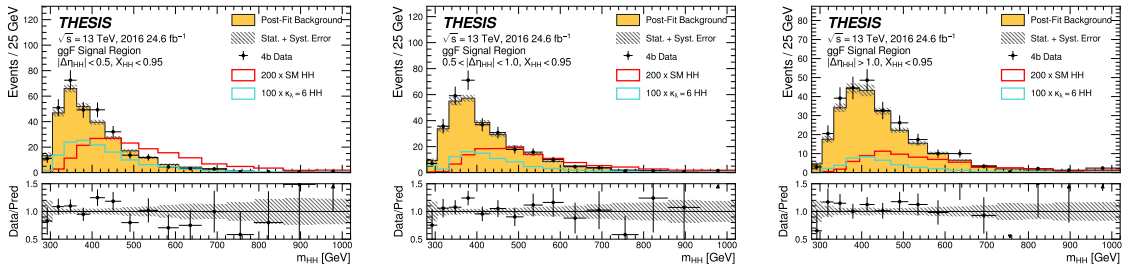

(a) $|\Delta\eta_{HH}| < 0.5$ & $X_{HH} < 0.95$ (b) $0.5 \leq |\Delta\eta_{HH}| < 1.0$ & $X_{HH} < 0.95$ (c) $|\Delta\eta_{HH}| \geq 1.0$ & $X_{HH} < 0.95$

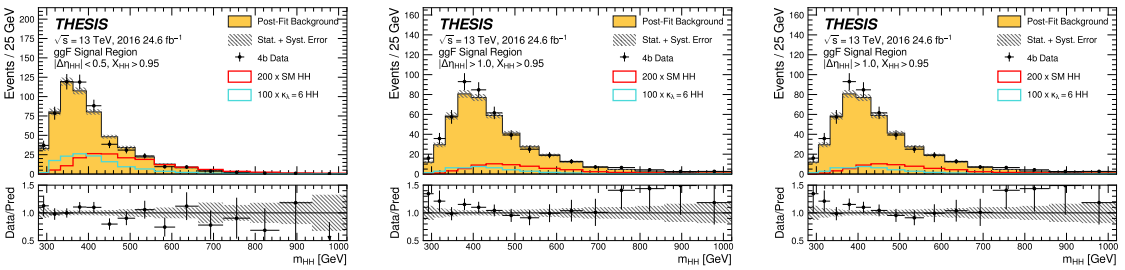

(d) $|\Delta\eta_{HH}| < 0.5$ & $X_{HH} \geq 0.95$ (e) $0.5 \leq |\Delta\eta_{HH}| < 1.0$ & $X_{HH} \geq 0.95$ (f) $|\Delta\eta_{HH}| \geq 1.0$ & $X_{HH} \geq 0.95$

Figure 11.6 m_{HH} distribution of SM and $\kappa_\lambda = +6$ ggF HH signals (shown by the red and blue histograms), unblinded 4b data (shown by the black points) and background estimation (shown by the yellow histogram) after the background-only fitting in the signal regions with the ggF selection and the $|\Delta\eta_{HH}|$ and X_{HH} categorization in 2016.

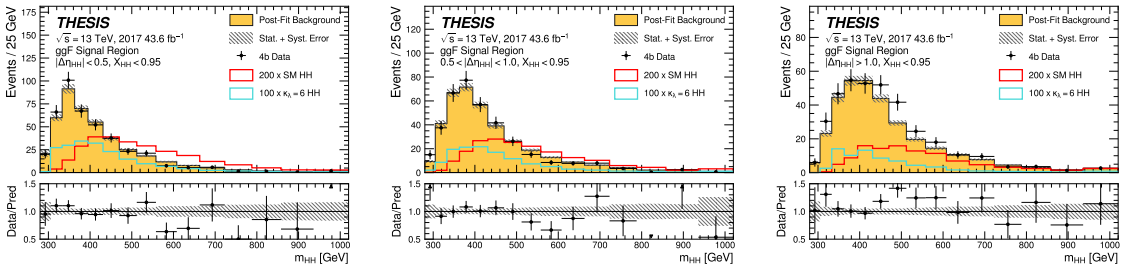

(a) $|\Delta\eta_{HH}| < 0.5$ & $X_{HH} < 0.95$ (b) $0.5 \leq |\Delta\eta_{HH}| < 1.0$ & $X_{HH} < 0.95$ (c) $|\Delta\eta_{HH}| \geq 1.0$ & $X_{HH} < 0.95$

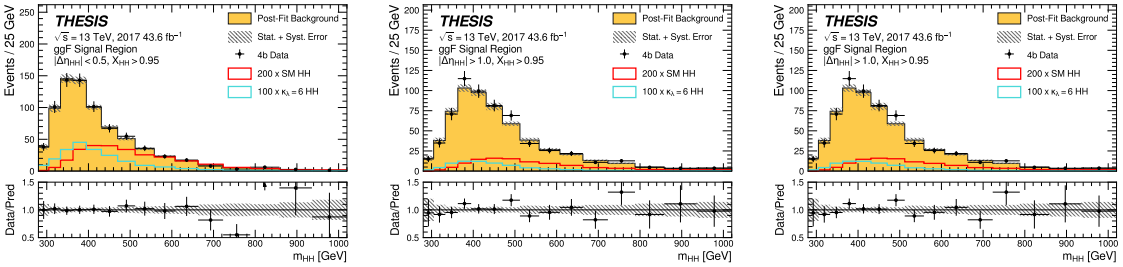

(d) $|\Delta\eta_{HH}| < 0.5$ & $X_{HH} \geq 0.95$ (e) $0.5 \leq |\Delta\eta_{HH}| < 1.0$ & $X_{HH} \geq 0.95$ (f) $|\Delta\eta_{HH}| \geq 1.0$ & $X_{HH} \geq 0.95$

Figure 11.7 m_{HH} distribution of SM and $\kappa_\lambda = +6$ ggF HH signals (shown by the red and blue histograms), unblinded 4b data (shown by the black points) and background estimation (shown by the yellow histogram) after the background-only fitting in the signal regions with the ggF selection and the $|\Delta\eta_{HH}|$ and X_{HH} categorization in 2017.

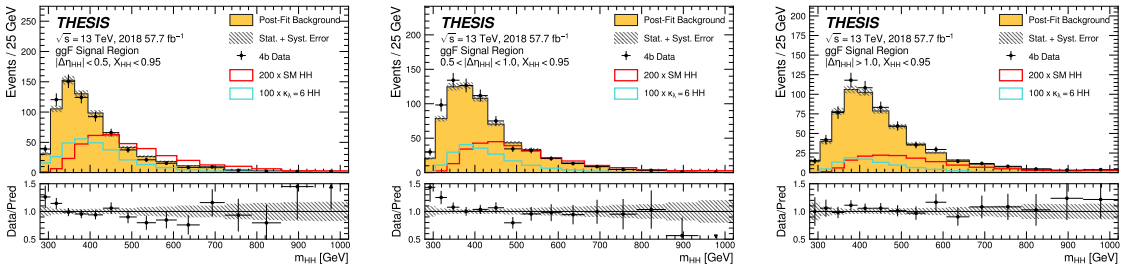

(a) $|\Delta\eta_{HH}| < 0.5$ & $X_{HH} < 0.95$ (b) $0.5 \leq |\Delta\eta_{HH}| < 1.0$ & $X_{HH} < 0.95$ (c) $|\Delta\eta_{HH}| \geq 1.0$ & $X_{HH} < 0.95$

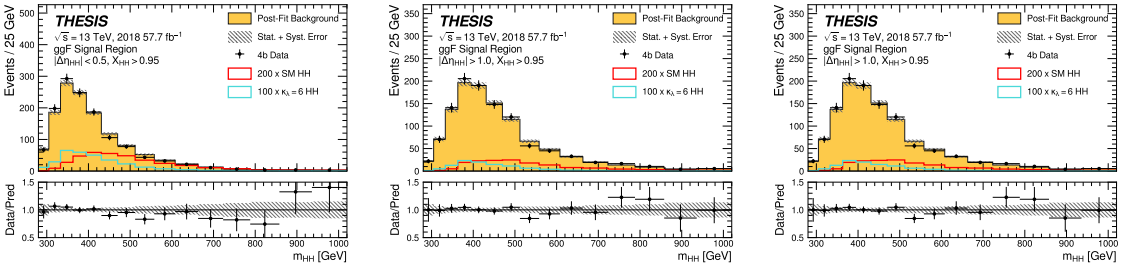

(d) $|\Delta\eta_{HH}| < 0.5$ & $X_{HH} \geq 0.95$ (e) $0.5 \leq |\Delta\eta_{HH}| < 1.0$ & $X_{HH} \geq 0.95$ (f) $|\Delta\eta_{HH}| \geq 1.0$ & $X_{HH} \geq 0.95$

Figure 11.8 m_{HH} distribution of SM and $\kappa_\lambda = +6$ ggF HH signals (shown by the red and blue histograms), unblinded 4b data (shown by the black points) and background estimation (shown by the yellow histogram) after the background-only fitting in the signal regions with the ggF selection and the $|\Delta\eta_{HH}|$ and X_{HH} categorization in 2018.

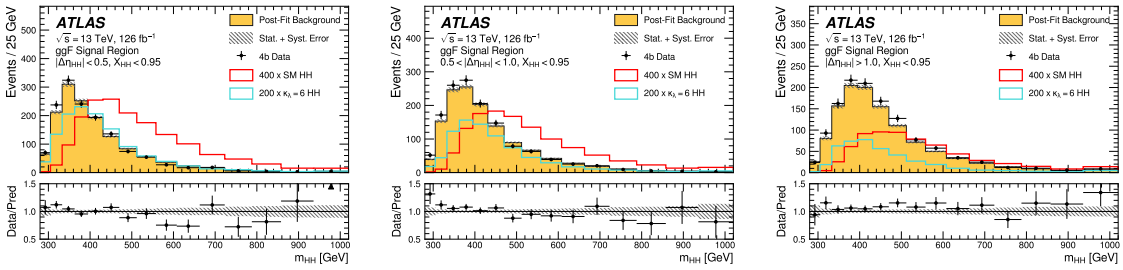

(a) $|\Delta\eta_{HH}| < 0.5$ & $X_{HH} < 0.95$ (b) $0.5 \leq |\Delta\eta_{HH}| < 1.0$ & $X_{HH} < 0.95$ (c) $|\Delta\eta_{HH}| \geq 1.0$ & $X_{HH} < 0.95$

(d) $|\Delta\eta_{HH}| < 0.5$ & $X_{HH} \geq 0.95$ (e) $0.5 \leq |\Delta\eta_{HH}| < 1.0$ & $X_{HH} \geq 0.95$ (f) $|\Delta\eta_{HH}| \geq 1.0$ & $X_{HH} \geq 0.95$

Figure 11.9 m_{HH} distribution of SM and $\kappa_\lambda = +6$ ggF HH signals (shown by the red and blue histograms), unblinded 4b data (shown by the black points) and background estimation (shown by the yellow histogram) after the background-only fitting in the signal regions with the ggF selection and the $|\Delta\eta_{HH}|$ and X_{HH} categorization in all years.

Since the non-resonant HH process is not observed, I set the upper limit on the signal strength of the SM ggF HH cross-section and constrain the Higgs self-coupling from the observed data. Table 11.2 and Figure 11.10 show the upper limit on the signal strength and the exclusion limit on the ggF HH cross-section as a function of κ_λ at 95% confidence level (CL) in the ggF channel. The observed (expected) upper limit on the signal strength is 5.3 (7.5). The observed (expected) κ_λ constraint is [-4.6, 13.2] ([-5.1, 12.0]).

Table 11.2 The observed and expected upper limits on the ggF HH cross-section at 95% CL in the ggF region, assuming the SM kinematic shape.

Observed Limit	-2σ	-1σ	Expected Limit	$+1\sigma$	$+2\sigma$
5.3	4.0	5.4	7.5	10.7	15.0

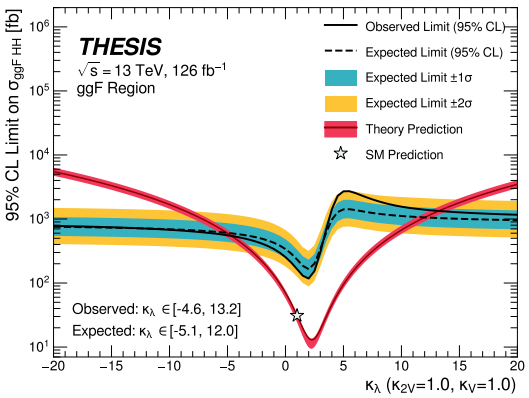

Figure 11.10 The 95% CL limit on the ggF HH cross-section as a function of κ_λ in the ggF channel. The solid black line denotes the observed 95% CL upper limits, and the dashed black line denotes the expected 95% CL upper limits. The inner blue band and outer yellow band indicate the $\pm1\sigma$ and $\pm2\sigma$ uncertainty ranges. The red line denotes the theoretical prediction of the ggF HH cross section.

11.1.2 VBF Channel Results

The observed data and the background prediction before fitting in the VBF signal regions with the VBF categorization are shown in Figure 11.11.

The background-only fit is then performed in the VBF signal regions, where the SM ggF HH events are treated as background. The background and signal modelling uncertainties are treated the same as the ggF channel. The pulls with the background-only fitting are shown in Figure 11.12. No large pull is observed in the VBF channel. The corresponding correlation matrix is shown in Figure 11.13. All pulls and correlation matrix including the signal modelling uncertainties are shown in Appendix G and H. The observed data and the background prediction after the background-only fitting are shown in Figure 11.14.

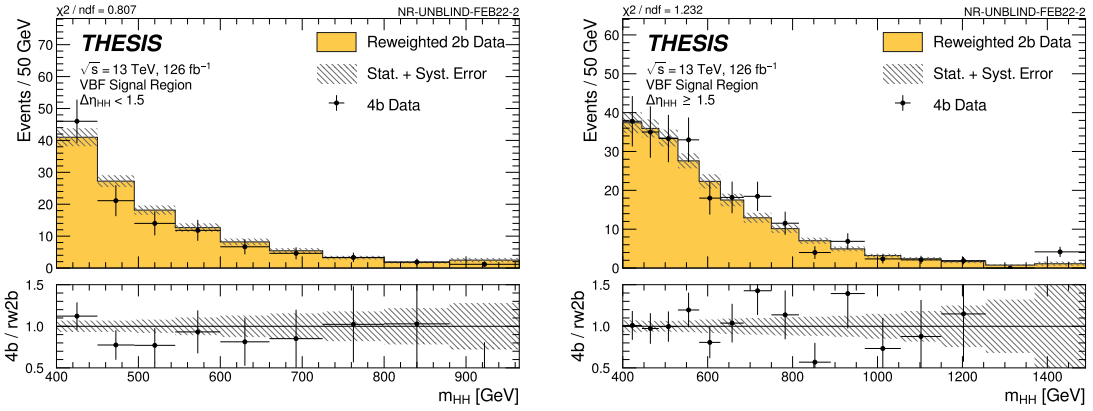

(a) $|\Delta\eta_{HH}| < 1.5$ (b) $|\Delta\eta_{HH}| \geq 1.5$

Figure 11.11 m_{HH} distribution of unblinded 4b data (shown by the black points) and background estimation (shown by the yellow histogram) before fitting in the signal regions with the VBF selection and the $|\Delta\eta_{HH}|$ categorization in all years.

The yields of the observed data and the expected background are shown in Table 11.3. Then I also tested several signal hypotheses with various κ_λ and κ_{2V} in the VBF signal regions. The conclusion is the same that no evidence for the VBF HH production is observed as the ggF channel.

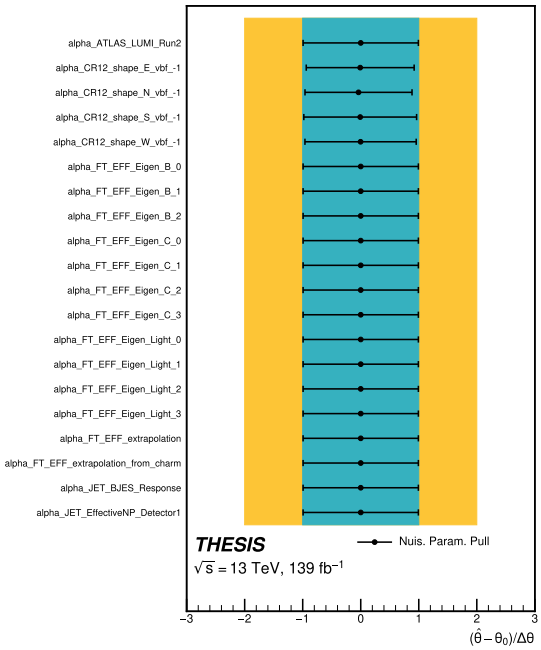

Figure 11.12 Pulls associated with the background systematic uncertainties when performing the background-only fit in the VBF channel. The pulls of the background shape systematic uncertainties, *alpha_CR12_shape_{E,N,S,W}_vbf_-1* are shown.

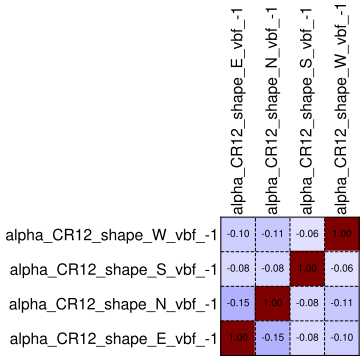

Figure 11.13 Correlation matrix associated with the background systematic uncertainty from the background-only fit in the VBF channel.

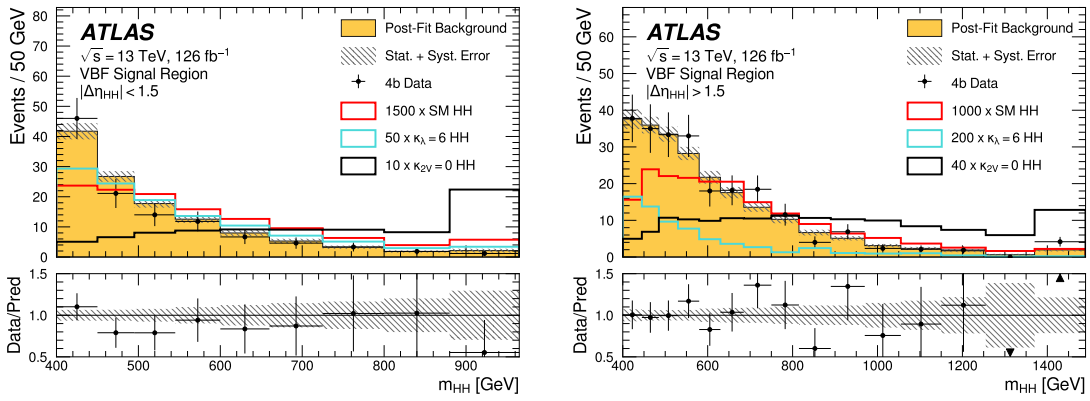

(a) $|\Delta\eta_{HH}| < 1.5$ (b) $|\Delta\eta_{HH}| \geq 1.5$

Figure 11.14 m_{HH} distribution of SM, $\kappa_\lambda = +6$ and $\kappa_{2V} = 0$ VBF HH signals (shown by the red, blue and black histograms), unblinded 4b data (shown by the black points) and background estimation (shown by the yellow histograms) after the background-only fitting in the signal regions with the VBF selection and the $|\Delta\eta_{HH}|$ categorization in all years.

Table 11.3 The yields of the observed data, expected background, and expected SM ggF and VBF signals in each VBF category. The expected background yields are obtained using a background-only fit to the observed data. The expected signal yields are obtained from MC simulations.

Category	**Observed Data**	**Expected Background**	**ggF Signal SM**	**VBF Signal SM**
$\lvert\Delta\eta_{HH}\rvert < 1.5$	116	125.3 ± 4.4	0.37	0.090
$\lvert\Delta\eta_{HH}\rvert > 1.5$	241	230.6 ± 5.3	0.06	0.21

I then set the upper limit on the signal strength of the SM VBF HH cross-section and constrain the Higgs self-coupling and the $HHVV$ coupling from the observed data. Table 11.4 and Figure 11.15 show the upper limit on the signal strength and the exclusion limit on the VBF HH cross-section as a function of κ_λ and κ_{2V} at 95% CL in the VBF channel. The observed (expected) upper limit on the signal strength is set to 122.3 (134.4). The observed (expected) κ_λ constraint is [-9.7, 12.9] ([-12.8, 15.9]). The observed (expected) κ_{2V} constraint is [0.09, 1.99] ([-0.08, 2.16]).

Table 11.4 The observed and expected upper limits on the VBF HH cross-section at 95% CL in the VBF region, assuming the SM kinematic shape. SM ggF HH events are treated as background here.

Observed Limit	-2σ	-1σ	Expected Limit	$+1\sigma$	$+2\sigma$
122.3	72.1	96.8	134.4	194.3	281.9

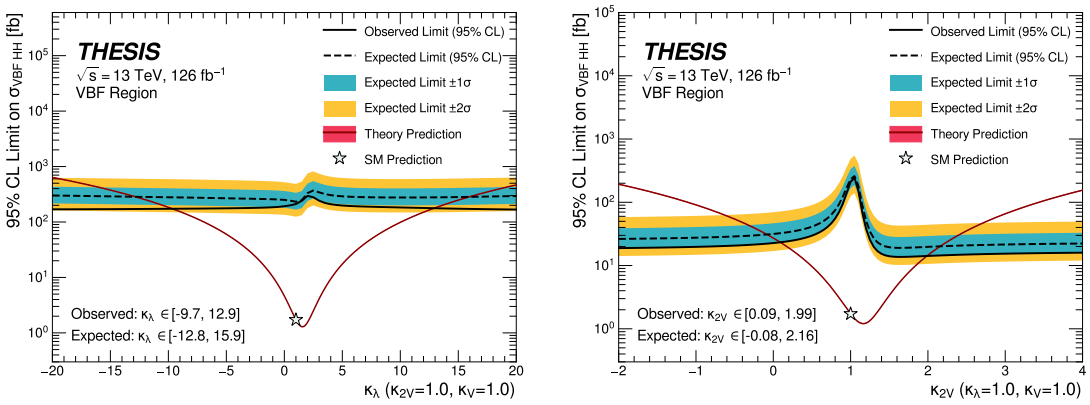

(a) κ_λ (b) κ_{2V}

Figure 11.15 The 95% CL limit on the VBF HH cross-section as a function of (a) κ_λ and (b) κ_{2V} in the VBF channel. The solid black line denotes the observed 95% CL upper limits, and the dashed black line denotes the expected 95% CL upper limits. The inner blue band and outer yellow band indicate the $\pm1\sigma$ and $\pm2\sigma$ uncertainty ranges. The red line denotes the theoretical prediction of VBF HH cross section. ggF HH events are treated as background.

11.1.3 ggF and VBF Combination Results

Finally, I tested signal hypotheses with various κ_λ and κ_{2V} in the combined ggF and VBF signal regions. Table 11.5 and Figure 11.16(a) show the upper limits on the signal strength of the SM ggF and VBF HH cross-section and the limit on the HH cross-section as a function of κ_λ and κ_{2V} at 95% CL. The observed (expected) upper limit on the signal strength of the SM ggF and VBF HH cross-section is set to 5.4 (8.1). The observed (expected) κ_λ constraint is [-3.9, 11.1] ([-4.6, 10.8]). The observed (expected) κ_{2V} constraint is [-0.03, 2.11] ([-0.05, 2.12]).

Table 11.5 The observed and expected upper limits on the signal strength of the SM HH cross-section in the combined ggF and VBF signal regions. When deriving the upper limit on the signal strength of the SM VBF HH production, the SM ggF HH events are treated as background.

	Observed Limit	-2σ	-1σ	Expected Limit	$+1\sigma$	$+2\sigma$
$\sigma_{ggF}/\sigma^{SM}_{ggF}$	5.5	4.4	5.9	8.2	12.4	19.6
$\sigma_{VBF}/\sigma^{SM}_{VBF}$	130.5	71.6	96.1	133.4	192.9	279.3
$\sigma_{ggF+VBF}/\sigma^{SM}_{ggF+VBF}$	5.4	4.3	5.8	8.1	12.2	19.1

Large improvements are archived compared to the previous analyses [5–7]. In the previous $HH \to b\bar{b}b\bar{b}$ search using 36.1 fb^{-1} of proton-proton collisions at $\sqrt{s} = 13$ TeV [5], the observed (expected) upper limit on the signal strength of the SM ggF HH cross-section was 12.9 (20.7) and the κ_λ constraint

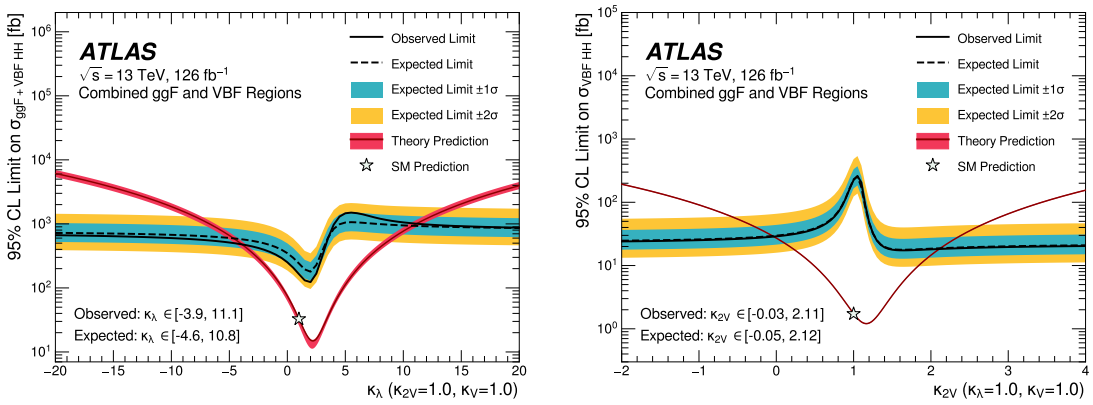

(a) κ_λ (b) κ_{2V}

Figure 11.16 The 95% CL limit on the HH cross-section as a function of (a) κ_λ and (b) κ_{2V} in the combinend ggF and VBF channels. The solid black line denotes the observed 95% CL upper limits, and the dashed black line denotes the expected 95% CL upper limits. The inner blue band and outer yellow band indicate the $\pm1\sigma$ and $\pm2\sigma$ uncertainty ranges. The red line denotes the theoretical prediction of the ggF + VBF HH cross section. In the κ_{2V} scan, the SM ggF HH events are treated as background.

was $[-10.9, 20.1]$ ($[-11.6, 18.8]$) at 95% CL. This analysis improved the observed (expected) upper limit on the signal strength by a factor of 2.4 (2.5). Since the improvement due to the statistic increase from 36.1 fb^{-1} to 126 fb^{-1} is a factor of 1.9, this analysis additionally improved by approximately a factor of 1.3 due to the analysis technique such as the analysis categorizations. In the previous VBF $HH \to b\bar{b}b\bar{b}$ search using 126 fb^{-1} of proton-proton collisions at $\sqrt{s} = 13$ TeV [6, 7], the observed (expected) upper limit on the signal strength of the SM VBF HH cross-section was 840 (550) and the κ_{2V} constraint was set to $[-0.43, 2.56]$ ($[-0.55, 2.72]$) at 95% CL. The observed (expected) upper limit on the signal strength is improved by a factor of 6.4 (4.1) though the same dataset is used. The improvement is carried out from the analysis technique, in particular by adding the $|\Delta\eta_{HH}| > 1.5$ region in the VBF channel described in Section 6.4.4 and Figure 7.4, which region was cut in the previous analysis.

11.2 Interpretation Results using Effective Field Theory

I interpolated the $HH \to b\bar{b}b\bar{b}$ results into the SMEFT and HEFT coefficiencts at the dimension 6 operators discussed in Section 2.3.2. Only the ggF HH events in the ggF channel are used to derive the results and the ggF HH events in the VBF channel are neglected. The SM VBF HH events are completely negligible. When the SM VBF HH events are taken as background, the maximum impact on the upper limit in the HEFT BMs is less than 0.1%. Compared with the results of the trilinear Higgs self-coupling and $HHVV$ coupling, the SMEFT and HEFT reweighting uncertainties are additionally included to account for the discrepancy between the kinematic distributions taken from MC simulation and modelled by the reweighting method, as discussed in Section 9.2.

11.2.1 SMEFT Interpretation Results

Figure 11.20 shows the exclusion limits on the ggF HH cross-section as a function of the dimension 6 coefficients in the SMEFT, c_H, $c_{H\Box}$, c_{HG}, c_{tH} and c_{tG}. When performing these 1-D upper limit scans, other coefficients are fixed to the SM predictions ($c_i = 0$). For example for the c_H 1-D upper limit, $c_{H\Box}$, c_{HG}, c_{tH} and c_{tG} are fixed to 0. The observed and expected constraints for the SMEFT coefficients at 95% CL are summarized in Table 11.6. The 2-D contour limits given a pair of c_H and others are also presented in Figure 11.18. It should be noted that interpretations for limits approaching or exceeding $\pm 4\pi$ must be carefully considered due to the potential impacts missing higher order contributions. In addition, $c_{HG} < -0.06$ region in the 2-D contour limits should be cautiously interpreted due to difficulty of the sigal modelling.

They are the first interpretation results for the SMEFT coefficients from the HH analysis. In particular, the first constraint for c_H is obtained by this analysis, because it is difficult to constrain it from the single Higgs measurements. The global constraints from the single Higgs measurements are $c_{H\Box} \in [-0.04, 1.04]$, $c_{HG} \in [-0.004, 0.008]$, $c_{tH} \in [-2.8, 5.4]$ and $c_{tG} \in [-0.3, 0.3]$ [121, 122]. The c_{tH} and c_{tG} constraints are a bit worse than the global constraints, but it is found to have nearly levels of the sensitivity. When performing the global fit on the single Higgs and HH analyses, further improvements on these constraints are expected.

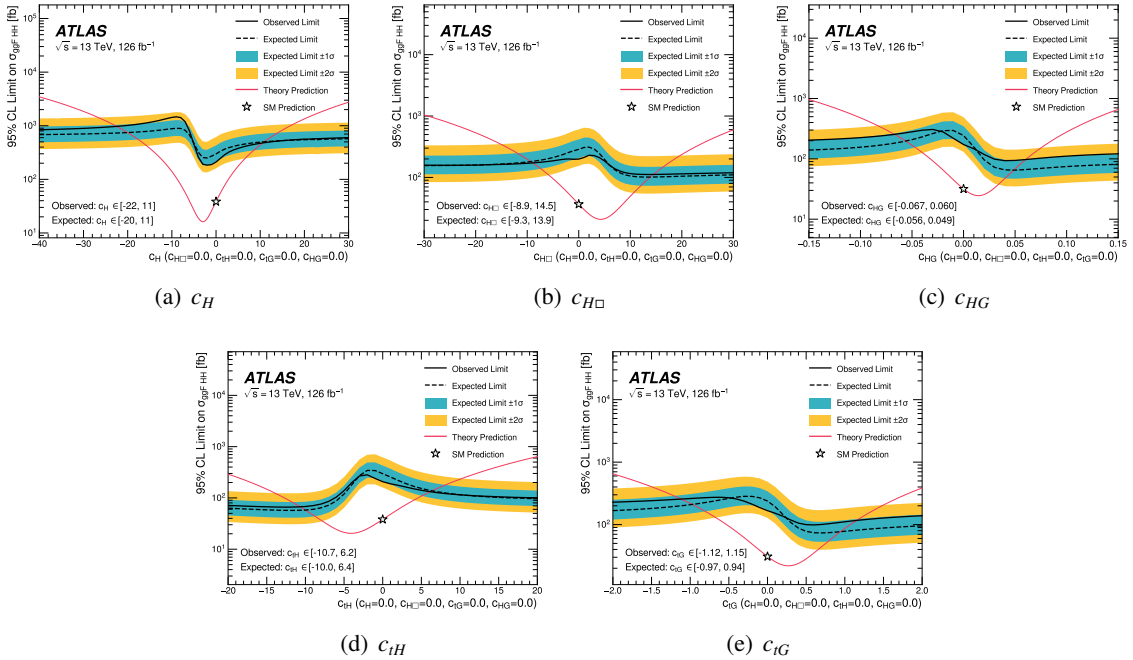

(a) c_H (b) $c_{H\Box}$ (c) c_{HG}

(d) c_{tH} (e) c_{tG}

Figure 11.17 SMEFT 1D limit results with the ggF selection and categorization. The solid black line denotes the observed 95% CL upper limits, and the dashed black line denotes the expected 95% CL upper limits. The inner blue band and outer yellow band indicate the $\pm 1\sigma$ and $\pm 2\sigma$ uncertainty ranges. The red line denotes the theoretical prediction of ggF HH cross section.

Table 11.6 The observed and expected constraints on the SMEFT parameters to which the analysis is sensitive. The ranges are allowed at 95% CL. For each parameter, the constraints are provided assuming the other parameters are fixed to the SM predictions. The VBF HH process is ignored when deriving the results.

Parameter	Observed Constraint	Expected Constraint
c_H	$[-22.5, 10.6]$	$[-20.0, 10.9]$
$c_{H\Box}$	$[-8.9, 14.5]$	$[-9.3, 13.9]$
c_{HG}	$[-0.07, 0.06]$	$[-0.06, 0.05]$
c_{tH}	$[-10.7, 6.2]$	$[-10.0, 6.4]$
c_{tG}	$[-1.12, 1.15]$	$[-0.97, 0.94]$

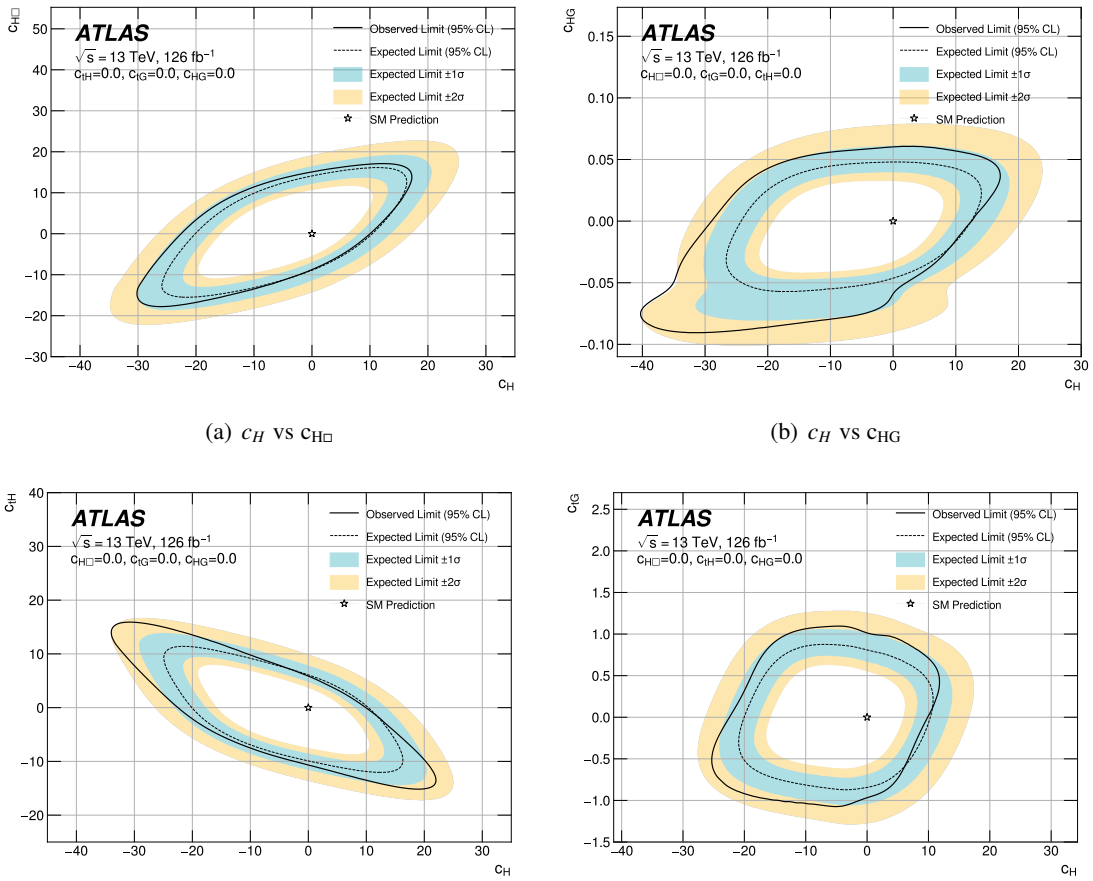

(a) c_H vs $c_{H\Box}$

(b) c_H vs c_{HG}

(c) c_H vs c_{tH}

(d) c_H vs c_{tG}

Figure 11.18 SMEFT 2D limit results with the ggF selection and categorization. The solid black line denotes the observed 95% CL upper limits, and the dashed black line denotes the expected 95% CL upper limits. The inner blue band and outer yellow band indicate the $\pm1\sigma$ and $\pm2\sigma$ uncertainty ranges.

11.2.2 HEFT Interpretation Results

The interpretations using the HEFT framework are also performed. Figure 11.19 shows the upper limits on the HEFT ggF HH production cross-section in the 7 BMs. These BM models reflect the sensitivity with the different shapes of m_{HH} distributions as discussed in Section 2.3.2. As can be seen, BM3, BM5 and BM7 are observed to be excluded at more than 95% CL. In addition, the 1-D upper limits on the ggF HH production cross-section as a function of c_{ggHH} and $c_{t\bar{t}HH}$ are presented, because c_{ggHH} and $c_{t\bar{t}HH}$ are only accessible via the HH analyses. When performing the 1-D scans, other HEFT coefficients are fixed to the SM predictions. The observed and expected constraints for the HEFT coefficients at 95% CL are summarized in Table 11.7.

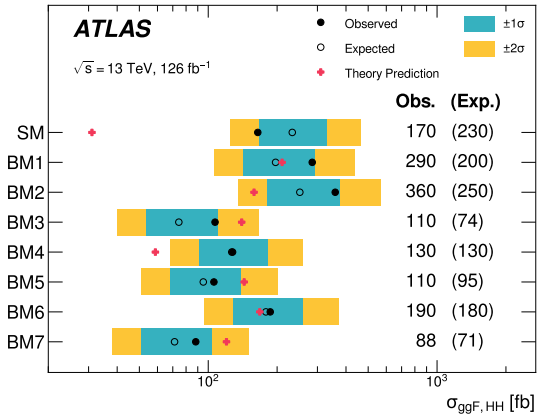

Figure 11.19 The exclusion limits on the ggF HH production cross-section in the SM and the HEFT benchmarks. The solid black points denote the observed 95% CL upper limits, and the open circles denote the expected 95% CL upper limits. The inner blue band and outer yellow band indicate the $\pm 1\sigma$ and $\pm 2\sigma$ uncertainty ranges. The red crosses show the theoretical predictions of the ggF HH production cross-section in the respective BMs.

Table 11.7 The observed and expected constraints on the HEFT parameters c_{ggHH} and $c_{t\bar{t}HH}$. The ranges are allowed at 95% CL. For each parameter, the constraints are provided assuming the other parameters are fixed to the SM predictions. The VBF HH process is ignored when deriving the results.

Parameter	Observed Constraint	Expected Constraint
c_{ggHH}	$[-0.55, 0.51]$	$[-0.46, 0.40]$
$c_{t\bar{t}HH}$	$[-0.36, 0.78]$	$[-0.42, 0.75]$

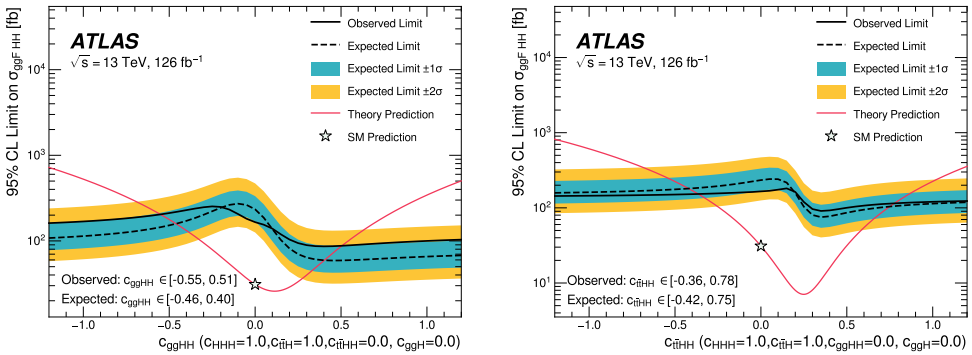

(a) c_{ggHH} (b) $c_{t\bar{t}HH}$

Figure 11.20 HEFT 1D exclusion limits for (a) c_{ggHH} and (b) $c_{t\bar{t}HH}$ on the ggF HH cross-section. The solid black line denotes the observed 95% CL upper limits, and the dashed black line denotes the expected 95% CL upper limits. The inner blue band and outer yellow band indicate the $\pm 1\sigma$ and $\pm 2\sigma$ uncertainty ranges. The red line denotes the theoretical prediction of ggF HH cross section.

Chapter 12

Discussion

I presented the results of the non-resonant $HH \to b\bar{b}b\bar{b}$ analysis that significantly improve the constraints on the signal strength, the trilinear Higgs self-coupling and the $HHVV$coupling with respect to the previous analyses in Chapter 11. In this chapter, I will discuss a statistical combination of the HH analyses to further improve the constraints and finally discuss future prospects of the HH search and the trilinear Higgs self-coupling measurement.

12.1 HH Combination Result using 126−139 fb^{-1} dataset

To obtain the leading constraints on the signal strength, the trilinear Higgs self-coupling and the $HHVV$ coupling, I additionally performed a statistical combination of searches for non-resonant HH production using the $b\bar{b}b\bar{b}$, $b\bar{b}\gamma\gamma$ and $b\bar{b}\tau\tau$ final states. These final states are the highest sensitive channels in non-resonant HH searches, because the $b\bar{b}b\bar{b}$ final state has the largest branching ratio, the $b\bar{b}\gamma\gamma$ final state provides the significantly clean signature over background despite the branching ratio is only 0.26% and the $b\bar{b}\tau\tau$ final state is the relatively clean channel with the larger branching ratio. The HH combination can provide the maximum sensitivity and further constrain on them, as discussed in Chapter 7. This section will discuss the combination results.

Input Analyses and Datasets

The non-resonant HH analyses in the $b\bar{b}\gamma\gamma$ and $b\bar{b}\tau\tau$ final states were recently updated and performed with the full Run-2 datasets in the ATLAS experiment [123, 124]. The integrated luminosities of the datasets used in each channel are shown in Table 12.1. Analysis details of the $HH \to b\bar{b}\gamma\gamma$ and $b\bar{b}\tau\tau$ are summarized in the references shown in the same table. They are used as inputs for the combination with the non-resonant $HH \to b\bar{b}b\bar{b}$ analysis.

I check an overlap between the datasets used in three input analyses. Because the signal regions used in these analyses are not defined to be orthogonal, an overlap event passing the event selections of both and being used in the statistical interpretation by both can exist. Such overlap events can cause any problems and ideally should be avoided.

Figure 12.1 shows the results of the overlap checks on the full Run-2 data. In Figure 12.1(a), the absolute number of events overlapping between two analysis signal regions are shown. For example, the

Table 12.1 Integrated luminosities of the dataset used in the non-resonant HH analyses in each channel. The last column provides publication references describing each non-resonant HH analysis.

Channel	Integrated Luminosity [fb^{-1}]	Ref.
$b\bar{b}b\bar{b}$	126	
$b\bar{b}\gamma\gamma$	139	[123]
$b\bar{b}\tau\tau$	139	[124]

number of events overlapping between the $b\bar{b}b\bar{b}$ signal region and the $b\bar{b}\gamma\gamma$ is zero. In Figure 12.1(b), the relative fraction of overlapping events with respect to the total number of events in the reference analysis signal region on the x-axis. As can be seen, only one event is overlapped between the $b\bar{b}b\bar{b}$ analysis and the full hadronic (hh) $b\bar{b}\tau\tau$ analysis. The contribution is less than 0.01% with respect to the total number of events in each signal region. Therefore the overlap is considered negligible.

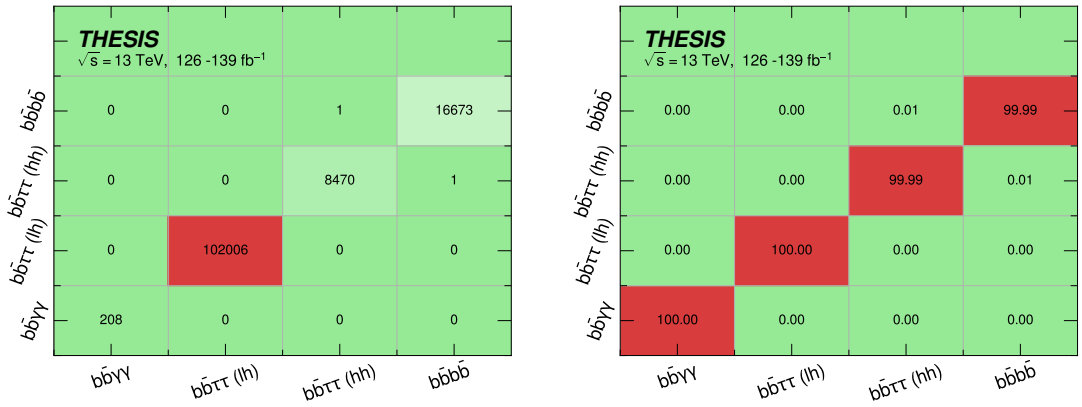

(a) Total number of events

(b) Relative fraction

Figure 12.1 Total overlap matrices in the signal regions in the non-resonant HH→ $b\bar{b}\gamma\gamma$, $b\bar{b}\tau\tau$ and $b\bar{b}b\bar{b}$ analyses. For the $b\bar{b}\tau\tau$ analysis, the number of events in two channels, full hadronic (hh) and semi-leptonic (lh), are shown. (a) shows the number of events overlapping between the analysis signal regions on the x-axis and the y-axis and (b) shows the relative fractions of events with respect to the total number of events in the reference analysis on the x-axis.

HH Combination Results

The HH statistical combination in the $b\bar{b}b\bar{b}$, $b\bar{b}\gamma\gamma$ and $b\bar{b}\tau\tau$ final states is performed with the full Run-2 dataset. The results are shown in Table 12.2-12.4 and Figure 12.2 and 12.3. The observed (expected) upper limit on the signal strength of ggF + VBF HH production from their statistical combination is

2.4 (2.9). The observed (expected) κ_λ constraint is [-0.6, 6.6] ([-1.0, 7.1]). The observed (expected) κ_{2V} constraint is [0.07, 2.03] ([0.02, 2.06]).

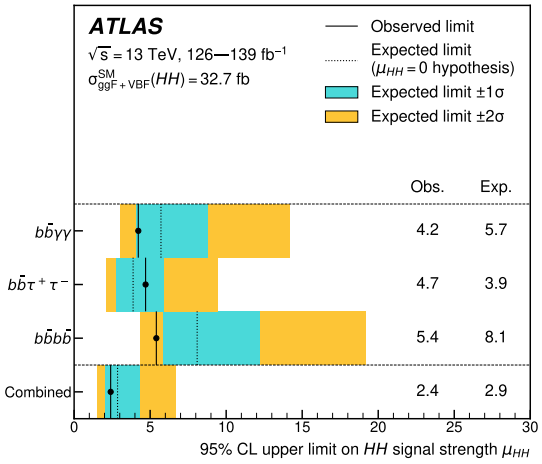

Figure 12.2 The observed and expected upper limits on the signal strength of ggF + VBF HH production from the $b\bar{b}b\bar{b}$, $b\bar{b}\gamma\gamma$ and $b\bar{b}\tau\tau$ channels and their statistical combination at 95% CL. The solid black line denotes the observed 95% CL upper limits, and the dashed black line denotes the expected 95% CL upper limits. The inner blue band and outer yellow band indicate the $\pm1\sigma$ and $\pm2\sigma$ uncertainty ranges.

Table 12.2 The observed and expected upper limits on the signal strength from the $b\bar{b}b\bar{b}$, $b\bar{b}\gamma\gamma$ and $b\bar{b}\tau\tau$ channels and their statistical combination at 95% CL.

Channel	Observed Limit	-2σ	-1σ	Expected Limit	$+1\sigma$	$+2\sigma$
$b\bar{b}\gamma\gamma$	4.2	3.1	4.1	5.7	8.8	14.2
$b\bar{b}\tau\tau$	4.7	2.1	2.8	3.9	5.9	9.4
$b\bar{b}b\bar{b}$	5.4	4.3	5.8	8.1	12.2	19.1
Combined	2.4	1.5	2.1	2.9	4.3	6.7

These results are now the leading upper limit on the signal strength and the leading constraints on the trilinear Higgs self-coupling and the $HHVV$ coupling. For the signal strength of the SM HH production cross-section, we have finally arrived in the range of a few times. In the previous HH combination analysis using 27.5 – 36.1 fb^{-1} dataset [125], the observed (expected) upper limits on the SM ggF HH cross-section were 6.9 (10). This analysis improves the observed (expected) upper limits by a factor of 2.9 (3.4). It should be noted that the analysis includes the VBF HH process but the previous analysis does not include it. The $b\bar{b}b\bar{b}$ channel improves the observed upper limit on the signal strength by approximately 23%, comparing that of the $b\bar{b}b\bar{b}$ and $b\bar{b}\gamma\gamma$ combination of 3.1 [126]. In addition, new observed (expected) constraints on the trilinear Higgs self-coupling are set to $[-0.6, 6.6]$ ($[-1.0, 7.1]$)

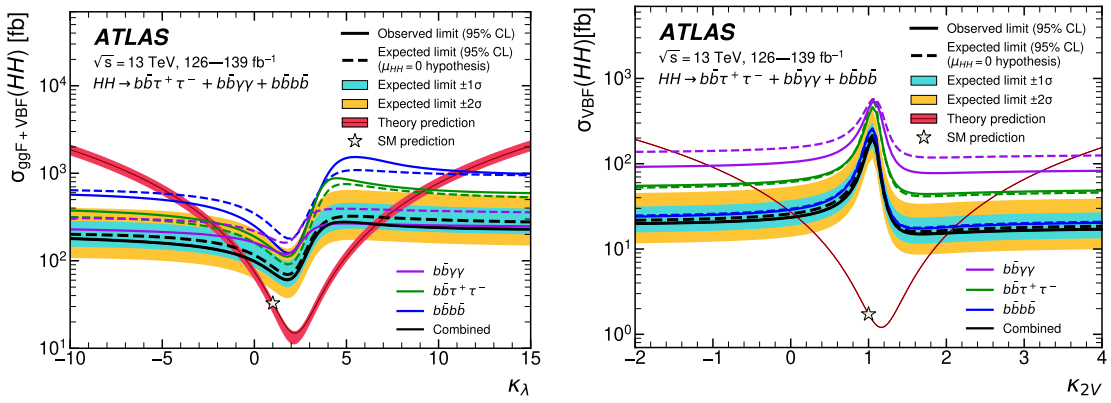

(a) κ_λ (b) κ_{2V}

Figure 12.3 The observed and expected exclusion limits on (a) the ggF + VBF HH production as a function of κ_λ and (b) the VBF HH production as a functio of κ_{2V} for the $b\bar{b}b\bar{b}$ (blue), $b\bar{b}\gamma\gamma$ (purple) and $b\bar{b}\tau\tau$ (green) channels and their statistical combination (black) at 95% CL. The solid lines denote the observed 95% CL upper limits, and the dashed lines denote the expected 95% CL upper limits. The inner blue band and outer yellow band indicate the $\pm1\sigma$ and $\pm2\sigma$ uncertainty ranges for the statistical combination. The red line denotes the theoretical prediction of the HH cross section.

in this analysis. Compared with the observed result of $[-5.0, 12.0]$ ($[-5.8, 12.0]$) in the previous HH combination, significantly improvement has been achieved. As discussed in Section 2.2, the experimental result can give us several understandings of the shape of the Higgs potential with $O(100)\%$ precisions over theoretical constraints. It is also expected to provide new constraints on BSM models such as the two Higgs double models from the measurement of the trilinear Higgs self-coupling. For the κ_{2V} constraint, this result shows that the $HHVV$ coupling exists.

Table 12.3 The observed and expected constraints on κ_λ from the $b\bar{b}b\bar{b}$, $b\bar{b}\gamma\gamma$ and $b\bar{b}\tau\tau$ channels and their statistical combination. The ranges are allowed at 95% CL.

Channel	Observed Constraint	Expected Constraint
$b\bar{b}\gamma\gamma$	$[-1.5, 6.7]$	$[-2.3, 7.6]$
$b\bar{b}\tau\tau$	$[-2.4, 9.3]$	$[-2.0, 9.1]$
$b\bar{b}b\bar{b}$	$[-3.9, 11.1]$	$[-4.6, 10.8]$
Combined	$[-0.6, 6.6]$	$[-1.0, 7.1]$

Table 12.4 The observed and expected constraints on κ_{2V} from the $b\bar{b}b\bar{b}$, $b\bar{b}\gamma\gamma$ and $b\bar{b}\tau\tau$ channels and their statistical combination. The ranges are allowed at 95% CL.

Channel	Observed Constraint	Expected Constraint
$b\bar{b}\gamma\gamma$	$[-1.05, 3.21]$	$[-1.52, 3.70]$
$b\bar{b}\tau\tau$	$[-2.42, 9.34]$	$[-1.98, 9.08]$
$b\bar{b}b\bar{b}$	$[-0.03, 2.11]$	$[-0.05, 2.12]$
Combined	$[0.07, 2.03]$	$[0.02, 2.06]$

12.2 Prospects of HH Search using $3000\ \text{fb}^{-1}$ in the High Luminosity LHC

As a major upgrade of the LHC, the High Luminosity LHC program (HL-LHC) is planned to start in 2029 and be operational until 2040 [127]. Total integrated luminosity of 3000-4000 fb^{-1} at $\sqrt{s} = 14$ TeV will be delivered in the period. A measurement of the trilinear Higgs self-coupling via the HH production strongly motivates the HL-LHC program. I will provide a prospect of the trilinear Higgs self-coupling measurement using 3000 fb^{-1} in the HL-LHC in this section.

In this study, projected constraints are obtained via a profile likelihood ratio method. There are slightly different assumptions between the 95% CL method used in Chapter 11 and the profile likelihood ratio method. The 95% CL method sets the signal strength μ as the POI, while the profile likelihood ratio method fixes the signal strength to the prediction obtained for a specific coupling modifier, e.g. the SM prediction. The 95% CL method thus allows for interpolation as standard search for an arbitrarily normalized set of signals with different shapes on the background prediction. On the other hand, the profile likelihood ratio method allows for interpolation as compatibility of the data with the specific cross-section and the shape prediction of the κ_λ coupling modifier. It should be noted that the obtained constraints from the two methods are expected not to be identical.

12.2.1 Projected Sensitivity of the $HH \to b\bar{b}b\bar{b}$ Analysis

Firstly, the HL-LHC conditions are considered when extrapolating the Run-2 $HH \to b\bar{b}b\bar{b}$ analysis to 3000 fb^{-1}. Two kinds of scale factors are applied to take into account the total integrated luminosity and the center-of-mass energy. The increase of the total integrated luminosity from 126 fb^{-1} to 3000 fb^{-1} is accounted by scaling a factor of 3000 fb^{-1} /126 fb^{-1} = 28.25 in both signal and background processes. The increase of the center-of-mass energy from 13 TeV to 14 TeV leads to the increases of the HH production and backgrounds. The ggF HH production cross-section increases by 12.6%, and the VBF HH production cross-section increases by 13.1%. The signals are scaled by them. For simplicity, background processes are scaled by a factor of 1.18 [128].

The theoretical systematic uncertainties and the experimental systematic uncertainties described in Chapter 9 are modified by scale factors to take into account improvements expected in the HL-LHC. In this thesis, three scenarios are evaluated to quantify the impacts of these systematic uncertainties.

No syst unc. Only statistical uncertainties are considered. All background systematic uncertainties and

signal modeling systematic uncertainties described in Chapter 9 are ignored in this scenario.

Baseline Signal modelling systematic uncertainties are scaled according to the conventions for HL-LHC projections [129]. For the data-driven background uncertainties, the bootstrap statistical uncertainty is scaled by a factor of 0.5 because it includes not only the statistical uncertainty of the training samples but also the fluctuation due to the initial conditions of neural networks. The background systematic uncertainties are assumed to be identical as the Run-2 analysis. The summary of these uncertainty treatments are shown in Table 12.5.

Run2 syst unc. All same systematic uncertainties as the Run-2 analysis are used without any scale.

Table 12.5 Summary of scale factors applied to the systematic uncertainties in the baseline scenario.

Type	Scale Factor for the baseline scenario
Luminosity uncertainty	0.6
Jet related uncertainties	1.0
b-tagging efficiency uncertainty	0.5
Theoretical systematic uncertainties	0.5
Background bootstrap statistical uncertainty	0.5
Background systematic uncertainties	1.0

Results of the HL-LHC projection of the non-resonant $HH \to b\bar{b}b\bar{b}$ analysis in the systematic scenarios are shown in Table 12.6. In the baseline scenario, the discovery significance of the SM HH production is found to be 1.0 σ. Figure 12.4 shows the projected results of profile likelihood ratio scans for κ_λ in the systematic scenarios. The scans are derived with an assumption that the data is regarded as background + the SM HH signal hypothesis. A primary minimum value at $\kappa_\lambda = 1$ and a secondary minimum value around $\kappa_\lambda = 5$ can be observed. The latter one is caused by a combined effect of the smaller signal acceptance due to their soft kinematics and the higher theoretical HH cross-section. The constraint on the trilinear Higgs self-coupling in the baseline scenario is found to be $\kappa_\lambda \in [-1.6, 7.5]$ at 95% CI.

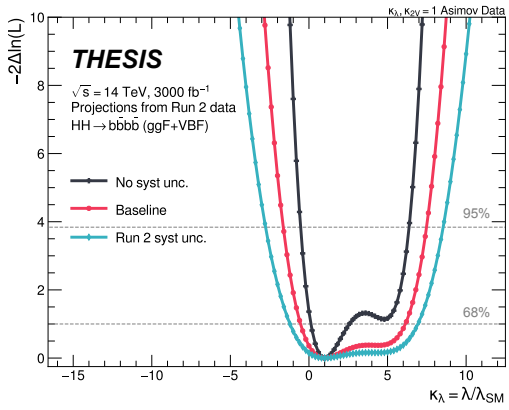

Figure 12.4 Profile likelihood ratio scans for κ_λ in the various systematic scenarios. The black line indicates the no syst unc. scenario, the red line is the baseline scenario and the blue line is the Run2 syst unc. scenario. They are derived with a SM Asimov dataset.

Table 12.6 Summary of the projected discovery significance of the SM HH production and the confidence intervals (CIs) for κ_λ at 3000 fb^{-1} at $\sqrt{s} = 14$ TeV for the systematic scenarios. The κ_λ ranges are allowed. The κ_λ confidence intervals are evaluated using an Asimov dataset with the SM hypothesis.

Scenarios	Discovery significance [σ]	κ_λ 68% CI	κ_λ 95% CI
No syst unc.	1.8	$[0.1, 2.7]$	$[-0.5, 6.4]$
Baseline	1.0	$[-0.5, 6.2]$	$[-1.6, 7.5]$
Run-2 syst unc.	0.6	$[-1.2, 7.0]$	$[-2.8, 8.6]$

12.2.2 Projected Sensitivity of HH Statistical Combination

In addition, this thesis presents the HH combination prospect using the $b\bar{b}b\bar{b}$, $b\bar{b}\gamma\gamma$ and $b\bar{b}\tau\tau$ channels in the HL-LHC. The HL-LHC prospects of the $HH \to b\bar{b}\gamma\gamma$ and $b\bar{b}\tau\tau$ analyses have been reported in Ref. [130]. The three analyses can be considered to be statistically independent because no impact of overlap events is observed in Section 12.1. To further know the potential sensitivity of the HH analyses, the projected combination using these channels is performed. Detail descriptions for the $HH \to b\bar{b}\gamma\gamma$ and $b\bar{b}\tau\tau$ analyses can be seen in Ref. [130].

Table 12.7 shows the discovery significances of the SM HH production on the statistical combination of the three channels. In the baseline scenario, the discovery significance is expected to be 3.4 σ. In that case of the no systematic uncertainty scenario, the discovery significance is expected to be 4.9 σ. This means we can potentially achieve to 4.9 σ even if the same analysis strategy as the Run-2 ones is used in the HL-LHC.

Table 12.8 shows the expected κ_λ constraints with the statistical combination in the HL-LHC. The constraints on κ_λ are expected to be $\kappa_\lambda \in [0.0, 2.5]$ ($[0.5, 1.6]$) at 95 (68)% CI in the baseline scenario.

Table 12.7 Projected discovery significances of the SM HH production combining the $b\bar{b}b\bar{b}$, $b\bar{b}\gamma\gamma$ and $b\bar{b}\tau\tau$ channels at 3000 fb^{-1} at $\sqrt{s}$ = 14 TeV for the systematic scenarios. They are evaluated using an Asimov dataset with the SM hypothesis.

	Discovery significance [σ]				Signal strength
Scenarios	$b\bar{b}b\bar{b}$	$b\bar{b}\gamma\gamma$	$b\bar{b}\tau\tau$	Combination	in HH combiation
No syst unc.	1.8	2.3	4.0	4.9	$1.0^{+0.22}_{-0.21}$
Baseline	1.0	2.2	2.8	3.4	$1.0^{+0.33}_{-0.30}$
Run2 syst unc.	0.6	1.1	1.5	1.9	$1.0^{+0.65}_{-0.53}$

In the no systematic uncertainty scenario, it is expected to be $\kappa_\lambda \in [0.3, 1.9]$ ($[0.7, 1.4]$) at 95 (68)% CI. The projected results show that the trilinear Higgs self-coupling will be promised to exist even if the HH production is not observed. In the HL-LHC, the trilinear Higgs self-coupling can be investigated with the precision of the electroweak baryogenesis, as described in Section 2.2.

Table 12.8 Summary of the projected confidence intervals (CIs) for κ_λ at 3000 fb^{-1} at $\sqrt{s}$ = 14 TeV for the systematic scenarios. The κ_λ ranges are allowed.

Scenarios	κ_λ 68% CI	κ_λ 95% CI
No syst unc.	[0.7, 1.4]	[0.3, 1.9]
Baseline	[0.5, 1.6]	[0.0, 2.5]
Run-2 syst unc.	[0.1, 2.4]	[−0.6, 5.6]

In addition, a simple combination of the SM HH measurements from the ATLAS and CMS experiments leads to the discovery significance of 5.8 σ in the statistical-only scenario and 4.4 σ in the baseline scenario (Appendix I). It should be noted that the CMS prospects I used here do not use the latest analysis strategy using the full Run-2 dataset and use the old ones [131, 132]. This means we expect to search for the SM HH production with higher sensitivity than what I show here. It will be promised to observe the HH production and measure the trilinear Higgs self-coupling if things are as the SM prediction at the HL-LHC.

12.3 Analysis Improvements for the Future Experiments

As discussed in the previous section, we expect to search for the SM HH production with a sensitivity of 5.8 σ in the statistical-only scenario and 4.4 σ in the baseline scenario with the combination in the ATLAS and CMS experiments. To further improve the sensitivity and ensure the discovery, I will present new ideas in the $HH \to b\bar{b}b\bar{b}$ analysis based on my experience.

12.3.1 Trigger Development

In the $HH \to b\bar{b}b\bar{b}$ analysis using the Run-2 dataset, the non-resonant $HH \to b\bar{b}b\bar{b}$ processes were found to be discarded by the trigger selection. In fact, the signal loss of the SM ggF HH process due to their soft kinematics of the decay b-jets is approximately 70% described in Section 6.6. To improve the sensitivity for future analysis, trigger development to increase signal acceptance is important. Recently, many upgrades, such as new reconstruction techniques, b-tagging algorithm improvements and a new data-taking strategy, have been implemented into the ATLAS trigger system for the Run-3 started in 2022. Therefore, I aggressively adopted these new techniques and suggested a new trigger strategy for the non-resonant $HH \to b\bar{b}b\bar{b}$ processes.

Multi b-jet trigger can be divided into two parts, jet kinematic selection and b-tagging selection. I optimized these selection criteria and improved the HH signal acceptance. In this section, the new trigger strategy will be discussed.

Optimization of jet kinematic selection

The main multi b-jet (2b2j) trigger used in the Run-2 analysis is prepared as the common trigger for all analyses targeting the final state with multiple b-jets. The jet E_{T} selection uses symmetric thresholds. For example, in the multi b-jet trigger in 2018, the hardware-based Level-1 (L1) trigger selection requires at least four jets with $E_{\mathrm{T}} > 15$ GeV and $|\eta| < 2.5$ (*L1_4J15p0ETA25*) and the software-based High-Level Trigger (HLT) selection requires at least four jets with $E_{\mathrm{T}} > 35$ GeV (*HLT_4j35*), as described in Table 5.1. However, E_{T} distributions of the decay b-jets of the SM $HH \to b\bar{b}b\bar{b}$ process reconstructed in the L1 trigger and the HLT are not symmetric, as can be seen in Figure 12.5. This means we can optimize the jet E_{T} thresholds in both L1 trigger and HLT and improve signal acceptance.

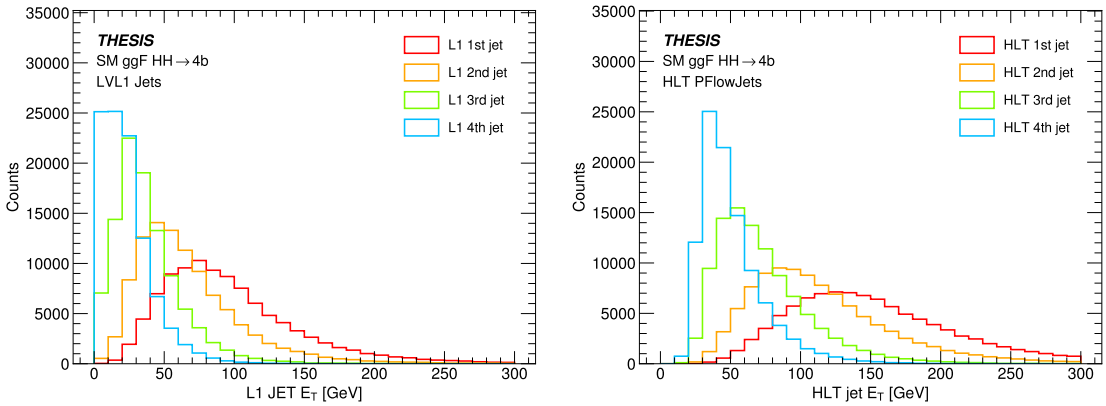

(a) L1 trigger (b) High Level Trigger

Figure 12.5 E_{T} distributions of the four leading jets reconstructed in (a) the hardware-based Level-1 (L1) trigger and (b) the software-based High-Level Trigger (HLT) for the SM $HH \to b\bar{b}b\bar{b}$ process. The red, orange, green and blue histograms show that of the first, second, third and fourth leading jets in E_{T}. If the jet is not reconstructed due to out of the detector acceptance, it is filled into a bin of 0 GeV.

Therefore, I optimized jet E_{T} selections in both L1 trigger and HLT. Figure 12.6(a) shows the trigger

efficiencies of each leading jet as a function of E_{T} threshold in the L1 trigger and the HLT for the SM $HH \to b\bar{b}b\bar{b}$ process. In the L1 trigger, any selection that requires a fourth leading jet is found to discard at least 20% of the SM signals. On the other hand, a selection that requires the first leading jet to be $E_{\mathrm{T}} > 45$ GeV can keep more than 90% of the SM signals. I thus prepared new selection criteria for the L1 trigger, where requires one jet with $E_{\mathrm{T}} > 45$ GeV and $|\eta| < 2.1$ and two extra jets with $E_{\mathrm{T}} > 15$ GeV and $|\eta| < 2.5$, referred to as *L1_J45p0ETA21_3J15p0ETA25*. The *eta* requirements are optimized to keep the acceptance after the E_{T} selection. The signal acceptance in the L1 trigger then increases from 53% to 73%. The improvement mainly comes from the removal of the fourth jet requirement. Similarly, I also prepared new jet selection criteria for the HLT that requires four jets with $E_{\mathrm{T}} > 80$ GeV, $E_{\mathrm{T}} > 55$ GeV, $E_{\mathrm{T}} > 28$ GeV and $E_{\mathrm{T}} > 20$ GeV (*HLT_j80_j55_j28_j20*), respectively. These E_{T} thresholds are optimized to keep more than 95% of the SM *HH* signals after the L1 trigger selection. The signal acceptance of the SM *HH* process in the Run-2 selection criteria is 50%, while that in the new selection criteria is 70%. It is improved by a factor of 1.4 on the jet kinematic selection. An increase of the data rate is acceptable because we can exploit the freed of L1 trigger bandwidth by the L1 trigger upgrades.

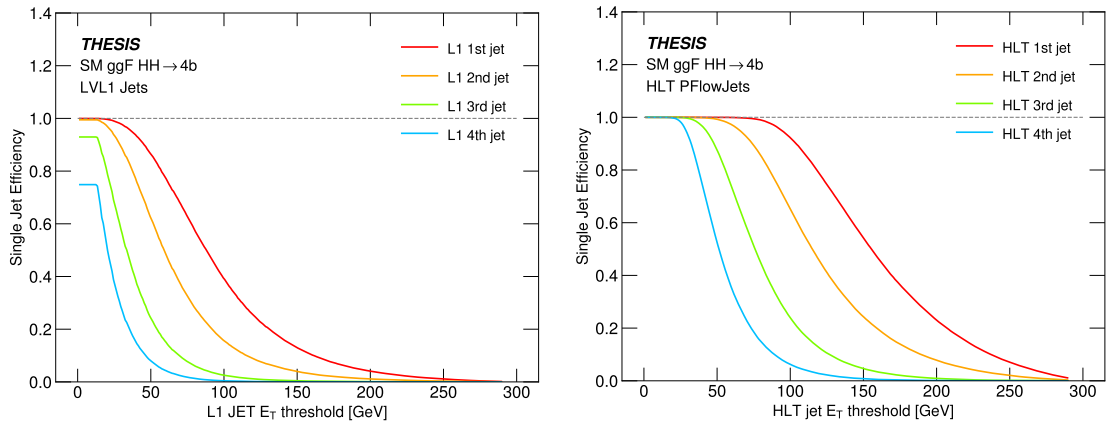

(a) L1 trigger (b) High Level Trigger

Figure 12.6 The trigger efficiencies of each leading jet as a function of E_{T} threshold in (a) the L1 trigger and (b) the HLT for the SM $HH \to b\bar{b}b\bar{b}$ process. The red, orange, green and blue histograms show that of the first, second, third and fourth leading jets in E_{T}. The HLT jet efficiencies show the relative ones to the new L1 trigger using only events passing *L1J45p0ETA21_3J15p0ETA25*.

Optimization of *b*-tagging selection

The *b*-tagging selection criteria for the new $HH \to b\bar{b}b\bar{b}$ trigger are selected according to a balance of the signal acceptance and the output data rate. The ATLAS trigger system is constrained by the bandwidth to store accepted events in HLT, and the output data rates in each trigger are strictly defined and controlled. A recent upgrade for the buffer increases the max bandwidth from 4 GB/s to 8 GB/s and allows us to store more events from 1.0 kHz to 1.7 kHz in the main physics stream. With the upgrade, the output data rate of up to 50 Hz is allowed for the new $HH \to b\bar{b}b\bar{b}$ trigger in the main physics

	Step	1st jet		2nd jet		3rd jet		4th jet		Rate
		E_{T} [GeV]	$\lvert\eta\rvert$	E_{T} [GeV]	$\lvert\eta\rvert$	E_{T} [GeV]	$\lvert\eta\rvert$	E_{T} [GeV]	$\lvert\eta\rvert$	
Run-2	L1	15	2.5	15	2.5	15	2.5	15	2.5	3.0 kHz
	HLT	35	2.4	35	2.4	35	2.4	35	2.4	2.5 kHz
Run-3	L1	45	2.1	15	2.5	15	2.5	×	×	7.5 kHz
	HLT	80	2.4	55	2.4	28	2.4	20	2.4	5.3 kHz

Table 12.9 Jet E_{T} and η thresholds and data rates for the Run-2 and Run-3 triggers. E_{T} selection requires E_{T} of the leading jet to be over the indicated value and η selection requires $|\eta|$ to be less than the indicated value. Data rates are estimated at an instantaneous luminosity of $2.0 \times 10^{34}\mathrm{cm}^{-2}\mathrm{s}^{-1}$.

stream. In addition, I exploit a dedicated stream called *delayed stream* to store more events. In the ATLAS trigger system, accepted events are usually reconstructed by the offline algorithms immediately to use the physics analysis. However, the rate is also constrained by the CPU resources, so that the rate of the main physics stream is forced to be up to 1.7 kHz. On the other hand, in the delayed stream, accepted events are directly recorded to tape and the offline reconstructions are performed when the CPU resources are available. The delayed stream can thus avoid the constraint due to the CPU resources and exploit the freed of bandwidth by the buffer upgrade. The additional rate of up to 200 Hz is allowed for the new $HH \to b\bar{b}b\bar{b}$ trigger in the delayed stream.

Table 12.10 shows the signal acceptances of the SM, $\kappa_\lambda = 5$ and 10 HH signals and the data rates in several b-tagging selection criteria. From the limit of output rate, the b-tagging selection criteria that require at least 3 b-jets with $E_{\mathrm{T}} > 20$ GeV at 85% working point (WP) is chosen for the main physics stream. Though the data rate is the almost same as the main multi b-jet trigger used in Run2, the signal acceptance of the SM HH process is improved by approximately 35% and that of the BSM HH process across the wide range of κ_λ values is also improved by approximately 10% relative to the main multi b-jet trigger used in Run2. For the delayed stream, the b-tagging selection criteria that require at least 2 b-jets with $E_{\mathrm{T}} > 20$ GeV at 77% working point (WP) is selected. The new $HH \to b\bar{b}b\bar{b}$ trigger in the delayed stream significantly improves the signal acceptance of the SM HH process by 80% and that of the BSM HH process by more than 50%. The new $HH \to b\bar{b}b\bar{b}$ triggers have been successfully included in the Run3 trigger menu [133] and are performed in the Run-3 data taking.

	Jet E_{T} thresholds	b-tagging		Signal acceptance			Rate
		b-jets	WP	SM	$\kappa_\lambda = 5$	$\kappa_\lambda = 10$	
Run-2	HLT_4j35_L1_4J15p0ETA25	2b35	60%	32%	20%	21%	27 Hz
Run-3	HLT_j80_j55_j28_j20 L1J45p0ETA21_3J15p0ETA25	3b20	85%	43%	23%	26%	30 Hz
		3b20	77%	37%	19%	22%	15 Hz
		3b20	70%	32%	16%	19%	10 Hz
		2b20	85%	61%	36%	39%	250 Hz
		2b20	77%	58%	33%	37%	160 Hz
		2b20	70%	55%	31%	35%	120 Hz
		2b20	60%	48%	26%	29%	80 Hz

Table 12.10 The signal acceptances of the SM, $\kappa_\lambda = 5$ and 10 HH signals and the data rates in several b-tagging selection criteria. $\{X\}b\{YY\}$ denotes a b-tagging selection criteria that requires at least X b-jets with $E_{\mathrm{T}} > YY$, where X indicates the number of b-jets and YY indicates E_{T} threshold. The b-tagging algorithm uses the DL1r algorithm. Data rates are estimated at an instantaneous luminosity of $2.0 \times 10^{34}\mathrm{cm}^{-2}\mathrm{s}^{-1}$.

12.3.2 Development of Additional Categories

I will discuss new ideas on the analysis strategy to further improve the sensitivity of the $HH \to b\bar{b}b\bar{b}$ analysis. In the $HH \to b\bar{b}b\bar{b}$ analysis, I adopted the analysis categorization that categorizes events inside the signal region into several categories and statistically improves the sensitivity, as described in Chapter 7. However, there is a limitation to improving the sensitivity with this approach in the future. The different approach that recovers the signal loss due to the analysis selection and exploits new phase space given by the trigger development must be thus considered.

Low p_{T} and 3b1l Categories

I suggest here two *outside* categories called *low p_T category* and *3b1l category*. In the $HH \to b\bar{b}b\bar{b}$ analysis, we also found that the main signal loss is caused by the b-jet selection, where at least 4 b-jets with $p_{\mathrm{T}} > 40$ GeV and b-tagged at 77% WP are required. Therefore, to recover the signal loss at this step, two *outside* categories are defined as described in Figure 12.7.

One is *low p_T category*, which picks up events with the fourth leading jet $p_{\mathrm{T}} \in (30, 40)$ GeV. The low p_{T} category is motivated by the kinematics of the BSM HH processes, because these signals have lower m_{HH} spectrum and the jet p_{T} distributions have a lower peak. Due to the jet kinematics difference between the low p_{T} category and the baseline 4b ggF signal region, I prepared here the analysis selection for the low p_{T} category that is briefly optimized to improve the sensitivity. The analysis selection is summarized below:

1. At least four jets with $p_{\mathrm{T}} > 30$ GeV and $|\eta| < 2.5$, but the 4th leading jet $p_{\mathrm{T}} \in (30, 40)$ GeV to make the low p_{T} category orthogonal to the baseline 4b ggF and VBF signal regions.
2. At least four b-tagged jets with 77% WP.
3. Use the same procedure to reconstruct two Higgs boson candidates as that used in the baseline described in Section 6.4.3.
4. Apply $|\Delta\eta_{HH}| < 1.5$ to reduce QCD multijet background, but no X_{wt} requirement because $X_{wt} < 1.5$ has the sensitivity.
5. Apply $X_{HH}^{Low p_{\mathrm{T}}} < 2.1$ to define the low p_{T} signal region, where $X_{HH}^{Low p_{\mathrm{T}}}$ is defined in Eq. 12.1.

$$X_{HH}^{Low p_{\mathrm{T}}} = \sqrt{\left(\frac{m_{H1} - 120\ \mathrm{GeV}}{0.1\ m_{H1}}\right)^2 + \left(\frac{m_{H2} - 111\ \mathrm{GeV}}{0.1\ m_{H2}}\right)^2}, \tag{12.1}$$

where the center values of m_{H1} and m_{H2} are optimized in the same procedure as the baseline and set to 120 GeV and 111 GeV, respectively. The low p_{T} category is defined to be orthogonal to the baseline 4b ggF and VBF signal regions by the jet p_{T} selection.

The other one is *3b1l category*, where pickups events with three b-tagged jets with 77% WP and one extra b-tagged jet with the looser b-tagging WP of 85% but failed with 77% (3b1l events). We use the b-tagging algorithm with the efficiency of 77% for the baseline 4b ggF and VBF signal regions, so that the signal acceptance in this step is less than 35%. The 3b1l category is thus motivated to recover events dropped at the four b-jet requirement. The extra b-tagging with 85% WP can reduce QCD multijet background and improve the sensitivity there. The same analysis selection as the baseline 4b ggF signal region is used for the 3b1l category because no large difference between 4b events and 3b1l events is observed. The 3b1l category is also defined to be orthogonal to the baseline 4b ggF and VBF signal regions by the b-tagging selection.

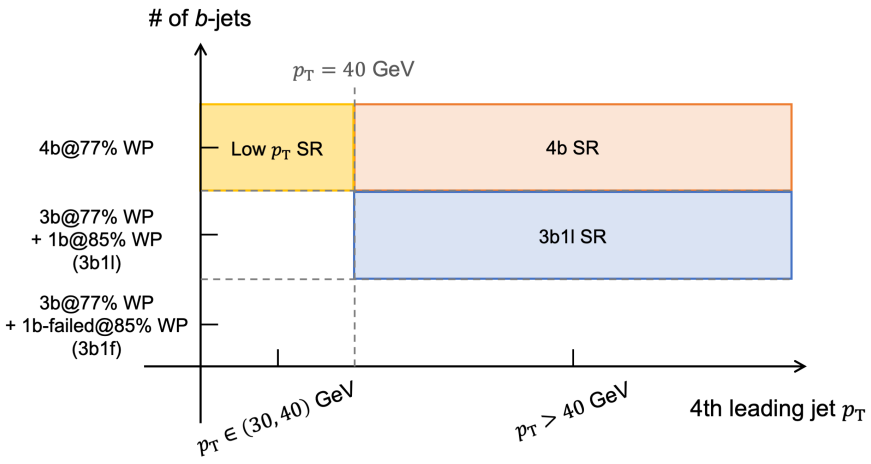

Figure 12.7 A illustration of the low p_{T} and 3b1l categories in the 2-D plane of the 4th leading jet p_{T} and the number of b-jets. The baseline 4b signal region (4b SR) is shown in the red box, the low p_{T} category is shown in the yellow box and the 3b1l category is shown in the blue box.

Background Estimation

We can optimize the background estimation procedure for both categories, in particular the low p_T category since the jet kinematics between the low p_T category and the baseline 4b ggF signal region are expected to be significantly different due to the differences on the analysis selection. However, the same background estimation procedure as the baseline 4b ggF channel is used in both low p_T and 3b1l categories to simplify this study. Good level of agreement between data and background prediction to check the potential of these categories is then observed in the CR1 kinematic reweighting and the 3b1f validation.

Expected Improvements

Table 12.11 shows the SM and $\kappa_\lambda = 10$ ggF HH signal yields and the background prediction yield in the baseline 4b ggF signal region, the low p_T signal region and the 3b1l signal region. As can be seen, the low p_T category can recover approximately 23% of the SM ggF HH events and 35% of the $\kappa_\lambda = 10$ ggF HH events with respect to that in the baseline 4b ggF signal region. The expected background yield is approximately the same amount of that in the baseline 4b ggF signal region. The 3b1l category can recover approximately 33% of the SM ggF HH events and 35% of the $\kappa_\lambda = 10$ ggF HH events. The expected background yield in the 3b1l category is also approximately the same amount of that in the baseline 4b ggF signal region.

Table 12.11 Yields of the SM and $\kappa_\lambda = 10$ ggF HH processes and the background prediction in the baseline 4b ggF signal region, the low p_T signal region and the 3b1l signal region.

	SM ggF HH	$\kappa_\lambda = 10$ ggF HH	Bakground Prediction
Baseline 4b ggF SR	29.1	181.0	1.56×10^4
Low p_T SR	6.8	62.5	1.31×10^4
3b1l SR	9.6	62.3	1.48×10^4

Figure 12.8 shows the sensitivity improvements on the ggF HH production cross-section limit as a function of κ_λ by the low p_T and 3b1l categories. The baseline 4b ggF signal region adopts the ggF categorization described in Chapter 7, but the low p_T and 3b1l categories don't use any categorizations. These expected limits are derived with only the background uncertainties except for the 3b1f non-closure uncertainty. The low p_T category can additionally improve the upper limits on the ggF HH production cross-sections in particular for the BSM processes by approximately 5% with respect to only the baseline 4b ggF signal region. The 3b1l category can also improve the upper limits by 5%. With the combined low p_T and 3b1l categories, totally 10% improvements across κ_λ variations are expected on the ggF HH production cross-section. We will need more studies, especially for the background validation, to implement these categories, but they are promised to improve the sensitivity in the $HH \to b\bar{b}b\bar{b}$ analysis as discussed above.

Due to the nature of our background estimation, we can not evaluate how much these outside categories can improve the sensitivity with the new $HH \to b\bar{b}b\bar{b}$ triggers. However, the new $HH \to b\bar{b}b\bar{b}$

triggers can extend the phase space that we use in the analysis to lower p_{T} and looser b-tagging so that the outside categories can further exploit it. Therefore, I expect that the combination of the new $HH \to b\bar{b}b\bar{b}$ triggers and the outside categories further improve the sensitivity more than what I show here.

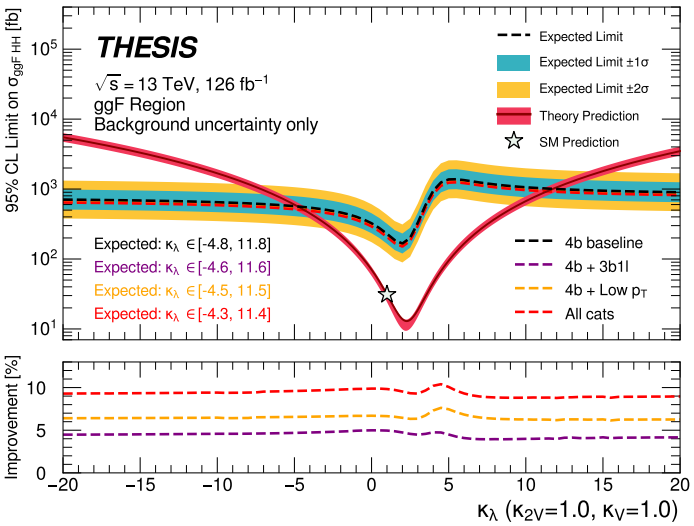

Figure 12.8 The 95% CL expected limit on the ggF HH cross-section as a function of κ_λ in the baseline 4b ggF signal region (black), the baseline + the low p_{T} signal region (orange), the baseline + the 3b1l signal region (purple) and these combined regions (red). The dashed lines denote the expected 95% CL upper limits. The inner blue band and outer yellow band indicate the $\pm1\sigma$ and $\pm2\sigma$ uncertainty ranges for only the baseline.

As discussed in this section, we can still improve the $HH \to b\bar{b}b\bar{b}$ analysis by more than 10% in the future. Similarly to the $HH \to b\bar{b}b\bar{b}$ analysis, the other channels can be potentially improved, in particular on the trigger. With future improvements including what I suggested here, it will be promised to observe the HH production and measure the trilinear Higgs self-coupling in the HL-LHC.

Chapter 13

Conclusion

It's been 10 years since the Higgs boson was discovered and the SM of particle physics was established. The SM succeeds in explaining the origin of *matters* we are familiar with and most of the phenomena. However, there are still open questions in the SM. The Higgs boson plays an important role in understanding the EWSB mechanism and proving BSM that attempts to resolve open questions. Though many studies of the Higgs boson property have been performed and have become increasingly precise, we have not found any clear evidence of new physics. I thought it is crucially important to not only increase the precision but also to expand the scope of these studies.

Therefore, I focused on non-resonant HH production with ggF and VBF. The non-resonant HH production has not been observed yet due to a rare production process. However, the search allows us more stringent constraints on the trilinear Higgs self-coupling and the $HHVV$ coupling. In addition, it allows us to access new physics not only at the electroweak scale but also at higher energy scale. The $b\bar{b}b\bar{b}$ final state is one of the most sensitive channels, thanks to the highest branching ratio. However, it's also a challenging channel due to a huge amount of QCD multijet background.

The thesis has outlined a search for non-resonant HH production in the $b\bar{b}b\bar{b}$ final state. This study was performed using 126 fb^{-1} of proton-proton collisions data at a center of mass energy of $\sqrt{s}$ = 13 TeV collected by the ATLAS detector at the LHC. The analysis is the first analysis targeting the non-resonant $HH \to b\bar{b}b\bar{b}$ with individual optimized selections for the ggF and VBF production processes in the ATLAS experiment. To improve the sensitivity, I provided two orthogonal selections targeting the ggF and VBF production and adopted the analysis categorizations. To properly estimate QCD multijet background, I utilized the fully data-driven approach using a neural network and validated with several tests. With the variety of improvements, the sensitivity on HH production is improved by totally 2.5 times for the ggF production and by 4.1 times for the VBF production with respect to the previous analyses. No significant excess is observed, and the exclusion limits at 95% CL are set. The observed (expected) upper limit of SM ggF and VBF HH production cross-section is 5.4 (8.4) times the SM prediction. The observed (expected) constraint of the trilinear Higgs self-coupling is $\kappa_\lambda \in [-3.9, 11.1]$ ($[-4.6, 10.8]$). The observed (expected) constraint of the $HHVV$ coupling is $\kappa_{2V} \in [-0.05, 2.11]$ ($[-0.05, 2.12]$). We have finally arrived at a precision of $O(100)\%$ on the κ_λ constraint via $HH \to b\bar{b}b\bar{b}$ analysis.

In addition, this thesis has presented interpretation results of Effective Field Theory (EFT) using the non-resonant $HH \to b\bar{b}b\bar{b}$ search. I performed the interpretations with two common EFT frameworks, the Higgs Effective Field Theory (HEF) and the Standard Model Effective Field Theory (SMEFT). The

EFT frameworks can parameterize a spectrum of potential high-energy BSM physics. In particular, this analysis provided the first SMEFT results from the HH analysis and the first constraint for c_H. They are also helpful to extend our physics scope to higher energy scale and exclude BSM models.

I also performed a statistical combination of non-resonant HH production in the $b\bar{b}b\bar{b}$, $bb\gamma\gamma$ and $bb\tau\tau$ final states to get the maximum constraints on the signal strength, the trilinear Higgs self-coupling and the $HHVV$ coupling. The observed (expected) upper limit of 2.4 (2.9) times on the signal strength of the SM ggF and VBF HH production is obtained at 95% CL. The observed (expected) constraint of the trilinear Higgs self-coupling is $\kappa_\lambda \in [-0.6, 6.6]$ ($[-1.0, 7.1]$). The observed (expected) constraint of the $HHVV$ coupling is $\kappa_{2V} \in [0.07, 2.03]$ ($[0.02, 2.06]$). These limits are the most stringent on these parameters. The result constrains the possible modification of the trilinear Higgs self-coupling on the BSM such as 2HDM as well as the UV-complete model discussed in Section 2.2, and gives us several understandings of the shape of the Higgs potential. This result also shows that the HHVV coupling exists.

Finally, I discussed the prospect of the non-resonant HH analysis and the trilinear Higgs self-coupling measurement in the HL-LHC. In the $HH \to b\bar{b}b\bar{b}$ analysis using 3000 fb^{-1} of proton-proton collisions at $\sqrt{s} = 14$ TeV, the SM HH production is expected to be searched for with a sensitivity of 1.0 (1.8) standard deviation in the baseline (statistical-only) strategy. In the HH statistical combination in the ATLAS and CMS experiments in the HL-LHC, the sensitivity is found to be 5.8 (4.4) standard deviation in the baseline (statistical-only) strategy. In addition, the HH analysis still has a potential to be improved furthermore, as I discussed in Section 12.3. I expect that the search for the SM HH production with a sensitivity of 5 standard deviation is promised in the HL-LHC with future improvements including what I suggested in this thesis. Thanks to the analysis method developed in this thesis, I expect that the trilinear Higgs self-coupling will be measured and provide proof of the EWSB mechanism in the HL-LHC.

Acknowledgements

I could not have written this thesis without the cooperation of many people. When I was a master student at Nagoya Univ., I was going to start working at private company after graduating from the master program. My supervisors convinced me to advance to the doctoral program. Needless to say, I don't regret anything. I was happy to study this analysis with N-Lab members and the ATLAS collaborators. I would like to take here to express my appreciation to you all.

First of all, I really appreciate Makoto Tomoto (Nagoya University, KEK[1]), Yu Nakahama (KEK), Yasuyuki Horii (Nagoya University) and Toru Iijima (Nagoya University). Makoto Tomoto, who is one of my supervisors, gave me a great opportunity to study in the doctoral program and gave a lot of comments on this analysis and this thesis. Yu Nakahama, who is the other of my supervisors, gave me great chances to study the HH analysis as well as the ATLAS trigger in the master program and organized the studies. Yasuyuki Horii gave a lot of comments on this thesis and always watched over me with his kind eyes. Toru Iijima always supported me with them. In particular, when I could not go to CERN and work well in Japan due to the COVID-19 pandemic, they negotiated so that I could study at CERN. Thanks to their supports, I concentrated on the analysis.

I would like to appreciate the ATLAS $HH \to b\bar{b}b\bar{b}$ analysis members and the HH combination members. Maximilian J Swiatlowski (TRIUMF) and Rafael Teixeira De Lima (SLAC) organized the $HH \to b\bar{b}b\bar{b}$ analysis team and gave me a lot of advice on the analysis. Max gave also many comments on not only the analysis but also this thesis. Chris Gubbels (University of British Columbia) and Iza Veliscek (University of Oxford) worked with me on finalizing our results. It was hard but I enjoyed working with you. Rui Zhang (University of Wisconsin) organized the ATLAS HH combination team, and we could publish our great results thanks to your great organization. Teng Jian Khoo (Humboldt University Berlin), Chris Pollard (University of Warwick) and Marco Valente (TRIUMF) gave me a lot of comments on the $HH \to b\bar{b}b\bar{b}$ trigger study. I really enjoyed working with all the analysis members including the other members I could not put here due to a lack of space.

I would like to express my appreciation to the ATLAS Japan members. Masahiro Morinaga (ICEPP[2]), Shion Chen (ICEPP) and Shunichi Akatsuka (Kyoto University) shared a lot of time at CERN as roommates in the master program. I thank them for suggesting interesting animes, instructing playing mahjongg, cooking ultimate curry, and instructing *double meals* at dinner. I will never forget eating all-you-can-eat sushi and then cheese fondue for dinner the day before returning to Japan. Hiroaki Hibi (Kobe University) and Yoshihiro Shimogama (Waseda University) shared a lot of time at CERN as roommates in the doctoral program. I was excited when Shimogama-kun found a burned car and told me it at 3

[1] High Energy Accelerator Research Organization

[2] International Center for Elementary Particle Physics and Department of Physics, The University of Tokyo

a.m. I really enjoyed drinking, drinking and drinking with Hibi-kun. Kenta Uno (Niigata University) and Atsushi Mizukami (KEK) took me out for a drink at CERN as well as KEK. Thanks for always treating me to drink! Thanks to all the members, I could refresh myself and enjoy my life at CERN.

I would like to thank the N-lab member, in particlar my colleagues, at Nagoya University. Yuki Sue (Nagoya University) and Hikari Hirata (Nagoya University) shared the tough time of the doctoral program with me. Sue-shi often went to *Toritori-tei*, which is our favorite izakaya, for drink with me, and we always tottered when going back to the N-lab. I will never forget Hirata-san said "I hate you"[3] at the N-lab welcome party, where we talked for the first time. But I feel so relieved now since she gets along with me. I could learn many things from my excellent colleagues and improve myself. I am glad to have met them and worked together.

Finally, I deeply appreciate my family. They always asked me "when will you graduate and work?" laughingly. I will finally be able to answer the question. Thanks to a lot of support from my family, I could study particle physics in the doctoral program as well as the master program and write this thesis.

This work was financially supported by JST SPRING, Grant Number JPMJSP2125. I would like to take this opportunity to thank the "Interdisciplinary Frontier Next-Generation Researcher Program of the Tokai Higher Education and Research System".

[3] According to her, it's "don't like" not "hate".

Appendices

Appendix A

HH Signal Reweighting

A.1 *ggF* κ_λ Reweighting

It is not easy to produce all signal samples with a wide range of κ_λ and κ_{2V} coupling values, because MC production is computationally expensive and takes a lot of time. Therefore, this analysis employs a reweighting method to model the cross-section and kinematic distributions of HH signals across the wide parameter space for κ_λ and κ_{2V}. The cross-section and kinematic distributions of the HH production processes fundamentally depend on the relevant coupling values. The *ggF* HH production cross-section and kinematics depend on κ_λ and k_t, as can be seen in Figure 2.9(b). The differential *ggF* HH cross-section on m_{HH} can be expressed as a function of κ_λ and k_t:

$$\frac{d\sigma_{ggF}(\kappa_\lambda, k_t)}{dm_{HH}} = |A(\kappa_\lambda, k_t)|^2 = \left|\kappa_\lambda k_t M_\triangle(m_{HH}) + k_t^2 M_\square(m_{HH})\right|^2 \tag{A.1}$$

$$= \kappa_\lambda^2 k_t^2 |M_\triangle(m_{HH})|^2 + \kappa_\lambda k_t^3 \left[M_\triangle^*(m_{HH}) M_\square(m_{HH}) + M_\square^*(m_{HH}) M_\triangle(m_{HH})\right] + k_t^4 |M_\square(m_{HH})|^2 \tag{A.2}$$

$$= \kappa_\lambda^2 k_t^2 a_1(m_{HH}) + \kappa_\lambda k_t^3 a_2(m_{HH}) + k_t^4 a_3(m_{HH}), \tag{A.3}$$

where $M_\triangle(m_{HH})$ indicates a contribution of the triangle diagram shown in Figure 2.9(a) and $M_\square(m_{HH})$ is of the box diagram shown in Figure 2.9(b) as a function of m_{HH}. In this analysis, the k_t coupling is set to the SM value of 1 and Eq. A.3 is thus simplified to an equation depending on only the κ_λ coupling value. The differential *ggF* HH cross-section on m_{HH} as a function of κ_λ can be then given by:

$$\frac{d\sigma_{ggF}(\kappa_\lambda)}{dm_{HH}} = \kappa_\lambda^2 a_1(m_{HH}) + \kappa_\lambda a_2(m_{HH}) + a_3(m_{HH}) \tag{A.4}$$

where a_1, a_2 and a_3 have a dependence on m_{HH}. The reweighting function used in this analysis is based on Eq. A.4. a_1, a_2 and a_3 in Eq. A.4 can not be trivially derived for a given κ_λ, but they can be mathematically determined by solving a set of linear equations using three different κ_λ samples in each m_{HH} bin. Therefore, the values of a_i are solved using three *ggF* HH samples with $\kappa_\lambda = 0, 1$ and 20, where no decays and cuts are applied to be common to all HH analyses [109]. Weights for every κ_λ value are then derived in each m_{HH} bin of 10 GeV by taking the ratio between the target κ_λ coupling and the SM. To model kinematic distributions of the target κ_λ coupling, these weights are applied to the SM *ggF* HH samples based on their truth m_{HH} values. Truth m_{HH} is selected here based on the assumption

that signal kinematics vary coherently with m_{HH} and signal acceptance times efficiency on the analysis selections only depends on m_{HH}. The reweighting procedure is only used to model the signal shapes. Therefore, these reweighted samples are normalized by their cross-section predictions [48].

A.2 VBF κ_λ and κ_{2V} Reweighting

VBF HH samples with a wide range of κ_λ and κ_{2V} are also modelled by the same reweighting procedure as the ggF HH samples. The VBF HH process depends on 3 diagrams in Figure 2.12. The differential VBF HH cross-section can be expressed as:

$$\frac{d\sigma_{VBF}(\kappa_\lambda,\kappa_{2V},\kappa_V)}{dm_{HH}} = |A(\kappa_\lambda,\kappa_{2V},\kappa_V)|^2 = \left|\kappa_V\kappa_\lambda M_s(m_{HH}) + \kappa_V^2 M_t(m_{HH}) + \kappa_{2V} M_x(m_{HH})\right|^2 \tag{A.5}$$

$$= \kappa_V^2\kappa_\lambda^2 a_1(m_{HH}) + \kappa_V^4 a_2(m_{HH}) + \kappa_{2V}^2 a_3(m_{HH}) + \kappa_V^3\kappa_\lambda a_4(m_{HH}) + \kappa_V\kappa_\lambda\kappa_{2V} a_5(m_{HH}) + \kappa_V^2\kappa_{2V} a_6(m_{HH}) \tag{A.6}$$

This requires a combination of six different samples to determine a_i. These samples are required only to be linearly independent of each other when selecting them. In this analysis, the six samples with $(\kappa_\lambda,\kappa_{2V},\kappa_V) = (1,1,1), (1,1.5,1), (2,1,1), (10,1,1), (1,1,0.5)$ and $(-5,1,0.5)$ are used. The reweighting function is then derived from these samples:

$$\begin{aligned}
\frac{d\sigma_{VBF}}{dm_{HH}}(\kappa_\lambda,\kappa_{2V},\kappa_V) = {} & \left(\frac{68\kappa_{2V}^2}{135} - 4\kappa_{2V}\kappa_V^2 + \frac{20\kappa_{2V}\kappa_V\kappa_\lambda}{27} + \frac{772\kappa_V^4}{135} - \frac{56\kappa_V^3\kappa_\lambda}{27} + \frac{\kappa_V^2\kappa_\lambda^2}{9}\right) \times \frac{d\sigma_{VBF}}{dm_{HH}}(1,1,1) \\
& + \left(-\frac{4\kappa_{2V}^2}{5} + 4\kappa_{2V}\kappa_V^2 - \frac{16\kappa_V^4}{5}\right) \times \frac{d\sigma_{VBF}}{dm_{HH}}\left(1,\frac{3}{2},1\right) \\
& + \left(\frac{11\kappa_{2V}^2}{60} + \frac{\kappa_{2V}\kappa_V^2}{3} - \frac{19\kappa_{2V}\kappa_V\kappa_\lambda}{24} - \frac{53\kappa_V^4}{30} + \frac{13\kappa_V^3\kappa_\lambda}{6} - \frac{\kappa_V^2\kappa_\lambda^2}{8}\right) \times \frac{d\sigma_{VBF}}{dm_{HH}}(2,1,1) \\
& + \left(-\frac{11\kappa_{2V}^2}{540} + \frac{11\kappa_{2V}\kappa_V\kappa_\lambda}{216} + \frac{13\kappa_V^4}{270} - \frac{5\kappa_V^3\kappa_\lambda}{54} + \frac{\kappa_V^2\kappa_\lambda^2}{72}\right) \times \frac{d\sigma_{VBF}}{dm_{HH}}(10,1,1) \\
& + \left(\frac{88\kappa_{2V}^2}{45} - \frac{16\kappa_{2V}\kappa_V^2}{3} + \frac{4\kappa_{2V}\kappa_V\kappa_\lambda}{9} + \frac{152\kappa_V^4}{45} - \frac{4\kappa_V^3\kappa_\lambda}{9}\right) \times \frac{d\sigma_{VBF}}{dm_{HH}}\left(1,1,\frac{1}{2}\right) \\
& + \left(\frac{8\kappa_{2V}^2}{45} - \frac{4\kappa_{2V}\kappa_V\kappa_\lambda}{9} - \frac{8\kappa_V^4}{45} + \frac{4\kappa_V^3\kappa_\lambda}{9}\right) \times \frac{d\sigma_{VBF}}{dm_{HH}}\left(-5,1,\frac{1}{2}\right)
\end{aligned} \tag{A.7}$$

For the VBF κ_λ reweighting, when κ_{2V} and κ_V are set to the SM value of 1, the second, fifth and sixth terms are zero. As a result, Eq. A.7 is simplified to only three terms and is expressed as:

$$\begin{aligned}
\frac{d\sigma_{VBF}}{dm_{HH}}(\kappa_\lambda,\kappa_{2V}=1,\kappa_V=1) = {} & \left(\frac{\kappa_\lambda^2}{9} - \frac{4\kappa_\lambda}{3} + \frac{20}{9}\right) \times \frac{d\sigma_{VBF}}{dm_{HH}}(1,1,1) \\
& \left(-\frac{\kappa_\lambda^2}{8} + \frac{11\kappa_\lambda}{8} - \frac{5}{4}\right) \times \frac{d\sigma_{VBF}}{dm_{HH}}(2,1,1) \\
& \left(\frac{\kappa_\lambda^2}{72} - \frac{\kappa_\lambda}{24} + \frac{1}{36}\right) \times \frac{d\sigma_{VBF}}{dm_{HH}}(10,1,1)
\end{aligned} \tag{A.8}$$

In this analysis, VBF HH samples with varied κ_λ and κ_{2V} are modelled by this reweighting function using the six basis samples.

A.3 HEFT and SMEFT Reweighting

Similarly, signal samples with various HEFT or SMEFT coefficient values are modelled by applying the reweighting method to the SM ggF HH sample. Only ggF production is considered for the HEFT and SMEFT results in this analysis because the process is the largest cross-section in the HH production.

The differential HH cross-section for HEFT can be expressed with the HEFT coupling combinations.

$$\begin{aligned}\frac{d\sigma_{HH}}{dm_{HH}} &= \text{Poly}(\mathbf{A}, c_{HHH}, c_{t\bar{t}H}, c_{t\bar{t}HH}, c_{ggH}, c_{ggHH}|m_{HH}) \\ &= A_1 c_{t\bar{t}H}^4 + A_2 c_{t\bar{t}HH}^2 + (A_3 c_{t\bar{t}H}^2 + A_4 c_{ggH}^2)\cdot c_{HHH}^2 + A_5 c_{ggHH}^2 + (A_6 c_{t\bar{t}HH} + A_7 c_{t\bar{t}H} c_{HHH})\cdot c_{HHH}^2 \\ &+ (A_8 c_{t\bar{t}H} c_{HHH} + A_9 c_{ggH} c_{HHH})\cdot c_{t\bar{t}HH} + A_{10} c_{t\bar{t}HH} c_{ggHH} + (A_{11} c_{ggH} c_{HHH} + A_{12} c_{ggHH})\cdot c_{t\bar{t}H}^2 \\ &+ (A_{13} c_{HHH} c_{ggH} + A_{14} c_{ggHH})\cdot c_{t\bar{t}H} c_{HHH} + A_{15} c_{ggH} c_{ggHH} c_{HHH} + A_{16} c_{t\bar{t}H}^3 c_{ggH} \\ &+ A_{17} c_{t\bar{t}H} c_{t\bar{t}HH} c_{ggH} + A_{18} c_{t\bar{t}H} c_{ggH}^2 c_{HHH} + A_{19} c_{t\bar{t}H} c_{ggH} c_{ggHH} + A_{20} c_{t\bar{t}H}^2 c_{ggH}^2 \\ &+ A_{21} c_{t\bar{t}HH} c_{ggH}^2 + A_{22} c_{ggH}^3 c_{HHH} + A_{23} c_{ggH}^2 c_{ggHH},\end{aligned} \tag{A.9}$$

where A_i $(i = 1, 2, ..., 23)$ are differential coefficients as a function of m_{HH}. In this analysis, the A_i values provided in Ref. [134] are used. They have been evaluated in the m_{HH} range between 240 GeV to 1040 GeV in bins of 20 GeV at NLO. Events with $m_{HH} > 1040$ GeV are reweighted by the weight in the highest m_{HH} bin with a central value of 1030 GeV.

Similarly, the differential HH cross-section for SMEFT can be expressed with the SMEFT coupling combinations.

$$\begin{aligned}\frac{d\sigma_{HH}}{dm_{HH}} &= \text{Poly}(\mathbf{A}, c_H, c_{H\Box}, c_{tH}, c_{tG}, c_{HG}|m_{HH}) \\ &= 1 + A_1 c_H + A_2 c_{H\Box} + A_3 c_{tH} + A_4 c_{tG} + A_5 c_{HG} + A_6 c_H^2 + A_7 c_{tH}^2 + A_8 c_{H\Box}^2 + A_9 c_{tG}^2 \\ &+ A_{10} c_{HG}^2 + A_{11} c_H c_{H\Box} + A_{12} c_H c_{tH} + A_{13} c_H c_{tG} + A_{14} c_H c_{HG} + A_{15} c_{H\Box} c_{tH} \\ &+ A_{16} c_{H\Box} c_{tG} + A_{17} c_{H\Box} c_{HG} + A_{18} c_{tH} c_{tG} + A_{19} c_{tH} c_{HG} + A_{20} c_{tG} c_{HG}\end{aligned} \tag{A.10}$$

Because there are no available SMEFT samples at NLO, these A_i values are derived at LO with the same setup as the HEFT reweighting. Therefore, additional k-factors are applied to the SMEFT samples. The k-factors are derived from the ratio of the NLO to LO cross-section at the equivalent HEFT points using the HEFT to SMEFT translation [58]. They have been also derived in the m_{HH} range between 240 GeV to 1040 GeV in bins of 20 GeV, similarly to the HEFT reweighting.

Appendix B

Formula for Estimating Significance

I follow the recommendation in Ref. [135] to estimate significance (Z) indicating a consistency between the observed data (n) and the background estimation ($b \pm \sigma$). The recommended formula to use for estimating significance is given by

$$Z = \begin{cases} +\sqrt{2\left(n \times \ln\left[\frac{n(b+\sigma^2)}{b^2+n\sigma^2}\right] - \frac{b^2}{\sigma^2}\ln\left[1+\frac{\sigma^2(n-b)}{b(b+\sigma^2)}\right]\right)} & \text{if } n > b \\ -\sqrt{2\left(n \times \ln\left[\frac{n(b+\sigma^2)}{b^2+n\sigma^2}\right] - \frac{b^2}{\sigma^2}\ln\left[1+\frac{\sigma^2(n-b)}{b(b+\sigma^2)}\right]\right)} & \text{if } n < b. \end{cases} \tag{B.1}$$

This formula is based on the asymptotic formulae for the distributions of profile likelihood test statistics. Detail discussions, such as the derivation approach and the validation tests, are shown in Ref. [135].

This formula is used in plots in the validation studies of our background estimation discussed in Chapter chap:bckd-estimation.

Appendix C

Kinematic Reweighting Plots

This section shows kinematic distribution plots of 4b data and 2b data before and after the neural network (NN) reweighting. As can be seen, there are large differences in these kinematics between 4b and 2b data before the NN reweighting. After the NN reweighting, good agreements are observed on all kinematic variables. The NN reweighting is validated to work well on not only m_{HH} but also the other kinematic variables.

C.1 ggF channel CR1

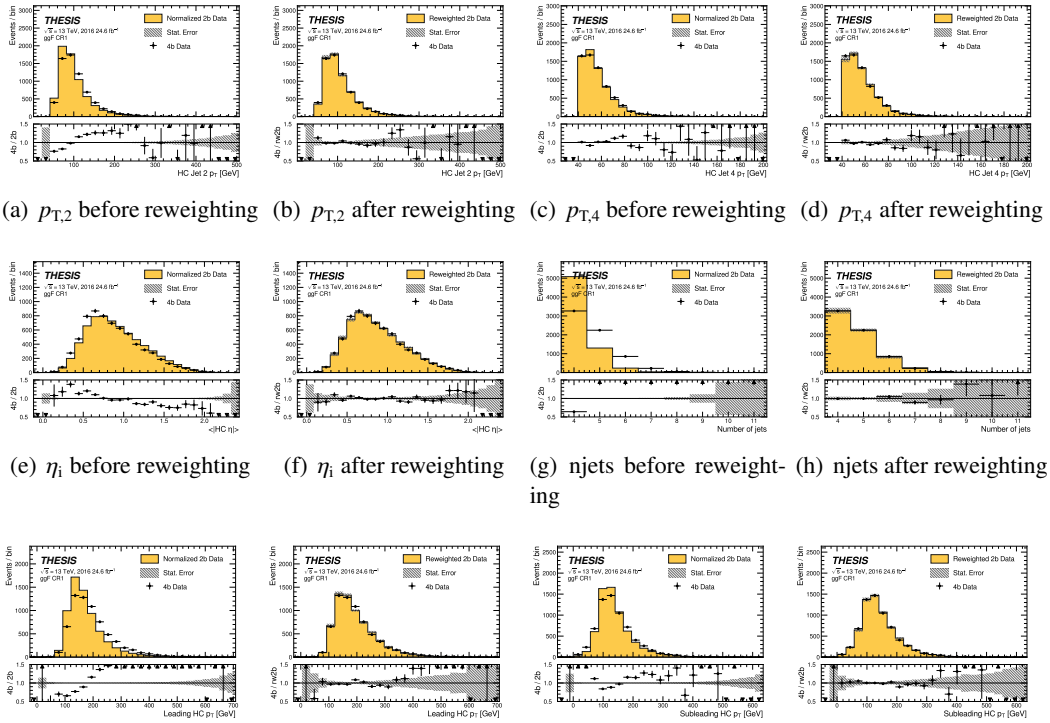

(a) $p_{\mathrm{T},2}$ before reweighting (b) $p_{\mathrm{T},2}$ after reweighting (c) $p_{\mathrm{T},4}$ before reweighting (d) $p_{\mathrm{T},4}$ after reweighting

(e) η_{i} before reweighting (f) η_{i} after reweighting (g) njets before reweighting (h) njets after reweighting

(i) $p_{\mathrm{T},H1}$ before reweighting (j) $p_{\mathrm{T},H1}$ after reweighting (k) $p_{\mathrm{T},H2}$ before reweighting (l) $p_{\mathrm{T},H2}$ after reweighting

Figure C.1 Kinematic distributions of normalized 2b data, reweighted 2b data and 4b data in the ggF control region 1 in 2016. For the normalized 2b data, the statistic uncertainty includes only 2b poisson uncertainty. For the reweighted 2b data, the statistic uncertainty includes 2b poisson uncertainty and the bootstrap statistic uncertainty.

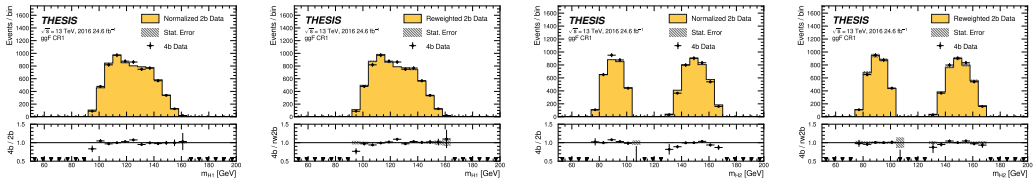

(a) m_{H1} before reweighting (b) m_{H1} after reweighting (c) m_{H2} before reweighting (d) m_{H2} after reweighting

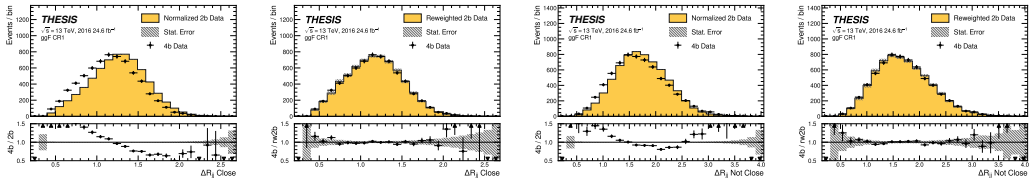

(e) $\Delta R_{jj,1}$ before reweighting (f) $\Delta R_{jj,1}$ after reweighting (g) $\Delta R_{jj,2}$ before reweighting (h) $\Delta R_{jj,2}$ after reweighting

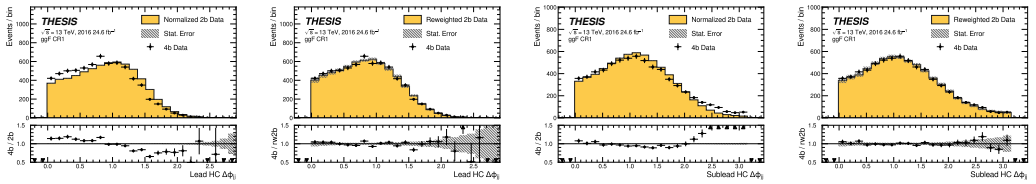

(i) $\Delta\phi_{H1}$ before reweighting (j) $\Delta\phi_{H1}$ after reweighting (k) $\Delta\phi_{H2}$ before reweighting (l) $\Delta\phi_{H2}$ after reweighting

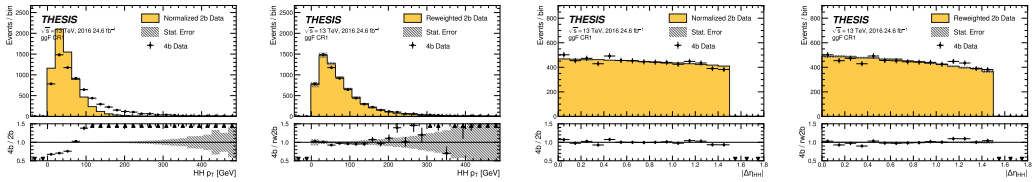

(m) $p_{T,HH}$ before reweighting (n) $p_{T,HH}$ after reweighting (o) $\Delta\eta_{HH}$ before reweighting (p) $\Delta\eta_{HH}$ after reweighting

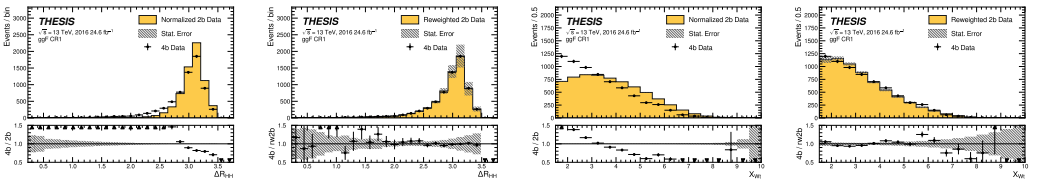

(q) ΔR_{HH} before reweighting (r) ΔR_{HH} after reweighting (s) X_{wt} before reweighting (t) X_{wt} after reweighting

Figure C.2 Kinematic distributions of normalized 2b data, reweighted 2b data and 4b data in the ggF control region 1 in 2016. For the normalized 2b data, the statistic uncertainty includes only 2b poisson uncertainty. For the reweighted 2b data, the statistic uncertainty includes 2b poisson uncertainty and the bootstrap statistic uncertainty.

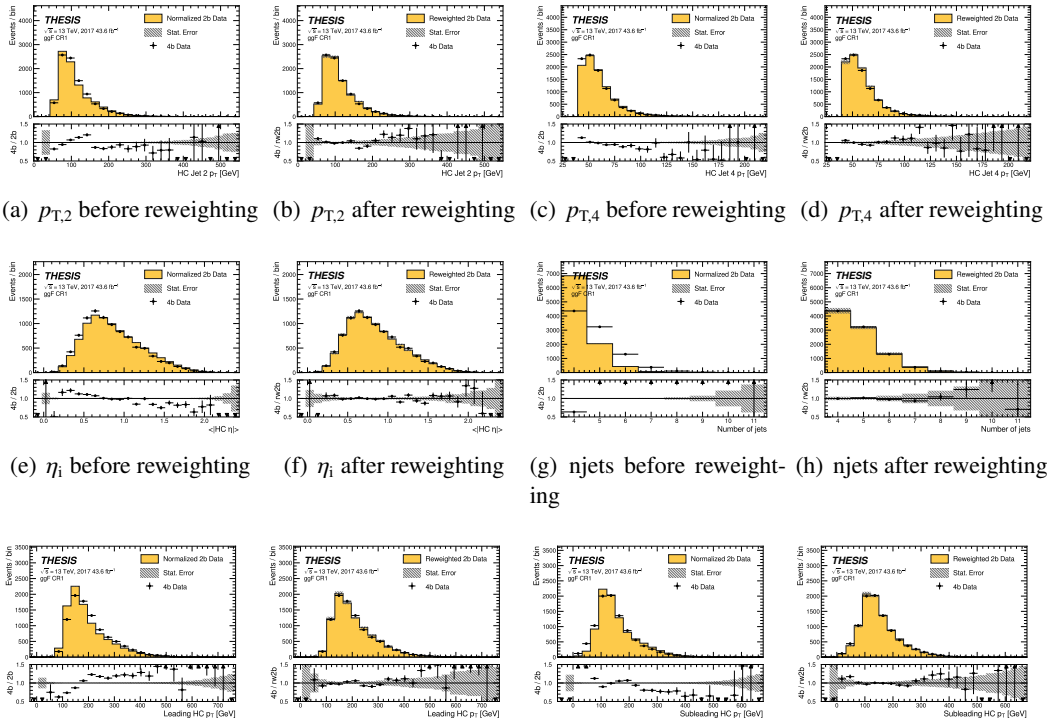

(a) $p_{T,2}$ before reweighting (b) $p_{T,2}$ after reweighting (c) $p_{T,4}$ before reweighting (d) $p_{T,4}$ after reweighting

(e) η_i before reweighting (f) η_i after reweighting (g) njets before reweighting (h) njets after reweighting

(i) $p_{T,H1}$ before reweighting (j) $p_{T,H1}$ after reweighting (k) $p_{T,H2}$ before reweighting (l) $p_{T,H2}$ after reweighting

Figure C.3 Kinematic distributions of normalized 2b data, reweighted 2b data and 4b data in the ggF control region 1 in 2017. For the normalized 2b data, the statistic uncertainty includes only 2b poisson uncertainty. For the reweighted 2b data, the statistic uncertainty includes 2b poisson uncertainty and the bootstrap statistic uncertainty.

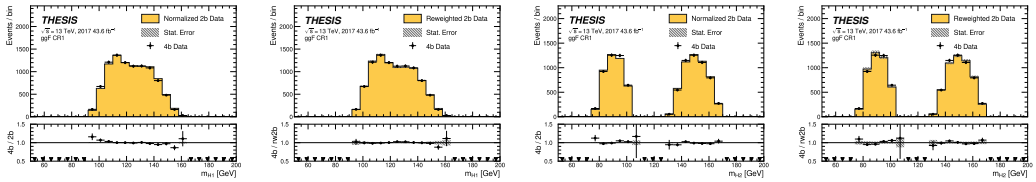

(a) m_{H1} before reweighting (b) m_{H1} after reweighting (c) m_{H2} before reweighting (d) m_{H2} after reweighting

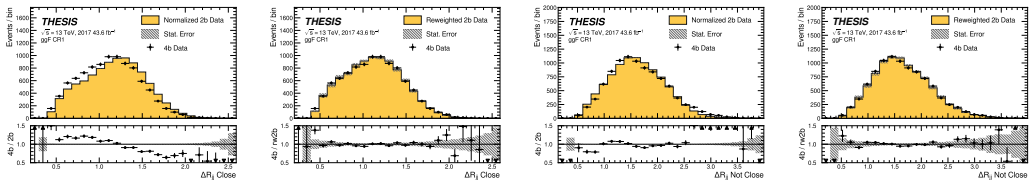

(e) $\Delta R_{jj,1}$ before reweighting (f) $\Delta R_{jj,1}$ after reweighting (g) $\Delta R_{jj,2}$ before reweighting (h) $\Delta R_{jj,2}$ after reweighting

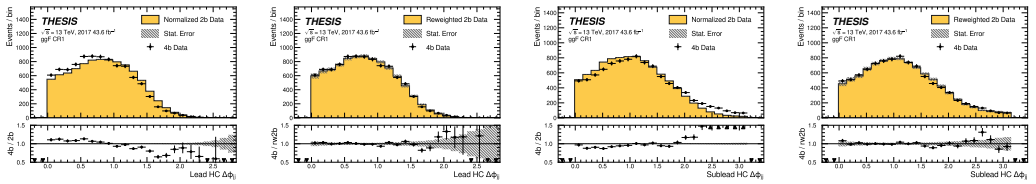

(i) $\Delta\phi_{H1}$ before reweighting (j) $\Delta\phi_{H1}$ after reweighting (k) $\Delta\phi_{H2}$ before reweighting (l) $\Delta\phi_{H2}$ after reweighting

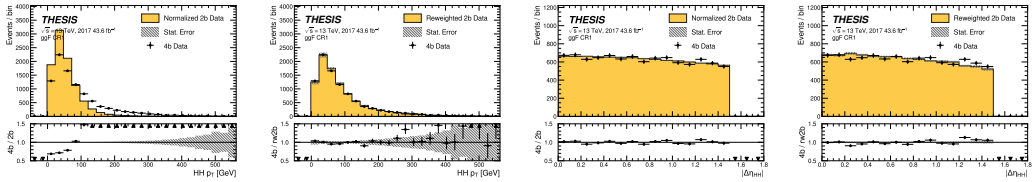

(m) $p_{T,HH}$ before reweighting (n) $p_{T,HH}$ after reweighting (o) $\Delta\eta_{HH}$ before reweighting (p) $\Delta\eta_{HH}$ after reweighting

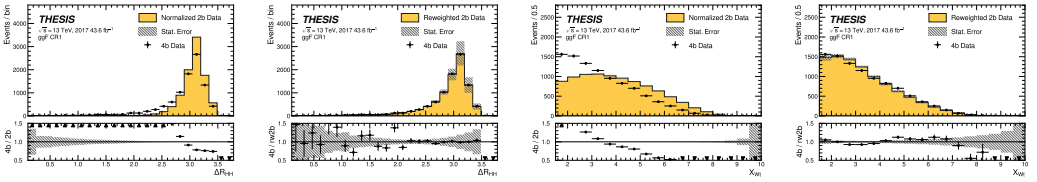

(q) ΔR_{HH} before reweighting (r) ΔR_{HH} after reweighting (s) X_{wt} before reweighting (t) X_{wt} after reweighting

Figure C.4 Kinematic distributions of normalized 2b data, reweighted 2b data and 4b data in the ggF control region 1 in 2017. For the normalized 2b data, the statistic uncertainty includes only 2b poisson uncertainty. For the reweighted 2b data, the statistic uncertainty includes 2b poisson uncertainty and the bootstrap statistic uncertainty.

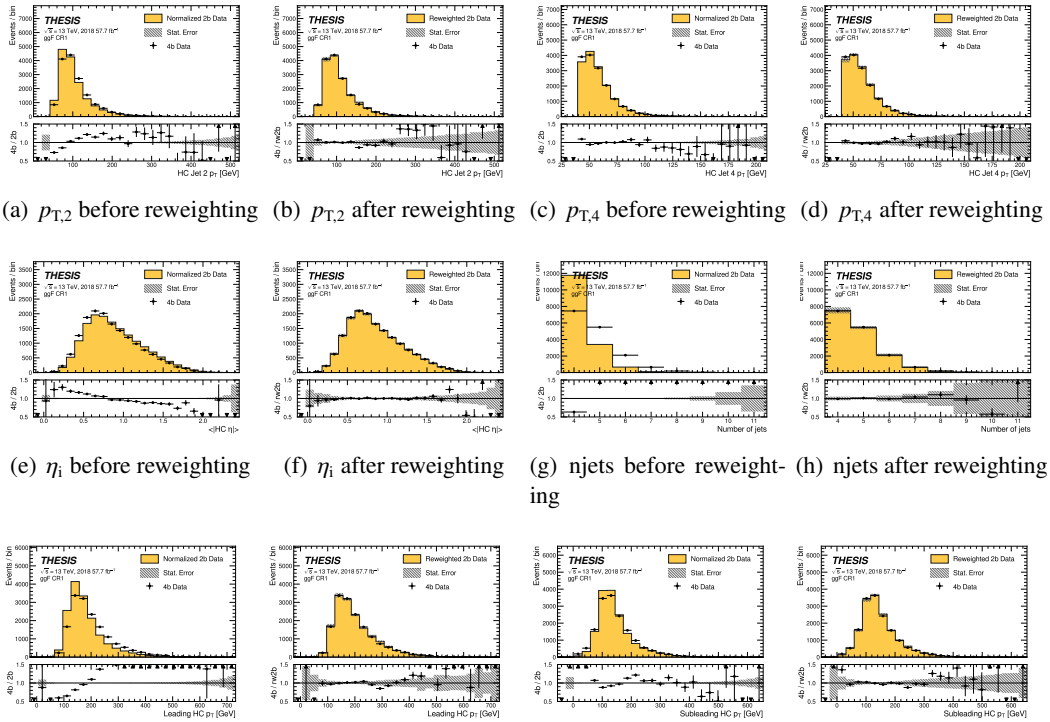

(a) $p_{T,2}$ before reweighting (b) $p_{T,2}$ after reweighting (c) $p_{T,4}$ before reweighting (d) $p_{T,4}$ after reweighting

(e) η_i before reweighting (f) η_i after reweighting (g) njets before reweighting (h) njets after reweighting

(i) $p_{T,H1}$ before reweighting (j) $p_{T,H1}$ after reweighting (k) $p_{T,H2}$ before reweighting (l) $p_{T,H2}$ after reweighting

Figure C.5 Kinematic distributions of normalized 2b data, reweighted 2b data and 4b data in the ggF control region 1 in 2018. For the normalized 2b data, the statistic uncertainty includes only 2b poisson uncertainty. For the reweighted 2b data, the statistic uncertainty includes 2b poisson uncertainty and the bootstrap statistic uncertainty.

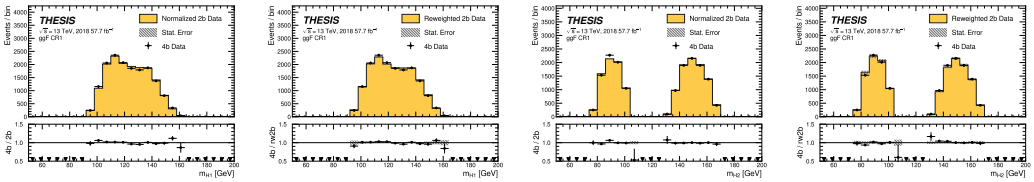

(a) m_{H1} before reweighting (b) m_{H1} after reweighting (c) m_{H2} before reweighting (d) m_{H2} after reweighting

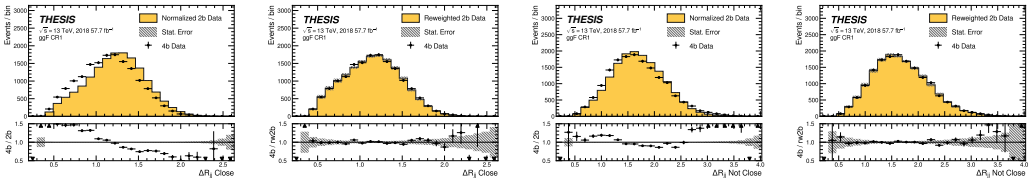

(e) $\Delta R_{jj,1}$ before reweighting (f) $\Delta R_{jj,1}$ after reweighting (g) $\Delta R_{jj,2}$ before reweighting (h) $\Delta R_{jj,2}$ after reweighting

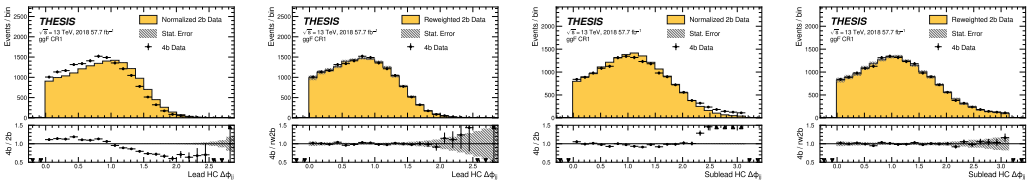

(i) $\Delta\phi_{H1}$ before reweighting (j) $\Delta\phi_{H1}$ after reweighting (k) $\Delta\phi_{H2}$ before reweighting (l) $\Delta\phi_{H2}$ after reweighting

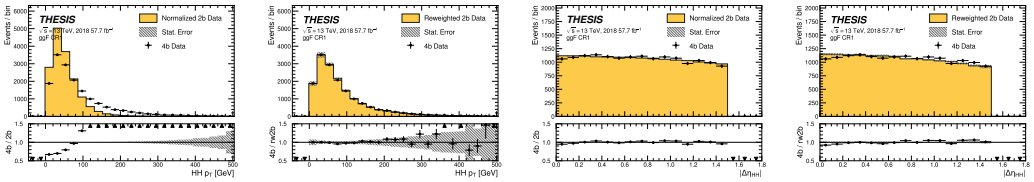

(m) $p_{T,HH}$ before reweighting (n) $p_{T,HH}$ after reweighting (o) $\Delta\eta_{HH}$ before reweighting (p) $\Delta\eta_{HH}$ after reweighting

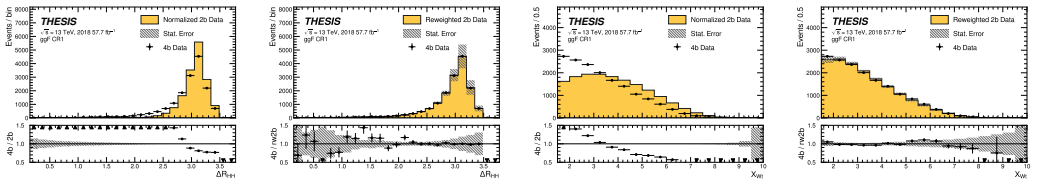

(q) ΔR_{HH} before reweighting (r) ΔR_{HH} after reweighting (s) X_{wt} before reweighting (t) X_{wt} after reweighting

Figure C.6 Kinematic distributions of normalized 2b data, reweighted 2b data and 4b data in the ggF control region 1 in 2018. For the normalized 2b data, the statistic uncertainty includes only 2b poisson uncertainty. For the reweighted 2b data, the statistic uncertainty includes 2b poisson uncertainty and the bootstrap statistic uncertainty.

C.2 VBF channel CR1

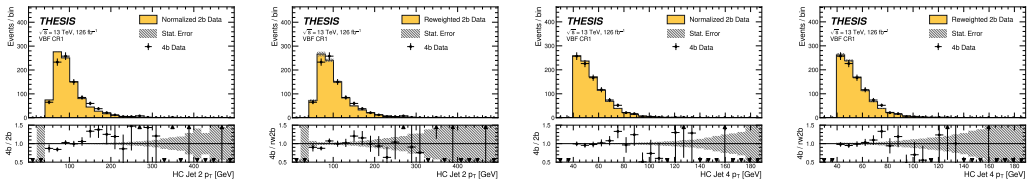

(a) $p_{T,2}$ before reweighting (b) $p_{T,2}$ after reweighting (c) $p_{T,4}$ before reweighting (d) $p_{T,4}$ after reweighting

(e) η_i before reweighting (f) η_i after reweighting (g) njets before reweighting (h) njets after reweighting

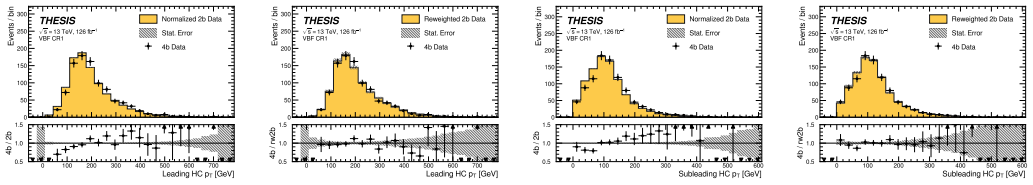

(i) $p_{T,H1}$ before reweighting (j) $p_{T,H1}$ after reweighting (k) $p_{T,H2}$ before reweighting (l) $p_{T,H2}$ after reweighting

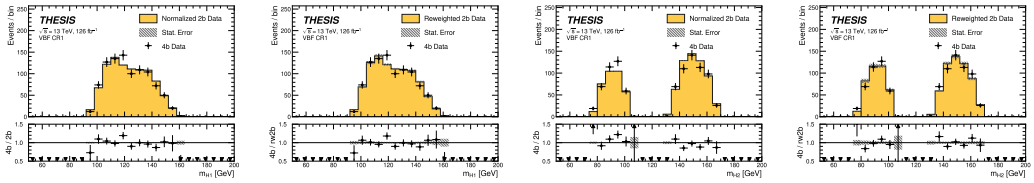

(m) m_{H1} before reweighting (n) m_{H1} after reweighting (o) m_{H2} before reweighting (p) m_{H2} after reweighting

Figure C.7 Kinematic distributions of normalized 2b data, reweighted 2b data and 4b data in the VBF control region 1 For the normalized 2b data, the statistic uncertainty includes only 2b poisson uncertainty. For the reweighted 2b data, the statistic uncertainty includes 2b poisson uncertainty and the bootstrap statistic uncertainty.

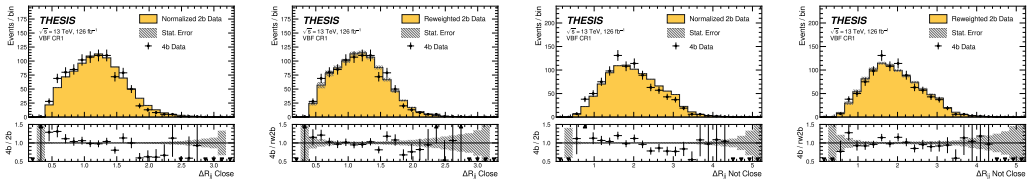

(a) $\Delta R_{jj,1}$ before reweighting (b) $\Delta R_{jj,1}$ after reweighting (c) $\Delta R_{jj,2}$ before reweighting (d) $\Delta R_{jj,2}$ after reweighting

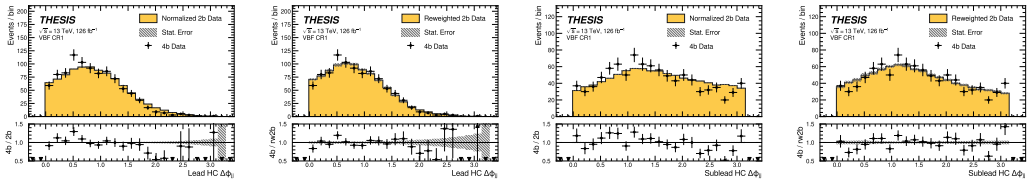

(e) $\Delta\phi_{H1}$ before reweighting (f) $\Delta\phi_{H1}$ after reweighting (g) $\Delta\phi_{H2}$ before reweighting (h) $\Delta\phi_{H2}$ after reweighting

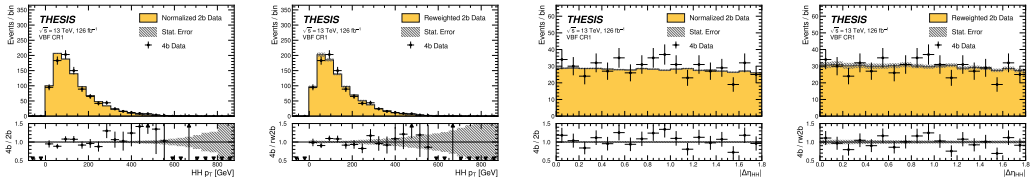

(i) $p_{\mathrm{T},HH}$ before reweighting (j) $p_{\mathrm{T},HH}$ after reweighting (k) $\Delta\eta_{HH}$ before reweighting (l) $\Delta\eta_{HH}$ after reweighting

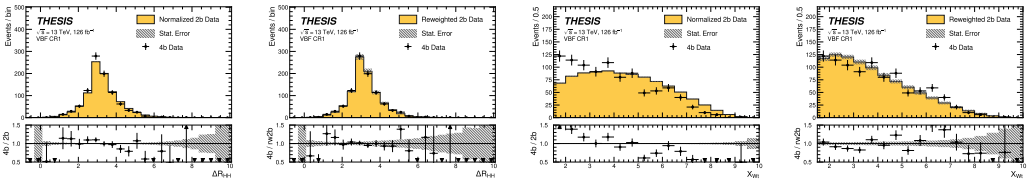

(m) ΔR_{HH} before reweighting (n) ΔR_{HH} after reweighting (o) X_{wt} before reweighting (p) X_{wt} after reweighting

Figure C.8 Kinematic distributions of normalized 2b data, reweighted 2b data and 4b data in the VBF control region 1. For the normalized 2b data, the statistic uncertainty includes only 2b poisson uncertainty. For the reweighted 2b data, the statistic uncertainty includes 2b poisson uncertainty and the bootstrap statistic uncertainty.

Appendix D

Full Statistics Plots in 3b1f Region

This section shows m_{HH} distributions of 3b1f data and the reweighted 2b data with the full statistics to support the 3b1f validation in Section 8.2.2. In the ggF channel, the non-closure between 3b1f data and the reweighted 2b data is observed. As can be seen in Section 8.2.2, the non-closure is observed in the 3b1f validation with the downsampled statistics too. This result shows that the non-closure is not due to statistical limits on the neural network training. Therefore, I decided to add an additional uncertainty for the 3b1f non-closure for the ggF channel. In the VBF channel, good agreements are observed between 3b1f data and the reweighted 2b data with full statistics too.

D.1 ggF channel

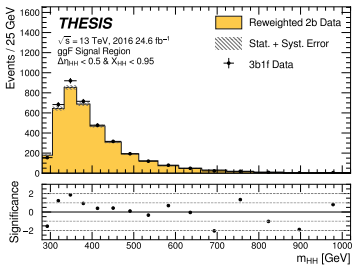

(a) $|\Delta\eta_{HH}| < 0.5$ & $X_{HH} < 0.95$

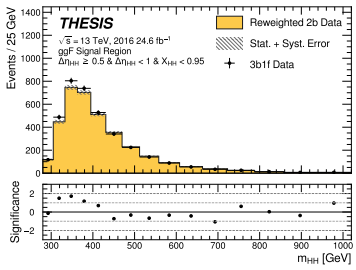

(b) $0.5 \leq |\Delta\eta_{HH}| < 1.0$ & $X_{HH} < 0.95$

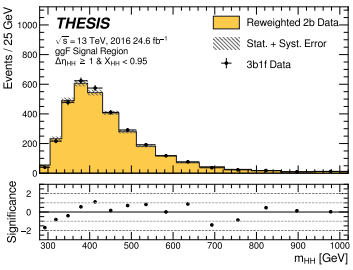

(c) $|\Delta\eta_{HH}| \geq 1.0$ & $X_{HH} < 0.95$

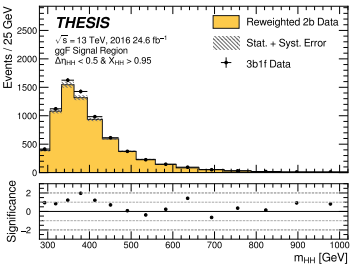

(d) $|\Delta\eta_{HH}| < 0.5$ & $X_{HH} \geq 0.95$

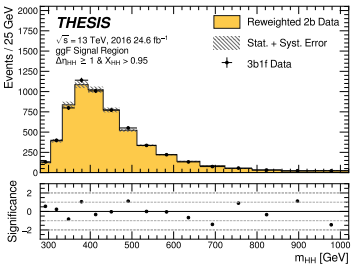

(e) $0.5 \leq |\Delta\eta_{HH}| < 1.0$ & $X_{HH} \geq 0.95$

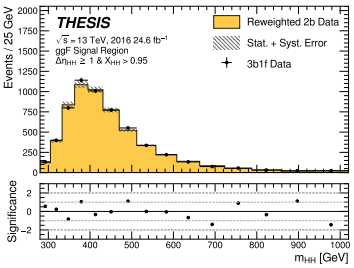

(f) $|\Delta\eta_{HH}| \geq 1.0$ & $X_{HH} \geq 0.95$

Figure D.1 m_{HH} distributions of 3b1f and the background estimation in the ggF signal region with the X_{HH} and $|\Delta\eta_{HH}|$ categorization in 2016.

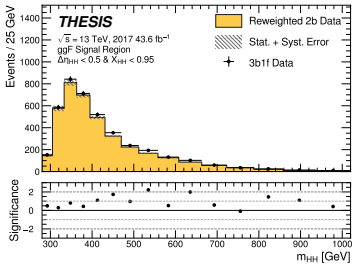

(a) $|\Delta\eta_{HH}| < 0.5$ & $X_{HH} < 0.95$

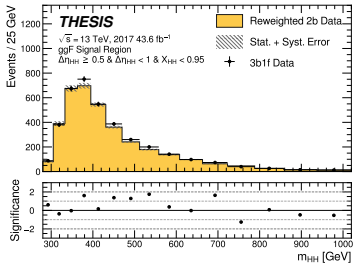

(b) $0.5 \leq |\Delta\eta_{HH}| < 1.0$ & $X_{HH} < 0.95$

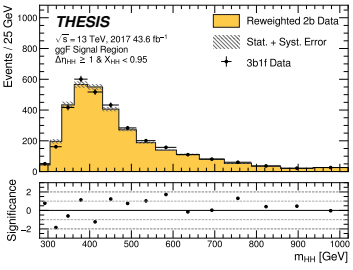

(c) $|\Delta\eta_{HH}| \geq 1.0$ & $X_{HH} < 0.95$

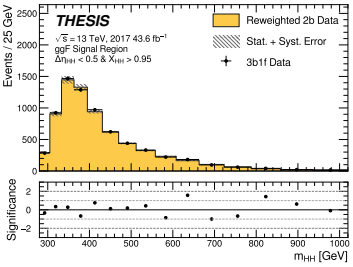

(d) $|\Delta\eta_{HH}| < 0.5$ & $X_{HH} \geq 0.95$

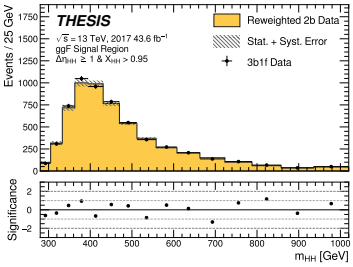

(e) $0.5 \leq |\Delta\eta_{HH}| < 1.0$ & $X_{HH} \geq 0.95$

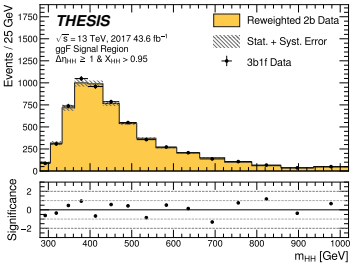

(f) $|\Delta\eta_{HH}| \geq 1.0$ & $X_{HH} \geq 0.95$

Figure D.2 m_{HH} distributions of 3b1f and the background estimation in the ggF signal region with the X_{HH} and $|\Delta\eta_{HH}|$ categorization in 2017.

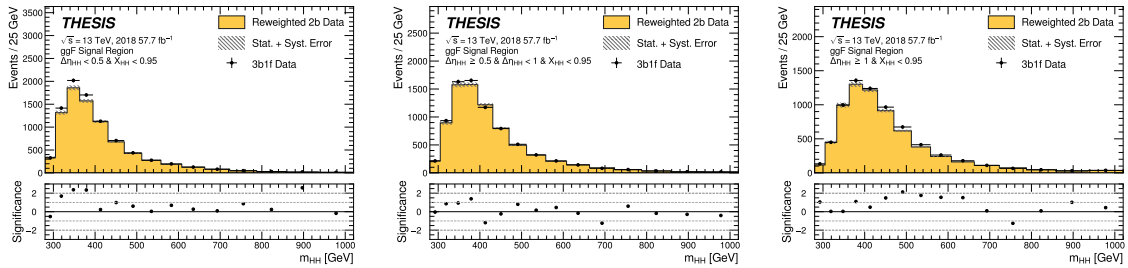

(a) $|\Delta\eta_{HH}| < 0.5$ & $X_{HH} < 0.95$ (b) $0.5 \leq |\Delta\eta_{HH}| < 1.0$ & $X_{HH} < 0.95$ (c) $|\Delta\eta_{HH}| \geq 1.0$ & $X_{HH} < 0.95$

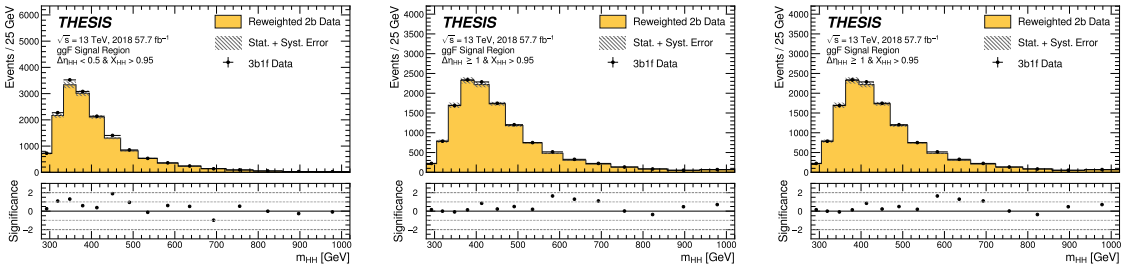

(d) $|\Delta\eta_{HH}| < 0.5$ & $X_{HH} \geq 0.95$ (e) $0.5 \leq |\Delta\eta_{HH}| < 1.0$ & $X_{HH} \geq 0.95$ (f) $|\Delta\eta_{HH}| \geq 1.0$ & $X_{HH} \geq 0.95$

Figure D.3 m_{HH} distributions of 3b1f and the background estimation in the ggF signal region with the X_{HH} and $|\Delta\eta_{HH}|$ categorization in 2018.

D.2 VBF channel

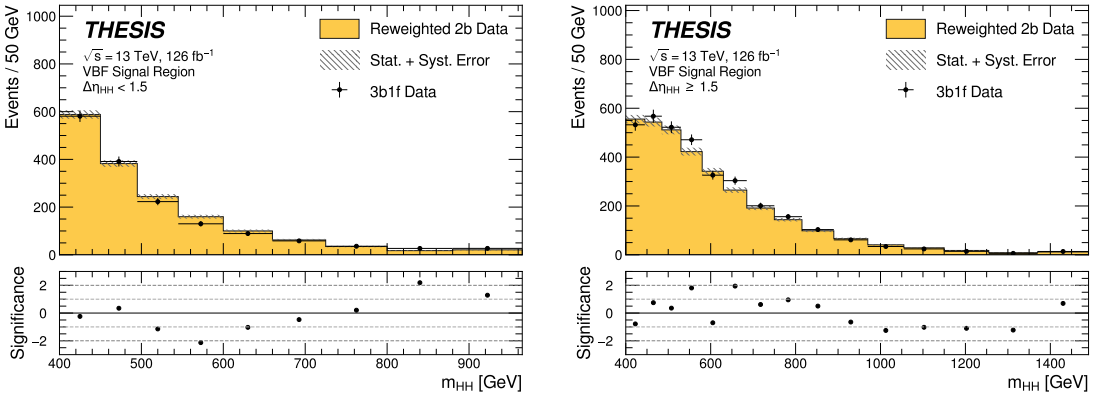

(a) $|\Delta\eta_{HH}| < 1.5$ (b) $1.5 \leq |\Delta\eta_{HH}|$

Figure D.4 m_{HH} distributions of 3b1f and the background estimation in the VBF signal region with the $|\Delta\eta_{HH}|$ categorization.

Appendix E

Summary of the Parton Shower and Hadronization Uncertainties

This section summarizes the parton shower and hadronization uncertainties for the ggF and VBF samples discussed in Section 9.2. The tables show the values used in this analysis.

E.1 ggF HH signals

Sample	Category	16	17	18
SM ggF HH	$\|\Delta\eta_{HH}\| < 0.5$ & $X_{HH} < 0.95$	±9.8%	±7.9%	±11.9%
	$0.5 < \|\Delta\eta_{HH}\| < 1.0$ & $X_{HH} < 0.95$	±10.0%	±8.5%	±8.5%
	$1.0 < \|\Delta\eta_{HH}\| < 1.5$ & $X_{HH} < 0.95$	±13.1%	±18.2%	±6.9%
	$\|\Delta\eta_{HH}\| < 0.5$ & $X_{HH} > 0.95$	±7.0%	±8.1%	±9.3%
	$0.5 < \|\Delta\eta_{HH}\| < 1.0$ & $X_{HH} > 0.95$	±8.1%	±7.1%	±8.8%
	$1.0 < \|\Delta\eta_{HH}\| < 1.5$ & $X_{HH} > 0.95$	±11.8%	±10.0%	±11.9%
$\kappa_\lambda = 10$ ggF HH	$\|\Delta\eta_{HH}\| < 0.5$ & $X_{HH} < 0.95$	±12.2%	±14.1%	±20.6%
	$0.5 < \|\Delta\eta_{HH}\| < 1.0$ & $X_{HH} < 0.95$	±23.1%	±32.8%	±19.2%
	$1.0 < \|\Delta\eta_{HH}\| < 1.5$ & $X_{HH} < 0.95$	±26.1%	±31.1%	±11.2%
	$\|\Delta\eta_{HH}\| < 0.5$ & $X_{HH} > 0.95$	±11.7%	±59.5%	±12.3%
	$0.5 < \|\Delta\eta_{HH}\| < 1.0$ & $X_{HH} > 0.95$	±20.4%	±25.1%	±18.5%
	$1.0 < \|\Delta\eta_{HH}\| < 1.5$ & $X_{HH} > 0.95$	±28.0%	±18.1%	±18.6%

Table E.1 Summary the parton shower and hadronization uncertainties for the ggF HH sigals in the ggF categories.

Sample	Category	All
SM ggF HH	$\|\Delta\eta_{HH}\| < 1.5$	±17.5%
	$1.5 < \|\Delta\eta_{HH}\|$	±37.3%
$\kappa_\lambda = 10$ ggF HH	$\|\Delta\eta_{HH}\| < 1.5$	±43.9%
	$1.5 < \|\Delta\eta_{HH}\|$	±38.5%

Table E.2 Summary the parton shower and hadronization uncertainties for the ggF HH sigals in the VBF categories.

E.2 VBF HH signals

Sample	Category	16	17	18
SM VBF HH	$\|\Delta\eta_{HH}\| < 0.5$ & $X_{HH} < 0.95$	±39.5%	±29.6%	±25.7%
	$0.5 < \|\Delta\eta_{HH}\| < 1.0$ & $X_{HH} < 0.95$	±28.6%	±35.8%	±25.9%
	$1.0 < \|\Delta\eta_{HH}\| < 1.5$ & $X_{HH} < 0.95$	±32.5%	±24.8%	±26.9%
	$\|\Delta\eta_{HH}\| < 0.5$ & $X_{HH} > 0.95$	±30.3%	±30.4%	±29.7%
	$0.5 < \|\Delta\eta_{HH}\| < 1.0$ & $X_{HH} > 0.95$	±32.1%	±23.0%	±28.4%
	$1.0 < \|\Delta\eta_{HH}\| < 1.5$ & $X_{HH} > 0.95$	±26.3%	±28.8%	±32.8%
$\kappa_\lambda = 10$ VBF HH	$\|\Delta\eta_{HH}\| < 0.5$ & $X_{HH} < 0.95$	±20.9%	±17.1%	±16.0%
	$0.5 < \|\Delta\eta_{HH}\| < 1.0$ & $X_{HH} < 0.95$	±18.3%	±26.1%	±17.0%
	$1.0 < \|\Delta\eta_{HH}\| < 1.5$ & $X_{HH} < 0.95$	±27.4%	±41.6%	±19.1%
	$\|\Delta\eta_{HH}\| < 0.5$ & $X_{HH} > 0.95$	±24.0%	±19.1%	±17.3%
	$0.5 < \|\Delta\eta_{HH}\| < 1.0$ & $X_{HH} > 0.95$	±26.1%	±19.2%	±18.9%
	$1.0 < \|\Delta\eta_{HH}\| < 1.5$ & $X_{HH} > 0.95$	±33.9%	±26.6%	±24.1%
$\kappa_{2V} = 0$ VBF HH	$\|\Delta\eta_{HH}\| < 0.5$ & $X_{HH} < 0.95$	±12.4%	±9.5%	±8.7%
	$0.5 < \|\Delta\eta_{HH}\| < 1.0$ & $X_{HH} < 0.95$	±15.6%	±11.2%	±8.8%
	$1.0 < \|\Delta\eta_{HH}\| < 1.5$ & $X_{HH} < 0.95$	±18.1%	±18.3%	±15.4%
	$\|\Delta\eta_{HH}\| < 0.5$ & $X_{HH} > 0.95$	±20.8%	±8.3%	±10.5%
	$0.5 < \|\Delta\eta_{HH}\| < 1.0$ & $X_{HH} > 0.95$	±13.2%	±10.7%	±13.5%
	$1.0 < \|\Delta\eta_{HH}\| < 1.5$ & $X_{HH} > 0.95$	±19.8%	±14.9%	±11.6%

Table E.3 Summary the parton shower and hadronization uncertainties for the VBF HH sigals in the ggF categories.

Sample	Category	All
SM VBF HH	$\|\Delta\eta_{HH}\| < 1.5$	±10.1%
	$1.5 < \|\Delta\eta_{HH}\|$	±10.6%
$\kappa_\lambda = 10$ VBF HH	$\|\Delta\eta_{HH}\| < 1.5$	±10.5%
	$1.5 < \|\Delta\eta_{HH}\|$	±22.1%
$\kappa_{2V} = 0$ VBF HH	$\|\Delta\eta_{HH}\| < 1.5$	±4.6%
	$1.5 < \|\Delta\eta_{HH}\|$	±10.7%

Table E.4 Summary the parton shower and hadronization uncertainties for the VBF HH sigals in the VBF categories.

Appendix F

Summary of the SMEFT and HEFT Reweighting Uncertainties

This section summarizes the SMEFT and HEFT reweighting uncertainties discussed in Section 9.2. The tables show the values used in this analysis.

F.1 SMEFT Reweighting Uncertainty

Limit	Low bins	High bins
SMEFT c_H 1D	±9%	±10%
SMEFT $c_{H\Box}$ 1D	±10%	±26%
SMEFT c_{HG} 1D	±3%	±28%
SMEFT c_{tH} 1D	±9%	±23%
SMEFT c_{tG} 1D	±6%	±27%
SMEFT c_H −$c_{H\Box}$ 2D	±8%	±3%
SMEFT c_H −c_{HG} 2D	±3%	±28%
SMEFT c_H −c_{tH} 2D	±6%	±20%
SMEFT c_H −c_{tG} 2D	±5%	±16%

Table F.1 Summary of the SMEFT reweighting uncertainty for the SMEFT 1D and 2D results.

F.2 HEFT Reweighting Uncertainty

Limit	Low bins	High bins
BM1	±1%	±28%
BM2	±1%	±38%
BM3	±1%	±26%
BM4	±2%	±10%
BM5	±3%	±23%
BM6	±3%	±20%
BM7	±1%	±19%
HEFT c_{ggHH} 1D	±2%	±24%
HEFT $c_{t\bar{t}HH}$ 1D	±3%	±19%

Table F.2 Summary of the HEFT reweighting uncertainty for the HEFT BMs and 1D results.

Appendix G

Full Pulls Plots

This section shows pull plots with all systematic uncertainties from the background only fit in the *gg*F channel and the VBF channel to support Section 11.1. In Section 11.1, the pull plots showing the background modelling uncertainties are picked up and shown. From the pull plots in this section, no large pull associated with the signal modelling uncertainties is observed.

G.1 *gg*F channel

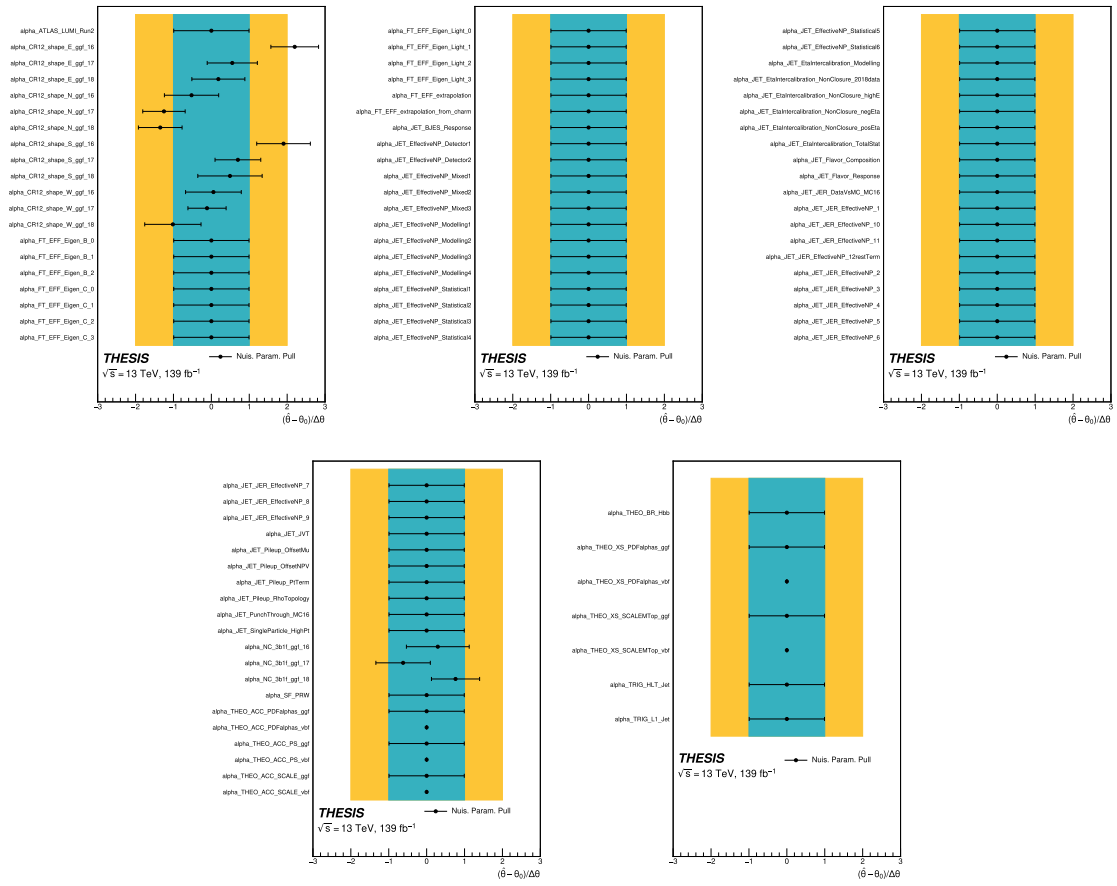

Figure G.1 Pulls when performing the background only fit in the ggF channel

G.2 VBF channel

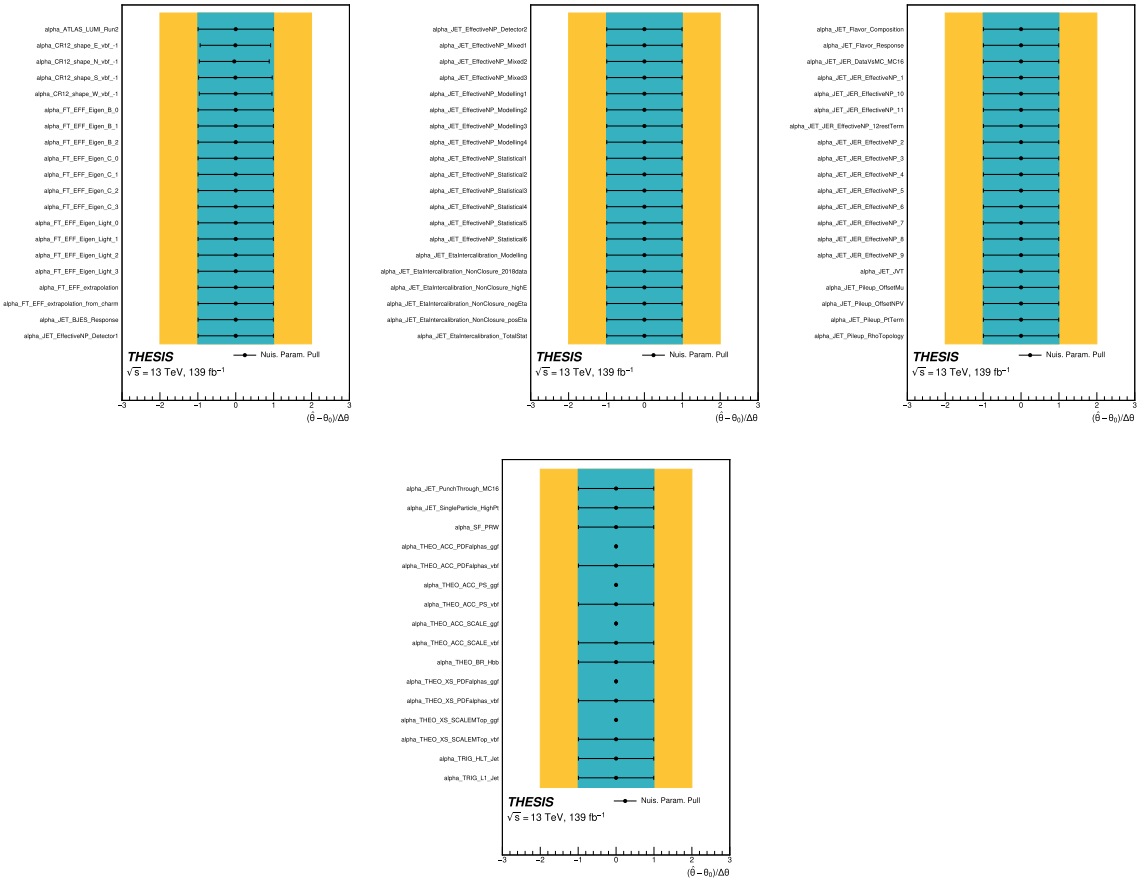

Figure G.2 Pulls when performing the background only fit in the VBF channel.

Appendix H

Full Correlation Matrix

This section shows correlation matrix plots with all systematic uncertainties from the background only fit in the *gg*F channel and the VBF channel to support Section 11.1. In Section 11.1, the correlation matrix plots with only the background modelling uncertainties are shown. From the correlation matrix plots in this section, it is observed that there is few correlation between the signal modelling uncertainties.

H.1 *gg*F channel

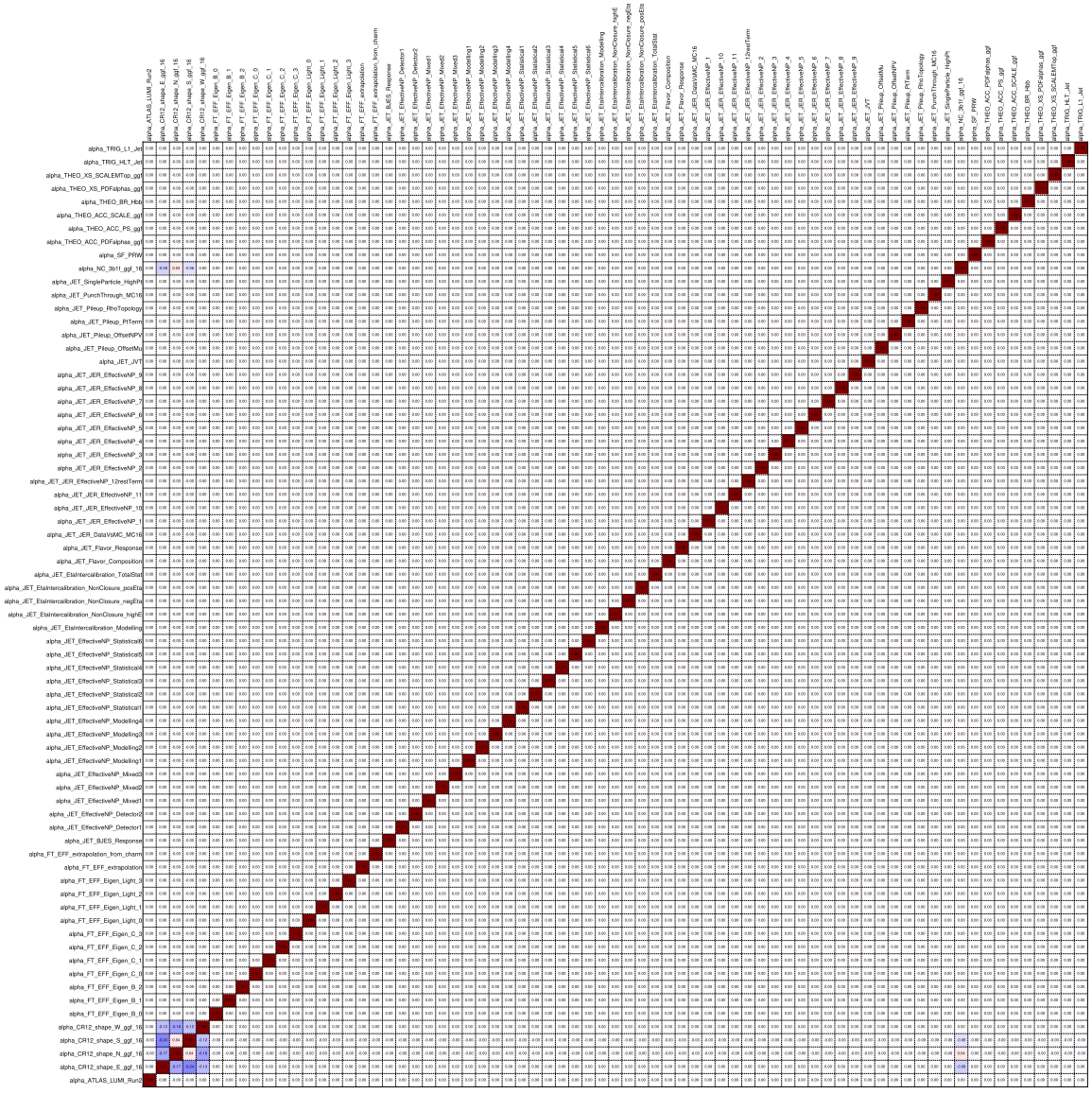

Figure H.1 Correlation matrix from the background only fit in the *gg*F channel in 2016. White boxes indicate no correlation (0.00), blue boxes indicate negative correlations (< 0.00) and red boxes indicate positive correlation (> 0.00). The color shade indicates the correlation strength.

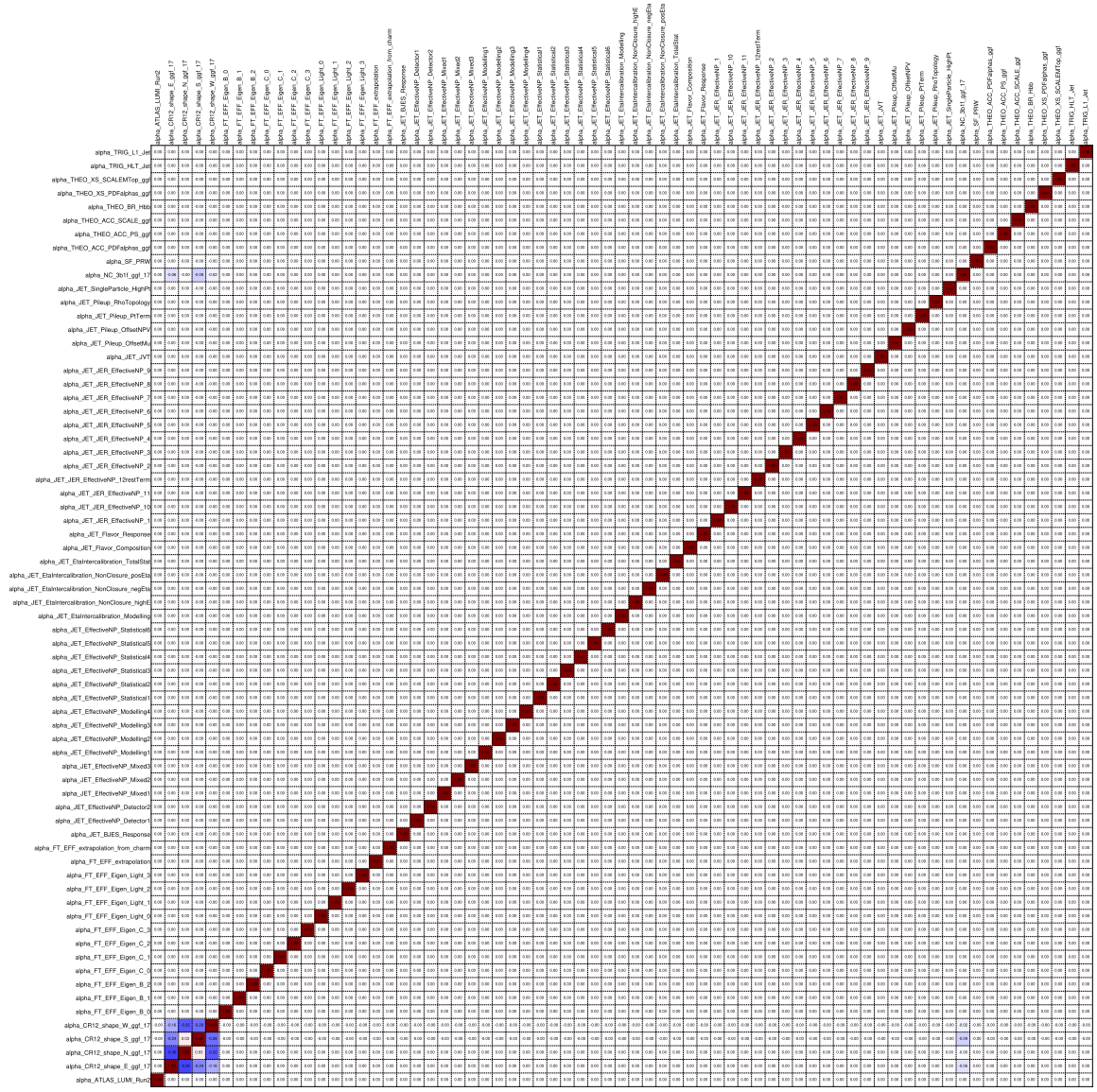

Figure H.2 Correlation matrix from the background only fit in the *gg*F channel in 2017. White boxes indicate no correlation (0.00), blue boxes indicate negative correlations (< 0.00) and red boxes indicate positive correlation (> 0.00). The color shade indicates the correlation strength.

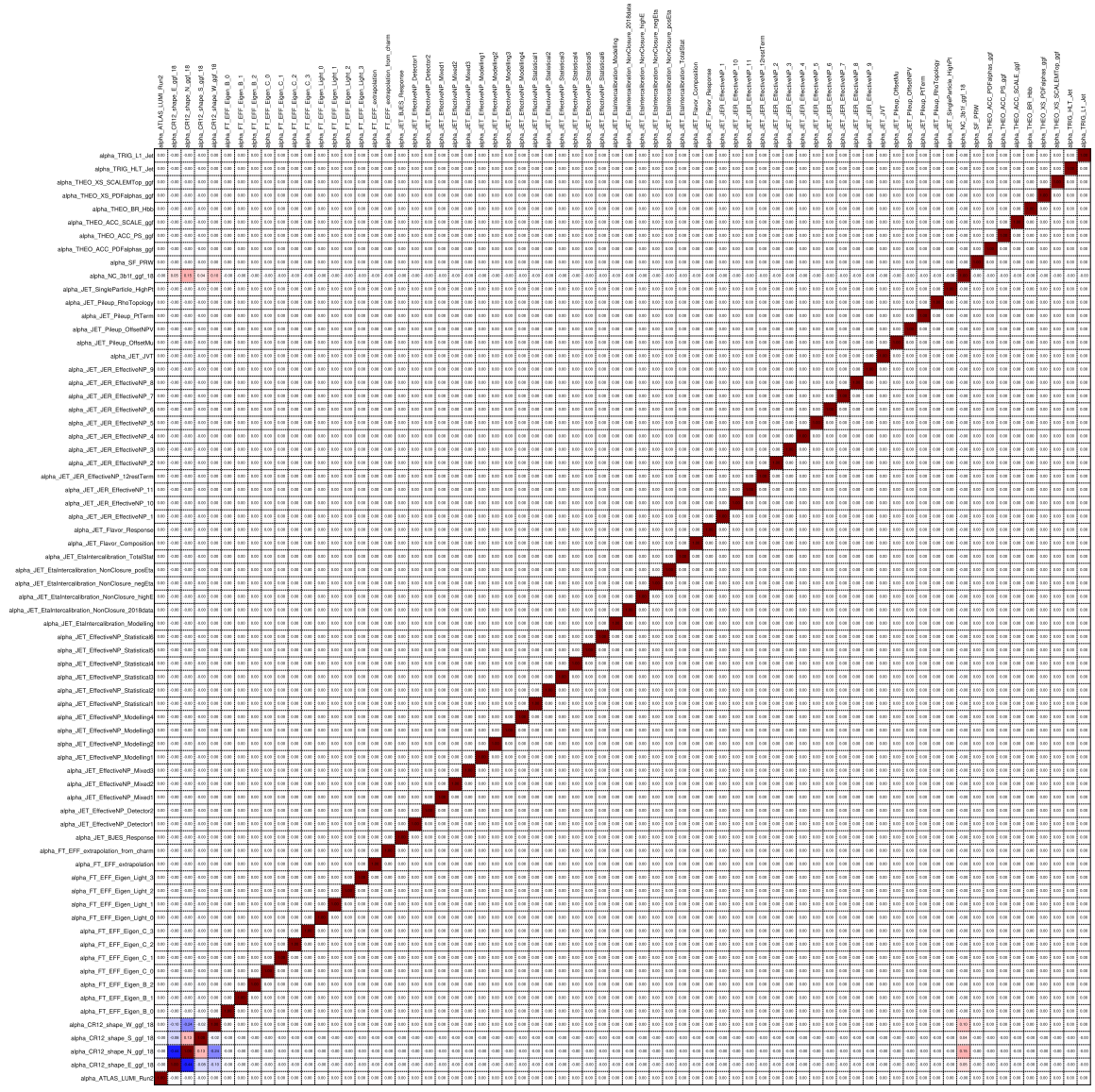

Figure H.3 Correlation matrix from the background only fit in the *gg*F channel in 2018. White boxes indicate no correlation (0.00), blue boxes indicate negative correlations (< 0.00) and red boxes indicate positive correlation (> 0.00). The color shade indicates the correlation strength.

H.2 VBF **channel**

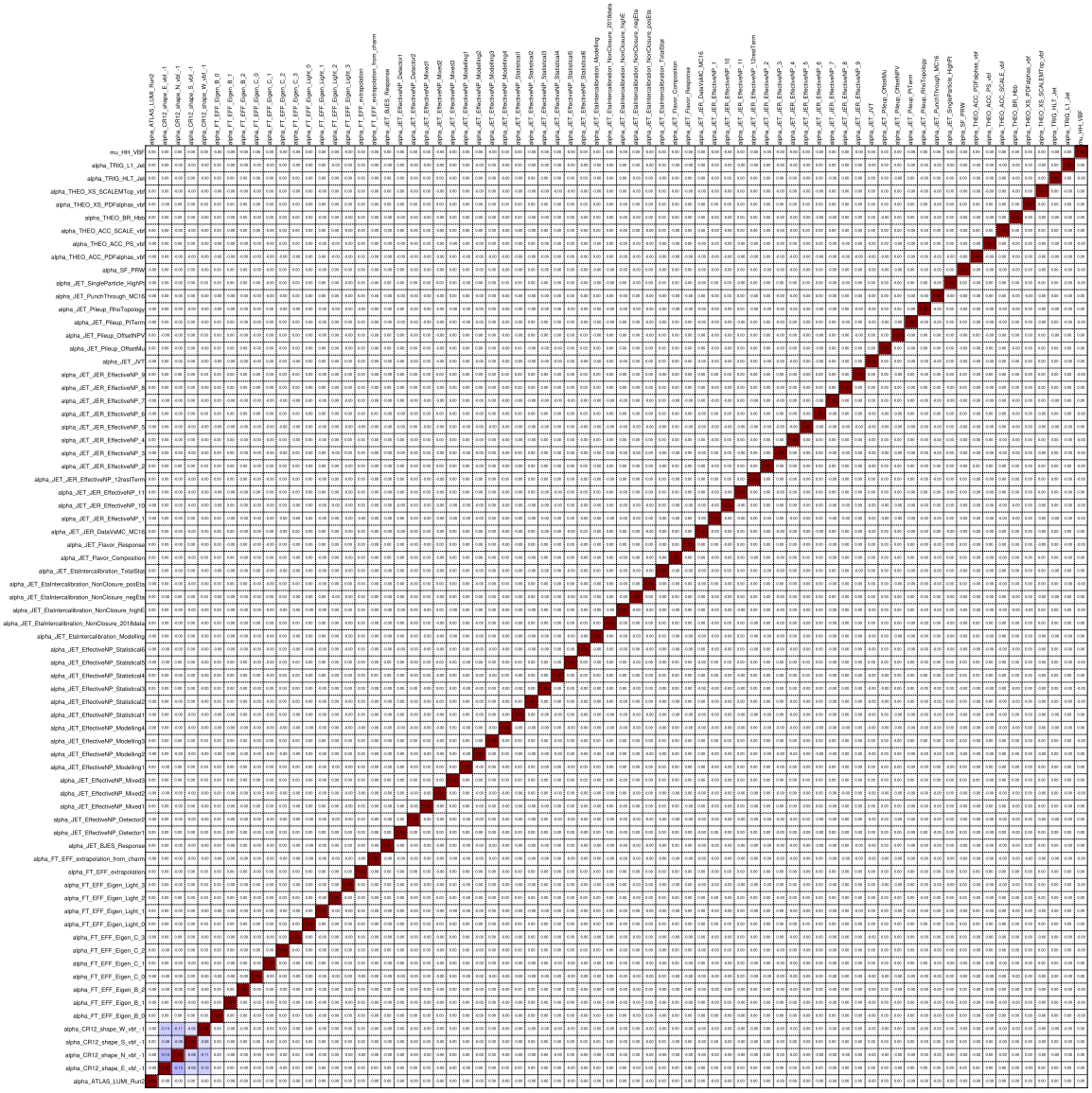

Figure H.4 Correlation matrix from the background only fit in the VBF channel. White boxes indicate no correlation (0.00), blue boxes indicate negative correlations (< 0.00) and red boxes indicate positive correlation (> 0.00). The color shade indicates the correlation strength.

Appendix I

Prospect of HH Search with the ATLAS and CMS Combination at the HL-LHC

A simple combination of the HH measurements from the ATLAS experiment and the CMS experiment is performed. The prospect measurements from the CMS experiment are taken from Ref. [131, 132] and shown in Table I.1. It should be noted that all the channels except for the $b\bar{b}\gamma\gamma$ are not updated to the latest analysis strategy. This means we can expect higher sensitivities in these channels than what I show here. These channels from the ATLAS and CMS experiments are treated as uncorrelated when performing the combination. Systematic uncertainties such as theoretical uncertainties are expected to be correlated between the experiments, but they have little impact on the results. A combined significance with the ATLAS and CMS experiments is expected to be 5.8 standard deviation in statistical-only scenario and 4.4 standard deviation in statistical + systematic scenario.

Table I.1 Significances in standard deviation of SM HH searches in the channels and the combination in the ATLAS and CMS experiments using 3000 fb^{-1} at $\sqrt{s} = 14$ TeV.

	Statistical-only		Statistical + Systematic	
Channel	ATLAS	CMS	ATLAS	CMS
$b\bar{b}b\bar{b}$	1.8	1.2	1.0	0.95
$b\bar{b}\gamma\gamma$	2.3	2.2	2.2	2.2
$b\bar{b}\tau\tau$	4.0	1.6	2.8	1.4
$b\bar{b}WW(l\nu l\nu)$	-	0.59	-	0.56
$b\bar{b}ZZ(llll)$	-	0.37	-	0.37
Combination	4.9	3.1	3.4	2.9
ATLAS + CMS Combination	5.8		4.4	

References

[1] ATLAS Collaboration, G. Aad et al., *Observation of a new particle in the search for the Standard Model Higgs boson with the ATLAS detector at the LHC*, Phys. Lett. B **716** (2012) 1–29, arXiv:1207.7214 [hep-ex].

[2] CMS Collaboration, S. Chatrchyan et al., *Observation of a new boson at a mass of 125 GeV with the CMS experiment at the LHC*, Phys. Lett. B **716** (2012) 30–61, arXiv:1207.7235 [hep-ex].

[3] G. Aad et al., *The ATLAS Experiment at the CERN Large Hadron Collider*, Journal of Instrumentation **3** (2008) S08003–S08003.

[4] S. Chatrchyan et al., *The CMS experiment at the CERN LHC*, Journal of Instrumentation **3** (2008) S08004–S08004.

[5] ATLAS Collaboration, M. Aaboud et al., *Search for pair production of Higgs bosons in the $b\bar{b}b\bar{b}$ final state using proton-proton collisions at $\sqrt{s} = 13$ TeV with the ATLAS detector*, Journal of High Energy Physics **2019** (2019) 30, arXiv:1804.06174 [hep-ex].

[6] ATLAS Collaboration, G. Aad et al., *Search for the $HH \to b\bar{b}b\bar{b}$ process via vector-boson fusion production using proton-proton collisions at $\sqrt{s} = 13$ TeV with the ATLAS detector*, Journal of High Energy Physics **2020** (2020) 108, arXiv:2001.05178 [hep-ex].

[7] ATLAS Collaboration, G. Aad et al., *Erratum to: Search for the $HH \to b\bar{b}b\bar{b}$ process via vector-boson fusion production using proton-proton collisions at s = 13 TeV with the ATLAS detector (Journal of High Energy Physics, (2020), 2020, 7, (108), 10.1007/JHEP07(2020)108)*, Journal of High Energy Physics **2021** (2021).

[8] K. Agashe, H. Davoudiasl, G. Perez, and A. Soni, *Warped Gravitons at the LHC and Beyond*, Phys. Rev. D **76** (2007) 036006, arXiv:hep-ph/0701186.

[9] A. L. Fitzpatrick, J. Kaplan, L. Randall, and L.-T. Wang, *Searching for the Kaluza-Klein Graviton in Bulk RS Models*, JHEP **09** (2007) 013, arXiv:hep-ph/0701150.

[10] T. D. Lee, *A Theory of Spontaneous T Violation*, Phys. Rev. D **8** (1973) 1226–1239.

[11] G. C. Branco, P. M. Ferreira, L. Lavoura, M. N. Rebelo, M. Sher, and J. P. Silva, *Theory and phenomenology of two-Higgs-doublet models*, Phys. Rept. **516** (2012) 1–102, arXiv:1106.0034 [hep-ph].

[12] P. Bagnaia et al., *Evidence for $Z^0 \to e^+e^-$ at the CERN pp collider*, Physics Letters B **129** (1983) 130–140.

[13] UA2 Collaboration, M. Banner et al., *Observation of Single Isolated Electrons of High Transverse Momentum in Events with Missing Transverse Energy at the CERN anti-p p Collider*, Phys. Lett. B **122** (1983) 476–485.

[14] D0 Collaboration, S. Abachi et al., *Observation of the top quark*, Phys. Rev. Lett. **74** (1995) 2632–2637, arXiv:hep-ex/9503003.

[15] S. L. Glashow, *Partial Symmetries of Weak Interactions*, Nucl. Phys. **22** (1961) 579–588.

[16] S. Weinberg, *A Model of Leptons*, Phys. Rev. Lett. **19** (1967) 1264–1266.

[17] A. Salam, *Weak and Electromagnetic Interactions*, Conf. Proc. C **680519** (1968) 367–377.

[18] T. D. Lee and C.-N. Yang, *Question of Parity Conservation in Weak Interactions*, Phys. Rev. **104** (1956) 254–258.

[19] C. S. Wu, E. Ambler, R. W. Hayward, D. D. Hoppes, and R. P. Hudson, *Experimental Test of Parity Conservation in β Decay*, Phys. Rev. **105** (1957) 1413–1414.

[20] F. Englert and R. Brout, *Broken Symmetry and the Mass of Gauge Vector Mesons*, Phys. Rev. Lett. **13** (1964) 321–323.

[21] P. W. Higgs, *Broken symmetries, massless particles and gauge fields*, Phys. Lett. **12** (1964) 132–133.

[22] ATLAS Collaboration,, *A detailed map of Higgs boson interactions by the ATLAS experiment ten years after the discovery*, Nature **607** (2022) 52–59, arXiv:2207.00092 [hep-ex].

[23] CMS Collaboration,, *A portrait of the Higgs boson by the CMS experiment ten years after the discovery*, Nature **607** (2022) 60–68, arXiv:2207.00043 [hep-ex].

[24] D. B. Kaplan, H. Georgi, and S. Dimopoulos, *Composite Higgs Scalars*, Phys. Lett. B **136** (1984) 187–190.

[25] G. Panico and A. Wulzer, *The Composite Nambu-Goldstone Higgs*, vol. 913. Springer, 2016. arXiv:1506.01961 [hep-ph].

[26] C. T. Hill, *Is the Higgs Boson Associated with Coleman-Weinberg Dynamical Symmetry Breaking?*, Phys. Rev. D **89** (2014) 073003, arXiv:1401.4185 [hep-ph].

[27] A. J. Helmboldt, P. Humbert, M. Lindner, and J. Smirnov, *Minimal conformal extensions of the Higgs sector*, JHEP **07** (2017) 113, arXiv:1603.03603 [hep-ph].

[28] K. Hashino, S. Kanemura, and Y. Orikasa, *Discriminative phenomenological features of scale invariant models for electroweak symmetry breaking*, Phys. Lett. B **752** (2016) 217–220, arXiv:1508.03245 [hep-ph].

[29] J. Galloway, M. A. Luty, Y. Tsai, and Y. Zhao, *Induced Electroweak Symmetry Breaking and Supersymmetric Naturalness*, Phys. Rev. D **89** (2014) 075003, arXiv:1306.6354 [hep-ph].

[30] S. Chang, J. Galloway, M. Luty, E. Salvioni, and Y. Tsai, *Phenomenology of Induced Electroweak Symmetry Breaking*, JHEP **03** (2015) 017, arXiv:1411.6023 [hep-ph].

[31] P. Agrawal, D. Saha, L.-X. Xu, J.-H. Yu, and C. P. Yuan, *Determining the shape of the Higgs potential at future colliders*, Phys. Rev. D **101** (2020) 075023, arXiv:1907.02078 [hep-ph].

[32] M. Gell-Mann, *A Schematic Model of Baryons and Mesons*, Phys. Lett. **8** (1964) 214–215.

[33] A. D. Sakharov, *Violation of CP Invariance, C asymmetry, and baryon asymmetry of the universe*, Pisma Zh. Eksp. Teor. Fiz. **5** (1967) 32–35.

[34] D. E. Morrissey and M. J. Ramsey-Musolf, *Electroweak baryogenesis*, New J. Phys. **14** (2012) 125003, arXiv:1206.2942 [hep-ph].

[35] A. Katz and M. Perelstein, *Higgs Couplings and Electroweak Phase Transition*, JHEP **07** (2014) 108, arXiv:1401.1827 [hep-ph].

[36] P. Huang, A. J. Long, and L.-T. Wang, *Probing the Electroweak Phase Transition with Higgs Factories and Gravitational Waves*, Phys. Rev. D **94** (2016) 075008, arXiv:1608.06619 [hep-ph].

[37] V. C. Rubin and J. Ford, W. Kent, *Rotation of the Andromeda Nebula from a Spectroscopic Survey of Emission Regions*, The Astrophysical Journal **159** (1970) 379.

[38] V. C. Rubin, J. Ford, W. K., and N. Thonnard, *Rotational properties of 21 SC galaxies with a large range of luminosities and radii, from NGC 4605 (R=4kpc) to UGC 2885 (R=122kpc).*, The Astrophysical Journal **238** (1980) 471–487.

[39] S. P. Martin, *A Supersymmetry primer*, Adv. Ser. Direct. High Energy Phys. **18** (1998) 1–98, arXiv:hep-ph/9709356.

[40] L. Wu, J. M. Yang, C.-P. Yuan, and M. Zhang, *Higgs self-coupling in the MSSM and NMSSM after the LHC Run 1*, Phys. Lett. B **747** (2015) 378–389, arXiv:1504.06932 [hep-ph].

[41] K. Lane and E. Pilon, *Phenomenology of the new light Higgs bosons in Gildener-Weinberg models*, Phys. Rev. D **101** (2020) 055032, arXiv:1909.02111 [hep-ph].

[42] V. Barger, T. Han, P. Langacker, B. McElrath, and P. Zerwas, *Effects of genuine dimension-six Higgs operators*, Phys. Rev. D **67** (2003) 115001, arXiv:hep-ph/0301097.

[43] L. Di Luzio, R. Gröber, and M. Spannowsky, *Maxi-sizing the trilinear Higgs self-coupling: how large could it be?*, Eur. Phys. J. C **77** (2017) 788, arXiv:1704.02311 [hep-ph].

[44] L. Di Luzio, J. F. Kamenik, and M. Nardecchia, *Implications of perturbative unitarity for scalar di-boson resonance searches at LHC*, Eur. Phys. J. C **77** (2017) 30, arXiv:1604.05746 [hep-ph].

[45] J. Alison et al., *Higgs boson potential at colliders: Status and perspectives*, Rev. Phys. **5** (2020) 100045, arXiv:1910.00012 [hep-ph].

[46] G. P. Salam, *Elements of QCD for hadron colliders*, arXiv:1011.5131 [hep-ph].

[47] J. Gao, L. Harland-Lang, and J. Rojo, *The Structure of the Proton in the LHC Precision Era*, Phys. Rept. **742** (2018) 1–121, arXiv:1709.04922 [hep-ph].

[48] M. Grazzini, G. Heinrich, S. Jones, S. Kallweit, M. Kerner, J. M. Lindert, and J. Mazzitelli, *Higgs boson pair production at NNLO with top quark mass effects*, JHEP **05** (2018) 059, arXiv:1803.02463 [hep-ph].

[49] ATLAS Collaboration, M. Aaboud et al., *Observation of Higgs boson production in association with a top quark pair at the LHC with the ATLAS detector*, Phys. Lett. B **784** (2018) 173–191, arXiv:1806.00425 [hep-ex].

[50] CMS Collaboration, A. M. Sirunyan et al., *Observation of* $\mathrm{t\bar{t}}H$ *production*, Phys. Rev. Lett. **120** (2018) 231801, arXiv:1804.02610 [hep-ex].

[51] M. Gouzevitch and A. Carvalho, *A review of Higgs boson pair production*, Rev. Phys. **5** (2020) 100039.

[52] W. Buchmuller and D. Wyler, *Effective Lagrangian Analysis of New Interactions and Flavor Conservation*, Nucl. Phys. B **268** (1986) 621–653.

[53] C. N. Leung, S. T. Love, and S. Rao, *Low-Energy Manifestations of a New Interaction Scale: Operator Analysis*, Z. Phys. C **31** (1986) 433.

[54] I. Brivio and M. Trott, *The Standard Model as an Effective Field Theory*, Phys. Rept. **793** (2019) 1–98, arXiv:1706.08945 [hep-ph].

[55] R. Alonso, M. B. Gavela, L. Merlo, S. Rigolin, and J. Yepes, *The Effective Chiral Lagrangian for a Light Dynamical "Higgs Particle"*, Phys. Lett. B **722** (2013) 330–335, arXiv:1212.3305 [hep-ph], [Erratum: Phys.Lett.B 726, 926 (2013)].

[56] G. Buchalla, O. Catà, and C. Krause, *Complete Electroweak Chiral Lagrangian with a Light Higgs at NLO*, Nucl. Phys. B **880** (2014) 552–573, arXiv:1307.5017 [hep-ph], [Erratum: Nucl.Phys.B 913, 475–478 (2016)].

[57] B. Grzadkowski, M. Iskrzynski, M. Misiak, and J. Rosiek, *Dimension-Six Terms in the Standard Model Lagrangian*, JHEP **10** (2010) 085, arXiv:1008.4884 [hep-ph].

[58] M. Capozi and G. Heinrich, *Exploring anomalous couplings in Higgs boson pair production through shape analysis*, JHEP **03** (2020) 091, arXiv:1908.08923 [hep-ph].

[59] *LHC Machine*, JINST **3** (2008) S08001.

[60] E. Mobs, *The CERN accelerator complex in 2019. Complexe des accélérateurs du CERN en 2019*, https://cds.cern.ch/record/2684277, General Photo.

[61] ATLAS Collaboration,, *Public ATLAS Luminosity Results for Run-2 of the LHC*, https://twiki.cern.ch/twiki/bin/view/AtlasPublic/LuminosityPublicResultsRun2.

[62] J. Pequenao and P. Schaffner, *How ATLAS detects particles: diagram of particle paths in the detector*, https://cds.cern.ch/record/1505342.

[63] T. Kawaguchi, *Search for the dimuon decay of the Higgs boson in* 139 fb^{-1} *of pp collisions at* $\sqrt{s}$ = 13 TeV *with the ATLAS detector.*, https://cds.cern.ch/record/2754084.

[64] ATLAS Collaboration,, *ATLAS magnet system: Technical design report*,.

[65] K. Potamianos, *The upgraded Pixel detector and the commissioning of the Inner Detector tracking of the ATLAS experiment for Run-2 at the Large Hadron Collider*, PoS **EPS-HEP2015** (2015) 261, arXiv:1608.07850 [physics.ins-det].

[66] G. Ripellino, *The alignment of the ATLAS Inner Detector in Run-2*, PoS **LHCP2016** (2016) 196.

[67] ATLAS Collaboration,, *ATLAS liquid-argon calorimeter: Technical Design Report*, https://cds.cern.ch/record/331061.

[68] M. INOKUTI, *Inelastic Collisions of Fast Charged Particles with Atoms and Molecules—The Bethe Theory Revisited*, Rev. Mod. Phys. **43** (1971) 297–347, https://link.aps.org/doi/10.1103/RevModPhys.43.297.

[69] ATLAS Collaboration, M. Aaboud et al., *Performance of the ATLAS Trigger System in 2015*, Eur. Phys. J. C **77** (2017) 317, arXiv:1611.09661 [hep-ex].

[70] R. Achenbach et al., *The ATLAS level-1 calorimeter trigger*, JINST **3** (2008) P03001.

[71] ATLAS Collaboration, M. Aaboud et al., *Performance of the ATLAS Track Reconstruction Algorithms in Dense Environments in LHC Run 2*, Eur. Phys. J. C **77** (2017) 673, arXiv:1704.07983 [hep-ex].

[72] A. Rosenfeld and J. L. Pfaltz, *Sequential Operations in Digital Picture Processing*, J. ACM **13** (1966) 471–494, https://doi.org/10.1145/321356.321357.

[73] ATLAS Collaboration, G. Aad et al., *A neural network clustering algorithm for the ATLAS silicon pixel detector*, JINST **9** (2014) P09009, arXiv:1406.7690 [hep-ex].

[74] ATLAS Collaboration, G. Aad et al., *Topological cell clustering in the ATLAS calorimeters and its performance in LHC Run 1*, Eur. Phys. J. C **77** (2017) 490, arXiv:1603.02934 [hep-ex].

[75] ATLAS Collaboration, M. Aaboud et al., *Reconstruction of primary vertices at the ATLAS experiment in Run 1 proton–proton collisions at the LHC*, Eur. Phys. J. C **77** (2017) 332, arXiv:1611.10235 [physics.ins-det].

[76] ATLAS Collaboration, M. Aaboud et al., *Jet reconstruction and performance using particle flow with the ATLAS Detector*, Eur. Phys. J. C **77** (2017) 466, arXiv:1703.10485 [hep-ex].

[77] M. Cacciari, G. P. Salam, and G. Soyez, *The anti-k_t jet clustering algorithm*, JHEP **04** (2008) 063, arXiv:0802.1189 [hep-ph].

[78] ATLAS Collaboration, G. Aad et al., *Jet energy scale and resolution measured in proton–proton collisions at $\sqrt{s}$ = 13 TeV with the ATLAS detector*, Eur. Phys. J. C **81** (2021) 689, arXiv:2007.02645 [hep-ex].

[79] M. Cacciari, G. P. Salam, and G. Soyez, *The Catchment Area of Jets*, JHEP **04** (2008) 005, arXiv:0802.1188 [hep-ph].

[80] ATLAS Collaboration,, *Tagging and suppression of pileup jets*,.

[81] A. Hoecker, P. Speckmayer, J. Stelzer, J. Therhaag, E. von Toerne, H. Voss, M. Backes, T. Carli, O. Cohen, A. Christov, D. Dannheim, K. Danielowski, S. Henrot-Versille, M. Jachowski, K. Kraszewski, A. Krasznahorkay, M. Kruk, Y. Mahalalel, R. Ospanov, X. Prudent, A. Robert, D. Schouten, F. Tegenfeldt, A. Voigt, K. Voss, M. Wolter, and A. Zemla, *TMVA - Toolkit for Multivariate Data Analysis*,.

[82] ATLAS Collaboration, G. Aad et al., *ATLAS b-jet identification performance and efficiency measurement with $t\bar{t}$ events in pp collisions at $\sqrt{s}$ = 13 TeV*, Eur. Phys. J. C **79** (2019) 970, arXiv:1907.05120 [hep-ex].

[83] ATLAS Collaboration, C. Magliocca, *Measurement of the track impact parameters resolution with the ATLAS experiment at LHC using 2016-2018 data*, Nuovo Cim. C **44** (2021) 55.

[84] ATLAS Collaboration,, *Identification of Jets Containing b-Hadrons with Recurrent Neural Networks at the ATLAS Experiment*,.

[85] ATLAS Collaboration,, *Topological b-hadron decay reconstruction and identification of b-jets with the JetFitter package in the ATLAS experiment at the LHC*,.

[86] R. Fruhwirth, *Application of Kalman filtering to track and vertex fitting*, Nucl. Instrum. Meth. A **262** (1987) 444–450.

[87] ATLAS Collaboration,, *Expected performance of the 2019 ATLAS b-taggers*, http://atlas.web.cern.ch/Atlas/GROUPS/PHYSICS/PLOTS/FTAG-2019-005, Accessed on Nov. 2022.

[88] ATLAS Collaboration,, *Calibration of the ATLAS b-tagging algorithm in $t\bar{t}$ semi-leptonic events*,.

[89] A. D. Bukin, *Fitting function for asymmetric peaks*,.

[90] D. J. Lange, *The EvtGen particle decay simulation package*, Nucl. Instrum. Meth. A **462** (2001) 152–155.

[91] ATLAS Collaboration, G. Aad et al., *The ATLAS Simulation Infrastructure*, Eur. Phys. J. C **70** (2010) 823–874, arXiv:1005.4568 [physics.ins-det].

[92] GEANT4 Collaboration, S. Agostinelli et al., *GEANT4–a simulation toolkit*, Nucl. Instrum. Meth. A **506** (2003) 250–303.

[93] P. Nason, *A New method for combining NLO QCD with shower Monte Carlo algorithms*, JHEP **11** (2004) 040, arXiv:hep-ph/0409146.

[94] S. Frixione, P. Nason, and C. Oleari, *Matching NLO QCD computations with Parton Shower simulations: the POWHEG method*, JHEP **11** (2007) 070, arXiv:0709.2092 [hep-ph].

[95] S. Alioli, P. Nason, C. Oleari, and E. Re, *A general framework for implementing NLO calculations in shower Monte Carlo programs: the POWHEG BOX*, JHEP **06** (2010) 043, arXiv:1002.2581 [hep-ph].

[96] J. Butterworth et al., *PDF4LHC recommendations for LHC Run II*, J. Phys. G **43** (2016) 023001, arXiv:1510.03865 [hep-ph].

[97] T. Sjöstrand, S. Ask, J. R. Christiansen, R. Corke, N. Desai, P. Ilten, S. Mrenna, S. Prestel, C. O. Rasmussen, and P. Z. Skands, *An introduction to PYTHIA 8.2*, Comput. Phys. Commun. **191** (2015) 159–177, arXiv:1410.3012 [hep-ph].

[98] A. Buckley, *ATLAS Pythia 8 tunes to 7 TeV data*,.

[99] R. D. Ball et al., *Parton distributions with LHC data*, Nucl. Phys. B **867** (2013) 244–289, arXiv:1207.1303 [hep-ph].

[100] M. Bahr et al., *Herwig++ Physics and Manual*, Eur. Phys. J. C **58** (2008) 639–707, arXiv:0803.0883 [hep-ph].

[101] S. Gieseke, C. Rohr, and A. Siodmok, *Colour reconnections in Herwig++*, Eur. Phys. J. C **72** (2012) 2225, arXiv:1206.0041 [hep-ph].

[102] L. A. Harland-Lang, A. D. Martin, P. Motylinski, and R. S. Thorne, *Parton distributions in the LHC era: MMHT 2014 PDFs*, Eur. Phys. J. C **75** (2015) 204, arXiv:1412.3989 [hep-ph].

[103] J. Alwall, R. Frederix, S. Frixione, V. Hirschi, F. Maltoni, O. Mattelaer, H. S. Shao, T. Stelzer, P. Torrielli, and M. Zaro, *The automated computation of tree-level and next-to-leading order differential cross sections, and their matching to parton shower simulations*, JHEP **07** (2014) 079, arXiv:1405.0301 [hep-ph].

[104] F. A. Dreyer and A. Karlberg, *Vector-Boson Fusion Higgs Pair Production at N^3LO*, Phys. Rev. D **98** (2018) 114016, arXiv:1811.07906 [hep-ph].

[105] J. Baglio, A. Djouadi, R. Gröber, M. M. Mühlleitner, J. Quevillon, and M. Spira, *The measurement of the Higgs self-coupling at the LHC: theoretical status*, JHEP **04** (2013) 151, arXiv:1212.5581 [hep-ph].

[106] L.-S. Ling, R.-Y. Zhang, W.-G. Ma, L. Guo, W.-H. Li, and X.-Z. Li, *NNLO QCD corrections to Higgs pair production via vector boson fusion at hadron colliders*, Phys. Rev. D **89** (2014) 073001, arXiv:1401.7754 [hep-ph].

[107] F. A. Dreyer and A. Karlberg, *Fully differential Vector-Boson Fusion Higgs Pair Production at Next-to-Next-to-Leading Order*, Phys. Rev. D **99** (2019) 074028, arXiv:1811.07918 [hep-ph].

[108] C. Degrande, G. Durieux, F. Maltoni, K. Mimasu, E. Vryonidou, and C. Zhang, *Automated one-loop computations in the standard model effective field theory*, Phys. Rev. D **103** (2021) 096024, arXiv:2008.11743 [hep-ph].

[109] ATLAS Collaboration,, *Validation of signal Monte Carlo event generation in searches for Higgs boson pairs with the ATLAS detector*,.

[110] T. Kanamori, S. Hido, and M. Sugiyama, *A Least-squares Approach to Direct Importance Estimation*, J. Mach. Learn. Res. **10** (2009) 1391–1445.

[111] K. B. George V. Moustakides, *Training Neural Networks for Likelihood/Density Ratio Estimation*, arXiv:1911.00405 [eess.SP].

[112] B. Efron, *Bootstrap Methods: Another Look at the Jackknife*, The Annals of Statistics **7** (1979) 1 – 26.

[113] ATLAS Collaboration, M. Aaboud et al., *Luminosity determination in pp collisions at* $\sqrt{s} = 8$ *TeV using the ATLAS detector at the LHC*, Eur. Phys. J. C **76** (2016) 653, arXiv:1608.03953 [hep-ex].

[114] LHC Higgs Cross Section Working Group Collaboration, D. de Florian et al., *Handbook of LHC Higgs Cross Sections: 4. Deciphering the Nature of the Higgs Sector*, arXiv:1610.07922 [hep-ph].

[115] J. Baglio, F. Campanario, S. Glaus, M. Mühlleitner, J. Ronca, and M. Spira, $gg \to HH$ *: Combined uncertainties*, Phys. Rev. D **103** (2021) 056002, arXiv:2008.11626 [hep-ph].

[116] B. Mellado Garcia, P. Musella, M. Grazzini, and R. Harlander, *CERN Report 4: Part I Standard Model Predictions*, https://cds.cern.ch/record/2150771.

[117] G. Cowan, K. Cranmer, E. Gross, and O. Vitells, *Asymptotic formulae for likelihood-based tests of new physics*, Eur. Phys. J. C **71** (2011) 1554, arXiv:1007.1727 [physics.data-an], [Erratum: Eur.Phys.J.C 73, 2501 (2013)].

[118] ROOT Collaboration, K. Cranmer, G. Lewis, L. Moneta, A. Shibata, and W. Verkerke, *HistFactory: A tool for creating statistical models for use with RooFit and RooStats*,.

[119] J. Neyman and E. S. Pearson, *On the Problem of the Most Efficient Tests of Statistical Hypotheses*, Phil. Trans. Roy. Soc. Lond. A **231** (1933) 289–337.

[120] G. Cowan, K. Cranmer, E. Gross, and O. Vitells, *Erratum to: Asymptotic formulae for likelihood-based tests of new physics*, Eur. Phys. J. C **73** (2013) 2501.

[121] J. Ellis, M. Madigan, K. Mimasu, V. Sanz, and T. You, *Top, Higgs, Diboson and Electroweak Fit to the Standard Model Effective Field Theory*, JHEP **04** (2021) 279, arXiv:2012.02779 [hep-ph].

[122] J. Ellis, C. W. Murphy, V. Sanz, and T. You, *Updated Global SMEFT Fit to Higgs, Diboson and Electroweak Data*, JHEP **06** (2018) 146, arXiv:1803.03252 [hep-ph].

[123] ATLAS Collaboration, G. Aad et al., *Search for Higgs boson pair production in the two bottom quarks plus two photons final state in pp collisions at* $\sqrt{s} = 13$ TeV *with the ATLAS detector*, Phys. Rev. D **106** (2022) 052001.

[124] ATLAS Collaboration,, *Search for resonant and non-resonant Higgs boson pair production in the* $b\bar{b}\tau^+\tau^-$ *decay channel using 13 TeV pp collision data from the ATLAS detector*, arXiv:2209.10910 [hep-ex].

[125] ATLAS Collaboration, G. Aad et al., *Combination of searches for Higgs boson pairs in pp collisions at* $\sqrt{s}$ *=13 TeV with the ATLAS detector*, Phys. Lett. B **800** (2020) 135103, arXiv:1906.02025 [hep-ex].

[126] ATLAS Collaboration,, *Combination of searches for non-resonant and resonant Higgs boson pair production in the* $b\bar{b}\gamma\gamma$, $b\bar{b}\tau^+\tau^-$ *and* $b\bar{b}b\bar{b}$ *decay channels using pp collisions at* $\sqrt{s} = 13$ *TeV with the ATLAS detector*,.

[127] I. Zurbano Fernandez et al., *High-Luminosity Large Hadron Collider (HL-LHC): Technical design report*,.

[128] ATLAS Collaboration,, *Measurement prospects of the pair production and self-coupling of the Higgs boson with the ATLAS experiment at the HL-LHC*,.

[129] ATLAS, CMS Collaboration,, *Addendum to the report on the physics at the HL-LHC, and perspectives for the HE-LHC: Collection of notes from ATLAS and CMS*, CERN Yellow Rep. Monogr. **7** (2019) Addendum, arXiv:1902.10229 [hep-ex].

[130] ATLAS Collaboration Collaboration,, *Projected sensitivity of Higgs boson pair production combining the* $b\bar{b}\gamma\gamma$ *and* $b\bar{b}\tau^+\tau^-$ *final states with the ATLAS detector at the HL-LHC*, https://cds.cern.ch/record/2802127.

[131] M. Cepeda et al., *Report from Working Group 2: Higgs Physics at the HL-LHC and HE-LHC*, CERN Yellow Rep. Monogr. **7** (2019) 221–584, arXiv:1902.00134 [hep-ph].

[132] CMS Collaboration,, *Prospects for non-resonant Higgs boson pair production measurement in* $bb\gamma\gamma$ *final states in proton-proton collisions at* $\sqrt{s} = 14$ *TeV at the High-Luminosity LHC*, https://cds.cern.ch/record/2803918.

[133] A. Ruiz-Martinez, J. Montejo Berlingen, D. Zanzi, T. J. Khoo, M. A. Owen, and S. Shaw, *Run 3 trigger menu design*, https://cds.cern.ch/record/2683881.

[134] G. Buchalla, M. Capozi, A. Celis, G. Heinrich, and L. Scyboz, *Higgs boson pair production in non-linear Effective Field Theory with full* m_t*-dependence at NLO QCD*, JHEP **09** (2018) 057, arXiv:1806.05162 [hep-ph].

[135] W. Buttinger and M. Lefebvre, *Formulae for Estimating Significance*, tech. rep., CERN, Geneva, 2018. https://cds.cern.ch/record/2643488.